UNIVERSITY OF SOUTHAMPTON

Faculty of Social Sciences
School of Mathematical Sciences

Neutron star asteroseismology: composition modes and tidal effects

by

Andrew Rhys Counsell

February 2026

University of Southampton

Abstract

Faculty of Social Sciences
School of Mathematical Sciences

Doctor of Philosophy

Neutron star asteroseismology: composition modes and tidal effects

by Andrew Rhys Counsell

In the decade that has passed since the first observation of gravitational waves, a new opportunity to study the physics of neutron stars has presented itself. Gravitational waves emitted by neutron star oscillations can be used to obtain information about the equation of state of dense nuclear matter. The identification of such oscillations gives rise to the field of neutron star asteroseismology. In this work we focus on two types of quadrupolar oscillations: gravity g-modes and interface i-modes. We also examine the different regimes under which the mode equations are solved: Newtonian gravity; general relativity and the Cowling approximation to general relativity. Their various benefits and inaccuracies are discussed.

The effects of stratification, composition and nuclear reactions on the g-mode spectrum are studied for equations of state from the BSk family. By incorporating the reaction rates directly into the mode calculations we see that at the low temperatures expected in the neutron star during inspiral, the damping of the modes is insignificant but for the higher order g-modes. However extending the analysis to include hyperons and their strong reactions, the f-modes is affected for sufficiently massive stars, warranting further investigation.

Second, using a family of nuclear-matter equations of state generated from chiral effective field theory (EFT), we find that the detection of an interface mode would be a *smoking-gun* signature of a first-order phase transition, distinguishable in a single gravitational-wave event. Our estimates show that an i-mode resonance may be observable with Cosmic Explorer and the Einstein Telescope, and possibly already with LIGO A+ for sufficiently strong gravitational wave signals from binary neutron star mergers. One such phase transition that could be probed by this method is that from hadronic matter to deconfied quarks in the neutron star core, a robust prediction of quantum chromodynamics. The exact nature of this transition remains unsolved and therefore an i-mode detection would be a breakthrough discovery for nuclear physics.

Lastly, the tidal response of a neutron star in a binary and its relation to the Love number is investigated. In this work we present a new approach to this problem, that calculates the effective Love number without using the traditional mode sum approach but instead utilizes the matching of ingoing and outgoing solutions in the weak field near zone.

Contents

List of Figures

List of Tables

Declaration of Authorship

I, Andrew Rhys Counsell, declare that this thesis and the work presented in it is my own and has been generated by me as the result of my own original research.

I confirm that:

1. This work was done wholly or mainly while in candidature for a research degree at this University;
2. Where any part of this thesis has previously been submitted for a degree or any other qualification at this University or any other institution, this has been clearly stated;
3. Where I have consulted the published work of others, this is always clearly attributed;
4. Where I have quoted from the work of others, the source is always given. With the exception of such quotations, this thesis is entirely my own work;
5. I have acknowledged all main sources of help;
6. Where the thesis is based on work done by myself jointly with others, I have made clear exactly what was done by others and what I have contributed myself;
7. Parts of this work have been published as:
    - Counsell et al. (2024)
    - Counsell et al. (2025a)
    - Counsell et al. (2025b)
    - Andersson et al. (2025)

Signed:... Date:..................

Acknowledgements

It is hard to believe four years have passed but I have learned soo much in that time and have many fond memories to take with me.

First, I would like to thank my supervisor Nils, who has been a wonderful mentor throughout, always willing to provide guidance and help on my research. I will miss his random walks around the office and his frequent attempts to sneak up on me. I would also like to thank my second supervisor Ian who gave my the chance to study here in Southampton, despite me not being Welsh.

Next, I would like to thank all my colleagues from the office that survived the floods and many technical mishaps that befell building 54. To name a few: Fabian, who was in effect my 3rd supervisor; Shanshan, for her many fun questions; Rahime, for our many coffee breaks while we waited for our code to magically work; Yashaswi for always being on the desk beside equally confused as me and Ayush, for having someone to vent to about the England cricket team.

An even greater thanks must go to my partner in chaos, Jade. Between the many adventures we have had together, she has been my confidante and rock, and has more importantly helped thwart my many attempts to procrastinate. She has always supported this endeavour or as she calls it ”playing with numbers”.

Lastly, and most certainly not least, I thank my family: my parents and my brother, Ashley. They have always nurtured and supported my love of questions and science and nothing I have done would’ve been possible without them.

P.S. and Bob.

To my parents, for always encouraging me to shoot for the stars. . .

Notation

Indices

Spatial indices are denoted with Latin characters $i, j, k, \ldots$ and spacetime indices are denoted with early Latin characters $a, b, c, \ldots$, the indices l and m will be used exclusively for spherical-harmonic modes. The Einstein summation convention will be used, where repeated indices indicate a summation, e.g.,

$$v^i v_i = \sum_i v^i v_i,$$

$$u^a u_a = \sum_a u^a u_a,$$

where v^i and u^a are an arbitrary three-vector and four-vector respectively. Summations over repeated l and m are not assumed. The signature of the spacetime metric g_{ab} is $(-,+,+,+)$. Hence, time-like four-vectors have negative lengths.

Derivatives

The covariant and partial derivatives are denoted by ∇_a and ∂_a, respectively. We use the traditional conventions for the covariant derivative so that it reduces to the partial derivative for scalars, i.e.

$$\nabla_a f = \partial_a f \, .$$

Chapter 1

Introduction

> It's the job that's never started as takes longest to finish
>
> *The Lord of the Rings*
> *J.R.R. Tolkien*

The universe is a vast expanse of space and time, full of almost uncountable objects, each fascinating to scientists in their own way but in this work, there is one object in particular that has taken a central role.

1.1 Neutron Stars

Neutron stars are highly compact objects that involve a rich and complex variety of physics. They are formed in the remnants of supernovae and have a mass of order a solar mass and typically have a radius of approximately 10 km, with only effects such as neutron degeneracy pressure preventing collapse to black holes. As with black holes, neutron stars are relativistic objects and thus require general relativity in order to accurately describe their dynamics. If that were not interesting enough, they are able to spin-up to high frequencies of order 700Hz (Hessels et al., 2006) and can support magnetic fields that can reach magnitudes of order 10^{15} G (Duncan and Thompson, 1992). Due to these extreme conditions, neutron stars are an invaluable testing ground for probing the fundamental laws of physics.

Neutron stars were first discovered in 1967 when pulsating radio sources were detected by Hewish et al. (1968). This was to be the first of many pulsating neutron stars discovered, now known as pulsars. While that was the first detection, they had been predicted long before that, with the initial idea attributed to Baade and Zwicky (1934a,b). This was just two years after the discovery of the neutron (Chadwick, 1932). Almost 60 years later over 3000 neutron stars have

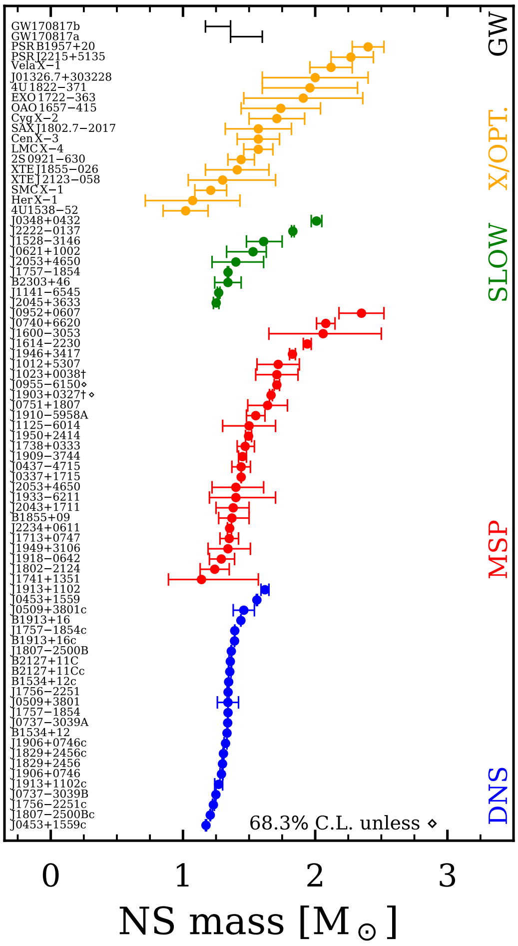

FIGURE 1.1: This plot is taken from Suleiman et al. (2021). Mass measurements of 73 Neutron Stars (NS) within 68.3% confidence level (1σ). The following classification is adopted: binaries with two neutron stars (DNS); millisecond pulsars (MSPs) with spin frequency ≥ 50 Hz and with a companion that is not a NS; slowly rotating pulsars (SLOW) with spin frequency ≤ 50 Hz not in a DNS; X/OPT for NSs measured through x-ray or optical observations (as opposed to radio in previous categories) and lastly GW for NS mass measurements using detection of gravitational waves.

now been detected and dozens of masses have been measured, this is shown in Figure 1.1 taken from (Suleiman et al., 2021).

Since their discovery, the field of neutron star research has rapidly grown to encompass a wide range of physics from the large scale of general relativity down to small scale of the interior nuclear physics. An important observational discovery was the first detection of a pulsar in a neutron star binary system, the Hulse-Taylor binary (Hulse and Taylor, 1975). It was realised that this system could serve as an indirect test for the existence of gravitational waves (Wagoner, 1975). If the system were emitting gravitational waves, this should lead to a decrease of the system's orbital period. This became another testable prediction of Einstein's general relativity. It was confirmed with remarkable accuracy, leading to Hulse and Taylor being awarded the Nobel prize in 1993. Today, several pulsar binaries have been discovered and have continued to show remarkable agreement with Einstein's theory of gravity (Will, 2014). At last, in 2015, the two laser interferometers at LIGO and the one at Virgo, observed a gravitational wave signal from a binary black hole system (Abbott et al., 2016) and then in 2017, a binary neutron star system dubbed GW170817 (Abbott et al., 2017, 2018).

An illustration of the structure of a neutron star is shown in Fig. 1.2. The various layers expected to be present from both experimental observation and theory are indicated along with the estimated thickness of each region and the estimated density at the boundary between regions. The outermost layer is the atmosphere consisting of plasma primarily composed of hydrogen, helium and heavy elements such as carbon. Below that is the solid crust which is split into two regions: an inner and outer crust. The outer crust is composed of a solid lattice of atomic nuclei and a sea of free electrons. As the density increases in the star it reaches a threshold value at which it becomes energetically favourable to have free neutrons instead of nuclei (Chamel et al., 2015). This is called the neutron drip point because the effect is that neutrons drip out of the nuclei. This marks the boundary between the outer and inner crust occurring at $n_{nd} \sim 4 \times 10^{11}\,\mathrm{g\,cm^{-3}}$. The inner crust is then a mixture of nuclei, free neutrons and electrons. As the density further increases, the solid crust transitions to a fluid core of protons, neutrons and electrons. The exact value of the crust core transition density, n_{cc}, and n_{nd} depend on the specific nuclear model considered. The last region is the inner core whose composition is still uncertain as the high densities expected at the centre of neutron stars are beyond our current experimental and theoretical understanding. It is unknown whether another phase transition occurs at the "boundary" between the outer and inner cores. It is theorised that for sufficiently massive neutron stars a transition could occur from nucleonic matter to exotic particles such as deconfined quarks or hyperons (Spinella, 2017; Kovensky and Schmitt, 2020; Logoteta, 2021). The density at which it could become energetically favourable for hyperons to appear is estimated at $n_H \sim 5 - 8 \times 10^{14}\,\mathrm{g\,cm^{-3}}$ (Logoteta, 2021). While Fig. 1.2 illustrates the main features of the interior composition of a neutron star, it ignores prominent details such as superfluidity and magnetic fields to name but a few. These features will not be considered in this thesis but for a more comprehensive review on the neutron star structure see Haensel et al. (2007).

1.2 Equation of State

Despite significant research effort, one of the greatest unknowns in the field is the equation of state, the function describing the relationship between the pressure, density and temperature of the star. The equation of state can be categorised as either "stiff" or "soft" depending on how compressible the star is, with stiff models being less compressible and thus supporting higher masses than the soft models. The equation of state depends strongly on the nuclear interactions and microphysics that take place at the extreme densities present inside the neutron star. A detailed description is key if one wants to build realistic neutron star models.

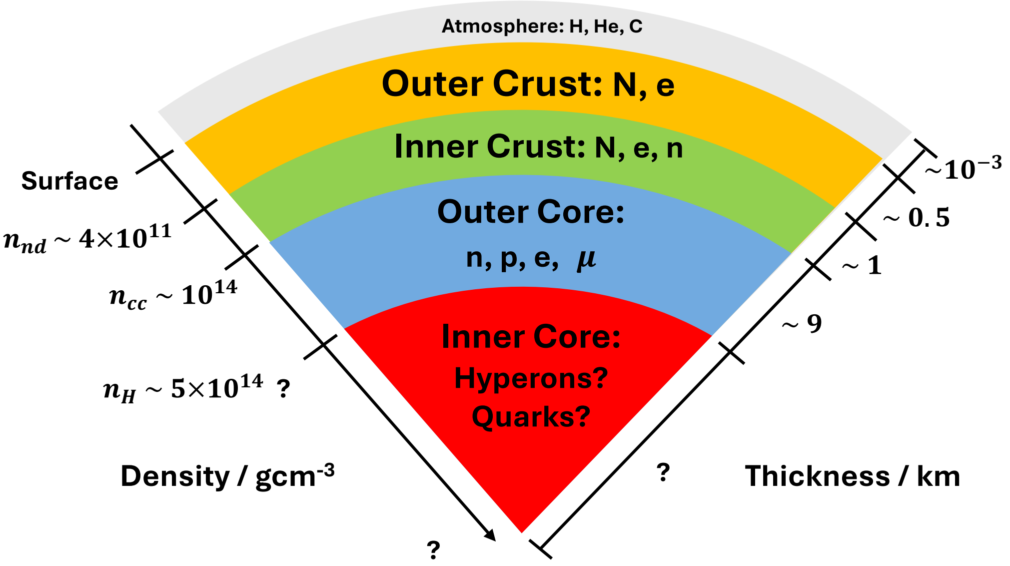

FIGURE 1.2: Illustration of the structure of a neutron star along with estimates for density and thickness of each layer. The particles expected to be present in each region are shown: nuclei (N); neutrons (n); protons (p); electrons (e) and muons (μ).The inner core composition is still uncertain and various exotic possibilities exist, including hyperons and deconfined quark matter.

There exist numerous different theories for how to build the equation of state and here we will discuss a few of the most common approaches. The majority of equations of state can be approximately categorised into three types: microscopic; phenomenological and parametric. We will give a general description of these different approaches along with examples.

Microscopic equations of state start from fundamental particles (nucleons, quarks) and incorporate many-body interactions to describe quantities such as the pressure and energy density. An example of this approach would be chiral effective field theory (Epelbaum et al., 2009; Machleidt and Entem, 2011), which provides an order-by-order expansion based on symmetries of quantum chromodynamics. The advantage of this approach is its reliability at low densities due to its nature as a model derived from first principles. Models such as chiral effective field theory, that allow for order-by-order expansions, are able to provide systematic and quantifiable errors for their predictions. The main disadvantage of this approach, is at the extreme densities found in the neutron star core the uncertainties in these theories become significant.

Phenomenological equations of state instead use a combination of experimental data and theoretical models. Numerous adjustable parameters are used alongside a functional form to constrain the equation of state to fit data from terrestrial experiments and astrophysical observations. Equations of state in this approach can be either relativistic or non-relativistic. Two examples that use different methods within this approach are the BSk family (Potekhin et al., 2013) and HTZCS (Hornick et al., 2018). The BSk family of equations of state uses generalised Skyrme-type forces (Köhler, 1976) fitted to nuclear masses via the Hartree-Fock-Bogoliubov method described in Chamel et al. (2009) and is thus non-relativistic.

The BSk family places particular emphasis on the crustal physics and features of the neutron star. Meanwhile HTZCS uses a relativistic mean field method which models nucleons interacting via meson fields (σ, ω, ρ) in a mean field approximation, (for details see Walecka (1974); Boguta and Bodmer (1977); Serot (1979)), while fitting to chiral effective field theory at low densities and astrophysical data at high densities. The major advantage of both these approaches is that they produce a unified description that is valid throughout the entirety of the star, unlike the microscopic approach. The disadvantage of these models is their reliance on their parameters, which can be numerous, leading to vastly different results between different parameter sets. One additional advantage that relativistic mean field models have is that they are causal by design unlike other phenomenological models such as BSk. Models such as BSk are acausal at high densities and therefore must only be used within valid density ranges.

Lastly parametric equations of state use mathematical functions such as polynomials along with a set of parameters to approximate the complex, unknown relationship between pressure and density and then fit to observational data. This method reduces the reliance on specific nuclear theories, instead focusing on observable constraints. An example of this approach is a polytrope, which will be explained in Chapter 2. These methods are often computationally efficient allowing for exploration of the parameter space. However the simplistic nature of these models may not be able to capture all of the complex physics that could be present in the neutron star such as phase transitions.

As can be seen from these descriptions each of these approaches have their own advantages and disadvantages, therefore it is important to understand the limitations of an equation of state when using it in calculations and discussing results. The mass-radius curves for a selection of equations of state that will be used later on in thesis are shown in Fig. 1.3, specifically: HTZCS (Hornick et al., 2018) with the inclusion of Λ hyperons and BSk21; BSk22; BSk24; BSk25 and BSk26 from the BSk family (Pearson et al., 2012; Potekhin et al., 2013). Included in the plot are constraints on the neutron star mass and radius observed by the Neutron Star Interior Composition ExploreR (NICER) for the pulsars: PSR J0030+0451 and PSR J0740+6620 (Riley et al., 2021; Miller et al., 2021b). NICER is an X-ray telescope on board the International Space Station, that aims to observe joint mass-radius measurements for pulsars using pulse-profile modelling (see Watts (2019), and references therein for a description of the technique). Additionally the constraint from the gravitational wave measurement GW170817 (Abbott et al., 2018) is included. Also indicated by the grey region in the top left corner of Fig. 1.3 is a region of the mass-radius parameter space that is excluded due to the requirement that the neutron star remains causal independent of equation of state (see Koranda et al. (1997); Lattimer and Prakash (2007) for further details). The main takeaway from this plot is the vast range of possibilities for the equation of state and that any additional information that can be obtained about neutron stars are vital.

At this point it is worth highlighting the HTZCS equation of state in Fig. 1.3. Unlike the BSk equations of state shown alongside it, the original formulation of HTZCS was adjusted to include hyperons, specifically the Λ hyperon, using the methodology of Ghosh et al. (2022,

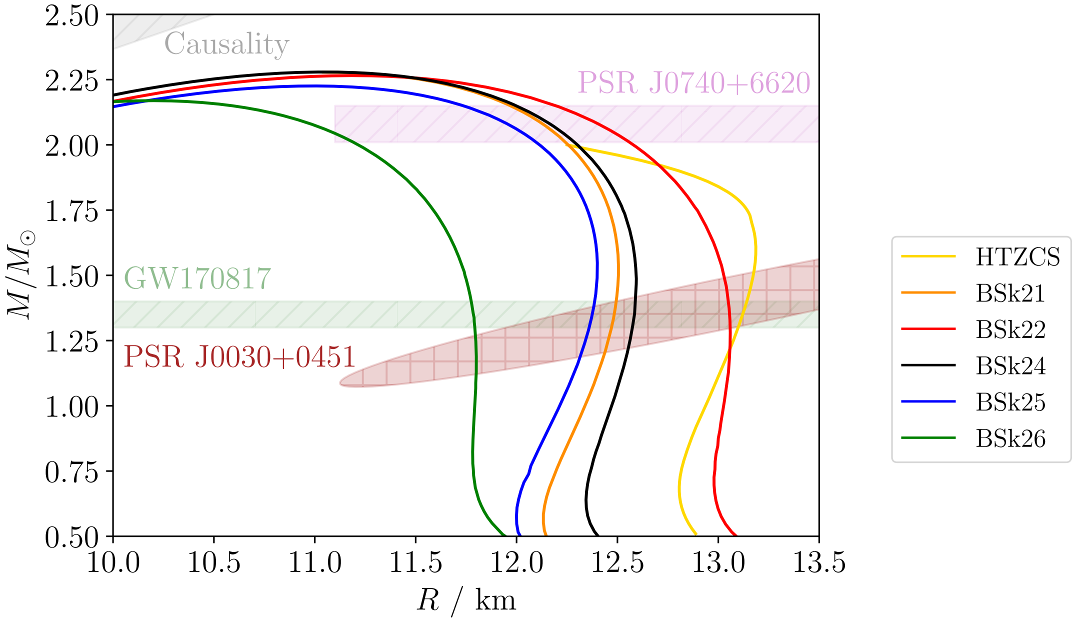

FIGURE 1.3: Plotted are the mass-radius curves for the different theoretically constructed equations of state, specifically: HTZCS (Hornick et al., 2018) with the inclusion of Λ hyperons and BSk21; BSk22; BSk24; BSk25 and BSk26 from the BSk family (Pearson et al., 2012; Potekhin et al., 2013). Also included are observational constraints on the neutron star mass and radius from NICER: J0030+0451 (light brown ellipse) and MSP J0740+6620 (pink rectangle) (Riley et al., 2021; Miller et al., 2021b) and from the gravitational wave measurement of GW170817 (light green rectangle) (Abbott et al., 2017, 2018). The grey region in the top left corner of the plot is excluded due to the requirement of causality throughout the neutron star (Köhler, 1976; Lattimer and Prakash, 2004).

2024). As can be seen in Fig. 1.3, the maximum mass of this version of HTZCS is $\sim 2\,M_\odot$ which is the lower limit of the constraint from PSR J0740+6620 (Riley et al., 2021; Miller et al., 2021b). Along with the other mass measurements shown in Fig. 1.1, it is widely accepted that the neutron star maximum mass is $\gtrsim 2\,M_\odot$. When hyperons are included in models such as HTZCS it leads to a softening of the equation of state and consequently to a reduction of the neutron star mass and, particularly, of its maximum value (Glendenning, 1982). Reconciling the presence of hyperons in neutron stars with current mass observations is still an open problem and is known in the literature as the "hyperon puzzle" (Bombaci, 2017). This problem is not the focus of this thesis, for a review of current approaches to addressing the "hyperon puzzle" see Logoteta (2021).

1.3 Gravitational Waves

Having mentioned that one can detect neutron star mergers using gravitational waves, we have reached an appropriate point to discuss how these waves arise in general relativity. For more detail, I recommended the textbooks by Maggiore (2007) and Andersson (2019).

It was Einstein himself who first showed that relativity permitted small wave-like solutions that travelled at the speed of light on flat, Minkowskian spacetime (Einstein, 1916b, 1918). Despite this, Einstein was sceptical on whether gravitational waves existed in nature and at one point published a paper claiming they were unphysical upon finding a singularity in a non-linear cylindrical wave solution in Einstein and Rosen (1937). This paper was later retracted with the realisation that it was merely a coordinate singularity.

This theoretical debate over whether gravitational waves were physical solutions or simply an artifact of gauge or coordinate choices would not be resolved until the Chapel Hill conference of 1957 (Bergmann, 1957). There, arguments by Pirani (Pirani, 1956, 1957), which later inspired Bondi's famous "sticky bead" thought experiment (Bondi, 1957), lead to the acceptance of gravitational waves by the theoretical community.

1.3.1 Wave Equation

Let us start with the Einstein equations (Einstein, 1916a)

$$G_a^b = 8\pi T_a^b, \tag{1.1}$$

where G_a^b is the Einstein tensor and T_a^b is the stress-energy tensor corresponding to the matter content. This equation describes how the matter content shapes the geometry of the spacetime around it. Consider a region of spacetime where the metric is close to flat

$$g_{ab} = \eta_{ab} + h_{ab}, \quad |h_{ab}| \ll 1, \tag{1.2}$$

where η_{ab} is the Minkowski metric and h_{ab} is the perturbation. In Cartesian coordinates, the Minkowski metric is given by

$$\eta_{ab} dx^a dx^b = -dt^2 + dx^2 + dy^2 + dz^2. \tag{1.3}$$

In linearised gravity one can substitute (1.2) into the Einstein equations (1.1) and retain terms up to linear order in h_{ab}. The inverse metric is then

$$g^{ab} = \eta^{ab} - h^{ab} + O(|h_{ab}|^2), \tag{1.4}$$

where

$$h^{ab} = \eta^{ac}\eta^{bd}h_{cd}. \tag{1.5}$$

One can use the flat metric η_{ab} to raise and lower indices of terms of $O(|h_{ab}|)$. At this point, we should make it clear that we are choosing a frame in (1.2) such that $|h_{ab}| \ll 1$ holds on a sufficiently large region of space. In making this choice of frame, we are leaving a residual gauge freedom. A gauge freedom corresponds to the invariance of a quantity under a coordinate transformation. Consider a transformation of coordinates x^a such that

$$x^a \longrightarrow x'^a = x^a + \zeta^a(x^a), \tag{1.6}$$

where ζ^a is the generator of the transformation and the derivatives $|\partial_a \zeta_b|$ are of the same order of smallness as $|h_{ab}|$. As tensors transform under coordinate changes as

$$g_{ab}(x^a) \rightarrow g'_{ab}(x'^a) = \frac{\partial x^c}{\partial x'^a}\frac{\partial x^d}{\partial x'^b} g_{cd}(x^a), \tag{1.7}$$

we have to leading order

$$h_{ab}(x^a) \rightarrow h'_{ab}(x'^a) = h_{ab}(x^a) - [\partial_a \zeta_b(x^a) + \partial_b \zeta_a(x^a)]\,. \tag{1.8}$$

If $|\partial_a \zeta_b|$ is small then our condition $|h_{ab}| \ll 1$ is preserved under a transformation. Moving on to curvature, as the background is flat, to linear order in h_{ab}, the Riemann tensor of the metric is

$$R_{abcd} = \frac{1}{2}\left(\partial_b \partial_c h_{ad} + \partial_a \partial_d h_{bc} - \partial_a \partial_c h_{bd} - \partial_b \partial_d h_{ac}\right). \tag{1.9}$$

Using the transformation laws (1.8), one can show that R_{abcd} is invariant under our gauge transformation. In order to simplify the equations, we introduce the trace-reversed metric perturbation

$$\bar{h}_{ab} \equiv h_{ab} - \frac{1}{2}\eta_{ab} h, \tag{1.10}$$

where $h = \eta^{ab} h_{ab}$. This can be inverted to give

$$\bar{h} = \eta^{ab}\bar{h}_{ab} = -h. \tag{1.11}$$

The Einstein equations can then be rewritten as

$$G_{ab} = -\frac{1}{2}\left(\Box \bar{h}_{ab} + \eta_{ab}\partial^c \partial^d \bar{h}_{cd} - \partial^c \partial_b \bar{h}_{ac} - \partial^c \partial_a \bar{h}_{bc}\right), \tag{1.12}$$

where $\Box \equiv \partial^a \partial_a$ is the flat-space d'Alembertian. As the background is flat, the stress-energy tensor will only enter the problem at $O(|\bar{h}_{ab}|)$. To use this fact we make the following gauge choice

$$\partial^b \bar{h}_{ab} = 0, \tag{1.13}$$

known as the Lorenz gauge. To check our freedom to make this choice let us consider the transformation of $\bar{h}_{ab}$,

$$\bar{h}_{ab} \rightarrow \bar{h}'_{ab} - \left(\partial_a \zeta_b + \partial_b \zeta_a - \eta_{ab}\partial_c \zeta^c\right), \tag{1.14}$$

thus

$$\partial^b \bar{h}_{ab} \rightarrow \left(\partial^b \bar{h}_{ab}\right)' = \partial^b \bar{h}_{ab} - \Box \zeta_a. \tag{1.15}$$

Therefore (1.13) can be satisfied if

$$\Box\zeta_a = \partial^b \bar{h}_{ab}. \tag{1.16}$$

In this gauge (1.12) gives us the wave equation

$$\Box\bar{h}_{ab} = -16\pi T_{ab}. \tag{1.17}$$

Using (1.13) and (1.17), $\partial^b T_{ab} = 0$ is automatically satisfied. We have shown how small perturbations on a flat background satisfy a wave equation in general relativity, those waves travel at the speed of light and correspond to gravitational waves. One caveat to note is that, in the linearised theory we have used, the bodies that source the gravitational waves are assumed to move in flat spacetime. In effect, this means the dynamics are governed by Newtonian gravity.

1.3.2 Test Masses

Let us know consider how these gravitational waves propagate through spacetime and interact with test masses. Outside of the source (1.17)

$$\Box\bar{h}_{ab} = 0. \tag{1.18}$$

The Lorenz gauge is not sufficient to fix the full gauge freedom as one can introduce an additional coordinate transformation $x^a \longrightarrow x^a + \zeta^a$ where

$$\Box\zeta_a = 0, \tag{1.19}$$

that still satisfies (1.15). To account for this, one can impose four further conditions. For convenience, we choose $\bar{h} = 0$, $\bar{h}_{ab} = h_{ab}$ and $h_{ti} = 0$. The Lorenz gauge is now

$$\partial^t h_{tt} = 0, \quad \partial^j h_{ij} = 0. \tag{1.20}$$

The term h_{tt} corresponds to the static part of the gravitational interaction, which is related to the Newtonian potential of the source of the waves. As the gravitational wave is the time-dependent part of the perturbation, we have the freedom to set $h_{tt} = 0$. The time-varying aspect of the wave is then contained in h_{ij}. To summarise, the gauge is fixed by

$$h_{ta} = 0, \quad h^i_i = 0, \quad \partial^j h_{ij} = 0, \tag{1.21}$$

which is know as the transverse-traceless gauge, denoted by h^{TT}. In this gauge, the solution to (1.18)

$$h^{TT}_{ij} = e_{ij} e^{ik_a x^a}, \tag{1.22}$$

where $k^a = (\omega, k^i)$ is the wave four-vector, ω is the angular frequency of the gravitational waves and e_{ij} is the polarisation tensor. Assuming the waves propagate along the z-axis

$$h_{ij}^{TT} dx^i dx^j = h_+ \cos[\omega(t-z)]dx^2 + 2h_\times \cos[\omega(t-z)]dxdy - h_+ \cos[\omega(t-z)]dy^2, \quad (1.23)$$

where h_+ and $h_\times$ are the two independent wave polarisations corresponding to the two degrees of freedom. Given a plane wave h_{ab} travelling in the direction of the unit vector $\hat{n}^i$, already in the Lorenz gauge, one can transform the solution to the transverse-traceless gauge using the projection operator

$$\Lambda_{ij}^{kl} = P_i^k P_j^l - \frac{1}{2} P_{ij} P^{kl}, \quad P_{ij} = \delta_{ij} - \hat{n}_i \hat{n}_j, \quad (1.24)$$

where δ_{ij} are the spatial parts of η_{ab}. The solution can then be projected into the transverse-traceless gauge by

$$h_{ij}^{TT} = \Lambda_{ij}^{kl} h_{kl}. \quad (1.25)$$

Now that the gauge freedom has been addressed, let us examine how test masses move due to gravitational waves. Consider two point particles freely falling in flat space. The four-vector $\xi^a(\tau)$ describes the separation between the masses, so the masses are at $x^a(\tau)$ and $x^a(\tau) + \xi^a(\tau)$ and τ is the proper time as measured by a clock carried along the trajectory $x^a(\tau)$. The masses follow geodesics which are governed by the geodesic equation

$$u^b \nabla_b u^a = \frac{du^a}{d\tau} + \Gamma_{bc}^a u^b u^c = 0, \quad (1.26)$$

where $u^a = \frac{dx^a}{d\tau}$ and Γ_{bc}^a is the usual Christoffel symbol given by

$$\Gamma_{bc}^a = \frac{1}{2} g^{ad} (\partial_b g_{cd} + \partial_c g_{bd} - \partial_d g_{bc}). \quad (1.27)$$

In flat space with Cartesian coordinates the Christoffel symbols vanish giving the classical result that particles follow straight lines in the absence of a force. Making the assumption that $|\xi^a|$ is smaller than the variation of the gravitational field, one can show that the geodesics followed by the test masses, to first order in ξ^a,

$$\frac{D^2 \xi^a}{D\tau^2} = -R_{bcd}^a u^b \xi^c u^d, \quad (1.28)$$

where the operator $\frac{D}{D\tau} \equiv u^a \nabla_a$ is the directional derivative along the four-velocity u^a. This is known as the equation of geodesic deviation, which states that two nearby time-like geodesics experience a tidal gravitational force, given by the Riemann tensor. In flat space where $R_{bcd}^a = 0$, this means the separation is constant or changing at a constant rate, whereas in curved spacetime ξ^a will accelerate, causing initially parallel geodesics to converge or diverge. As R_{bcd}^a is also affected by the gravitational wave according to (1.9), we can rewrite (1.28), to linear order in h_{ij} where $t = \tau$,

$$\partial_t^2 \xi^i = \frac{1}{2} \delta^{ij} \partial_t^2 h_{jk}^{TT} \xi^k. \quad (1.29)$$

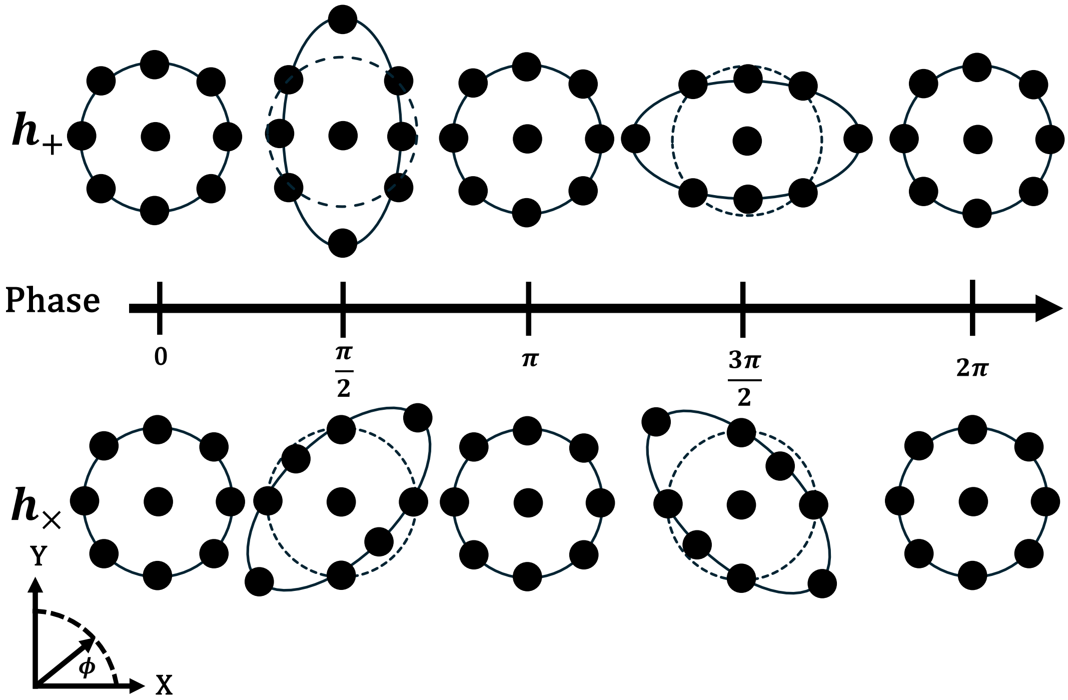

FIGURE 1.4: A gravitational wave passing through a ring of freely falling test masses in the transverse traceless gauge. The top and bottom rows show the + and × polarisations respectively. The separation between the masses illustrated here corresponds to the proper distance in this frame.

which has the following solution,

$$\xi^i(t) = \left[\delta^i_k + \frac{1}{2}\delta^{ij}h^{TT}_{jk}(t)\right]\xi^k(0). \tag{1.30}$$

which describes how freely falling test masses move according to a gravitational wave in the transverse-traceless frame. The effect of the two modes: h_+ and $h_\times$ of a gravitational wave passing through a ring of freely falling test masses is shown in Fig. 1.4.

1.3.3 Sourcing

After discussing the theory of gravitational waves let us now look at how they are sourced. An issue that appears immediately is that the stress-energy tensor of gravitational waves t_{ab} is not gauge invariant. This is a manifestation of the equivalence principle of general relativity, as one is free to choose a local inertial frame at any point in spacetime where the gravitational wave vanishes. Therefore we cannot localise the effect of the wave. While t_{ab} is not well-defined locally, it does carry energy. In order to get around this and understand the physical effect of the wave, one needs to average over several wavelengths. Doing so, one can show that the averaged stress-energy tensor $\langle t_{ab} \rangle$ is gauge invariant. Taking the time average as done in Isaacson (1968)

$$\langle t_{ab} \rangle = \frac{1}{32\pi} \langle \partial_a h_{ij}^{TT} \partial_b h^{TTij} \rangle. \tag{1.31}$$

The solution of (1.17) can be obtained using a retarded Green's function,

$$\bar{h}_{ab}(t, X^i) = 4 \int_V \frac{1}{|X^i - x^i|} T_{ab}(t - |X^i - x^i|, x^i) dV, \tag{1.32}$$

where the integration is over the volume of the star, x^i is a point inside the star and X^i is the position of an observer measuring the field, outside the mass distribution. For simplicity, we assume that the waves are generated by a weak source and are observed far from the source, $r \ll \mathcal{R}$, where $r^2 = x^i x_i$ and $\mathcal{R}^2 = X^i X_i$. In this limit, we have

$$\bar{h}_{ab}(t, X^i) = \frac{4}{\mathcal{R}} \int_V T_{ab}(t - r, x^i) dV + O\left(\frac{1}{\mathcal{R}^2}\right). \tag{1.33}$$

By using the conservation law $\partial_b T_{ab} = 0$, and noting how the divergence terms vanish on the surface, one can derive the relation

$$2 \int_V T_{ij} dV = \int_V \partial_t^2 T_{tt} x_i x_j dV. \tag{1.34}$$

We can then rewrite

$$\bar{h}_{ij}(t, X^i) = \frac{2}{\mathcal{R}} \partial_t^2 \left[\int_V T_{tt}(t - r, x^i)_i x_j dV \right] \equiv \frac{2}{\mathcal{R}} \partial_t^2 M_{ij}(t - r), \tag{1.35}$$

where M_{ij} is the (non-traceless) mass-quadrupole moment. Transforming this to the transverse-traceless frame,

$$h_{ij}^{TT}(t, X^i) = \frac{2}{\mathcal{R}} \Lambda_{ij}^{kl} \partial_t^2 M_{kl}(t - r) = \frac{2}{\mathcal{R}} \partial_t^2 Q_{ij}(t - r), \tag{1.36}$$

where Q_{ij} is the trace-reduced analogue of M_{ij}. This is the quadrupole formula and from it we learn three important features of gravitational waves:

- gravitational waves are generated by accelerating sources of matter,
- the radiation falls off, to leading order, as $\frac{1}{\mathcal{R}}$,
- gravitational waves are quadrupolar.

This last result is also true in the full non-linear theory; monopole and dipole radiation are absent in general relativity. The lack of monopole radiation turns out to be a consequence of Birkhoff's theorem (Jebsen, 1921; Birkhoff and Langer, 1923), that any spherically symmetric spacetime must be static and asymptotically flat. Dipole radiation does not exist because there are no opposite charges in gravity. As a consequence of this, we will focus on the quadrupolar gravitational wave radiation when discussing the detectability of neutron star oscillation modes.

1.4 Asteroseismology

One of the great questions in neutron star physics and astronomy as a whole, is how can one make insights into the internal structure of stellar objects that are many light years away? There is a rich field of research currently being undertaken to answer this question but the aim of this thesis has been in the field asteroseismology, the study of oscillation modes of stellar objects. Mature neutron stars are predicted to support complex oscillation spectra, with modes corresponding to each new piece of physics added to the problem, such as the internal composition; rotation; state of matter; phase transitions; presence of superfluid components etc. The importance of neutron star seismology as well as the oscillations of stars in general have been appreciated since Pekeris (1938) and Cowling (1941). While originally the focus was on the mathematical formulation of the problem, recent X-ray timing observations and the detection of gravitational waves from the GW170817 neutron star merger event have led to renewed focus on the problem (see e.g. Ho (2018); Andersson (2021); Gittins and Andersson (2024)). While this thesis is restricted to neutron stars, the field of asteroseismology has provided great insights into other stellar objects as well. Helioseismology, the branch of asteroseismology that focuses on the Sun, has provided detailed insights into its internal structure, such as the rotational profile and the dependence of sound speed on depth (Kosovichev et al., 1998). Asteroseismology has been applied to objects much farther away than our Sun, as well as examining exoplanets and their host stars. Researches have been able to apply the methods of this field to calculate properties such as the radii of exoplanets and eccentricity of their orbits (Lundkvist et al., 2018). Given the success of these branches of asteroseismology there is much hope for neutron stars.

Whereas the previous applications have involved electromagnetic signals, one can instead utilise gravitational waves. One of the main scenarios for emission is from binary inspiral sources such as GW170817. If one considers a binary system where one or both compact objects are a neutron star, as the two stars inspiral and move closer and closer together, the orbital frequency Ω increases, sweeping through a range of values in the detector sensitivity band. Therefore the frequency will pass through the characteristic frequencies of various neutron star oscillation modes. Coupling and resonance can occur between a mode frequency ω and the orbital frequency when $\omega \approx 2\Omega$ for $m = 2$ modes. This causes energy to be transferred into the mode, exciting an oscillation and drawing energy from the orbit. As the orbit has lost energy, it will decrease faster, manifesting as a change in the gravitational waveform (Andersson and Ho, 2018). This can also be seen as a decrease in the number of orbits the binary system undergoes before coalescence. There are extreme cases where it is possible enough energy is transferred into the neutron star that its crust could fracture or shatter, producing an electromagnetic flare fractionally before the merger (Penner et al., 2012; Tsang et al., 2012). Another possible outcome is modes being driven unstable (Andersson et al., 1999).

We can thus see that the field of astereoseismology is intricately linked to the dynamical tides of neutron stars. As the sensitivity of the gravitational-wave interferometers is improved, in first instance to the LIGO A+ level and eventually to the next-generation instruments, Cosmic Explorer (Evans et al., 2023) and the Einstein Telescope (Abac et al., 2025), the expectation is that the tidal constraints measured from gravitational wave signals will become more precise (Khadkikar et al., 2025) and that additional tidal aspects, such as the mode resonances, will come within reach (Hinderer et al., 2016; Steinhoff et al., 2016; Kuan and Kokkotas, 2023; Yu et al., 2024a; Pnigouras et al., 2025a). However, to fully utilise these advances we need to develop models of dynamical tides in neutron-star binaries to the level of precision required by future instruments, providing a robust description of the signal emitted as a system evolves through the detector sensitivity band and sharp statements regarding the observability of fine print features connected with the composition and state of matter. Such models inevitably require a fully relativistic description of the response of the stellar matter to the external tidal driving. However, developments in this direction have long been hampered by technical issues (see Pitre and Poisson (2024) for a concise summary of relevant points). We will see later on in this thesis that the dynamical tide is related to a parameter called the effective Love number which can then be linked backed to the neutron star oscillation modes.

As previously mentioned, the equation of state influences internal features of the star which then impact observables such as the oscillation modes, therefore a better understanding and measurement of the modes could serve as a test for the equation of state.

As previously mentioned, understanding the composition and state of matter inside neutron stars is important for next generation gravitational wave detectors. Two types of oscillation modes that are directly linked to these features are gravity modes and interface modes which will be the main focus of this thesis. Current research involves incorporating finite temperature effects (Gittins and Andersson, 2024) and exotic particles such as hyperons (Tran et al., 2023) and even dark matter (Kumar and Sotani, 2025). A significant portion of the field is focussed on identifying relationships between oscillation frequencies/damping times and stellar parameters (like mass and radius) that are largely independent of the specific equation of state used, so called “universal relations” (Sotani and Kumar, 2021; Kumar et al., 2023). The goal of these “universal relations” is to constrain the equation of state from observations and to break degeneracies between parameters in measurements such as mass and radius. For further details on the field of astereoseismology see the following reviews: Andersson (2021) and Li et al. (2024).

1.5 Outlook

This work is focused on using the oscillations of neutron to stars to better understand the composition and state of the matter in the core. The layout of this work is as follows: in Chapter 2, the mode problem is solved for neutron stars in Newtonian gravity for both non-rotating and slowly rotating neutron stars. Chapter 3 examines the main problem of adding in weak reactions, again in Newtonian gravity. Also included in this chapter is a plane-wave approach to the fast and slow reaction regimes. In Chapter 4, the focus is on extending the mode calculations into general relativity and introducing the Cowling approximation, which drops the metric perturbations. Chapter 5 then goes beyond the Cowling approximation and solves the fully relativistic mode equations. Chapter 6 aims to quantify how much physical information can be obtained from observations of the modes in gravitational wave signals. Chapter 7 examines the calculation of the Love number for neutron stars in Newtonian and General relativity. This dimensionless parameter characterises how a material object deforms in the presence of a tidal field. Lastly Chapter 8 concerns the method of detecting first-order phase transitions using the dynamical effect of interface mode resonances in neutron star binary inspirals.

Chapter 2

Frozen Composition Stars

While the overall aim of this thesis is to model a realistic neutron star, the idea is to first consider the simplest case, that of oscillations of a non-rotating star in Newtonian gravity and by gradually adding more physics one may then see how the spectra of the modes changes and evolves. While this scenario has been studied before, including the extension to slow rotation, (Pnigouras, 2017; Unno et al., 1989; Saio, 1981), it is a good starting point to understanding the problem. The methods used in this Chapter translate well to the case in Chapter 3 where the effect of reaction rates is considered and Chapter 4 where the problem is extended to general relativity.

2.1 Hydrodynamics

Assuming the star can be modelled as a perfect fluid, that is one which has no viscosity or heat flow, rotating with angular velocity $\boldsymbol{\Omega}$, the hydrodynamics equations are the conservation equation and the Euler equation:

$$\partial_t \rho + \nabla \cdot (\rho \boldsymbol{v}) = 0, \tag{2.1}$$

$$\partial_t \boldsymbol{v} + (\boldsymbol{v} \cdot \nabla)\boldsymbol{v} + 2\boldsymbol{\Omega} \times \boldsymbol{v} + \boldsymbol{\Omega} \times (\boldsymbol{\Omega} \times \boldsymbol{r}) = -\frac{\nabla p}{\rho} - \nabla \Phi, \tag{2.2}$$

where the coordinates are in a reference frame rotating with the star; ρ is the density; p is the pressure; $\boldsymbol{v}$ is the velocity and Φ is the gravitational potential given by Poisson's equation:

$$\nabla^2 \Phi = 4\pi G \rho. \tag{2.3}$$

The oscillations are then modelled as perturbations of these equations. Imposing small perturbations on (2.1) - (2.3) and retaining only first-order perturbation terms,

$$\partial_t \delta\rho + \nabla \cdot (\rho \delta \boldsymbol{v}) = 0, \tag{2.4}$$

$$\partial_t \delta \boldsymbol{v} + 2\boldsymbol{\Omega} \times \delta \boldsymbol{v} + \frac{\nabla \delta p}{\rho} - \frac{\nabla p}{\rho^2}\delta\rho + \nabla\delta\Phi = 0, \tag{2.5}$$

$$\nabla^2 \delta\Phi = 4\pi G \delta\rho \tag{2.6}$$

where δ denotes an Eulerian perturbation as described in Friedman and Schutz (1978b).

A new variable $\boldsymbol{\xi}$ is defined, measuring the displacement of the fluid from its equilibrium position. This relates to the Lagrangian perturbation scheme from Friedman and Schutz (1978b). The Lagrangian Perturbation, denoted Δ, involves tracking where the fluid elements are displaced to during the perturbation. Mathematically this is defined as

$$f(\mathbf{r}, t) = f_0(\mathbf{r}_0) + \Delta f(\mathbf{r}, t), \tag{2.7}$$

where $\mathbf{r}_0$ is the equilibrium position of the fluid element in the unperturbed background star. This description can be combined with the Eulerian description according to,

$$\Delta f(\mathbf{r}, t) = \delta f(\mathbf{r}_0, t) + \mathcal{L}_\xi f(\mathbf{r}, t), \tag{2.8}$$

where $\mathcal{L}_\xi$ is the Lie derivative with respect to the displacement vector $\boldsymbol{\xi}$, defined as $\boldsymbol{\xi} = \mathbf{r} - \mathbf{r}_0$.

Taking the Lagrangian perturbation of the velocity

$$\Delta \boldsymbol{v} = \dot{\boldsymbol{\xi}} + (\boldsymbol{v} \cdot \nabla)\boldsymbol{\xi}. \tag{2.9}$$

As the reference frame chosen is one co-rotating with the star, $\boldsymbol{v} = 0$ in the background. Using this one gets $\delta \boldsymbol{v} = \dot{\boldsymbol{\xi}}$ which follows from the Lagrangian definition. This can be substituted into (2.5) to give

$$-\omega^2 \boldsymbol{\xi} + i\omega \mathcal{B}(\boldsymbol{\xi}) + C(\boldsymbol{\xi}) = \mathbf{0}, \tag{2.10}$$

where

$$\mathcal{B}(\boldsymbol{\xi}) = 2\boldsymbol{\Omega} \times \boldsymbol{\xi}, \tag{2.11}$$

$$C(\boldsymbol{\xi}) = \frac{\nabla \delta p}{\rho} - \frac{\nabla p}{\rho^2}\delta\rho + \nabla\delta\Phi. \tag{2.12}$$

The assumption that the solutions are harmonic was also used

$$\boldsymbol{\xi}(\mathbf{r}, t) = \boldsymbol{\xi}(\mathbf{r})e^{i\omega t}. \tag{2.13}$$

Together with suitable boundary conditions, (2.10) can then be solved as an eigenvalue equation for the oscillation modes to give the eigenfunctions $\boldsymbol{\xi}$ and eigenfrequencies ω.

2.1.1 Equation of State

In order to close the system of equations, an equation of state is needed. The star is assumed to be a perfect fluid consisting of different particle species, so in general, the pressure will have the following form

$$p = p(\rho, s, x_i), \tag{2.14}$$

where s is the entropy per particle and x_i is the fraction of particles in the star that are species i. This is a complicated function that depends strongly on the microscopic physics and the inter-particle reactions present in the neutron star. In order to simplify this, if one assumes that the system is in chemical equilibrium with respect to those microscopic reactions, then over the reaction timescales, the equation of state can be simplified to

$$p = p(\rho, s). \tag{2.15}$$

In this chapter, it is assumed that the neutron stars being examined are mature and cold, therefore, setting the temperature of the star as $T = 0$ and assuming chemical equilibrium, gives

$$p = p(\rho). \tag{2.16}$$

This form of one parameter equation of state is termed barotropic. One can then define the following quantity known as the adiabatic index

$$\Gamma = \left(\frac{\partial \ln p}{\partial \ln \rho}\right)_\beta \tag{2.17}$$

where the index β indicates that the partial derivative is taken to be in beta equilibrium by which we mean that the composition of the star is stationary with regards to the Urca processes. Imposing small perturbations on the equation of state gives:

$$\frac{\Delta p}{p} = \Gamma_1 \frac{\Delta \rho}{\rho}, \tag{2.18}$$

where

$$\Gamma_1 = \left(\frac{\partial \ln p}{\partial \ln \rho}\right)_{x_p}. \tag{2.19}$$

Γ_1 is known as the adiabatic index of the perturbed matter and x_p corresponds to the proton fraction, taken as the proton number density over the baryon number density. In deriving (2.18) it is assumed that $\Delta x_p = 0$. This is assuming that the composition of the fluid element remains unchanged during the oscillation. This is known as taking the composition as 'frozen'. The weak interaction processes, assumed to be Urca reactions, need much more time than an oscillation period to restore chemical equilibrium between the displaced fluid element and the surrounding matter (Reisenegger and Goldreich, 1992b). This assumption is tested in Chapter 3. For simplicity we will choose a polytropic equations of state. Here, the equation of state is idealised to

$$p(\rho) = K\rho^\gamma, \tag{2.20}$$

where K is the polytropic constant and γ is the polytropic index, which for neutron stars is often taken to be 2. For a solution to a given polytropic index, one can choose K and a central density

ρ_c to give a specific radius and mass for the star. In Newtonian gravity, using (2.17) and (2.20) $\Gamma = \gamma$. We will in subsequent chapters that this is not the case in General Relativity.

2.2 Non-Rotating Stars

The presence of $\mathcal{B}$ makes the equations complicated to solve, therefore the initial starting point is the non rotating case, setting $\mathbf{\Omega} = 0$, which in terms of (2.10) is setting $\mathcal{B}(\boldsymbol{\xi}) = 0$, giving

$$-\omega^2\boldsymbol{\xi} + \frac{\nabla\delta p}{\rho} - \frac{\nabla p}{\rho^2}\delta\rho + \nabla\delta\Phi = 0. \tag{2.21}$$

To make progress in solving the equations, the spherical symmetry of the problem can be exploited, the radial and angular components of $\boldsymbol{\xi}$, can be separated as $\xi_r(r,\theta,\phi) = \xi_r(r)Y_l^m(\theta,\phi)$ where Y_l^m is a spherical harmonic and $|m| \leq l$. The use of spherical harmonics arises from the spherical symmetry of the unperturbed non-rotating star, therefore the variables: $\delta p, \delta\rho, \xi_r, \delta\Phi$ only depend on radial position r .

Due to this separation, each oscillation mode in a non-rotating star is uniquely described by a single spherical harmonic Y_m^l. The degree l denotes the total number of nodal lines on the stellar surface along which no motion occurs, while the order m characterises the azimuthal dependence of the spherical harmonic, $e^{im\phi}$. As the star is non-rotating, there is actually no dependence on m, as the equations are independent of ϕ. The modes are also assigned an overtone n, which describes the number of radial nodes in their eigenfunctions. Examples of this will be provided later.

Using the spherical harmonics on (2.4) (2.6) (2.21) with (2.18) used to substitute out $\delta\rho$,

$$\frac{1}{r^2}\frac{d}{dr}(r^2\xi_r) - \frac{\rho g}{\Gamma_1 p}\xi_r + \left[\frac{\rho}{\Gamma_1 p} - \frac{l(l+1)}{\omega^2 r^2}\right]\frac{\delta p}{\rho} - \frac{l(l+1)}{\omega^2 r^2}\delta\Phi = 0, \tag{2.22}$$

$$\frac{1}{\rho}\left(\frac{d}{dr} + \frac{\rho g}{\Gamma_1 p}\right)\delta p - (\omega^2 + gA)\xi_r + \frac{d\delta\Phi}{dr} = 0, \tag{2.23}$$

$$\frac{1}{r^2}\frac{d}{dr}(r^2\frac{d\delta\Phi}{dr}) - \frac{l(l+1)}{r^2}\delta\Phi - 4\pi G\rho\left(\frac{\delta p}{\Gamma_1 p} - A\xi_r\right) = 0, \tag{2.24}$$

where

$$g = \frac{d\Phi}{dr}, \tag{2.25}$$

$$A = \frac{d\ln\rho}{dr} - \frac{1}{\Gamma_1}\frac{d\ln p}{dr}. \tag{2.26}$$

To solve the problem, four suitable boundary conditions are needed, two at the centre of the star and two at the surface. Near the origin as $r \longrightarrow 0$:

$$\frac{d\delta\Phi}{dr} - \frac{l\delta\Phi}{r} = 0, \tag{2.27}$$

$$\xi_r - \frac{l}{\omega^2 r}\left(\frac{\delta p}{\rho} + \delta\Phi\right) = 0. \tag{2.28}$$

Near the surface as $r \longrightarrow R$:

$$\frac{d\delta\Phi}{dr} + \frac{l+1}{r}\delta\Phi = 0, \tag{2.29}$$

$$\Delta p = 0. \tag{2.30}$$

The conditions at the origin arise from assuming the parameters are regular at the centre. The first surface condition arises from requiring the continuity of $\delta\Phi$ and its derivative at the surface and assuming that the density vanishes there. The second condition is that there exists a distinct boundary of the star where $\rho, p \approx 0$.

The equations (2.22) - (2.24) now form a boundary value problem with ω^2 as the eigenvalue. Each solution corresponds to a particular mode of oscillation, where the eigenfunctions are $(\xi_r, \delta p, \delta\Phi)$. In order to simplify the numerical problem, the equations are rewritten in a dimensionless form. The following new variables are defined, as in Unno et al. (1989),

$$y_1 = \frac{\xi_r}{r}, \tag{2.31}$$

$$y_2 = \frac{1}{gr}\left(\frac{\delta p}{\rho} + \delta\Phi\right), \tag{2.32}$$

$$y_3 = \frac{1}{gr}\delta\Phi, \tag{2.33}$$

$$y_4 = \frac{1}{g}\partial_r\delta\Phi. \tag{2.34}$$

$$x = \frac{r}{R} \tag{2.35}$$

Insert these into (2.22) – (2.24) to get

$$x\frac{dy_1}{dr} = \left(V_g - 3\right) y_1 + \left[\frac{l(l+1)}{\tilde{\omega}^2 c_1} - V_g\right] y_2 + V_g y_3, \tag{2.36}$$

$$x\frac{dy_2}{dr} = (\tilde{\omega}^2 c_1 - A^*) y_1 - (A^* - U + 1) y_2 - A^* y_3, \tag{2.37}$$

$$x\frac{dy_3}{dr} = (1 - U) y_3 + y_4, \tag{2.38}$$

$$x\frac{dy_4}{dr} = U A^* y_1 + U V_g y_2 + [l(l+1) - U V_g] y_3 - U y_4, \tag{2.39}$$

where the equation for y_3 is obtained by the trivial relationship between y_3 and y_4 and where:

$$\tilde{\omega}^2 = \frac{\omega^2}{GM/R^3}, \tag{2.40}$$

$$c_1 = \left(\frac{r}{R}\right)^3 \frac{M}{m}, \tag{2.41}$$

$$m = \int_0^r 4\pi r^2 \, dr \tag{2.42}$$

$$U = \frac{d \ln m}{d \ln r}, \tag{2.43}$$

$$V_g = \frac{V}{\Gamma_1} = \frac{\rho g r}{\Gamma_1 p}, \tag{2.44}$$

$$A^* = -rA, \tag{2.45}$$

with M and R being the total stellar mass and radius of the background star respectively. The boundary conditions (2.27)-(2.30) are also written in this dimensionless form. Near the origin as $r \longrightarrow 0$:

$$c_1 \tilde{\omega}^2 y_1 - l y_2 = 0, \tag{2.46}$$

$$l y_3 - y_4 = 0. \tag{2.47}$$

Near the surface as $r \longrightarrow R$:

$$(l+1) y_3 + y_4 = 0, \tag{2.48}$$

$$y_1 - y_2 + y_3 = 0. \tag{2.49}$$

In practice, to solve these perturbation equations numerically, one first needs to generate the background stellar model that is being perturbed in order to calculate the equilibrium variables. This is achieved by solving the Newtonian stellar structure equations, which are,

$$\frac{\mathrm{d}m}{\mathrm{d}r} = 4\pi r^2 \rho, \tag{2.50}$$

$$\frac{\mathrm{d}\Phi}{\mathrm{d}r} = \frac{Gm}{r^2}, \tag{2.51}$$

$$\frac{\mathrm{d}p}{\mathrm{d}r} = -\rho \frac{\mathrm{d}\Phi}{\mathrm{d}r} = -\frac{Gm\rho}{r^2}. \tag{2.52}$$

These equations are solved with the equation of state and different central densities in order to generate the desired neutron stars with particular masses and radii. When solving these equations, 3 distinct types of modes are found: fundamental or f-modes; pressure or p-modes and gravity or g-modes. Each mode corresponds to a different piece of physics in the model, each with their own restoring force. The f-modes are the fundamental oscillations of the fluid and have no radial nodes in their eigenfunctions which corresponds to $n = 0$. The p-modes are acoustic waves with pressure as a restoring force and higher frequencies than the f-modes. The g-modes have buoyancy as a restoring force and exist when $\Gamma_1 \neq \Gamma$. Physically this is due to either composition or entropy gradients. They have lower frequencies than the f-modes. These g-modes can be further classified by whether they are stable or unstable to convection. If, $\Gamma < \Gamma_1$, the bouncy force acts as a restoring force and drives the oscillating fluid element back to its equilibrium position. This is known as convective stability, and the resulting modes are denoted as g^+-modes or simply g-modes. If, $\Gamma > \Gamma_1$, the buoyancy force tends to increase the displacement of a fluid element and the star is unstable to convective phenomena. Such displacements are often called g^{-}-modes. In this thesis we will only consider convectively stable g-modes.

By studying the form of ξ_r and looking at the frequency one can roughly determine if a mode is a p- or f- mode. The g-modes have small ω and a ξ_r that shows prominent features beneath the surface of the star. On the other hand p-modes will have higher ω and a ξ_r that shows prominent features around the surface, $r = R$. The fundamental f-mode can be thought of as the p-mode with the lowest frequency. One can also then distinguish between overtones of the p- and g-modes. As the overtone n increases, ω will decrease for g-modes but increase for p-modes. Also by examining ξ_r again, the number of nodes in the diagram is roughly equal to n. Where ξ_r is most prominent is indicative of the region of the neutron star where the mode is most prominent. Included in Fig. 2.1 are examples of these modes solved numerically for the equations discussed in this section. The frequencies of these modes agree with those from Pnigouras (2017), which also includes tables for different values of Γ_1 and Γ. While these plots are instructive for identifying the type of oscillation mode, care is needed when working quantitatively with $\xi_r(r)$. Since linear perturbations yield the linear homogeneous differential equation (2.21), the eigenfunctions $\xi_r(r)$ are determined only to within a constant factor. In Fig. 2.1 the modes are normalised such that $\xi_r(R) = R$, hence why the numbers appear quite large. In practice when we are extracting other quantities and observables from the mode equations, such as mode amplitudes or mode energies, a different normalisation is used, this will be discussed in later chapters.

2.3 Slowly Rotating Stars

As previously stated, the presence of $\mathcal{B}(\boldsymbol{\xi})$ in (2.10) complicates the solution, rotation removes spherical symmetry and the variables are no longer described by a single spherical harmonic, instead they are a sum over several multipoles.

In order to make progress, the slow rotation approximation is used, where it is assumed that the rotation is slow compared to the break-up frequency of the star, the Keplerian limit, Ω_k such that the problem is a perturbative one. In practice all quantities are expanded in powers of Ω, e.g.

$$\omega(\Omega) = \omega^{(0)} + \omega^{(1)}(\Omega) + \omega^{(2)}(\Omega^2) + ..., \tag{2.53}$$

where the superscript (0) corresponds to the solution in the limit of no rotation. This is however not a controlled expansion and the validity of it is discussed later on. Deviations of the unperturbed star from its original spherical shape are due to the centrifugal force which is a second order effect in Ω, therefore equilibrium quantities can be expanded as

$$\rho(\Omega) = \rho^{(0)} + \rho^{(2)}(\Omega^2) + ... \tag{2.54}$$

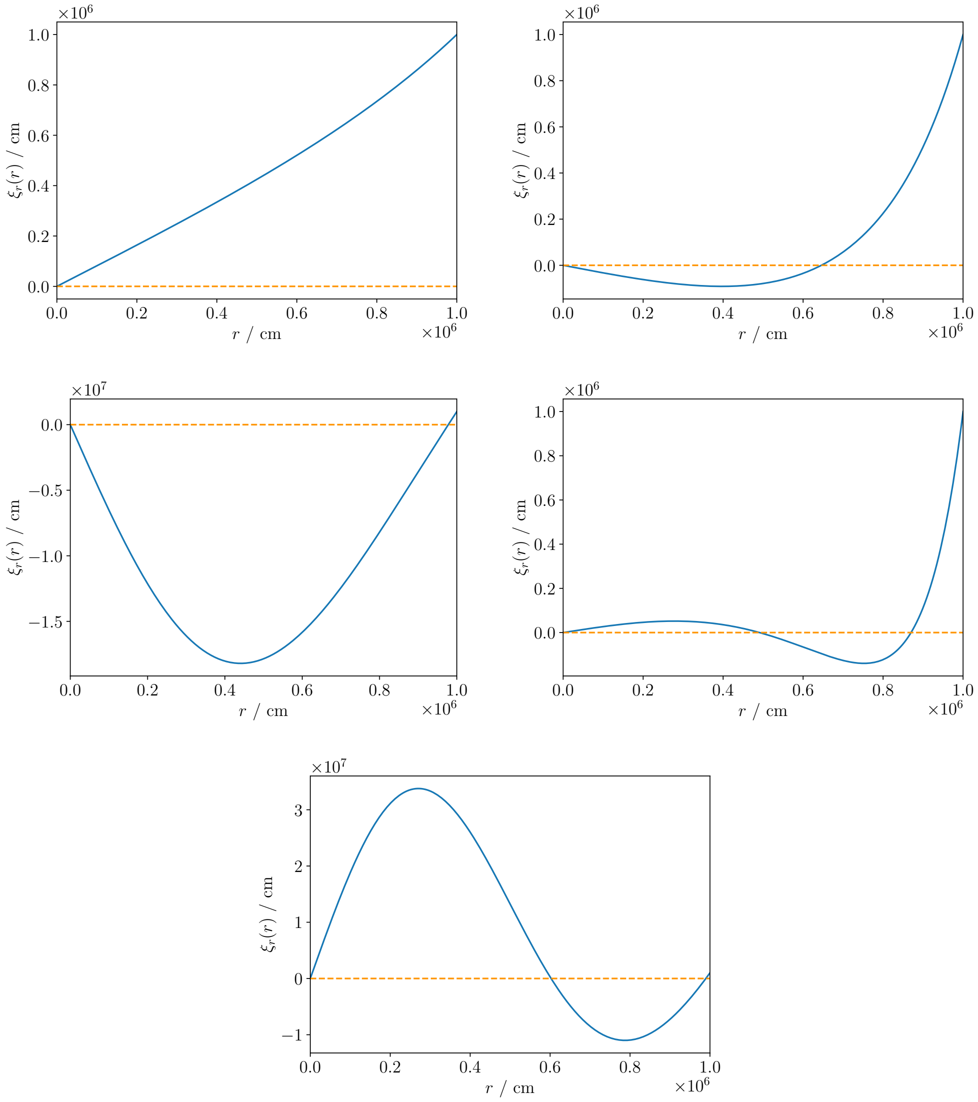

Figure 2.1: Solution for the $l = 2$ modes of a star with mass, $M = 1.4\,M_\odot$, $R = 10\,\mathrm{km}$ and $\Gamma_1 = 2.1$. Plotted is the radial eigenfunction ξ_r against the stellar radius r. The orange dashed line corresponds to $\xi_r = 0$. From left to right the modes are: f and p_1 on the top row, g_1 and p_2 on the middle row and g_2 on the bottom row. The subscript denotes the overtone n of the mode.

Inserting these series expansions into (2.10) and collecting zeroth and first order terms gives

$$\omega^{(0)2}\boldsymbol{\xi}^{(0)} = C^{(0)}(\boldsymbol{\xi}^{(0)}), \tag{2.55}$$

$$-\omega^{(0)2}\boldsymbol{\xi}^{(1)} + C^{(0)}(\boldsymbol{\xi}^{(1)}) - 2\omega^{(0)}\omega^{(1)}\boldsymbol{\xi}^{(0)} + i\omega^{(0)}\mathcal{B}^{(1)}(\boldsymbol{\xi}^{(0)}) = 0. \tag{2.56}$$

As expected the zeroth order equation is the non-rotating equation (2.21) solved in the previous section. As the deformation of the star is a second order effect it can be ignored when only considering the first order equation, therefore can make use of spherical harmonics as was done in the non-rotating case, $\xi_r^{(1)}(r,\theta,\phi) = \xi_r^{(1)}(r)Y_l^m(\theta,\phi)$. From the literature, (Saio, 1981), one can express the first order correction to the eigenfrequency as,

$$\omega^{(1)} = mC_1\Omega, \tag{2.57}$$

where m is the azimuthal order and C_1 is a correction parameter that can be calculated from just the zeroth order solution. The magnitudes of rotational corrections are shown in Table 2.1 for various eigenfrequencies. As expected the frequencies for the f- and p-modes are minimally affected by stratification compared to the g-modes. What is interesting is that C_1 varies most for the p-modes. One can also see how C_1 varies with n. For p-modes C_1 increases with increasing n whereas for g-modes the opposite is observed with C_1 decreasing with increasing n.

TABLE 2.1: Zeroth order eigenfrequencies $\tilde{\omega}_0$ and the first order correction parameter C_1 for $l = 2$ oscillation modes of a star with mass, $M = 1.4M_\odot$, $R = 10$km and varying stratification Γ_1. The frequencies are normalised as $\tilde{\omega} = \omega/\sqrt{GM/R^3}$

Mode	$\Gamma_1 = 2.01$		$\Gamma_1 = 2.05$		$\Gamma_1 = 2.1$		$\Gamma_1 = 2.2$		$\Gamma_1 = 2.3$	
	$\tilde{\omega}$	C_1	$\tilde{\omega}$	C_1	$\tilde{\omega}$	C_1	$\tilde{\omega}$	C_1	$\tilde{\omega}$	C_1
f	1.2270	0.4991	1.2273	0.4990	1.2277	0.4989	1.2284	0.4988	1.2291	0.4986
p_1	3.4733	0.1103	3.5204	0.1044	3.5785	0.0973	3.6928	0.0844	3.8044	0.0730
p_2	5.4305	0.0527	5.4949	0.0502	5.5743	0.0473	5.7300	40.0418	5.8818	0.0369
g_1	0.0836	0.0579	0.1845	0.0639	0.2566	0.0709	0.3515	0.0839	0.4178	0.0954
g_2	0.0574	0.1138	0.1270	0.1163	0.1770	0.1193	0.2434	0.1248	0.2904	0.1297
g_3	0.0441	0.1349	0.0975	0.1363	0.1361	0.1380	0.1875	0.1411	0.2240	0.1439

It is shown in Saio (1981) and Pnigouras (2017) that C_1 scales with the overtone n and degree l and the different modes have different scaling relations.

- f-mode: $C_1 = \frac{1}{l}$.
- p-mode: $C_1 \longrightarrow 0$ as $n \longrightarrow \infty$.
- g-mode: $C_1 \longrightarrow \frac{1}{l(l+1)}$ as $n \longrightarrow \infty$.

This relation explains why the f-mode has little variance in Table 2.1, which agrees approximately with the theoretical value of 0.5.

Next on to solving the mode equations. One can use the same method as the previous section by using (2.56) instead of (2.21). This generates a version of (2.22) - (2.24) now in terms of $(\xi_{r,l}^{(1)}, \delta p_l^{(1)}, \delta\Phi_l^{(1)})$.

$$\begin{aligned} x\frac{dy_1^{(1)}}{dr} = \left(V_g - 3\right) y_1^{(1)} + \left[\frac{l(l+1)}{\tilde{\omega}^{(0)2}c_1} - V_g\right] y_2^{(1)} + V_g y_3^{(1)} \\ + \frac{2m\Omega}{\omega^{(0)}}\left(y_0^{(1)} + \left[1 - \frac{\omega^{(1)}}{m\Omega} l(l+1)\right]\frac{y_2^{(0)}}{c_1\tilde{\omega}^{(0)2}}\right), \end{aligned} \tag{2.58}$$

$$\begin{aligned} x\frac{dy_2^{(1)}}{dr} = (\tilde{\omega}^2 c_1 - A^*)y_1^{(1)} - (A^* - U + 1)y_2^{(1)} - A^* y_3^{(1)} \\ + \frac{2m\Omega}{\omega^{(0)}}\left(\frac{\omega^{(1)}}{m\Omega}c_1\tilde{\omega}^{(0)2}y^{(0)} - y_2^{(0)}\right), \end{aligned} \tag{2.59}$$

$$x\frac{dy_3^{(1)}}{dr} = (1 - U)y_3^{(1)} + y_4^{(1)}, \tag{2.60}$$

$$x\frac{dy_4^{(1)}}{dr} = UA^* y_1^{(1)} + UV_g y_2^{(1)} + [l(l+1) - UV_g]y_3^{(1)} - Uy_4^{(1)}. \tag{2.61}$$

Again four boundary conditions are used, with the same physical interpretations. Near the origin as $r \longrightarrow 0$:

$$c_1\tilde{\omega}^{(0)2}y_1^{(1)} - ly_2^{(1)} + \frac{2m\Omega}{\omega^{(0)}}\left(\frac{\omega^{(1)}}{m\Omega} - \frac{1}{l}\right)c_1\tilde{\omega}^{(0)2}y_1^{(0)} = 0, \tag{2.62}$$

$$ly_3^{(1)} - y_4^{(1)} = 0. \tag{2.63}$$

Near the surface as $r \longrightarrow R$:

$$Uy_1^{(1)} + (l+1)y_3^{(1)} + y_4^{(1)} = 0, \tag{2.64}$$

$$\begin{aligned} \left(1 - \frac{4 + c_1\tilde{\omega}^{(0)2}}{V}\right)y_1^{(1)} + \left[\frac{l(l+1)}{c_1\tilde{\omega}^{(0)2}V} - 1\right]y_2^{(1)} + \left(1 - \frac{l+1}{V}\right)y_3^{(1)} \\ + \frac{2m\Omega}{\omega^{(0)}V}\left\{\left(1 - \frac{\omega^{(1)}}{m\Omega}c_1\tilde{\omega}^{(0)2}\right)y_1^{(0)} + \left[1 - \frac{\omega^{(1)}}{m\Omega}l(l+1) + c_1\tilde{\omega}^{(0)2}\right]\frac{y_0^{(0)}}{c_1\tilde{\omega}^{(0)2}}\right\} = 0. \end{aligned} \tag{2.65}$$

These equations were solved numerically with a polytropic equation of state. The first order correction to the eigenfunction $\xi_r^{(1)}$ is shown in Fig. 2.2 for the same modes and neutron star as in Fig. 2.1 but now with $\Omega = 100\,\mathrm{Hz}$, $\Gamma_1 = 2.1$ and $m = 2$. The problem can also be extended to second order in Ω, the methodology and equations can be found in Saio (1981) and Pnigouras (2017).

The validity of this approximation depends on the equation of state and oscillation mode but work by Reese et al. (2006) indicates that the error compared to the frequencies and eigenfunctions calculated using a non-perturbative approach is within 1% for rotation frequencies up to $\sim 0.1\Omega_k$.

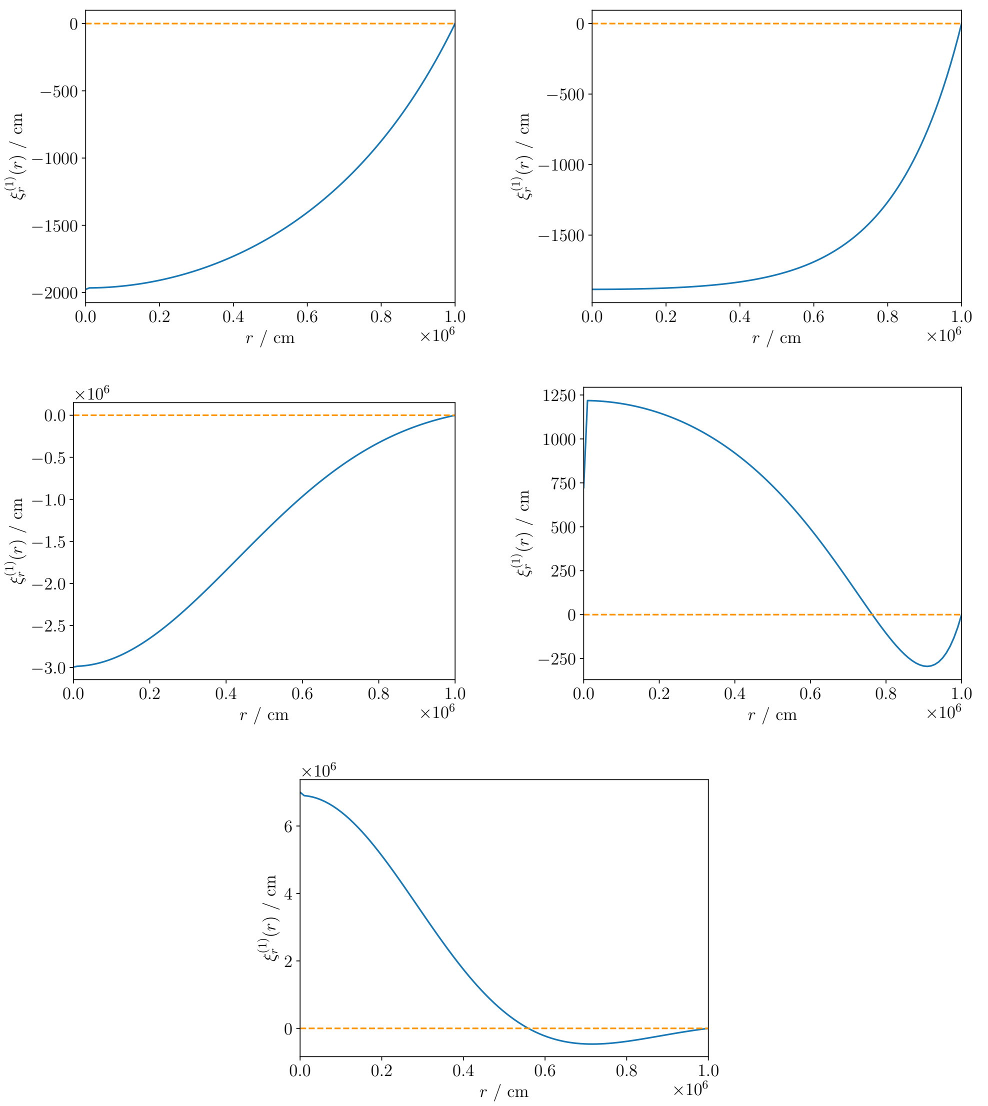

FIGURE 2.2: First order corrections to eigenfunctions $\xi_r^{(1)}$ against the stellar radius r for the modes from Fig. 2.1 for the same star but now with $\Omega = 100\,\mathrm{Hz}$ and $m = 2$. The orange dashed line corresponds to $\xi_r^{(1)} = 0$. From left to right the modes are: f and p_1 on the top row, g_1 and p_2 on the middle row and g_2 on the bottom row.

Chapter 3

G-modes for Arbitrary Reaction Rates

In the previous chapter we discussed how the restoring force of g-modes is the buoyancy associated with the varying composition of matter in neutron stars (Reisenegger and Goldreich, 1992b). The typical frequency of the leading neutron star g-mode is of the order of a few 100 Hz, dependent on the equation of state, and the higher overtones lie at lower frequencies. In a neutron star, with stable stratification, one would expect to find an infinite set of undamped, low-frequency g-modes based on the non-dissipative analysis of the previous chapter. As these modes rely on stable composition stratification for their existence, they are sensitive to nuclear reactions which will strive to reinstate equilibrium in the matter and hence lead to each g-mode becoming damped. In this chapter, we expand on the work of Andersson and Pnigouras (2019) and establish a more precise understanding of how the g-modes are affected by reactions and what happens to the mode spectrum when the reaction rate becomes fast compared to the dynamics. Even though the overall aim is always for realism, this chapter will be restricted to the context of Newtonian gravity. This makes the results somewhat phenomenological, but as it will later become necessary to exaggerate the reaction rates in order to demonstrate the features this work is interested in anyway, this lack of precision is not a great concern. This formalism has since been adapted to general relativity in Zhao et al. (2025).

3.1 Introducing Reactions

The first step is to write $\boldsymbol{\xi}$ in a more general form, expressed in spherical polar coordinates $[r, \theta, \phi]$

$$\xi^i_n(t, r, \theta, \varphi) = \xi^i(r, \theta) e^{i\omega_n t} , \tag{3.1}$$

where, in a coordinate basis,

$$\xi^i = \sum_l \frac{1}{r} W_l Y_l^m e_r^i + \left(\frac{1}{r^2} V_l \partial_\theta Y_l^m + \frac{m}{r^2} \sin\theta U_l Y_l^m \right) e_\theta^i + \\ \frac{i}{r^2} \sin^2\theta \left(m V_l Y_l^m + U_l \sin\theta \partial_\theta Y_l^m \right) e_\phi^i, \tag{3.2}$$

where W_l and V_l are referred to as polar perturbations, and U_l is axial. The sign convention of Lockitch and Friedman (1999) is being used here. It it easy to show that for nonrotating stars there cannot exist a purely axial mode with a non-zero frequency, so in the following only purely polar modes, with $U_l = 0$ are considered.

Along with this, all scalar perturbations are expanded in spherical harmonics. That is

$$\delta\rho_n = \delta\rho(r, \theta, \phi) e^{i\omega_n t} , \tag{3.3}$$

with

$$\delta\rho = \sum_l \delta\rho_l Y_l^m \tag{3.4}$$

and similar for all other scalar quantities.

Using this new form of $\boldsymbol{\xi}$, the radial component of the perturbed Euler (2.5) becomes,

$$-\omega_n^2 W_l + r\partial_r \delta\Phi_l + \frac{1}{\rho} r\partial_r \delta p_l - \frac{1}{\rho^2} \delta\rho_l r\partial_r p = 0 , \tag{3.5}$$

or

$$\partial_r \delta p_l - \left(\frac{\partial_r p}{\rho} \right) \delta\rho_l = \frac{\omega_n^2 \rho}{r} W_l - \rho \partial_r \delta\Phi_l , \tag{3.6}$$

and then from the ϕ component of the Euler equation,

$$\omega_n^2 V_l = \delta\Phi_l + \frac{\delta p_l}{\rho} . \tag{3.7}$$

Next the perturbed continuity equation (2.4) becomes,

$$\delta\rho_l = -\frac{W_l}{r} \partial_r \rho - \frac{\rho}{r^2} \left[\partial_r (r W_l) - l(l+1) V_l \right] . \tag{3.8}$$

Combining the last two equations,

$$\delta\rho_l = -\frac{W_l}{r} \partial_r \rho - \frac{\rho}{r^2} \left[\partial_r (r W_l) - \frac{l(l+1)}{\omega_n^2} \left(\delta\Phi_l + \frac{\delta p_l}{\rho} \right) \right] , \tag{3.9}$$

or

$$\partial_r (r W_l) + \frac{r W_l}{\rho} \partial_r \rho = -\frac{r^2}{\rho} \delta\rho_l + \frac{l(l+1)}{\omega_n^2} \left(\delta\Phi_l + \frac{\delta p_l}{\rho} \right) . \tag{3.10}$$

As the moving fluid is no longer in equilibrium, additional parameters must be considered in the equation of state. A natural option, which helps account for nuclear reactions driven by the deviation from beta equilibrium, is to introduce a new variable $\beta = \mu_{\rm n} - \mu_{\rm p} - \mu_{\rm e}$ which depends on the chemical potentials of the neutrons, protons and electrons (labelled n, p and e, respectively). In cold equilibrium, $\beta = 0$. This condition allows one to solve for the matter composition, specifically the lepton/proton fraction $x_{\rm p}$ for a given mass density. For simplicity, it is assumed that there is only pure npe matter (and that the star is cold enough to be transparent to neutrinos) which means that the relevant reactions will be the Urca and modified Urca reactions. The modified Urca reactions act on a timescale of (Haensel et al., 2002)

$$t_R \sim 10^{13}\left(\frac{10^8 \mathrm{K}}{T}\right)^6 \mathrm{s}\,. \tag{3.11}$$

These reaction rates are expected to be many orders of magnitude slower than the timescale of the modes and therefore far too slow (at least for the temperatures considered in this work) to have significant impact on the low-order g-modes. Hence, the focus is now on a parametrised model and a wide range of reaction rates. While this means that the numerical results that will be obtained are, inevitably, phenomenological, it is believed the behaviour is robust enough that an extrapolation to realistic reaction rates/high order modes is straightforward. In order to keep track of the matter composition, the equation of state will now be a two parameter function unlike in the previous chapters, $p = p(\rho, x_{\rm p})$ where $x_{\rm p}$ is the proton fraction. From Andersson and Pnigouras (2019),

$$\Delta\beta = \frac{\mathcal{B}}{1 + i\mathcal{A}/\omega}\Delta\rho\,, \tag{3.12}$$

where,

$$\mathcal{B} = \left(\frac{\partial\beta}{\partial\rho}\right)_{x_{\rm p}}\,, \tag{3.13}$$

and

$$\mathcal{A} = -\frac{1}{t_r}\,, \tag{3.14}$$

where t_r is the characteristic reaction time and the minus sign is a convention used in this thesis. Note that $\beta = 0$ for the unperturbed star (as it is assumed to be in chemical equilibrium) leading to $\Delta\beta = \delta\beta$. Using this and combining (3.12) and (3.8) to get,

$$i\omega_n\delta\beta_l - \mathcal{A}\delta\beta_l = -i\omega_n\frac{\rho\mathcal{B}}{r^2}\left[\partial_r(rW_l) - l(l+1)V_l\right]\,. \tag{3.15}$$

As it is common to work with the perturbed pressure, this is rewritten as

$$i\omega_n\delta\beta_l - \mathcal{A}\delta\beta_l = i\omega_n\mathcal{B}\left(\delta\rho_l + \frac{W_l}{r}\partial_r\rho\right)\,, \tag{3.16}$$

also needed is

$$\delta p_l = \left(\frac{\partial p}{\partial\rho}\right)_\beta\delta\rho_l + \left(\frac{\partial p}{\partial\beta}\right)_\rho\delta\beta_l\,, \tag{3.17}$$

leading to

$$\delta p_l = \left(\frac{\partial p}{\partial \rho}\right)_\beta \delta\rho_l + \frac{1}{1+i\mathcal{A}/\omega_n}\left(\frac{\partial \beta}{\partial \rho}\right)_{x_\mathrm{p}}\left(\frac{\partial p}{\partial \beta}\right)_\rho \left(\delta\rho_l + \frac{W_l}{r}\partial_r\rho\right) , \tag{3.18}$$

or

$$\begin{aligned}\delta p_l = &\left[\left(\frac{\partial p}{\partial \rho}\right)_\beta + \frac{1}{1+i\mathcal{A}/\omega_n}\left(\frac{\partial \beta}{\partial \rho}\right)_{x_\mathrm{p}}\left(\frac{\partial p}{\partial \beta}\right)_\rho\right]\delta\rho_l \\ &+ \frac{1}{1+i\mathcal{A}/\omega_n}\left(\frac{\partial \beta}{\partial \rho}\right)_{x_\mathrm{p}}\left(\frac{\partial p}{\partial \beta}\right)_\rho\left(\frac{W_l}{r}\partial_r\rho\right) .\end{aligned} \tag{3.19}$$

For convenience it make sense to use the thermodynamic relation,

$$\left(\frac{\partial p}{\partial \rho}\right)_\beta + \left(\frac{\partial p}{\partial \beta}\right)_\rho\left(\frac{\partial \beta}{\partial \rho}\right)_{x_\mathrm{p}} = \left(\frac{\partial p}{\partial \rho}\right)_{x_\mathrm{p}} , \tag{3.20}$$

or

$$\left(\frac{\partial p}{\partial \beta}\right)_\rho\left(\frac{\partial \beta}{\partial \rho}\right)_{x_\mathrm{p}} = \left(\frac{\partial p}{\partial \rho}\right)_{x_\mathrm{p}} - \left(\frac{\partial p}{\partial \rho}\right)_\beta , \tag{3.21}$$

to get

$$\begin{aligned}\delta p_l = &\left\{1 + \frac{1}{1+i\mathcal{A}/\omega_n}\left[\left(\frac{\partial p}{\partial \rho}\right)_\beta^{-1}\left(\frac{\partial p}{\partial \rho}\right)_{x_\mathrm{p}} - 1\right]\right\}\left(\frac{\partial p}{\partial \rho}\right)_\beta \delta\rho_l \\ &+ \frac{1}{1+i\mathcal{A}/\omega_n}\left[\left(\frac{\partial p}{\partial \rho}\right)_\beta^{-1}\left(\frac{\partial p}{\partial \rho}\right)_{x_\mathrm{p}} - 1\right]\left(\frac{\partial p}{\partial \rho}\right)_\beta\left(\frac{W_l}{r}\partial_r\rho\right) .\end{aligned} \tag{3.22}$$

Next the speed of sound in equilibrium and at fixed proton fraction, are defined respectively as;

$$c_s^2 = \left(\frac{\partial p}{\partial \rho}\right)_\beta , \tag{3.23}$$

$$C^2 = \left(\frac{\partial p}{\partial \rho}\right)_{x_\mathrm{p}} , \tag{3.24}$$

and the density scale height (which is convenient as it avoids involving an actual stellar background model in the plane-wave analysis below)

$$\frac{1}{H} = \frac{1}{\rho}\partial_r\rho = \partial_r \ln\rho . \tag{3.25}$$

These quantities are related to the commonly used adiabatic indices via

$$c_s^2 = \frac{p\Gamma}{\rho} , \quad \text{and} \quad C^2 = \frac{p\Gamma_1}{\rho} , \tag{3.26}$$

where Γ and Γ_1 are, again, the adiabatic indices of the background and perturbed matter, respectively. If the equation of state is polytropic as in (2.20), then $\Gamma = \gamma$. Then

$$\delta p_l = \left[1 + \frac{1}{1 + i\mathcal{A}/\omega_n}\left(\frac{C^2}{c_s^2} - 1\right)\right] c_s^2 \delta\rho_l + \frac{1}{1 + i\mathcal{A}/\omega_n}\left(\frac{C^2}{c_s^2} - 1\right) c_s^2 \left(\frac{\rho W_l}{rH}\right) . \tag{3.27}$$

When solving the equations numerically later on, $\delta\rho_l$ will be removed, so it is useful to have the following equation

$$\delta\rho_l = \left[1 + \frac{1}{1 + i\mathcal{A}/\omega_n}\left(\frac{C^2}{c_s^2} - 1\right)\right]^{-1} \left\{\frac{1}{c_s^2}\delta p_l - \frac{1}{1 + i\mathcal{A}/\omega_n}\left(\frac{C^2}{c_s^2} - 1\right)\left(\frac{\rho W_l}{rH}\right)\right\} . \tag{3.28}$$

Finally, define the Brunt-Väisälä frequency as

$$\mathcal{N}^2 = g^2\left(\frac{1}{c_s^2} - \frac{1}{C^2}\right) = \frac{c_s^4}{H^2}\left(\frac{1}{c_s^2} - \frac{1}{C^2}\right) = -\frac{c_s^4}{H^2C^2}\left(1 - \frac{C^2}{c_s^2}\right) , \tag{3.29}$$

where

$$g = \frac{d\Phi}{dr} , \tag{3.30}$$

which leads to

$$\frac{C^2}{c_s^2} - 1 = \frac{\mathcal{N}^2 H^2 C^2}{c_s^4} \equiv \bar{\mathcal{N}}^2 , \tag{3.31}$$

and hence

$$\delta\rho_l = \left[1 + \frac{\bar{\mathcal{N}}^2}{1 + i\mathcal{A}/\omega_n}\right]^{-1} \left\{\frac{1}{c_s^2}\delta p_l - \frac{\bar{\mathcal{N}}^2}{1 + i\mathcal{A}/\omega_n}\left(\frac{\rho W_l}{rH}\right)\right\} . \tag{3.32}$$

As mentioned previously we will only consider convectively stable g-modes, which corresponds to $\mathcal{N}^2 > 0$. Also, rewriting (3.6) and (3.10)

$$\partial_r \delta p_l - \frac{c_s^2}{H}\delta\rho_l = \frac{\omega_n^2 \rho}{r} W_l - \rho\partial_r\delta\Phi_l , \tag{3.33}$$

and

$$\partial_r\left(r\rho W_l\right) = -r^2\delta\rho_l + \frac{l(l+1)}{\omega_n^2}\left(\rho\delta\Phi_l + \delta p_l\right) . \tag{3.34}$$

These last three equations are the main equations that will be used to determine the neutron star g-modes. In order to solve them numerically, the dimensionless form from the previous chapter is used with the following redefinition

$$y_1 = \frac{W_l}{r^2} . \tag{3.35}$$

Therefore, rewriting (3.32) – (3.34) and the perturbed Poisson equation,

$$r\frac{dy_1}{dr} = \left(-\frac{d\ln\rho}{d\ln r} - 3\right) y_1 + \frac{l(l+1)}{\tilde{\omega}_n^2 c_1} y_2 - \left[1 + \frac{\bar{\mathcal{N}}^2}{1 + i\mathcal{A}/\omega_n}\right]^{-1} \left\{\frac{1}{c_s^2} g r (y_2 - y_3) - \frac{\bar{\mathcal{N}}^2}{1 + i\mathcal{A}/\omega_n}\left(\frac{r y_1}{H}\right)\right\}, \tag{3.36}$$

$$r\frac{dy_2}{dr} = \tilde{\omega}_n^2 c_1 y_1 - \left[1 + \frac{d\ln(\rho g)}{d\ln r}\right] y_2 + \frac{d\ln\rho}{d\ln r} y_3 + \left[1 + \frac{\bar{\mathcal{N}}^2}{1 + i\mathcal{A}/\omega_n}\right]^{-1} \left\{\frac{r}{H}(y_2 - y_3) - \frac{\bar{\mathcal{N}}^2}{1 + i\mathcal{A}/\omega_n}\frac{c_s^2}{H^2}\left(\frac{ry_1}{g}\right)\right\}, \quad (3.37)$$

$$r\frac{dy_3}{dr} = (1 - U)y_3 + y_4, \quad (3.38)$$

$$r\frac{dy_4}{dr} = l(l+1)y_3 - Uy_4 + 4\pi G\rho\left[1 + \frac{\bar{\mathcal{N}}^2}{1 + i\mathcal{A}/\omega_n}\right]^{-1} \left\{\frac{1}{c_s^2}r^2(y_2 - y_3) - \frac{\bar{\mathcal{N}}^2}{1 + i\mathcal{A}/\omega_n}\left(\frac{r^2 y_1}{gH}\right)\right\}. \quad (3.39)$$

Using

$$g = -\frac{c_s^2}{H}, \quad (3.40)$$

the equations can be simplified to

$$x\frac{dy_1}{dx} = (V - 3)y_1 + \frac{l(l+1)}{\tilde{\omega}_n^2 c_1}y_2 - V\left[1 + \frac{\bar{\mathcal{N}}^2}{1 + i\mathcal{A}/\omega_n}\right]^{-1}\left\{y_2 - y_3 + \frac{\bar{\mathcal{N}}^2}{1 + i\mathcal{A}/\omega_n}y_1\right\}, \quad (3.41)$$

$$x\frac{dy_2}{dx} = \tilde{\omega}_n^2 c_1 y_1 + (V - U + 1)y_2 - Vy_3 - V\left[1 + \frac{\bar{\mathcal{N}}^2}{1 + i\mathcal{A}/\omega_n}\right]^{-1}\left\{y_2 - y_3 + \frac{\bar{\mathcal{N}}^2}{1 + i\mathcal{A}/\omega_n}y_1\right\}, \quad (3.42)$$

$$x\frac{dy_3}{dx} = (1 - U)y_3 + y_4, \quad (3.43)$$

$$x\frac{dy_4}{dx} = l(l+1)y_3 - Uy_4 - UV\left[1 + \frac{\bar{\mathcal{N}}^2}{1 + i\mathcal{A}/\omega_n}\right]^{-1}\left\{y_2 - y_3 + \frac{\bar{\mathcal{N}}^2}{1 + i\mathcal{A}/\omega_n}y_1\right\}. \quad (3.44)$$

As in previous cases, four boundary conditions are needed. These are the same as in the frozen composition case, (2.46)-(2.49). In order to close these equations an equation of state and reaction rates are needed.

3.2 Plane-wave analysis

To check that these equations seem realistic, a sanity check is needed. This is done by checking how the equations behave in the limits of a fast or slow reaction rate. For simplicity, introduce

$$\bar{W}_l = \frac{\rho W_l}{r}, \quad (3.45)$$

and insert into (3.32) - (3.34) to get the, fairly concise, equations

$$\partial_r \delta p_l - \frac{c_s^2}{H}\delta\rho_l = \omega_n^2 \bar{W}_l - \rho\partial_r\delta\Phi_l, \tag{3.46}$$

$$\partial_r\left(r^2\bar{W}_l\right) = -r^2\delta\rho_l + \frac{l(l+1)}{\omega_n^2}\left(\rho\delta\Phi_l + \delta p_l\right), \tag{3.47}$$

$$\delta\rho_l = \left[1 + \frac{\bar{\mathcal{N}}^2}{1 + i\mathcal{A}/\omega_n}\right]^{-1}\left\{\frac{1}{c_s^2}\delta p_l - \frac{\bar{\mathcal{N}}^2}{1 + i\mathcal{A}/\omega_n}\left(\frac{\bar{W}_l}{H}\right)\right\}. \tag{3.48}$$

As this is just for examining qualitative trends, next make the Cowling approximation by setting $\delta\Phi_l = 0$ and also remove $\delta\rho_l$

$$\begin{aligned}\partial_r\delta p_l - \left[1 + \frac{\bar{\mathcal{N}}^2}{1 + i\mathcal{A}/\omega_n}\right]^{-1}\left(\frac{\delta p_l}{H}\right)& \\ = \left\{\omega_n^2 - \frac{c_s^2}{H^2}\left[1 + \frac{\bar{\mathcal{N}}^2}{1 + i\mathcal{A}/\omega_n}\right]^{-1}\frac{\bar{\mathcal{N}}^2}{1 + i\mathcal{A}/\omega_n}\right\}\bar{W}_l,&\end{aligned} \tag{3.49}$$

$$\begin{aligned}\frac{1}{r^2}\partial_r(r^2\bar{W}_l) - \left[1 + \frac{\bar{\mathcal{N}}^2}{1 + i\mathcal{A}/\omega_n}\right]^{-1}\frac{\bar{\mathcal{N}}^2}{1 + i\mathcal{A}/\omega_n}\left(\frac{\bar{W}_l}{H}\right)& \\ = \left\{\frac{\mathcal{L}_l^2}{\omega_n^2} - \left[1 + \frac{\bar{\mathcal{N}}^2}{1 + i\mathcal{A}/\omega_n}\right]^{-1}\right\}\frac{\delta p_l}{c_s^2},&\end{aligned} \tag{3.50}$$

where the Lamb frequency is defined as

$$\mathcal{L}_l^2 = \frac{l(l+1)c_s^2}{r^2}. \tag{3.51}$$

In order to explore the nature of the waves this project is interested in, the plane-wave approach is adopted with

$$\hat{p} = \delta p_l\,, \qquad \hat{W} = r^2\bar{W}_l\,, \qquad \partial_r \longrightarrow ik, \tag{3.52}$$

leading to

$$\left(ik - \left[1 + \frac{\bar{\mathcal{N}}^2}{1 + i\mathcal{A}/\omega_n}\right]^{-1}\frac{1}{H}\right)\hat{p} = \left(\omega_n^2 - \left[1 + \frac{\bar{\mathcal{N}}^2}{1 + i\mathcal{A}/\omega_n}\right]^{-1}\frac{\bar{\mathcal{N}}^2 c_s^2}{1 + i\mathcal{A}/\omega_n}\frac{1}{H^2}\right)\frac{\hat{W}}{r^2}, \tag{3.53}$$

$$\left(ik - \left[1 + \frac{\bar{\mathcal{N}}^2}{1 + i\mathcal{A}/\omega_n}\right]^{-1}\frac{\bar{\mathcal{N}}^2}{1 + i\mathcal{A}/\omega_n}\frac{1}{H}\right)\frac{\hat{W}}{r^2} = \left(\frac{\mathcal{L}_l^2}{\omega_n^2} - \left[1 + \frac{\bar{\mathcal{N}}^2}{1 + i\mathcal{A}/\omega_n}\right]^{-1}\right)\frac{\hat{p}}{c_s^2}. \tag{3.54}$$

The question is what can be learned from this. First assume that $\bar{\mathcal{N}}^2 \ll 1$, as the aim is to find low frequency solutions i.e. g-modes, in which case,

$$\left(ik - \frac{1}{H}\right)\hat{p} = \left(\omega_n^2 - \frac{\bar{\mathcal{N}}^2 c_s^2}{1 + i\mathcal{A}/\omega_n}\frac{1}{H^2}\right)\frac{\hat{W}}{r^2}, \tag{3.55}$$

$$\left(ik - \frac{\bar{\mathcal{N}}^2}{1 + i\mathcal{A}/\omega_n}\frac{1}{H}\right)\frac{\hat{W}}{r^2} = -\left(1 - \frac{\mathcal{L}_l^2}{\omega_n^2}\right)\frac{\hat{p}}{c_s^2}. \tag{3.56}$$

These approximations obviously involve a sacrifice in precision, but they retain the main qualitative behaviour, with $\mathcal{N}$ regulating the importance of stratification. It is also easy to see that the expected barotropic result emerges in the $\mathcal{N}^2 \rightarrow 0$ limit.

Now different limits are considered. For fast reactions, one gets (for short wavelengths, so $kH \gg 1$, as this is a local calculation, and all background quantities are taking to be constant)

$$\left(ik - \frac{1}{H}\right)\hat{p} \approx ik\hat{p} = \omega_n^2\frac{\hat{W}}{r^2}, \tag{3.57}$$

$$ik\frac{\hat{W}}{r^2} = -\left(1 - \frac{\mathcal{L}_l^2}{\omega_n^2}\right)\frac{\hat{p}}{c_s^2}, \tag{3.58}$$

leading to the dispersion relation

$$\omega_n^2 = c_s^2k^2 + \mathcal{L}_l^2. \tag{3.59}$$

This solution represents sound waves—the pressure p-modes in the full mode calculation. Higher overtone modes have shorter scales (=larger k) so the frequencies increase. In a neutron star, there is an infinite set of high-frequency p-modes, $n \rightarrow \infty$, $\omega_n \rightarrow \infty$. In the opposite limit of slow reactions,

$$ik\hat{p} = \left(\omega_n^2 - \frac{\bar{\mathcal{N}}^2c_s^2}{H^2}\right)\frac{\hat{W}}{r^2}, \tag{3.60}$$

$$ik\frac{\hat{W}}{r^2} = -\left(1 - \frac{\mathcal{L}_l^2}{\omega_n^2}\right)\frac{\hat{p}}{c_s^2}. \tag{3.61}$$

Now one arrives at

$$k^2c_s^2 = \left(\omega_n^2 - \frac{\bar{\mathcal{N}}^2c_s^2}{H^2}\right)\left(1 - \frac{\mathcal{L}_l^2}{\omega_n^2}\right). \tag{3.62}$$

This equation has two sets of roots. If it is also the case that

$$\omega_n^2 \ll \mathcal{L}_l^2, \tag{3.63}$$

then

$$\omega_n^2 \equiv \omega_0^2 \approx \mathcal{N}^2\frac{C^2}{c_s^2}\left(\frac{k^2c_s^2 + \mathcal{L}_l^2}{\mathcal{L}_l^2}\right)^{-1} \approx \mathcal{N}^2\frac{C^2}{c_s^2}\frac{k^2r^2}{l(l+1)}. \tag{3.64}$$

In the opposite limit, when

$$\omega_n^2 \gg \mathcal{L}_l^2, \tag{3.65}$$

it is easy to see that the p-modes are retained from the barotropic case. In essence, the introduction of the stratification has added a set of low-frequency modes to the spectrum. These are the g-modes. It is easy to see that, as the wavelength decreases (=larger k) the frequency decreases. In a neutron star, with fixed stratification, there is an infinite set of undamped low-frequency g-modes, as $n \rightarrow \infty$, $\omega_n \rightarrow 0$. This changes when the nuclear reactions are considered. For finite reaction rates, (if $\omega_n^2 \ll \mathcal{L}_l^2$)

$$ik\hat{p} = \left(\omega_n^2 - \frac{\mathcal{N}^2}{1 + i\mathcal{A}/\omega_n} \frac{C^2}{c_s^2}\right)\frac{\hat{W}}{r^2}, \tag{3.66}$$

$$ik\frac{\hat{W}}{r^2} = \frac{\mathcal{L}_l^2}{\omega_n^2}\frac{\hat{p}}{c_s^2}. \tag{3.67}$$

That is,

$$\frac{k^2c_s^2 + \mathcal{L}_l^2}{\mathcal{L}_l^2} \approx \frac{t_R}{\omega_n t_R - i}\frac{C^2}{c_s^2}\frac{\mathcal{N}^2}{\omega_n}, \tag{3.68}$$

or

$$\omega_n \approx \frac{t_R}{\omega_n t_R - i}\mathcal{N}^2\frac{C^2}{c_s^2}\left(\frac{k^2c_s^2 + \mathcal{L}_l^2}{\mathcal{L}_l^2}\right)^{-1} = \frac{t_R}{\omega_n t_R - i}\omega_0^2. \tag{3.69}$$

In general, the reactions lead to complex-frequency (damped) oscillations. It is, however, easy to see that the previous (undamped!) results are retained in both the fast and slow reaction limits. Now solving for the frequency,

$$\omega_n(\omega_n t_R - i) - \omega_0^2 t_R = 0, \tag{3.70}$$

or

$$\omega_n^2 - \frac{i}{t_R}\omega_n - \omega_0^2 = 0, \tag{3.71}$$

leading to

$$\omega_n \approx \frac{1}{2t_R}\left[i \pm \left(4\omega_0^2 t_R^2 - 1\right)^{1/2}\right], \tag{3.72}$$

both roots are purely damped. That is, in this limit the system does not have oscillatory modes. The implications of this are important. While the classic analysis suggests that the g-mode spectrum is infinite, in a neutron star this cannot be so. The (potentially very) high overtones, for which $\omega_0 t_R$ is small, will be overdamped. This accords with the results from Andersson and Pnigouras (2019).

In the slow reaction limit, from equation (3.64), the g-mode solution is

$$\omega_n \approx \omega_0. \tag{3.73}$$

In the fast reaction limit, from equation (3.72), when ω_n first becomes purely imaginary is when the two roots are equal, which is

$$\omega_n \approx i\omega_0. \tag{3.74}$$

This solution is i times the slow reaction limit frequency. From this one can see that as the reaction rate tends to zero, the g-mode frequencies will move through the complex plane starting on the real axis and finishing on the imaginary axis. From this equation one also get the reaction rate at which it should hit the imaginary axis,

$$t_r = \frac{1}{2\omega_0}. \tag{3.75}$$

One can also calculate the ratio,

$$\frac{|\mathcal{A}_{\text{Crit}}|}{\omega_0} \approx 2. \tag{3.76}$$

Therefore, if the slow reaction limit frequency $\omega_{n,slow}$ is known, as is the critical frequency.

$$|\mathcal{A}_{Crit}| \approx 2\omega_{n,slow}. \tag{3.77}$$

In this regime the mode solutions represent pure diffusion. Instead of having a damped oscillatory motion, the fluid simply relaxes towards equilibrium. Also from (3.72), one sees that $|\omega_n|^2 \approx \omega_0^2$. This suggests that the magnitude of the mode frequency remains constant even as the mode is being damped.

3.3 Results

In order to solve the equations, a model of a background neutron star is needed for the perturbations to exist on and an equation of state must be chosen. In order to make this model more realistic the BSk family of equations of state was chosen (Pearson et al., 2012; Potekhin et al., 2013; Fantina et al., 2013). Specifically, mainly as proof of principle, the BSk21 model was chosen, which has been used in recent oscillation mode research (Gittins and Andersson, 2023; Andersson and Gittins, 2023). This allows one to employ a realistic description of the matter stratification. While the same information can be extracted from many other "realistic" equation of state models, the BSk family has the advantage of being expressed in closed form, which means that the thermodynamical derivatives required for the g-mode calculation do not have to be worked out numerically. This is convenient as it avoids the numerical errors that would be unavoidable if one were to work out these derivatives from tabulated equation of state data.

First from the BSk21 formulae, the relationship $p(n_B)$ and $\tilde{N}^2(n_B)$ were obtained, where n_B is the baryon number density. As the final equations are in Newtonian gravity, n_B can be converted to density using $\rho = m_B n_B$, where m_B is baryon mass. However, in order to solve the equations, one needs to convert $p(\rho)$ to $p(r)$ and $\rho(r)$. To do this, the Newtonian stellar structure equations were solved numerically using the obtained $p(\rho)$. Having fixed the equation of state, one still needs to pick a sample neutron star. The particular neutron star chosen has central density $\rho = 5.06 \times 10^{14}\,\text{gcm}^{-3}$, which leads to a radius of $R = 13.49\,\text{km}$ and a mass of $M = 1.4\,M_\odot$, this was so the mass and radius would be similar to the values used in the non-reacting case in Figs. 2.1 and 2.2. Equations (3.41) - (3.44) along with the boundary conditions (2.27) - (2.30) were solved numerically using this background star and for different reaction rates by varying $\mathcal{A}$.

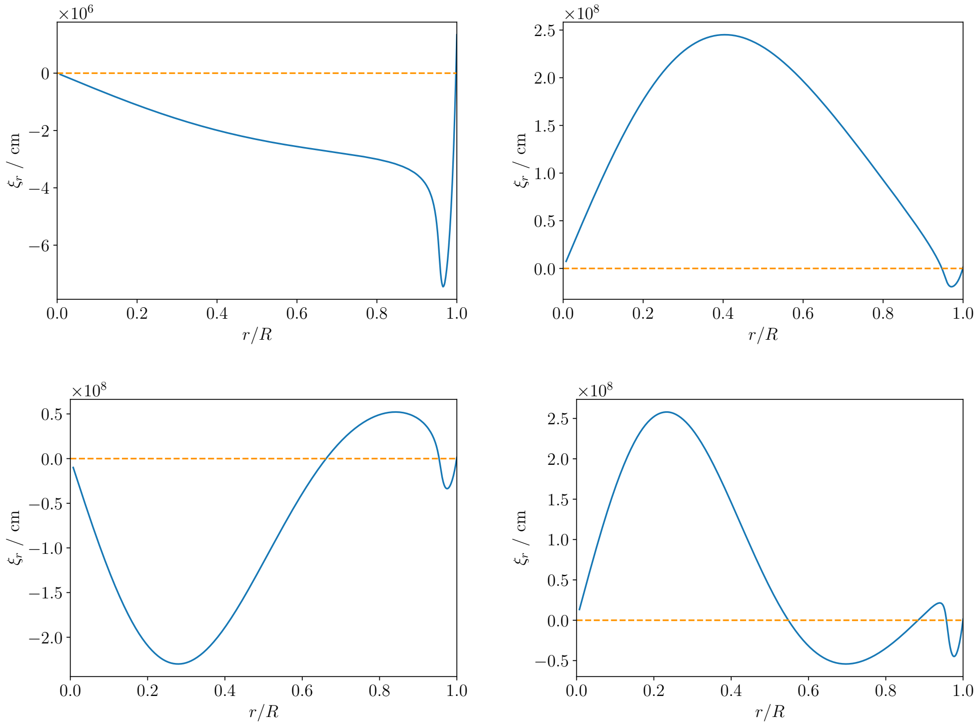

FIGURE 3.1: The radial eigenfunction ξ_r for the $l = 2$ modes of a star with mass, $M = 1.4 M_\odot$, $R = 13.49\,\mathrm{km}$ in the slow reaction limit, $\mathcal{A} = -0.1$. The orange dashed line corresponds to $\xi_r = 0$. From left to right the modes are: g_1 and g_2 on the top row and g_3 and g_4 on the bottom row.

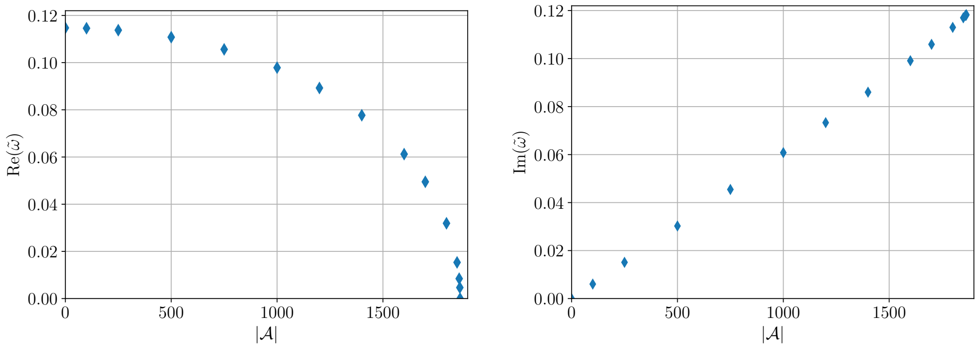

FIGURE 3.2: Plots showing how the dimensionless mode frequency of the fundamental g-mode, g_1, varies with $\mathcal{A}$. Plotted separately are the real and imaginary parts of the frequency on the left and right respectively

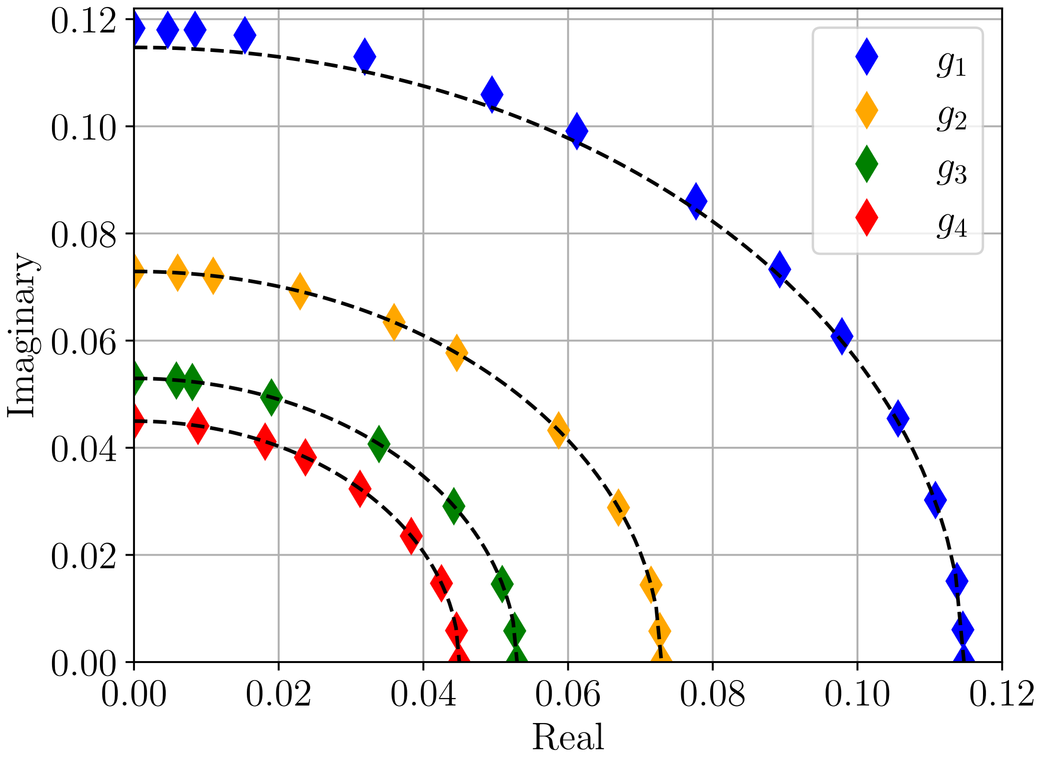

FIGURE 3.3: Plot showing how the dimensionless frequencies $\tilde{\omega}_n$ of the first four g-modes ($g_1 - g_4$) move in the complex plane when the reaction rate is varied. The diamonds represent the numerical values and the dashed lines represent the plane-wave prediction of a circle centred at the origin with a radius equal to the numerical value of the g-mode frequency when $\mathcal{A} = 0$ as shown in Table 3.1.

Looking at the results, for slow reaction rates, $t_r > 1$ s, the modes exhibit minuscule damping, $Re(\omega) \gg Im(\omega) \approx 0$. The expected modes are found, the f-mode and then the g- and p-modes with their respective overtones. The first four g-modes are shown in Fig. 3.1 for $\mathcal{A} = -0.1\,\mathrm{s}^{-1}$. As in the previous chapter these modes are identified as g-modes due to their frequency being lower than that of the f-mode and ξ_r having a peak around the outer core of the star. However, in Fig. 3.1, a small peak can be seen near the surface in all the modes. It is believed that this is due to the crust core transition. In this work, the neutron star is considered to be a fluid object consisting purely of npe matter, whereas the analytical formulae of BSk equation of state consider the star to also contain a crust, which is split into two regions, an inner and outer crust. The outer crust consists of electrons and atomic nuclei while the inner crust consists of electrons, neutron-proton clusters, and free neutrons. This transition from nuclei to unbound neutrons marks the boundary between the inner and outer crusts of the neutron star and it is defined as the point at which neutron drip occurs. This is the point at which, as the density of matter increases inside the star, it reaches a threshold value in which it becomes energetically favourable to have free neutrons instead of nuclei (Chamel et al., 2015). This is called neutron drip because the effect is that neutrons drip out of the nuclei. Going back to Fig. 3.1, the peak near the surface can then be interpreted as the matter in the crust oscillating due to the excitation of the g-mode in the core. For BSk21, the crust core transition occurs at $n_{cc} = 0.0809\,\mathrm{fm}^{-3}$ which in the background star is found at $r \approx 12.57\,\mathrm{km}$, which lines up with the surface features of Fig. 3.1. As this crustal region constitutes less than 1 km of the star, this is a small fraction of the stellar matter and the resulting peak in ξ_r is negligible, this is thought to not have any effect on the phenomenological trends and results of this work and can be ignored.

Moving back to the effect of reactions, when $t_r < 1s$, the damping begins to increase for all the modes. As expected this has a greater affect on the g-modes due to their relatively low frequency in comparison to the f- and p-modes. As can be seen in Fig. 3.2 as $|\mathcal{A}|$ increases, which corresponds to $t_r \longrightarrow 0$, the real part of the mode frequency decreases while the imaginary part increases. From Fig. 3.3, the g-modes tend to move in unison with each other until a mode hits a critical reaction rate, at which point the real part of the frequency quickly tends to 0 and the mode becomes ”purely” imaginary, $Re(\omega) = 0$.

Beyond the critical reaction rate from (3.76), a pair of pure imaginary modes are found for each specific g-mode, g_n. As the reaction rate becomes faster, the pair diverge, both staying on the imaginary axis but one increasing and the other tending towards the origin. This is illustrated for the specific case of g_1 in Fig. 3.4, but the same behaviour is exhibited by all other g-modes we have considered. The result agrees with the expectations from the plane-wave analysis of the fast reaction limit.

As expected, the lowest frequency g-modes are the first to reach their critical reaction rate and tend to the imaginary line. This is akin to the “switch off” predicted in previous sections.

In agreement with the plane wave argument, one also sees that the frequency at which the g-modes first hit the imaginary axis is approximately the imaginary counterpoint of initial g-mode frequencies in the slow reaction cases. The data is shown in Table 3.1 which shows good agreement with the predicted behaviour in (3.76). What can also be seen is that as the g-modes sweep through the complex plane, they appear to trace a circular path, with centre at the origin and radius of the initial slow reaction limit frequency. The other solution with a negative real part traces the same pattern. Once the g-modes hit the imaginary axis, this trajectory breaks and the two mode solutions diverge along the imaginary axis, as previously discussed.

3.4 Summary

Expanding on the work of Andersson and Pnigouras (2019), it has been shown how the presence of nuclear reactions in a neutron star leads to a damping of the composition g-modes for arbitrary reaction rates. As a consequence, the higher order modes are the first to be removed from the oscillation spectrum, until, at a certain reaction rate, there would be no oscillatory g-modes left in the neutron star. The good agreement between the numerical results and those derived from the plane-wave analysis provides strong confidence in these conclusions.

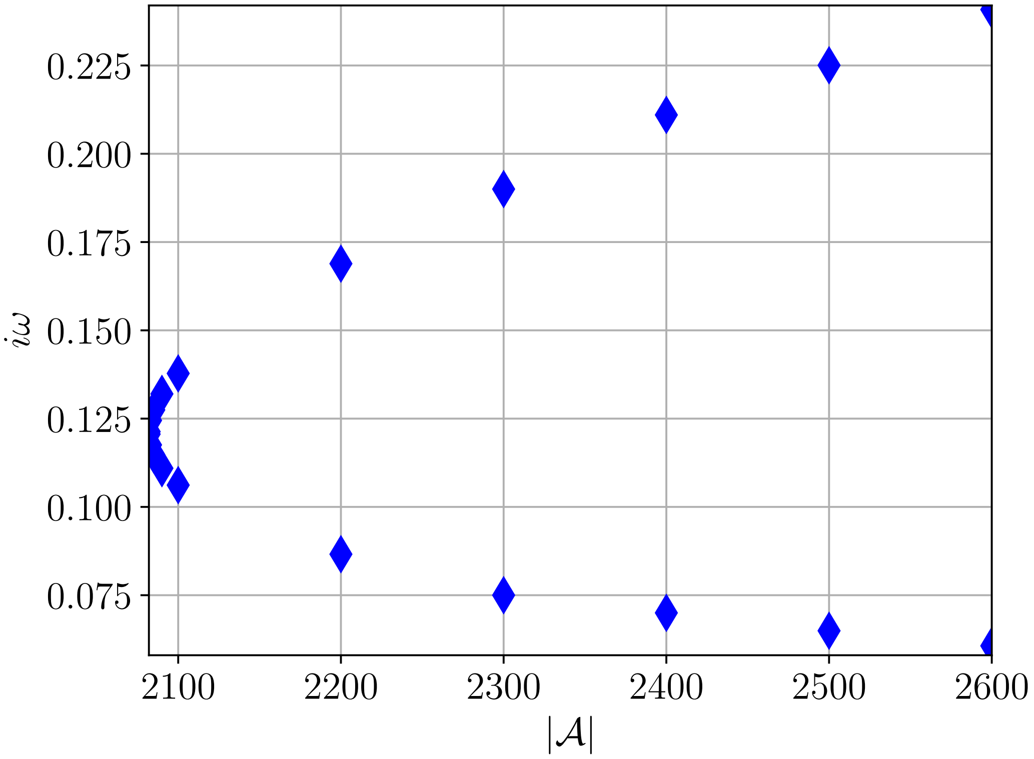

FIGURE 3.4: Plot of the pair of g_1 modes with purely imaginary frequencies beyond the critical reaction time, for different values of $\mathcal{A}$.

While this concept has only been demonstrated for a specific equation of state and a single background neutron star, the results serve as an important proof of principle. Qualitatively, the results should extend to other equation of state models. Quantitatively, changing the equation of state and varying parameters such as the mass and radius of the star will obviously affect the specific mode frequencies. However, the close agreement with the local plane-wave analysis strongly suggest that the collective behaviour and trends identified here should be universal.

The results provided may not have immediate implications for most astrophysical applications, as realistic nuclear reactions tend to be very slow compared to the oscillation timescale of the low-order g-modes, very high order modes must be considered in order for the reactions to play a dominant role. Despite this, three relevant problems can be identified. First, the nonlinear saturation of mode driven unstable by gravitational-wave emission is effected by the coupling to higher order pressure p-modes and gravity g-modes (Schenk et al., 2001; Pnigouras and Kokkotas, 2015). The nature of the higher order modes clearly impacts on the result. Second, the so-called p-g instability, which has been proposed to operate in neutron star binaries (Weinberg et al., 2013), involves the non-resonant coupling of very high order p-modes and g-modes to the dynamical tide. The presence or absence of the instability depends on the spectrum of high-order g-modes. Lastly, still in the context of dynamical tides, the mode-sum decomposition that is used to describe the dynamical tide in a binary system in Newtonian gravity, assumes that the mode problem is Hermitian (Pnigouras et al., 2024). If that is not so,

Table 3.1: In the table are the dimensionless frequencies of the first 10 g-modes, calculated numerically for $\mathcal{A} = 0$ and for when the mode frequency first becomes purely imaginary which is defined as the critical frequency, $\mathcal{A}_{Crit}$. The ratio is defined as $\frac{|\mathcal{A}_{Crit}|}{Im(\omega_{\mathcal{A}_{Crit}})}$. As one can see this agrees well with (3.76) which predicted a value of 2.

Mode	$\tilde{\omega}_{\mathcal{A}=0}$	$\tilde{\omega}_{\mathcal{A}_{Crit}}$	$\lvert\mathcal{A}_{Crit}\rvert$	Ratio
g_1	0.121	0.121i	2082.14	1.95
g_2	0.114	0.117i	1883.56	1.83
g_3	0.0836	0.0837i	1447.32	1.96
g_4	0.0672	0.0672i	1160.74	1.96
g_5	0.0577	0.0577i	991.50	1.95
g_6	0.0505	0.0505i	866.43	1.95
g_7	0.0447	0.0447i	767.32	1.95
g_8	0.0401	0.0401i	688.52	1.95
g_9	0.0363	0.0363i	623.87	1.95
g_{10}	0.0332	0.0332i	569.68	1.95

e.g., if we account for bulk viscosity damping associated with nuclear reactions, then one might have to rethink the formal validity of the standard argument. In essence, while the low-order modes are likely to be the most relevant from an observational point of view, there are good reasons to explore the high-order g-mode spectrum.

Chapter 4

G-modes in the Cowling Approximation

In the previous chapters all the calculations have been done in Newtonian gravity. While insights can still be gleaned from such work, due to neutron stars possessing high masses and relatively small radii they are relativistic objects and therefore for more accurate results general relativity must be used. This is needed in order to use more realistic equations of state. In this chapter, the aim is to generalise the work done in Chapter 2 to relativistic gravity, though some assumptions must be made which will be discussed. Again the focus will largely be on g-modes.

4.1 General-Relativistic Hydrodynamics

Focusing as before on a perfect fluid, the stress-energy tensor

$$T^{ab} = \frac{1}{c^2}\left(\varepsilon + p\right) u^a u^b + p g^{ab} = \frac{\varepsilon}{c^2} u^a u^b + p \perp^{ab}, \tag{4.1}$$

where ε is the energy density, the fluid four velocity u^a is normalised in such a way that

$$u_a u^a = g_{ab} u^a u^b = -c^2, \tag{4.2}$$

and the orthogonal projection is defined by

$$\perp^{ab} = g^{ab} + \frac{1}{c^2} u^a u^b, \tag{4.3}$$

where g^{ab} is the usual spacetime metric. For a barotropic fluid, the energy density is $\varepsilon = \varepsilon(n_B)$, where n_B is the baryon number density, and the associated pressure follows from

$p = p(\varepsilon)$. In order to write down the equations of fluid dynamics one needs

$$\begin{aligned}\nabla_b T^{ab} &= \nabla_b \left(\frac{\varepsilon}{c^2} u^a u^b + p \perp^{ab}\right) \\ &= \frac{1}{c^2}\left[u^a \nabla_b \left(\varepsilon u^b\right) + \varepsilon u^b \nabla_b u^a\right] + \perp^{ab} \nabla_b p + p \nabla_b \left(g^{ab} + \frac{1}{c^2} u^a u^b\right) \\ &= \frac{1}{c^2}\left[u^a \nabla_b \left(\varepsilon u^b\right) + \varepsilon u^b \nabla_b u^a\right] + \perp^{ab} \nabla_b p + \frac{p}{c^2}\left(u^a \nabla_b u^b + u^b \nabla_b u^a\right) = 0. \end{aligned} \tag{4.4}$$

Projecting along u_a the energy equation is

$$u^b \partial_b \varepsilon + (p + \varepsilon) \nabla_b u^b = 0. \tag{4.5}$$

Here it is useful to recall that the covariant derivative of $\sqrt{-g}$ is such that

$$\nabla_a(\sqrt{-g}) = \partial_a(\sqrt{-g}) - \Gamma^b_{ba}\sqrt{-g} = 0, \tag{4.6}$$

where Γ^b_{ba} is the usual Christoffel symbol given by (1.27) and

$$g = det(g_{ab}). \tag{4.7}$$

One must have

$$\Gamma^b_{ba} = \frac{1}{\sqrt{-g}} \partial_a(\sqrt{-g}), \tag{4.8}$$

which then allows one to write the energy equation as

$$\left(\sqrt{-g} u^b\right) \partial_b \varepsilon + (p + \varepsilon) \partial_b \left(\sqrt{-g} u^b\right) = 0. \tag{4.9}$$

This form is convenient as it only involves partial derivatives.

Further, without introducing approximations, one may assume that

$$u^a = N \left(c \delta^a_0 + \delta^a_j v^j\right), \tag{4.10}$$

which introduces the Lorentz factor N associated with the fluid flow (relative to some chosen observer). In effect, one has

$$g_{ab} u^a u^b = N^2 c^2 \left(g_{00} + g_{ij} \frac{v^i v^j}{c^2}\right) = -c^2, \tag{4.11}$$

which evidently leads back to the standard special relativity result

$$N \to \left(1 - \frac{v^2}{c^2}\right)^{-1/2} \quad \text{as} \quad g_{ab} \to \eta_{ab}. \tag{4.12}$$

Before moving on, it is useful to state the consistency with thermodynamics and baryon number conservation. The relevant conservation law takes the form

$$\nabla_a \left(n_B u^a\right) = 0, \tag{4.13}$$

or

$$\partial_a \left(\sqrt{-g} n_B u^a\right) = 0, \tag{4.14}$$

or

$$\left(\sqrt{-g} u^b\right) \partial_b n_B + n_B \partial_b \left(\sqrt{-g} u^b\right) = 0. \tag{4.15}$$

Going back to (4.9) and making use of the thermodynamical relation for a barotropic model, $\varepsilon = \varepsilon(n_B)$,

$$p + \varepsilon = n_B \mu, \tag{4.16}$$

where the chemical potential is defined as

$$\mu = \frac{d\varepsilon}{dn_B}, \tag{4.17}$$

it is easy to demonstrate consistency with (4.15). This is important if one wants to build models based on realistic microphysics. For a barotrope, one needs to solve either (4.9) or (4.15). If, on the other hand, one has a multi-parameter model (like finite temperature) then one needs to solve both.

Next, the orthogonal projection of (4.4) leads to the momentum equation:

$$\frac{p+\varepsilon}{c^2} u^b \nabla_b u^c + \perp^{cb} \partial_b p = 0. \tag{4.18}$$

That is,

$$\frac{p+\varepsilon}{c^2} u^b \left(\partial_b u^c + \Gamma^c_{ab} u^a\right) + \perp^{cb} \partial_b p = 0, \tag{4.19}$$

where one clearly needs to involve the precise nature of the spacetime metric.

4.2 Perturbations

The focus of this chapter is on perturbations of non-rotating stars. The first step involves establishing the background model. For reasons which will become clear later, the next few steps will be taken without committing to a specific choice of spatial coordinates. Later, the conventional choice of Schwarzschild coordinates will be considered. At this point, progress can be made by assuming that the unperturbed metric is obtained from

$$ds^2 = -e^\nu c^2 dt^2 + \gamma_{ij} dx^i dx^j \ . \tag{4.20}$$

where the spatial part of the metric, γ_{ij}, is diagonal.

For the background velocity, one has (for a static star)

$$u^a = Ac\delta^a_0, \tag{4.21}$$

which leads to

$$-c^2 = u^a u_a = g_{ab} A^2 c^2 \delta^a_0 \delta^b_0 = g_{00} c^2 A^2 = -e^\nu c^2 A^2, \tag{4.22}$$

so

$$A = e^{-\nu/2}. \tag{4.23}$$

Meanwhile, the equation for hydrostatic equilibrium becomes, from (4.19),

$$g^{ij}\partial_j p = \gamma^{ij}\partial_j p = -(p+\varepsilon)e^{-\nu}\Gamma^c_{00}. \tag{4.24}$$

Here one needs

$$\Gamma^c_{00} = \frac{1}{2} g^{ca}\left(\partial_0 g_{a0} + \partial_0 g_{0a} - \partial_a g_{00}\right) = \frac{1}{2} g^{ca}\partial_a e^\nu. \tag{4.25}$$

As the body is spherically symmetric, $p = p(r)$ and it follows that

$$\frac{dp}{dr} = -\frac{p+\varepsilon}{2}\frac{d\nu}{dr}. \tag{4.26}$$

Now consider perturbations. For the velocity, the Eulerian perturbation is introduced such that the total four velocity is

$$\bar{u}^a = u^a + \delta u^a \implies \bar{u}_a \bar{u}^a = \bar{g}_{ab}\left(u^a + \delta u^a\right)\left(u^b + \delta u^b\right) = -c^2. \tag{4.27}$$

Including perturbations, the metric is

$$\bar{g}_{ab} = g_{ab} + \delta g_{ab}. \tag{4.28}$$

This means that, to linear order

$$\begin{aligned}\left(g_{ab} + \delta g_{ab}\right)\left(u^a + \delta u^a\right)\left(u^b + \delta u^b\right) &= g_{ab}(u^a u^b + u^b \delta u^a + u^a \delta u^b) + u^a u^b \delta g_{ab} \\ = -c^2 + g_{ab} c e^{-\nu/2}\left(\delta^b_0 \delta u^a + \delta^a_0 \delta u^b\right) &+ e^{-\nu} c^2 \delta g_{00} = -c^2 + 2 g_{00} c e^{-\nu/2}\delta u^0 + e^{-\nu} c^2 \delta g_{00} \\ &= -c^2 - 2 c e^{\nu/2}\delta u^0 + e^{-\nu} c^2 \delta g_{00} = -c^2, \end{aligned} \tag{4.29}$$

or

$$\delta u^0 = \frac{c}{2} e^{-3\nu/2}\delta g_{00}. \tag{4.30}$$

Evidently, the normalisation does not involve the spatial components δu^i. Rather, it fixes the time component so that the perturbed four-velocity has three components, just like in classical fluid dynamics.

We introduce metric perturbations “inspired” by the ADM formalism (Arnowitt et al., 2008) in order to split the spacetime metric into its spatial and temporal parts. That is,

$$\delta g_{00} = \delta\alpha, \tag{4.31}$$

$$\delta g_{0i} = \delta g_{i0} = \delta\beta_i, \tag{4.32}$$

and

$$\delta g_{ij} = \delta\gamma_{ij}. \tag{4.33}$$

The reason for this renaming of variables will become apparent shortly. One then has

$$\delta u^0 = \frac{c}{2}e^{-3\nu/2}\delta\alpha. \tag{4.34}$$

4.2.1 Baryon number conservation

The equation for baryon number conservation

$$\nabla_a\left(n_B u^a\right) = 0 \tag{4.35}$$

or

$$\frac{1}{\sqrt{-g}}\partial_a\left(\sqrt{-g}n_B u^a\right) = 0, \tag{4.36}$$

is automatically satisfied in the background since

$$\partial_t n_B = \partial_t\left(\sqrt{-g}u^0\right) = 0. \tag{4.37}$$

It follows that

$$\partial_t\delta n_B + \frac{e^{\nu/2}}{\sqrt{-g}}\partial_i\left[\sqrt{-g}n_B\delta u^i\right] = -\frac{n_B}{2}e^{-\nu}\partial_t\delta. \tag{4.38}$$

Next , note that

$$\sqrt{-g} = e^{\nu/2}\sqrt{\gamma}. \tag{4.39}$$

and introduce a covariant derivative associated with γ_{ij} such that

$$D_i(\sqrt{\gamma}) = \partial_i(\sqrt{\gamma}) - \tilde{\Gamma}^j_{ji}\sqrt{\gamma} = 0, \tag{4.40}$$

and hence

$$\tilde{\Gamma}^j_{ji} = \frac{1}{\sqrt{\gamma}}\partial_i(\sqrt{\gamma}), \tag{4.41}$$

to get

$$\partial_t\delta n_B + D_i\left[e^{\nu/2}n_B\delta u^i\right] = -\frac{n_B}{2}e^{-\nu}\partial_t\delta\alpha. \tag{4.42}$$

4.2.2 Energy equation

Moving on to the perturbed equations of motion. For the energy we have

$$\left(\sqrt{-g}u^b\right)\partial_b\varepsilon + (p+\varepsilon)\partial_b\left(\sqrt{-g}u^b\right) = 0. \tag{4.43}$$

which is automatically satisfied in the background since

$$\partial_t\varepsilon = \partial_t\left(\sqrt{-g}u^0\right) = 0. \tag{4.44}$$

It follows that

$$\sqrt{-g}e^{-\nu/2}\left[\partial_t\delta\varepsilon + \frac{1}{2}(p+\varepsilon)e^{-\nu}\partial_t\delta\alpha\right] + \sqrt{-g}\delta u^j\partial_j\varepsilon + (p+\varepsilon)\partial_i\left(\sqrt{-g}\delta u^i\right) = 0. \tag{4.45}$$

This leads to

$$\partial_t\delta\varepsilon + \frac{1}{2}(p+\varepsilon)e^{-\nu}\partial_t\delta\alpha + e^{\nu/2}\delta u^i\partial_i\varepsilon + (p+\varepsilon)\frac{1}{\sqrt{\gamma}}\partial_i\left[e^{\nu/2}\sqrt{\gamma}\delta u^i\right] = 0. \tag{4.46}$$

If, at this point, one introduces the covariant derivative associated with γ_{ij} one has

$$\partial_t\delta\varepsilon + e^{\nu/2}\delta u^i\partial_i\varepsilon + (p+\varepsilon)D_i\left[e^{\nu/2}\delta u^i\right] = -\frac{1}{2}(p+\varepsilon)e^{-\nu}\partial_t\delta\alpha. \tag{4.47}$$

4.2.3 Momentum equation

For the momentum equation one needs

$$\frac{p+\varepsilon}{c^2}u^b\left(\partial_b u^c + \Gamma^c_{ab}u^a\right) + \perp^{cb}\partial_b p = 0. \tag{4.48}$$

In the end, this leads to

$$\begin{aligned}\frac{p+\varepsilon}{c^2}e^{-\nu/2}\partial_t\delta u^i + \frac{1}{2}(\delta p+\delta\varepsilon)g^{ij}\partial_j\nu + g^{ij}\partial_j\delta p\\ - \frac{p+\varepsilon}{2}e^{-\nu}g^{ij}\partial_j\nu\,\delta\alpha - \frac{p+\varepsilon}{2}g^{ij}e^{-\nu}\left(\frac{2}{c}\partial_t\delta\beta_j - \partial_j\delta\alpha\right) = 0.\end{aligned} \tag{4.49}$$

At this point, it is notable that there is no direct coupling to $\delta\gamma_{ij}$ in the final momentum equation. Any coupling to the spatial part of the metric enters via the Einstein equations. This observation is useful for several reasons. For example, it helps explain how different versions of the relativistic Cowling approximation—e.g. whether we assume that all components of the perturbed metric are ignored (as in McDermott et al. 1983) or retain the "momentum parts" (as advocated by Finn 1988)—impact on the problem. Moreover, the absence of $\delta\gamma_{ij}$ in (4.49) may help explain why oscillation modes obtained in the conformal flatness approximation can be quite accurate, as demonstrated by, for example, Torres-Forné et al. (2019). These issues would be worth closer inspection, but we will not explore them further in this thesis.

4.3 Cowling Approximation

In order to simplify these equations one must make assumptions. We choose the Cowling approximation, where all metric perturbations are set to zero (Cowling, 1941), i.e.

$$\delta\alpha = \delta\beta_i = 0. \tag{4.50}$$

Along with this, introducing the definition of the displacement vector, ξ^i, where

$$\delta u^i = ce^{-\nu/2}\partial_0\xi^i = e^{-\nu/2}\partial_t\xi^i. \tag{4.51}$$

Adding this into (4.49) leads to

$$\frac{p+\varepsilon}{c^2}e^{-\nu}\partial_t^2\xi_i + \frac{1}{2}(\delta p + \delta\varepsilon)\partial_i\nu + \partial_i\delta p = 0. \tag{4.52}$$

Now, considering the problem for non-rotating stars, as in the Newtonian case, one assumes that the oscillation modes, with frequency ω, are associated with a polar perturbation displacement vector, again expressed in the coordinate basis associated with the spherical polar coordinates $[r, \theta, \varphi]$,

$$\xi^i(t, r, \theta, \varphi) = \xi^i_l(r, \theta, \varphi)e^{i\omega t} , \tag{4.53}$$

with

$$\xi^i_l = \frac{1}{r}W_l Y^m_l \delta^i_r + \frac{1}{r^2}V_l\partial_\theta Y^m_l \delta^i_\theta + \frac{im}{r^2\sin^2\theta}V_l Y^m_l \delta^i_\varphi , \tag{4.54}$$

where the multipole amplitudes, W_l and V_l, are functions of r only. Along with this, all scalar perturbations are expanded in spherical harmonics. Also the perturbed pressure is

$$\delta p = \delta p_l Y^m_l e^{i\omega t}, \tag{4.55}$$

and similar for ε. Here we choose the metric to have the Schwarzschild form

$$\mathrm{d}s^2 = -e^\nu c^2\mathrm{d}t^2 + e^\lambda\mathrm{d}r^2 + r^2\mathrm{d}\theta^2 + r^2\sin^2\theta\mathrm{d}\varphi^2 , \tag{4.56}$$

and comparing with (4.20) we can identify

$$\gamma_{ij} = \begin{pmatrix} e^\lambda & 0 & 0 \\ 0 & r^2 & 0 \\ 0 & 0 & r^2\sin^2\theta \end{pmatrix}. \tag{4.57}$$

Substituting these expressions into (4.52) gives the following: for the r-component

$$\frac{p+\varepsilon}{c^2}\omega^2 e^{\lambda-\nu}\frac{W_l}{r} = \frac{\delta p_l + \delta\varepsilon_l}{2}\frac{d\nu}{dr} + \partial_r\delta p_l, \tag{4.58}$$

and for the φ-component

$$\frac{p+\varepsilon}{c^2}\omega^2 e^{-\nu} V_l = \delta p_l. \tag{4.59}$$

Next, applying the Cowling approximation to the perturbed energy equation (4.47) gives

$$\partial_t \delta\varepsilon + e^{\nu/2}\delta u^i \partial_i \varepsilon + (p+\varepsilon)\frac{1}{\sqrt{\gamma}}\partial_i\left[e^{\nu/2}\sqrt{\gamma}\delta u^i\right] = 0\,, \tag{4.60}$$

where

$$\sqrt{\gamma} = e^{\lambda/2} r^2 \sin\theta. \tag{4.61}$$

In terms of the defined variables, this becomes

$$\begin{aligned}\partial_t \delta\varepsilon + e^{\nu/2}\delta u^r \partial_r \varepsilon + (p+\varepsilon)\frac{1}{\sqrt{\gamma}}\partial_r\left[e^{\nu/2}\sqrt{\gamma}\delta u^r\right] \\ + (p+\varepsilon)\frac{1}{\sqrt{\gamma}}\partial_\theta\left[e^{\nu/2}\sqrt{\gamma}\delta u^\theta\right] + (p+\varepsilon)\frac{1}{\sqrt{\gamma}}\partial_\varphi\left[e^{\nu/2}\sqrt{\gamma}\delta u^\varphi\right] = 0\,,\end{aligned} \tag{4.62}$$

which can be simplified to

$$\frac{p+\varepsilon}{r^2}\left[\partial_r\left(rW_l\right) - l(l+1)V_l\right] + \left(\frac{d\varepsilon}{dr} + \frac{p+\varepsilon}{2}\frac{d\lambda}{dr}\right)\frac{W_l}{r} + \delta\varepsilon_l = 0\,. \tag{4.63}$$

Putting all these equations together, gives:

$$\frac{p+\varepsilon}{c^2}\omega^2 e^{\lambda-\nu}\frac{W_l}{r} = \frac{\delta p_l + \delta\varepsilon_l}{2}\frac{d\nu}{dr} + \partial_r \delta p_l, \tag{4.64}$$

$$\frac{p+\varepsilon}{c^2}\omega^2 e^{-\nu} V_l = \delta p_l, \tag{4.65}$$

$$\frac{p+\varepsilon}{r^2}\left[\partial_r\left(rW_l\right) - l(l+1)V_l\right] + \left(\frac{d\varepsilon}{dr} + \frac{p+\varepsilon}{2}\frac{d\lambda}{dr}\right)\frac{W_l}{r} + \delta\varepsilon_l = 0\,. \tag{4.66}$$

In order to solve these equations one needs to relate δp and $\delta\varepsilon$, this is achieved with the following relation,

$$\Delta p = \frac{\Gamma_1 p}{\varepsilon + p}\Delta\varepsilon, \tag{4.67}$$

where

$$\Gamma_1 = \frac{p+\varepsilon}{p}\left(\frac{\partial p}{\partial\varepsilon}\right)_{s,x_p}, \tag{4.68}$$

where s is entropy and x_p is the proton fraction of the star. This is the relativistic analogue of the Γ_1 used in Chapter 3. Next using the definition of the Lagrangian perturbation,

$$\delta p = \frac{\Gamma_1 p}{\varepsilon + p}\left(\delta\varepsilon + \xi^\mu \nabla_\mu \varepsilon\right) - \xi^\mu \nabla_\mu p, \tag{4.69}$$

$$\delta p = \frac{\Gamma_1 p}{\varepsilon + p}\left(\delta\varepsilon + \frac{W_l}{r}\frac{d\varepsilon}{dr}\right) - \frac{W_l}{r}\frac{dp}{dr}. \tag{4.70}$$

Using this one can now get differential equations for W_l and V_l:

$$\frac{dW_l}{dr} = \left(\frac{l(l+1)}{r} - \frac{\omega^2}{c^2}\frac{p+\varepsilon}{\Gamma_1 p} r e^{-\nu}\right) V_l - \left(\frac{1}{r} + \frac{1}{2}\frac{d\lambda}{dr} + \frac{1}{\Gamma_1 p}\frac{dp}{dr}\right) W_l, \tag{4.71}$$

$$\frac{dV_l}{dr} = \left(e^{\lambda} - \frac{1}{p+\varepsilon}\frac{dp}{dr}\frac{c^2}{\omega^2} A_+ e^{\nu+\lambda/2}\right)\frac{W_l}{r} - A_- e^{\lambda/2} V_l, \tag{4.72}$$

where,

$$A_{\pm} = e^{-\lambda/2}\left[\frac{1}{p+\varepsilon}\frac{d(p+\varepsilon)}{dr} - \frac{1}{\Gamma_1 p}\frac{dp}{dr}\left(1 \pm \frac{\Gamma_1 p}{p+\varepsilon}\right)\right]. \tag{4.73}$$

If one makes the following substitutions:

$$Z_1 = \frac{W_l}{r^2}\left(\frac{r}{R}\right)^{2-l} e^{\lambda/2}, \tag{4.74}$$

$$Z_2 = \frac{\omega^2 r}{c^2 m_r} V_l \left(\frac{r}{R}\right)^{2-l}, \tag{4.75}$$

where R is the stellar radius and m_r is the mass enclosed in radius r, given by

$$\frac{dm_r}{dr} = 4\pi r^2 \varepsilon, \tag{4.76}$$

one can rewrite our differential equations in the following form,

$$r\frac{\mathrm{d}Z_1}{\mathrm{d}r} = \left(\frac{V}{\Gamma_1} - l - 1\right) Z_1 + \left[l(l+1)\frac{m_r}{r^3}\frac{c^2}{\omega^2} e^{\lambda/2} - \frac{V}{\Gamma_1 \beta}\right] Z_2, \tag{4.77}$$

$$r\frac{\mathrm{d}Z_2}{\mathrm{d}r} = \left(\frac{\omega^2}{c^2}\frac{r^3}{m_r} + A_+ r\beta\right) e^{\lambda/2} Z_1 + \left(3 - l - U - A_- e^{\lambda/2} r\right) Z_2, \tag{4.78}$$

where

$$U = \frac{\mathrm{d}\ln m_r}{\mathrm{d}\ln r}, \tag{4.79}$$

$$V = -\frac{\mathrm{d}\ln p}{\mathrm{d}\ln r}, \tag{4.80}$$

$$\beta = e^{\nu+\lambda/2}\left(1 + \frac{4\pi r^3 p}{m_r}\right). \tag{4.81}$$

These are the same equations as in McDermott et al. (1983). Two boundary conditions are still required for this system, one at the centre and one at the surface of the star. At the stellar surface one requires that $\Delta p = 0$, using (4.65) this gives

$$Z_2 - \beta Z_1 = 0. \tag{4.82}$$

At the centre of the star, the differential equations (4.71) and (4.72) are required to be regular as $r \longrightarrow 0$, this leads to

$$Z_1 - \frac{l m_r}{r^3}\frac{c^2}{\omega^2} Z_2 = 0. \tag{4.83}$$

Finally a normalisation condition for our solutions is added at the stellar surface

$$Z_1 e^{-\lambda/2} = 1, \tag{4.84}$$

which ensures that

$$\frac{\xi^r}{r} = 1, \tag{4.85}$$

when $r = R$.

As in the Newtonian case in previous chapters, before one can solve these equations numerically one first needs to generate the background equilibrium star. This involves solving the relativistic equations of stellar structure also known as the Tolman-Oppenheimer-Volkoff equations (Oppenheimer and Volkoff, 1939; Tolman, 1939), which are

$$\frac{\mathrm{d}m_r}{\mathrm{d}r} = 4\pi r^2 \varepsilon, \tag{4.86}$$

$$\frac{\mathrm{d}\nu}{\mathrm{d}r} = \frac{2(m_r + 4\pi r^3 p)}{r(r-2m_r)}, \tag{4.87}$$

$$\frac{\mathrm{d}p}{\mathrm{d}r} = -\frac{\varepsilon + p}{2}\frac{\mathrm{d}\nu}{\mathrm{d}r} = -\frac{(\varepsilon + p)(m_r + 4\pi r^3 p)}{r(r-2m_r)}. \tag{4.88}$$

Again, this set of equations can then be solved numerically with the chosen equation of state and different central energy densities to generate the desired neutron stars with different masses and radii. One additional boundary condition is needed, that is that the metric potential must match the exterior Schwarzschild solution, i.e.

$$e^{\nu(R)} = 1 - \frac{2M}{R}, \tag{4.89}$$

where M is the total mass-energy of the star given by

$$M = \int_0^R 4\pi r^2 \varepsilon(r) \mathrm{d}r. \tag{4.90}$$

One can also define the relativistic analogues of the Brunt-Väisälä and Lamb frequency, which are, respectively,

$$\mathcal{N}^2 = e^{\nu-\lambda}\frac{1}{p+\varepsilon}\frac{\mathrm{d}p}{\mathrm{d}r}\left[\frac{1}{p+\varepsilon}\frac{\mathrm{d}\varepsilon}{dr} - \frac{1}{\Gamma_1 p}\frac{\mathrm{d}p}{\mathrm{d}r}\right] = -\frac{m_r}{r^2}A_+\beta, \tag{4.91}$$

$$S_l^2 = \frac{l(l+1)}{r^2}\frac{\Gamma_1 p}{p+\varepsilon}e^{\nu}. \tag{4.92}$$

These will be used when analysing the mode spectrum.

4.3.1 Orthogonality

Before continuing onto the numerical results, first let us check if the mode equations are Hermitian for some inner product. The reason for doing this is that if the equations are Hermitian it means one would be able to derive a basis for a mode expansion, which will prove useful later, in Chapter 6.

First, we express the momentum equation (4.52) as (Friedman and Schutz, 1978a)

$$-\omega_n^2 A\xi_i + C_{ij}\xi^j = 0\,. \tag{4.93}$$

In order for this equation to be Hermitian, we need a suitable inner product

$$\langle \eta^i, \xi_i \rangle = \int \eta^{i*} f \xi_i dV = \int \eta^{i*} f \xi_i \sqrt{-g}\, d^3x, \tag{4.94}$$

where ξ^i and η^i are solutions to the perturbation equations and $*$ denotes the complex conjugate. Specifically, we need to identify a function $f(r)$, such that

$$\langle \eta^i, C_{ij}\xi^j \rangle = \langle \xi^i, C_{ij}\eta^j \rangle^*, \tag{4.95}$$

and similarly for A. Once we establish this result, we can define the symplectic product

$$\mathcal{W}(\eta^i, \xi_i) = \langle \eta^i, A\partial_t \xi_i \rangle - \langle A\partial_t \eta^i, \xi_i \rangle, \tag{4.96}$$

such that

$$\partial_t \mathcal{W} = \langle \eta^i, A\partial_t^2 \xi_i \rangle - \langle A\partial_t^2 \eta^i, \xi_i \rangle = -\langle \eta^i, C\xi_i \rangle + \langle C\eta^i, \xi_i \rangle = -\langle \eta^i, C\xi_i \rangle + \langle \xi^i, C\eta_i \rangle^* = 0. \tag{4.97}$$

This demonstrates that $\mathcal{W}$ provides a conserved quantity. Moreover, for two mode solutions, $\xi^i e^{i\omega_n t}$ and $\eta^i e^{i\omega_{n'} t}$, we have

$$\left(\omega_{n'}^2 - \omega_n^2\right)\left(\langle \eta^i, A\xi_i \rangle + \langle A\eta^i, \xi_i \rangle\right) e^{i(\omega_n - \omega_{n'})t} = 0. \tag{4.98}$$

Since A and $f(r)$ are both real, it is easy to see that one must have

$$\left(\omega_{n'}^2 - \omega_n^2\right) \langle \eta^i, A\xi_i \rangle e^{i(\omega_n - \omega_{n'})t} = 0. \tag{4.99}$$

Assuming that the modes are not degenerate, this means that

$$\langle \eta^i, A\xi_i \rangle = \mathcal{A}_n^2 \delta_{nn'}, \tag{4.100}$$

for some amplitude $\mathcal{A}_n^2$ (where n and n' correspond to oscillation modes rather than indices). This would then provide a basis for a mode expansion (following the steps from the Newtonian analysis).

In order to make progress towards (4.95), the starting point is

$$\langle \eta^i, C_{ij}\xi^j\rangle = \int \eta^{i*}\left[\frac{1}{2}(\delta_\xi\varepsilon + \delta_\xi p)\partial_i\nu + \partial_i\delta_\xi p\right] f\sqrt{-g}\, d^3x, \tag{4.101}$$

where δ_ξ indicates the perturbation associated with mode ξ^i. Integrate by parts to find

$$\langle \eta^i, C_{ij}\xi^i\rangle = \oint \eta^{i*}\delta_\xi p f\sqrt{-g}\, dS_i + \int\left[\frac{1}{2}(\delta_\xi\varepsilon + \delta_\xi p)\eta^{i*}\partial_i\nu f\sqrt{-g} - \delta_\xi p\,\partial_i(\eta^{i*} f\sqrt{-g})\right] d^3x, \tag{4.102}$$

where dS_i is an outward-facing vectorial two-surface element arrived at through the divergence theorem. At the surface, $\delta_\xi p$ vanishes, hence we have

$$\langle \eta^i, C_{ij}\xi^j\rangle = \int\left[\frac{1}{2}(\delta_\xi\varepsilon + \delta_\xi p)\eta^{i*}\partial_i\nu f\sqrt{-g} - \delta_\xi p\,\partial_i(\eta^{i*} f\sqrt{-g})\right] d^3x. \tag{4.103}$$

To keep this as general as possible, we require

$$\frac{\Delta\varepsilon}{\varepsilon + p} = \frac{\Delta n}{n} = -\frac{1}{\sqrt{-g}}\partial_i(\sqrt{-g}\xi^i) - \frac{1}{2}\xi^i\partial_i\nu. \tag{4.104}$$

Therefore,

$$\frac{\delta\varepsilon}{\varepsilon + p} = -\frac{1}{\sqrt{-g}}\partial_i(\sqrt{-g}\xi^i) - \frac{1}{\varepsilon + p}\left(1 + \frac{\varepsilon + p}{\Gamma p}\right)\xi^i\partial_i p, \tag{4.105}$$

$$\frac{\delta p}{\Gamma_1 p} = -\frac{1}{\sqrt{-g}}\partial_i(\sqrt{-g}\xi^j) - \frac{1}{\Gamma_1 p}\left(1 + \frac{\Gamma_1 p}{\varepsilon + p}\right)\xi^i\partial_i p, \tag{4.106}$$

where

$$\Gamma = \frac{\varepsilon + p}{p}\frac{dp}{d\varepsilon}, \tag{4.107}$$

represents the adiabatic index of the background configuration.

Thus, the inner product becomes

$$\begin{aligned}\langle \eta^i, C_{ij}\xi^j\rangle = &\int \frac{1}{\sqrt{-g}}\left(1 + \frac{\Gamma_1 p}{\varepsilon + p}\right)\left[\partial_j(\sqrt{-g}\xi^j)\eta^{j*}\partial_i p + \xi^j\partial_j p\,\partial_i(\sqrt{-g}\eta^{i*})\right] f\sqrt{-g}\, d^3x\\ &+ \int \frac{1}{\varepsilon + p}\left(2 + \frac{\varepsilon + p}{\Gamma p} + \frac{\Gamma_1 p}{\varepsilon + p}\right)\xi^j\partial_j p\,\eta^{i*}\partial_i p f\sqrt{-g}\, d^3x\\ &+ \int \frac{\Gamma_1 p}{(\sqrt{-g})^2}\partial_j(\sqrt{-g}\xi^j)\partial_i(\sqrt{-g}\eta^{i*}) f\sqrt{-g}\, d^3x\\ &+ \int \Gamma_1 p\left[\frac{1}{\sqrt{-g}}\partial_j(\sqrt{-g}\xi^j) + \frac{1}{\Gamma_1 p}\left(1 + \frac{\Gamma_1 p}{\varepsilon + p}\right)\xi^j\partial_j p\right]\eta^{i*}\partial_i f\sqrt{-g}\, d^3x.\end{aligned} \tag{4.108}$$

In order to satisfy (4.95), all terms non-symmetric when $\eta^i \leftrightarrow \xi^j$ must cancel. Examining (4.108) we see that only the last integrand is non-symmetric and therefore the inner product is Hermitian only when $f = \text{const}$. In view of this, we take $f = 1$ in the following.

Going back to (4.100), we now have

$$\langle \eta^i, A\xi_i \rangle = \int \frac{p+\varepsilon}{c^2} e^{-\nu} \eta^{i*} \xi_i \sqrt{-g}\, d^3x = \mathcal{A}_n^2 \delta_{nn'}, \tag{4.109}$$

which shows how the mode solutions ξ^i should be normalised. For a single mode, substituting in (4.54), this simplifies to

$$\mathcal{A}_n^2 = \int_0^R e^{(\lambda-\nu)/2} \frac{(\varepsilon+p)}{c^2} \left[W_l^2 + \frac{l(l+1)}{r^2} V_l^2 \right] dr, \tag{4.110}$$

in agreement with the result from Detweiler and Ipser (1973) and the expression employed without derivation in Kuan et al. (2021a).

4.4 Testing

The use of the Cowling approximation will affect the accuracy of results. In particular, ignoring the metric perturbations forces the mode frequencies to be real (as the gravitational-wave degrees of freedom are suppressed). In full general relativity, the mode frequencies are complex as a result of damping due the emission of gravitational radiation. However, as this work will go on to focus on the g-modes, which have been shown to have an imaginary part $Re(\omega_n) \gg Im(\omega_n) \approx 0$ (Krüger, 2015), the Cowling approximation is thought to not have a significant effect on results. Therefore, to test the code and these equation, results were calculated for a polytropic equation of state and compared to previous literature (Krüger, 2015). An energy polytrope was used

$$P = K\varepsilon^{\gamma}, \tag{4.111}$$

with K and γ again the polytropic constant and index respectively. Unlike in (2.20), $\Gamma \neq \gamma$, instead

$$\Gamma = \frac{p+\varepsilon}{p} \frac{\mathrm{d}p}{\mathrm{d}\varepsilon}. \tag{4.112}$$

Stratification is then artificially added by setting $\Gamma_1 = 1.1\Gamma$ everywhere in the star. Even though the calculation in (Krüger, 2015) was done in full general relativity, comparing to the real part of the mode frequencies, the results of this paper showed good agreement. and as the overtones increased for both p- and g-modes, the percentage difference decreased to the percent level, this is shown in Table 4.1. This provided confidence to extend the analysis to more realistic equations of state.

4.5 Results

Once again the BSk family was chosen but this time, 4 different versions were chosen to compare against one another, specifically: BSk22; BSk24; BSk25 and BSk26 (Shchechilin

TABLE 4.1: Table showing the comparison between the fully relativistic mode frequencies of (Krüger, 2015) in column 2 and those calculated using (4.77) (4.78) in column 3, along with the percentage difference of column 2 with respect to column 3 in column 4. Results are calculated for a neutron star with total mass energy $M = 1.3M_\odot$ and with stratification $\Gamma_1 = 1.1\Gamma$. The notation e-p at the end of each number stands for $\times 10^{-p}$.

Mode	$Re(\omega M)$	ωM	Error %
f	0.1709	0.1832	7.197
p_1	0.3663	0.4109	12.18
p_2	0.5320	0.5773	8.515
p_3	0.6940	0.7329	5.605
g_1	4.535e-2	4.304e-2	-5.104
g_2	3.070e-2	2.993e-2	-2.519
g_3	2.323e-2	2.311e-2	-0.372

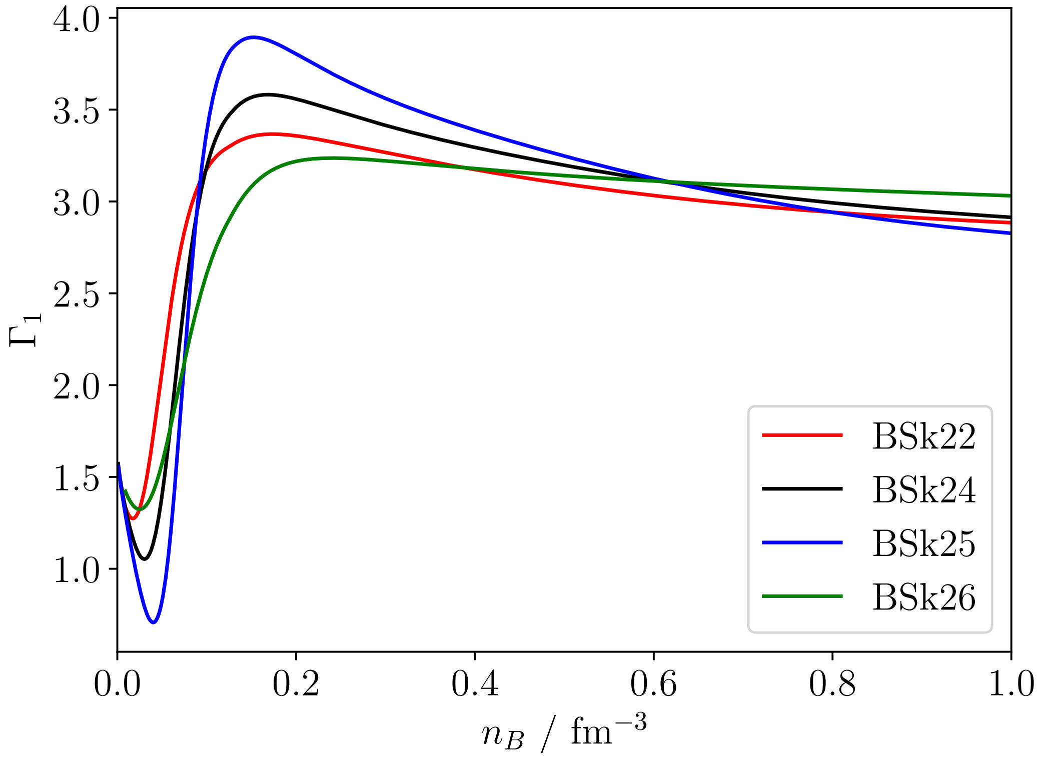

FIGURE 4.1: Plot showing Γ_1 vs baryon number density n_B for different equations of state of the BSk family. Specifically: BSk22; BSk24; BSk25 and BSk26 (Shchechilin et al., 2023; Goriely et al., 2013).

et al., 2023; Goriely et al., 2013). As with BSk21, each of these equations of state have analytical representations which can be used to calculate the necessary thermodynamic derivatives, though each have slightly different assumptions regarding the nuclear microphysics. This is demonstrated in Fig. 4.1, which shows the value of Γ_1 for each equation of state for different baryon number densities n_B. Strictly speaking, this calculation only applies to the neutron star core.

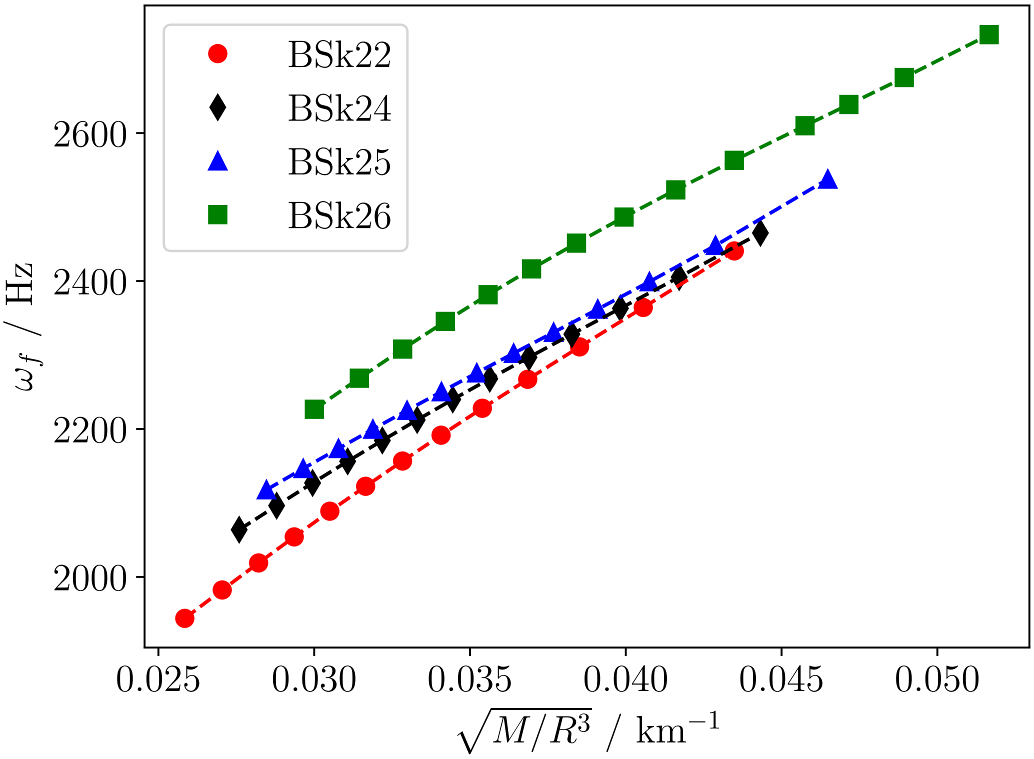

FIGURE 4.2: Plot of the f-mode frequency ω_f vs $\sqrt{M/R^3}$ for BSk22; BSk24; BSk25 and BSk26 for total mass energies ranging from $M = 1M_\odot$ up to the maximum allowed masses in each case.

Using each of the 4 different equations of state, (4.77) and (4.78) were solved for a variety of neutron stars with total mass-energies ranging from $M = 1M_\odot$ up to the maximum allowed masses given by Shchechilin et al. (2023). The code was written in geometric units where $G = c = 1$ and all variables were measured in powers of km. In order to test the code, the f-mode frequency ω_f was calculated and plotted against $\sqrt{M/R^3}$ in Fig. 4.2. It is well known since Andersson and Kokkotas (1998) that in neutron stars $\omega_f \propto \sqrt{M/R^3}$. Fig, 4.2 shows good agreement with this empirical relation with all four equations of state having a coefficient of determination $R^2 > 0.99$, meaning a strong linear relationship. However, we need to keep in mind that, due to the Cowling approximation these frequencies will only be accurate to within about 15% or so (Yoshida and Kojima, 1997), hence the results should be considered with this in mind. What we can still learn from Fig. 4.2, is that all four models exhibit the same empirical relationship with increasing density and it would require high precision observations to distinguish between these models, particularly for BSk24 and BSk25, when only considering the f-mode. This will not be the case when we examine the g-mode spectrums of the four models later on, where the differences in their nuclear model parameters will become more evident.

In order to examine the g-mode spectrum we need to contrast Γ_1 with the adiabatic index for the perturbations of the background, Γ. To do this, we will need to extend the model to lower

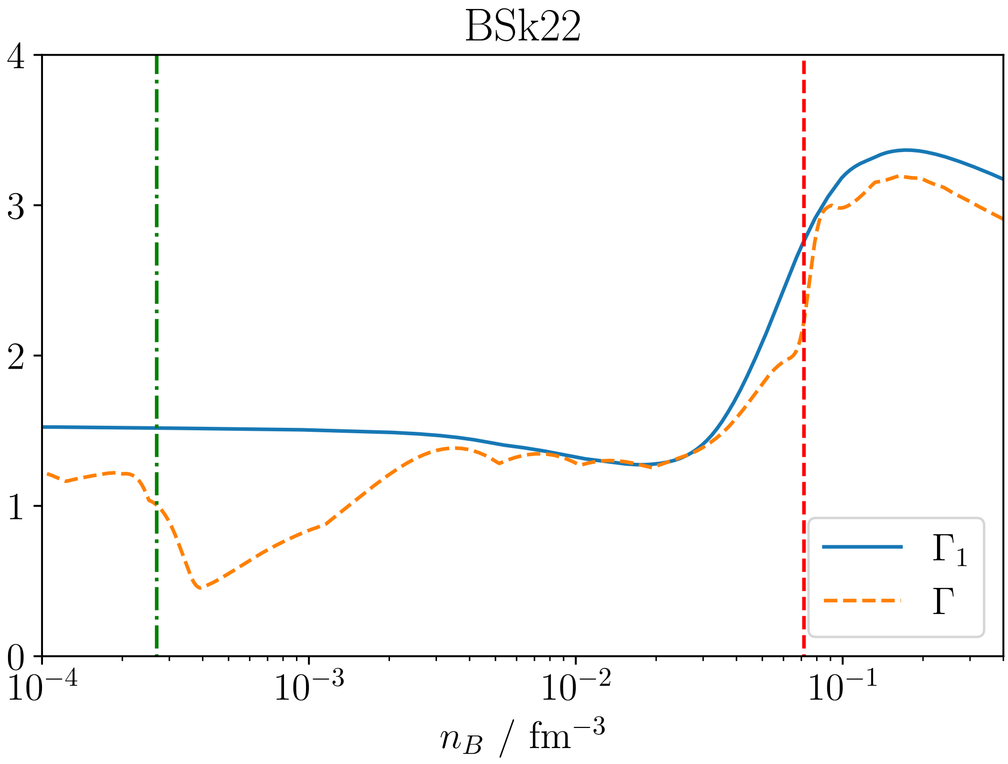

FIGURE 4.3: Plot of adiabatic and background indices Γ_1 and Γ vs baryon number density n for BSk22. The red dashed line corresponds to the location of the crust core interface density n_{cc} and the green dot dashed line corresponds to the neutron drip point density n_{nd} as given by Shchechilin et al. (2023).

densities, beyond the fluid core. For the background model, this is done by using the fits from Shchechilin et al. (2023) which smears out any sharp discontinuities, e.g. associated with distinct composition layers in the neutron star crust (Rüster et al., 2006; Chamel and Haensel, 2008). These discontinuities would give rise to interface modes if not smoothed out, an issue discussed later on. Γ and Γ_1 for the BSk22 example are shown in Fig. 4.3 (the plots for the other equations of state are very similar). The results show that the low-density background index varies significantly, a behaviour inherited from the fits of Shchechilin et al. (2023). For the perturbations, we opt to simply extend the fit for Γ_1 from the core model to lower densities. This assumption is not perfect, as it does not account for the underlying microphysics in the crust (or indeed the elasticity of the nuclear lattice), but as is clear from Fig. 4.3 it means that we are effectively treating Γ_1 as constant at low densities. This means that our low-density treatment is on a par with the vast majority of previous work on g-modes (see Kuan et al. 2021a,b for recent examples) which assumes that the adiabatic indices are constant throughout the star. In essence, our model may be inconsistent, but it is an improvement on previous work. Of course, we need to be mindful of the inconsistencies at low densities. Especially since there will be distinct mode features associated with this region. That this should be the case is evident from Fig. 4.3. It is generally the case that low-frequency waves (the g-modes) can propagate in regions where $\Gamma_1 > \Gamma$. Fig. 4.3 confirms that the neutron star core represents one such propagation region. In addition, we see that mode solutions may be supported in the low-density region near neutron drip. As we will soon see, this leads to the presence of a second family of g-modes, located in the neutron star crust. The fact that our model is somewhat artificial at low densities means that these additional mode results must be considered with caution. However, that there should exist g-modes associated with the neutron star crust is known since the work by Reisenegger and Goldreich (1992a). One would expect these modes to be sensitive to discontinuities between the different layers of nuclei (Finn, 1987; Miniutti et al., 2003), a feature that is not present in our model. The dynamics of the crust region will also be sensitive to the associated elasticity, which is not included here. Future efforts should aim towards a consistent treatment of both core and crust, ideally making use of a consistent equation of state model that covers both regions.

Examining the g-mode spectrum, Fig. 4.4 shows ξ_r vs r for the fundamental g-mode, g_1 for each equation of state, all with $M = 1.4M_{\odot}$. The red and green dashed lines correspond to the locations of the crust core interface density n_{cc} and the neutron drip point density n_{nd} for each equation of state given by Shchechilin et al. (2023). As explained in the previous chapter, these points mark the boundaries in the equation of the state between the core, outer crust and inner crust. The values of these densities is taken from Shchechilin et al. (2023) and shown in Table 4.2. From the plots one can see the characteristic g-mode peak near the core of the star but as was the case in Fig. 3.1 with BSk21, there are additional peaks near the surface, which for BSk26 are of comparable magnitude. These peaks are again believed to be caused by the fluid in the different regions of the star oscillating due to being excited by the g-mode of the core, although unlike Fig. 3.1 one can see evidence of the inner and outer crust oscillating separately in the case of BSk24 and BSk26. Even though the four equations of state are from the same family, there are notable differences between the plots, such as how deep into the core the peak of the oscillation is located. One explanation for the peak in BSk26 being noticebly weaker than the others is due to the peak being located near the crust and thus hinting at a more complicated interaction between the matter in the different regions of the star. Another consequence of these crustal regions in the equations of the star is the presence of another set of modes. As expected the usual f-, p- and g-modes were found for all the different BSk equations and the different total masses but other solutions were found in the mode spectrum below the f-mode frequency. Examples of these solutions are shown in Fig. 4.5 for BSk22 with $M = 1.4M_{\odot}$. While these plots were made using BSk22, these types of solutions appear for the other BSk equations of

TABLE 4.2: Table showing the crust core transition density n_{cc} and neutron drip point density n_{nd} for each of the four BSk equations of state taken from Shchechilin et al. (2023).The notation e-p at the end of each number stands for $\times 10^{-p}$.

Functional	n_{cc} / fm^{-3}	n_{nd} / fm^{-3}
BSk22	0.0716068	2.69e-4
BSk24	0.0807555	2.56e-4
BSk25	0.0855534	2.50e-4
BSk26	0.0849477	2.61e-4

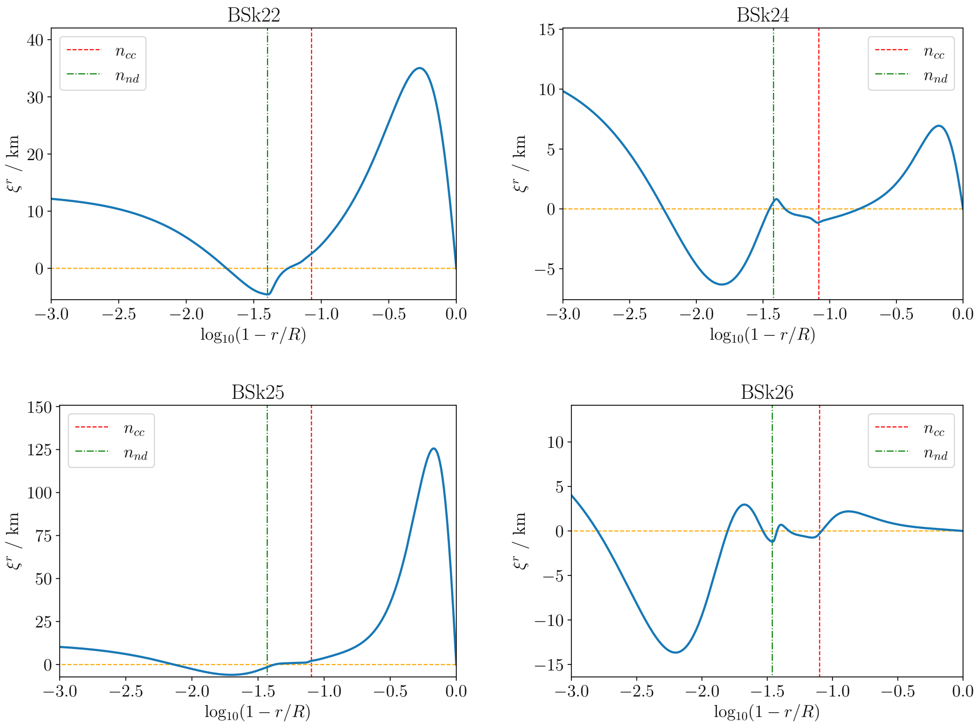

FIGURE 4.4: Plots of ξ^r for the fundamental g-mode, g_1, for neutron stars with $M = 1.4M_\odot$ for the BSk22 and BSk24-26 equations of state (as indicated in the respective panels). The red dashed line corresponds to the location of the crust-core interface density n_{cc} and the green dot-dashed line corresponds to the neutron drip point density n_{nd} for each equation of state, as given by Shchechilin et al. (2023). The orange line corresponds to $\xi^r = 0$.

state as well. These modes are crustal g-modes and are clearly identified by a more significant fluid motion in the crust region, while the mode amplitude in the star's core remains low. This allows us to distinguish the two families of mode solutions. In order to confirm that the second set of modes owe their existence to the low-density propagation region identified in Fig. 4.3 we

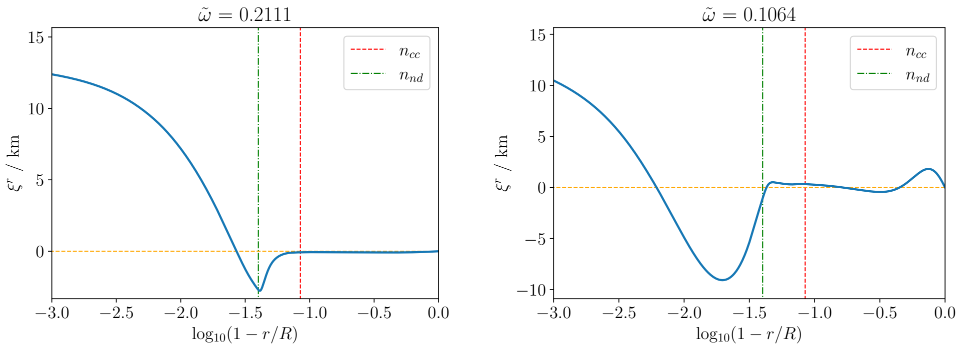

FIGURE 4.5: Plots of ξ^r for the first two crustal g-modes for a neutron star with $M = 1.4M_\odot$ and the BSk22 equation of state. On the left is the first crustal mode and on the right is the second one. The red dashed line corresponds to the location of the crust-core interface density n_{cc} and the green dot-dashed line corresponds to the neutron drip point density n_{nd} as given by Shchechilin et al. (2023). The orange line corresponds to $\xi^r = 0$ and the dimensionless mode frequency (2.40) is given on top.

TABLE 4.3: The dimensionless mode frequencies (2.40) for the first two $l = 2$ core and crust g-modes using the BSk22 equation of state for a few chosen gravitational masses. The results were obtained from the full analytic Γ_1 and also setting $\Gamma_1 = \Gamma$ in the crust while retaining the original Γ_1 in the core. The results confirm that one set of the identified g-modes originates from the physics in the neutron star crust.

$M_\odot$	Mode		Full Γ_1	$\Gamma_1 = \Gamma$ in crust
			$\tilde{\omega}_n$	$\tilde{\omega}_n$
1.4	core	g_1	0.1822	0.1814
		g_2	0.1263	0.1219
	crust	g_1	0.2111	-
		g_2	0.1064	-
1.6	core	g_1	0.1832	0.1831
		g_2	0.1240	0.1221
	crust	g_1	0.1890	-
		g_2	0.0934	-
1.8	core	g_1	0.1850	0.1847
		g_2	0.1232	0.1223
	crust	g_1	0.1689	-
		g_2	0.0847	-
2	core	g_1	0.1860	0.1858
		g_2	0.1224	0.1220
	crust	g_1	0.1501	-
		g_2	0.0745	-

have also calculated the modes for a model where we set $\Gamma_1 = \Gamma$ at densities below neutron drip (adopting the strategy from Krüger et al. 2015). The results of this exercise show that the first core g-modes are not significantly affected, while the crust g-modes disappear from the spectrum, see Table 4.3. This accords with our expectations. The results in Table 4.3 also show that the core/crust g-mode frequencies are interleaved in the mode spectrum.

Moving on, the behaviour of the core g-modes with varying M was examined and is shown in Fig. 4.6 by plotting $\tilde{\omega}$ vs M for the fundamental g-mode and its first ovetone, g_1 and g_2 respectively, for the different BSk equations of state. The range of M was chosen to be from $1M_\odot$ up to the approximate maximum masses given in Shchechilin et al. (2023). Unlike the f-modes in Fig. 4.2, there is much more variance in the behaviour between the different equations. For BSk22 and BSk26, $\tilde{\omega}$ decreases with increasing M, whereas the opposite behaviour is seen for BSk24 and BSk25. There is also a significant spike in BSk26 near the maximum mass. Examining this spike in greater detail, ξ_r vs r was plotted for g_1 for values of M either side of this spike and shown in Fig. 4.7. One can see clear differences in the shape of ξ_r, most notably the location in the star of the peak. For $M = 2.1M_\odot$ and $M = 2.15M_\odot$, the peak is very deep in the core of the neutron star, thus it is far away from any surface effects that could complicate the dynamics of the mode. This lack of interference could explain the sharp increase in $\tilde{\omega}$ seen in Fig. 4.6 though why the g-mode peak shifts so much remains unclear.

Finally, returning to the crustal g-modes, their frequency varies slightly with the mass again decreasing with increasing M. This is evident from Fig. 4.8, and should be expected as n_{cc} and n_{nd} do not depend on M, therefore the fraction of the stellar mass that is the crust, decreases with increasing M. This result agrees with the findings of Reisenegger and Goldreich (1992a).

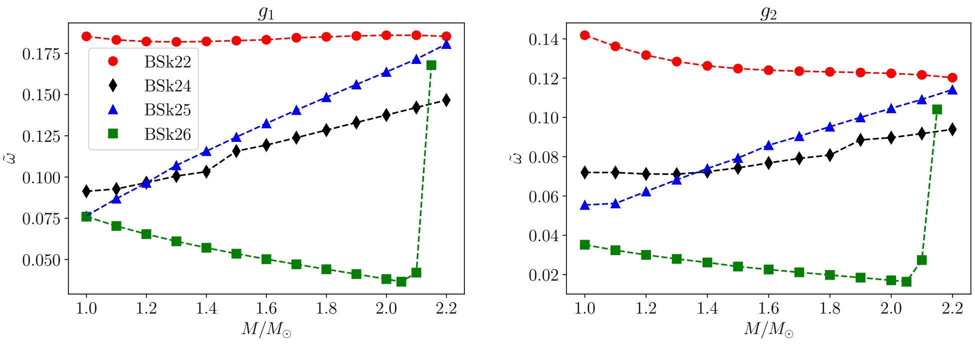

FIGURE 4.6: Plots of dimensionless frequencies $\tilde{\omega}$ vs total mass energy $M/M_\odot$ for the g-modes g_1 and g_2 for the equations of state: BSk22; BSk24; BSk25 and BSk26. On the left is the plot for the fundamental g-mode, g_1 and on the right is the plot for its first overtone g_2.

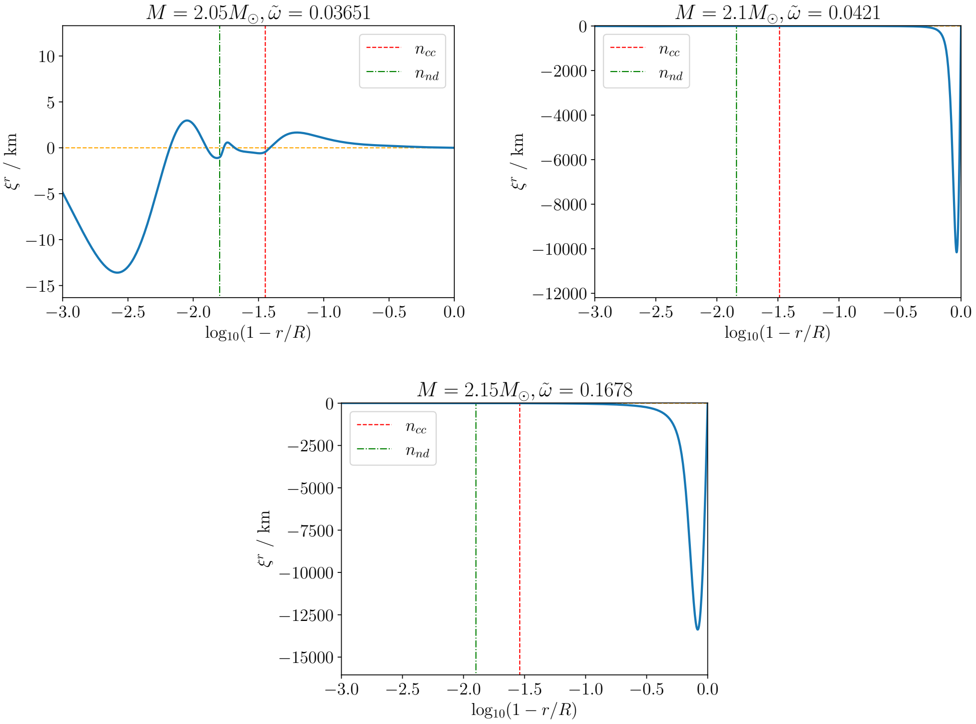

FIGURE 4.7: Plots of ξ_r vs r for g_1 mode using the BSk26 equations. The plots are labelled by their dimensionless frequencies $\tilde{\omega}$ and total mass energy of the background neuron star M.

Unlike the core g-modes, there is minimal difference between the crustal modes of the different BSk models. Again this is to be expected as they depend more on the crustal parameters than Γ_1. The results for the core g-modes will be used later on in Chapter 6 when looking at the impact of oscillations on the gravitational wave signal of a binary neutron star inspiral.

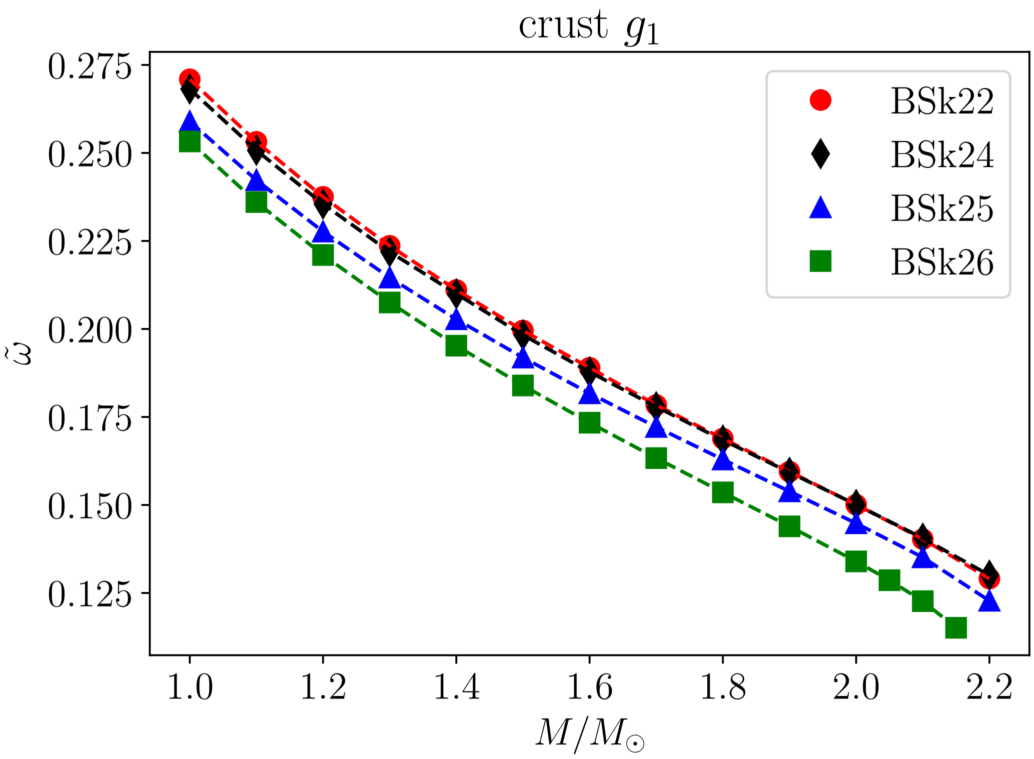

FIGURE 4.8: Plot of dimensionless frequency $\tilde{\omega}$ (2.40) vs total mass energy $M/M_\odot$ for the first crustal g-mode for the BSk22-26 equations of state.

4.6 Summary

We have demonstrated a new regime of oscillation mode calculations that goes beyond the Newtonian framework of the previous chapters. This was achieved by setting up the linear perturbation equations in a dimensionless formalism, within the Cowling approximation, in the spirit of work by McDermott et al. (1983) and others. While this is not a fully relativistic approach, due to the metric perturbations being ignored, it is expected to be a good approximation for modes that are weakly damped by gravitational-wave emission such as the *g*-modes.

By employing four models from the BSk equation of state family, we have shown how subtle differences in the nuclear matter assumptions impact on the g-mode oscillation spectrum of neutron stars. The advantage of the BSk family of models is that it allows us to employ a realistic description of the matter stratification, which is required to calculate the g-mode spectrum.

Along with the expected core g-modes, another class of mode solutions was observed, determined to be crustal g-modes of the kind discussed by Reisenegger and Goldreich (1992a). Such modes arise due to distinct features in the equation of state, like the crust-core interface and the onset of neutron drip, both of which are encoded into the pressure and energy density functionals of Shchechilin et al. (2023) that we employ in our calculations. These modes are, however, sensitive to aspects of the low-density physics (like the crust elasticity) that are not included in our model and hence the corresponding results are not expected to be robust. The fact that the modes originate in the crust is demonstrated by the modes disappearing from the oscillation spectrum when we artificially set $\Gamma_1 = \Gamma$ in the low-density region. This exercise also demonstrates that the core g-modes, which provide the main focus for our discussion, are fairly insensitive to the low-density physics.

The differences between the four BSk equation of state models are in their fitting to nuclear parameters that have not been constrained by experimental or theoretical observations. While our results for mode frequencies will quantitively change for different equation of state models, the g-mode spectrum is still expected to be highly sensitive to the underlying nuclear physics, thus highlighting the importance of composition and stratification. With this in mind, the precise dependence on uncertain aspects of the underlying nuclear physics need to be further explored in future work.

Chapter 5

General Relativistic Modes

5.1 Perturbation Equations

One can go beyond the Cowling approximation by keeping the metric perturbations and solving the mode equations in full GR. The standard approach was set out by Thorne and Campolattaro (1967) and Detweiler and Lindblom (1985). Using the Regge-Wheeler gauge (Regge and Wheeler, 1957) and focusing on quadrupolar oscillations, the metric perturbation can be written as

$$\delta g_{ab} dx^a dx^b = e^\nu H_0 Y_l^m dt^2 + 2HY_l^m dt dr + e^\lambda H_2 Y_l^m dr^2 + r^2 K Y_l^m (d\theta^2 + sin^2\theta d\varphi^2), \quad (5.1)$$

where $H_0(r), H_1(r), H_2(r)$ and $K(r)$ describe the response of the spacetime to the perturbations. In the Newtonian limit these functions, specifically H_0, can be related to the perturbed potential $\delta\Phi$ by

$$e^\nu H_0 = \frac{2}{c^2}\delta\Phi \,. \quad (5.2)$$

The perturbed metric is coupled to the perturbed matter content via the linearised Einstein equations

$$\delta G_a^b = 8\pi \delta T_a^b, \quad (5.3)$$

where δG_a^b and δT_a^b are the perturbed Einstein and stress-energy tensors respectively. The full derivation of δG_a^b is quite long, so we will only state the final result (Kojima, 1988)

$$\begin{aligned}\delta G_a^b = \delta g^{bc}(R_{ac} - \frac{1}{2} g_{ac} R) + \frac{1}{2} g^{bc} [\nabla_d \nabla_a \delta g_c^d + \nabla_d \nabla_c \delta g_a^d - \nabla_d \nabla^d \delta g_{ac} - \nabla_a \nabla_c \delta g \\ - \delta g_{ac} R - g_{ac}(\delta g^{de} R_{de} + \nabla_d \nabla^e \delta g_e^d - \nabla_d \nabla^d \delta g)], \quad (5.4)\end{aligned}$$

where $\delta g \equiv \delta g_a^a$, R_{ab} and R are the Ricci curvature tensor and scalar of the background, respectively, and the covariant derivatives are all associated with the background metric. Using the stress-energy tensor for a perfect fluid (4.1), we obtain

$$\delta T_a^b = (\delta\varepsilon + \delta p)\, u_a u^b + \delta p \delta_a^b + (\varepsilon + p)\left(\delta u_a u^b + u_a \delta u^b\right), \tag{5.5}$$

where δu^a is given by (4.30) and (4.51). As in the previous section, we solve for δT_a^b using conservation equations and the displacement vector ξ^a (4.54). The Lagrangian perturbation of baryon number density is given by (Andersson and Comer, 2021)

$$\Delta n_B = -\frac{1}{2} n_B \perp^{ab} \Delta g_{ab}, \tag{5.6}$$

where the Lagrangian perturbation of the metric is,

$$\Delta g_{ab} = \delta g_{ab} + \nabla_a \xi_b + \nabla_b \xi_a. \tag{5.7}$$

Using (5.1) and (4.54)

$$\Delta n_B = -\frac{n_B}{r^2}\left[r^2\left(K + \frac{1}{2}H_2\right) - l(l+1)V + r\frac{dW}{dr} + \left(1 + \frac{1}{2}r\frac{d\lambda}{dr}\right)W\right]. \tag{5.8}$$

This can then be linked to ε through the thermodynamic relations

$$\Delta\varepsilon = \frac{\varepsilon + p}{n_B}\Delta n_B \tag{5.9}$$

and then to p by (4.67). Using these thermodynamic relations along with (5.3) - (5.5) one can show that $H_0 = -H_2$, simplifying the equations (Thorne and Campolattaro, 1967). Before putting these pieces into the Einstein equation, it is useful to define

$$X = -r^{-l} e^{\frac{\nu}{2}} \Delta p. \tag{5.10}$$

This quantity removes the derivative of the energy density $\frac{d\varepsilon}{dr}$ from the perturbation equations. That derivative is not necessarily continuous which could pose numerical difficulties. Putting all these pieces together, the perturbation equations for a perfect fluid star can be written in the following form, first derived by Detweiler and Lindblom (1985)

$$\frac{dH_1}{dr} = \left[\frac{1}{2}\left(\frac{d\lambda}{dr} - \frac{d\nu}{dr}\right) - \frac{l+1}{r}\right]H_1 + \frac{e^{\lambda}}{r}\left[H_0 + K - 16\pi(\varepsilon + p)V\right], \tag{5.11a}$$

$$\frac{dK}{dr} = \frac{1}{r}H_0 + \frac{n+1}{r}H_1 + \left[\frac{1}{2}\frac{d\nu}{dr} - \frac{l+1}{r}\right]K - \frac{8\pi}{r}e^{\frac{\lambda}{2}}(\varepsilon + p)W, \tag{5.11b}$$

$$\frac{dW}{dr} = -\frac{l+1}{r}W + re^{\frac{\lambda}{2}}\left[\frac{e^{\frac{-\nu}{2}}}{\Gamma_1 p}X - \frac{l(l+1)}{r^2}V + \frac{1}{2}H_0 + K\right], \tag{5.11c}$$

$$\frac{dX}{dr} = -\frac{l}{r}X + \frac{1}{2}(\varepsilon + p)e^{\frac{\nu}{2}}\left\{\left[\frac{1}{r} - \frac{1}{2}\frac{d\nu}{dr}\right]H_0 + \left[r\omega^2 e^{-\nu} + \frac{n+1}{r}\right]H_1 + \left[\frac{3}{2}\frac{d\nu}{dr} - \frac{1}{r}\right]K \right.$$
$$\left. - \frac{d\nu}{dr}\frac{l(l+1)}{r}V - \frac{1}{r}\left[8\pi(\varepsilon + p)e^{\frac{\lambda}{2}} + 2\omega^2 e^{\frac{\lambda}{2}-\nu} - r^2\frac{d}{dr}\left(\frac{e^{\frac{-\lambda}{2}}}{r^2}\frac{d\nu}{dr}\right)\right]\right\}, \tag{5.11d}$$

where

$$n = \frac{1}{2}(l+2)(l-1), \tag{5.12}$$

not to be confused with the mode label or the baryon density n_B. The five perturbation variables:H_0, H_1, K, V and W can be linked by another equation

$$\left[\frac{re^{-\lambda}}{2}\left(r\frac{d\nu}{dr} - 2\right) + (n+1)r\right]H_0 = r^2 e^{-\lambda}\left[\omega^2 r e^{-\nu} - \frac{n+1}{2}\frac{d\nu}{dr}\right]H_1$$
$$+ \left[nr - \omega^2 r^3 e^{-\nu} - \frac{1}{4}r^2 e^{-\lambda}\frac{d\nu}{dr}\left(r\frac{d\nu}{dr} - 2\right)\right]K + 8\pi r^3 e^{\frac{-\nu}{2}}X, \tag{5.13}$$

and from the definition of X we get

$$X = \omega^2(\varepsilon + p)e^{\frac{-\nu}{2}}V - \frac{1}{r}\frac{dp}{dr}e^{\frac{\nu-\lambda}{2}}W + \frac{1}{2}(\varepsilon + p)e^{\frac{\nu}{2}}H_0. \tag{5.14}$$

The six perturbation variables: H_0, H_1, K, V, W and X are then described by two algebraic relations and four differential equations, which, when combined with an equation of state, is enough to close the problem. The addition of the metric perturbation variables, specifically H_1 and K, adds additional mode solutions such as the w-modes, which only exists in general relativity (Kokkotas and Schutz, 1992; Andersson et al., 1995).

5.1.1 External Solutions

The equations from the previous section, can be solved in the interior of the star but this solution is only unique up to a given amplitude. There exists only a discrete set of solutions that correspond to eigenfrequencies of the star. At an arbitrary frequency ω, the oscillations of the star can be interpreted to be the reaction to incoming gravitational waves but the star will also be emitting gravitational waves. Therefore the interior solution must be continued outside the star, into the vacuum, in order to decompose the solutions into incoming and outgoing waves. An eigenfrequency of the star can then be understood to be a solution consisting of purely outgoing gravitational radiation.

Outside the star, the fourth-order system of equations (5.11) reduces to a second-order system as there is no matter and thus the fluid perturbations vanish. Fackerell (1971) has shown that the perturbation equations (for polar perturbations) in the exterior can be written as a one-dimensional wave equation known as Zerilli's equation

$$\frac{d^2 Z}{dr_*^2} + \left[\omega^2 - V_Z(r_*)\right]Z = 0, \tag{5.15}$$

where r_* is the tortoise coordinate given by

$$r_* = r + 2M \log(r - 2M), \tag{5.16}$$

and the effective potential $V_Z(r_*)$ is

$$V_Z(r_*) = 2\left(1 - \frac{2M}{r}\right) \frac{n^2(n+1)r^3 + 3n^2Mr^2 + 9nM^2r + 9M^3}{r^3(nr+3M)^2}. \tag{5.17}$$

Initial values for $Z(R)$ and its derivative can be obtained from the interior solution via the transformation

$$\begin{pmatrix} Z \\ \frac{dZ}{dr} \end{pmatrix} = \frac{1}{fk - h} \begin{pmatrix} k & -1 \\ -h & f \end{pmatrix} \begin{pmatrix} K \\ H_1 \end{pmatrix}, \tag{5.18}$$

where

$$f = \frac{n(n+1)r^2 + 3nMr + 6M^2}{r^2(nr+3M)}, \tag{5.19}$$

$$h = \frac{nr^2 - 3nMr - 3M^2}{r(r-2M)(nr+3M)}, \tag{5.20}$$

$$k = \frac{r}{r-2M}. \tag{5.21}$$

Our numerical solution then follows the approach of Andersson et al. (1995). First one introduces a new variable

$$Z = \left(1 - \frac{2M}{r}\right)^{-\frac{1}{2}} \Psi, \tag{5.22}$$

which turns (5.15) into

$$\left(\frac{d^2}{dr^2} + U(r)\right) \Psi = 0, \tag{5.23}$$

where

$$U(r) = \left(1 - \frac{2M}{r}\right)^{-2} \left[\omega^2 - V_Z(r) + \frac{2M}{r^3} - \frac{3M^2}{r^4}\right]. \tag{5.24}$$

We expect two linearly independent solutions, corresponding to ingoing and outgoing radiation at spatial infinity. Therefore consider the ansatz

$$\Psi^{\pm} = q^{-\frac{1}{2}} \exp\left[\pm i \int_R^r q(r) dr\right], \tag{5.25}$$

which provides a non-linear differential equation for q

$$\frac{1}{2q}\frac{d^2q}{dr^2} - \frac{3}{4q^2}\left(\frac{dq}{dr}\right)^2 + q^2 - U = 0. \tag{5.26}$$

At first glance, this appears to be complicating the problem as we have gone from a linear wave equation to a non-linear equation. However, the new differential equation has favourable properties: while the solution to (5.23) may oscillate wildly, the function q will only be slowly varying making a numerical solution simpler. Next, when U is a slowly varying function of r (which is the case for $r \longrightarrow \infty$) then as a result of the ansatz (5.25), q is also varying slowly and its derivatives in (5.26) can be neglected. Therefore the following initial values can be used for the integration of (5.26) at distances far away from the star

$$q(r \gg R) = \sqrt{U}, \tag{5.27}$$

and

$$\left.\frac{dq}{dr}\right|_{r\gg R} = \frac{1}{2\sqrt{U}}\frac{dU}{dr}, \tag{5.28}$$

The next step is to solve (5.26) for a particular value of ω from a point sufficiently far away from the star; this gives us values for q as well as its derivative at the surface of the star. The physical solution will correspond to a mixture of $\Psi^{\pm}$,

$$\Psi = A_{\text{in}}\Psi^{+} + A_{\text{out}}\Psi^{-}. \tag{5.29}$$

Using (5.23) and (5.25) it can be seen that

$$\Psi^{\pm} = q^{-\frac{1}{2}}, \tag{5.30}$$

and with this we can solve the equations for the ingoing and outgoing amplitudes A_{in} and A_{out}. As the solution is only unique up to a constant factor, we shall investigate the ratio of the amplitudes,

$$\frac{A_{\text{in}}}{A_{\text{out}}} = \frac{Q\left\{\left(1 - \frac{2M}{R}\right)\left[iq + \frac{1}{2q}\frac{dq}{dr}\right] + \frac{M}{R^2}\right\} + \frac{dQ}{dr}}{Q\left\{\left(1 - \frac{2M}{R}\right)\left[iq - \frac{1}{2q}\frac{dq}{dr}\right] - \frac{M}{R^2}\right\} + \frac{dQ}{dr}}, \tag{5.31}$$

where all variables are evaluated at the surface. An eigenfrequency of the star then corresponds to a purely outgoing wave and thus a zero of this function. An important point to note is that we have not mentioned the fact that the coordinate r is taken to be complex in the exterior. The reason for this choice is that the desired outgoing wave solution to (5.23) will grow exponentially as $r \longrightarrow \infty$. This means that it is difficult to resolve the ingoing solution (that is exponentially small) given a finite numerical precision, a well known problem from studies of black hole normal modes (Andersson, 1992). Since $\psi^{-} \sim e^{-i\omega r}$ as $r \longrightarrow \infty$, the exponential divergence can be suppressed along a path in the complex r-plane. The preferred path is a straight line, the slope of which depends on the chosen value of ω and is optimally taken to be

$$\tan\theta = -\frac{\text{Im}(\omega)}{\text{Re}(\omega)}. \tag{5.32}$$

The derivatives with respect to (complex-valued) r can be implemented numerically using the relation

$$\frac{dq}{dr} = e^{-i\theta}\frac{dq}{d\rho} \tag{5.33}$$

where ρ is the real distance along the integration path from the surface of the star (not to be confused with the density).

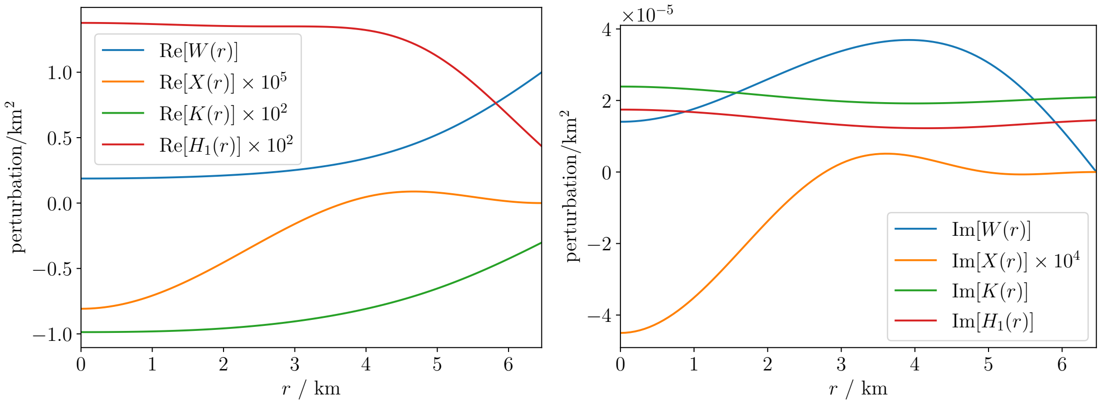

FIGURE 5.1: Perturbation functions of the f-mode for the $1.3M_\odot$ model used in Table 4.1. The real and imaginary parts are shown on the left and right respectively with the functions scaled for clarity.

5.1.2 Results

To demonstrate the formalism, we solve the mode equations using the method put forth in Gittins and Andersson (2025); Gittins et al. (2025), for a $1.3\,M_\odot$ neutron star for the same model used in Table 4.1. The perturbation functions for the quadrupolar f-mode are shown in Fig. 5.1 where the functions have been scaled for clarity. One key point to emphasise is that unlike the Newtonian and Cowling regimes the eigenmodes and eigenfunctions are now complex valued. As well as solving for the modes one can examine the oscillation spectrum by plotting A_{in} as done in Fig. 5.2. The discontinuities correspond to frequencies where there is no ingoing radiation but purely outgoing which we identify as the eigenmodes of the neutron star. The vertical orange dashed line is the f-mode.

One can also examine the low frequency oscillation regime. However, it turns out that when calculating low-frequency oscillations, such as g-modes, one runs into numerical difficulties, which lead to undesirable noise in the very low frequency regime in the stellar spectrum, where higher order g-modes reside, thus preventing us entirely from determining any eigenmode. The problem is of purely numerical origin and can be avoided by using the augmentation introduced by Krüger (2015). As this is a numerical problem rather than a physical one we will not go into further detail but simply utilise this approach when considering higher order g-modes. The real part of the radial displacement eigenfunction $W(r)$ is plotted for the first four quadrupolar g-modes in Fig. 5.3 and the corresponding location in the spectrum is shown in Fig. 5.4.

5.2 Hyperonic Cores

So far in this work, we have only considered the neutron star to be made of neutrons, protons and electrons. However, the cores of neutron stars reach densities beyond our current experimental understanding of nuclear matter. There is no consensus on what particle species

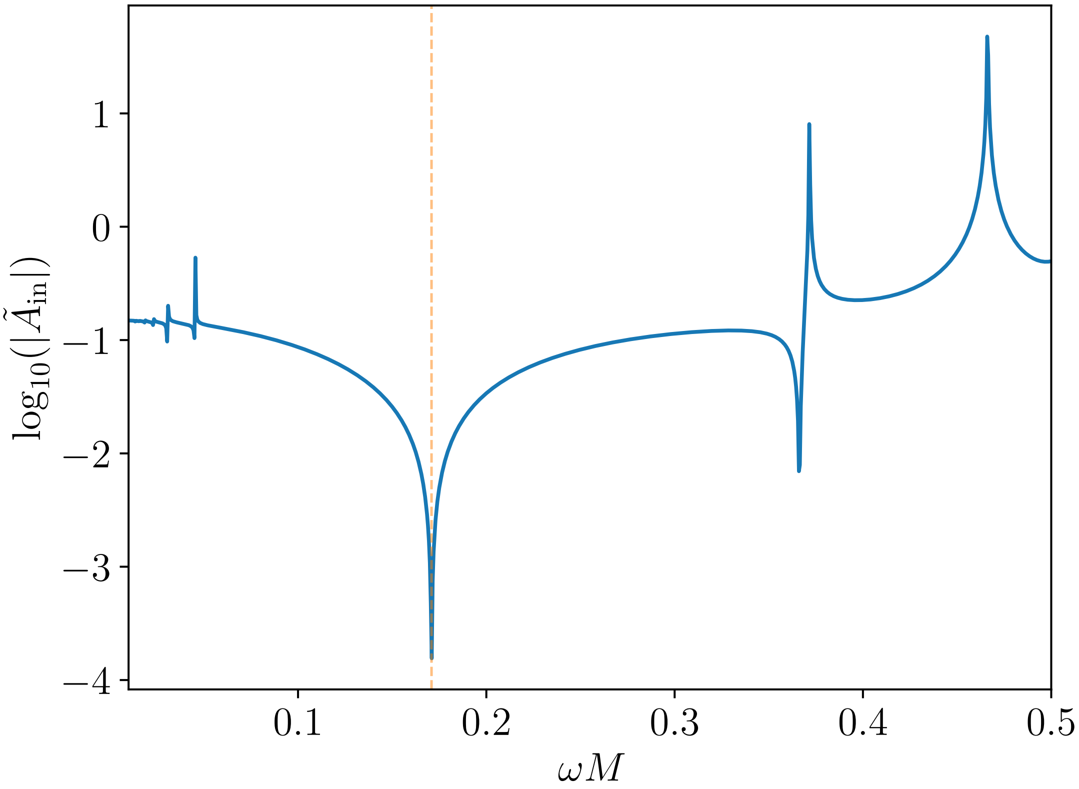

FIGURE 5.2: The oscillation spectrum for quadrupolar perturbations of the neutron star, visualised with the ingoing gravitational-wave amplitude against (real) oscillation frequency multiplied by the mass. The vertical orange dashed line corresponds to the f-mode.

will be present or in what state of matter. One possibility is the presence of strangeness containing exotic particles, such as hyperons or kaons (Lattimer and Prakash, 2004; Blaschke and Chamel, 2018). In Chapter 3 when beta equilibrium reaction rates were incorporated into the oscillation problem we saw that for nucleonic matter, the Urca and modified-Urca reactions were too slow compared to the oscillation frequencies to deviate from the standard frozen composition assumption. Instead if we consider the presence of hyperons in the core, non-leptonic channels involving the hyperons can have comparable rates with the g-mode frequencies and possibly even the f-mode at low temperatures (Ghosh et al., 2024).

As in Chapter 3 the rates can be incorporated into the perturbation equations via the Lagrangian change in pressure with energy density

$$\Delta p = \mathcal{D}\Delta\varepsilon, \tag{5.34}$$

where

$$\mathcal{D} = c_s^2 + \frac{\omega}{\omega + i\mathcal{A}}(C^2 - c_s^2), \tag{5.35}$$

where the terms are defined by (3.14) and (3.26). Using this definition one can define an “effective” adiabatic index,

$$\Gamma_{\mathcal{A}} = \frac{\varepsilon + p}{p}\mathcal{D}. \tag{5.36}$$

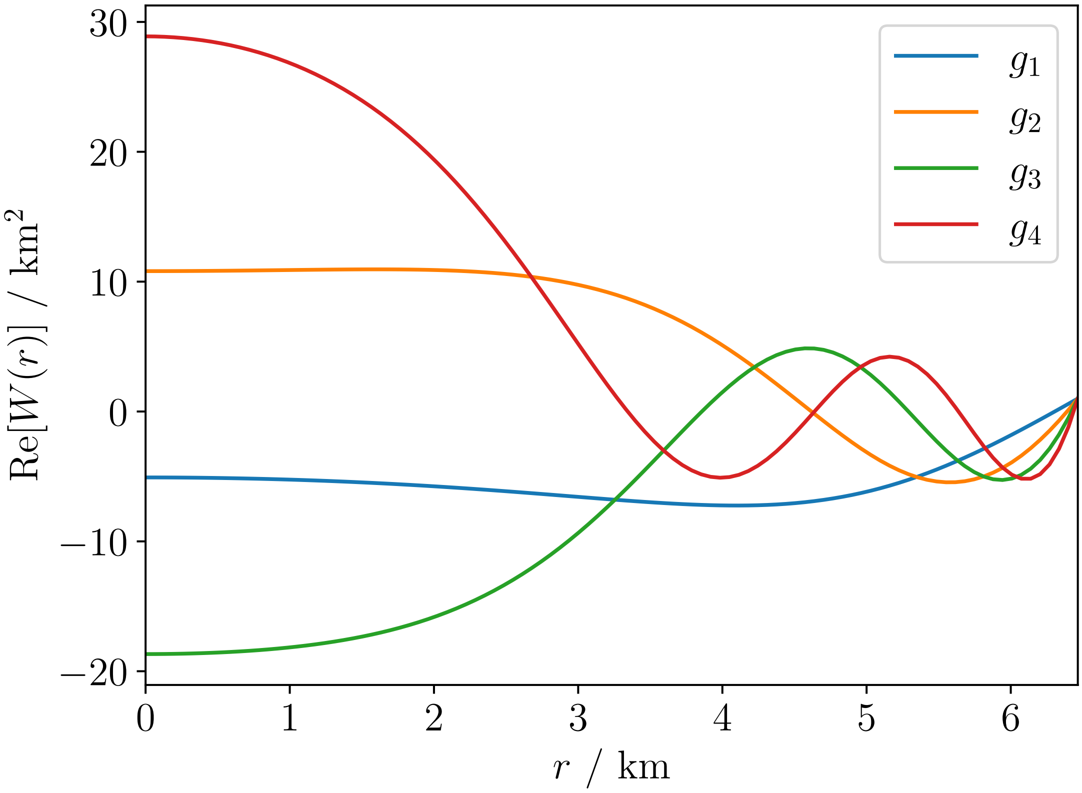

FIGURE 5.3: The real part of the radial-displacement eigenfunction $W(r)$ of the first four quadrupolar g-modes. They have all been normalised to $W(R) = 1$

Replacing Γ_1 in the previous section with $\Gamma_{\mathcal{A}}$, incorporates the microscopic nuclear rates into the mode equations. One can also use $\Gamma_{\mathcal{A}}$ in the Cowling approximation equations, as shown in Zhao et al. (2025).

Unlike in the previous nucleonic case, instead of considering arbitrary reaction rates we will incorporate a more realistic, density dependent form of $\mathcal{A}$. The microscopic reaction rates are calculated following the method of Lindblom and Owen (2002) which rely on the contact interaction matrix element.

There are several different hyperon species and reactions, so as a first step we just consider the Λ hyperon, which is thought to be the dominant contributor to the oscillation damping (Jones, 2001; Lindblom and Owen, 2002). The dominant non-leptonic weak interaction involving only the Λ hyperon is then

$$n + p \rightarrow p + \Lambda. \tag{5.37}$$

As previously mentioned the presence of the reactions damp the mode oscillations providing an imaginary component to the mode frequency. In Cowling and Newtonian this is the only imaginary contribution but in full general relativity the mode frequencies are already complex due to damping caused by the emission of gravitational waves. In order to quantify the impact of the reactions there are two methods we can use. The first method is to calculate the modes

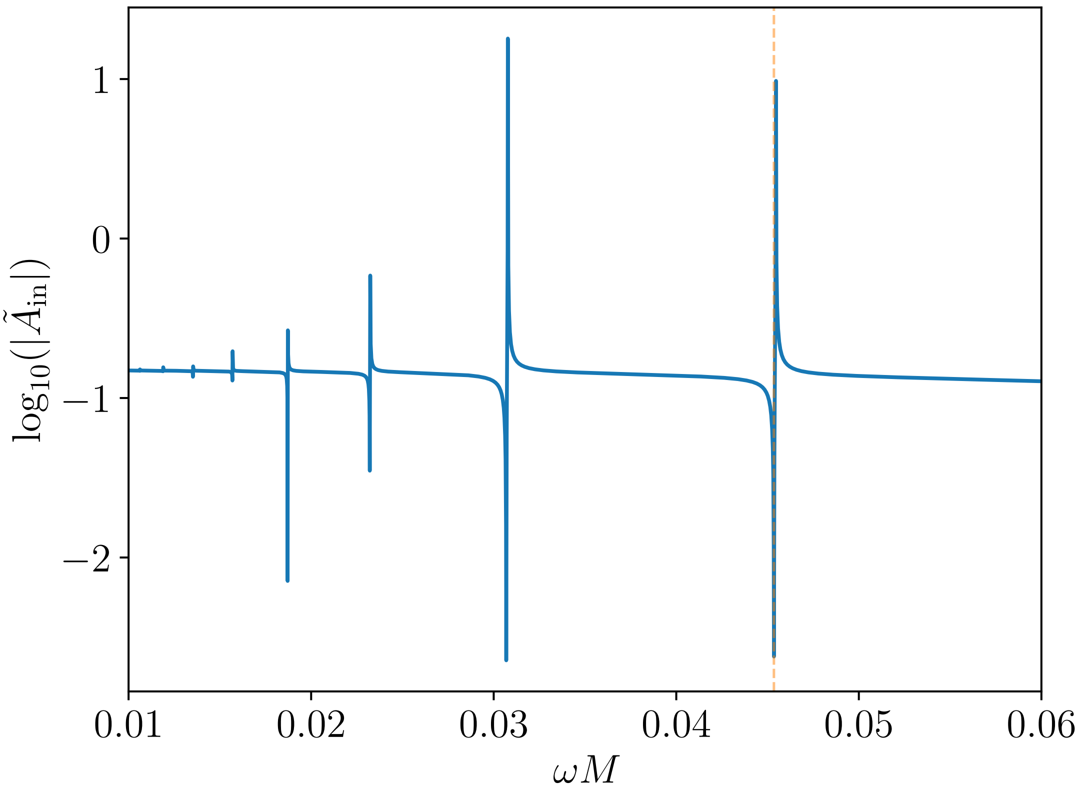

FIGURE 5.4: The oscillation spectrum for quadrupolar perturbations of the neutron star, visualised with the ingoing gravitational-wave amplitude against (real) oscillation frequency multiplied by the mass. The vertical orange dashed line corresponds to the first g-mode.

with $\mathscr{A}$ and compare the results to the limit $\mathscr{A} \to 0$ which corresponds to the limit of infinitely slow reactions, e.g. frozen composition. The imaginary part of the slow reaction limit will then only have the gravitational wave contribution. The second method is to calculate the mode frequencies in Cowling using the reaction rates and then compare to the full general relativity case. The imaginary component of the Cowling calculation will then only have the reaction component.

5.2.1 Results

The oscillation spectrum was calculated for a range of neutron star masses and temperatures using the HTZCS equation of state (Hornick et al., 2018) adjusted to include hyperons, specifically the Λ hyperon, using the methodology of Ghosh et al. (2022, 2024). This equation of state is a relativistic mean-field model that satisfies the standard constraints from NICER and gravitational wave observations as shown in Fig. 1.3. The reason we have chosen a relativistic mean field model to include hyperons instead of the BSk family used in previous chapters is that due to relativistic mean field models being causal by design, relativistic effects can accounted for at the high densities where hyperons are expected to be present. It is also computationally easier, in general, to incorporate additional particles, such as hyperons, in relativistic mean field models via a hyperon field as opposed to models such as BSk where more complicated microscopic interactions and potentials must be calculated.

In order for hyperons to be present in the core, the neutron stars should be $\gtrsim 1.5M_\odot$. The masses were chosen to range from $1.53M_\odot$ up to the maximum mass allowed by the TOV equations for the equation of state. The temperatures were chosen to range from 5×10^7 K to 10^9 K, which would correspond to the neutron star during the inspiral, away from merger. In this low temperature regime, the reaction rates are comparable to the mode frequencies. The damping time τ for the oscillation modes were then calculated for each configuration in Cowling and full general relativity where $\tau = 1/\mathrm{Im}(\omega)$. Due to the reactions the g-modes were suppressed and no longer appear in the oscillation spectrum as shown in Fig. 5.5 for a background neutron star with $1.99M_\odot$ and 5×10^8 K. Moving on to the f-mode, the results are shown in Fig. 5.6. We can see that the damping time decreases as the mass increases. As the mass increases the ratio of hyperonic to nucleonic matter increases, leading to greater damping from the hyperons. We also see a resonance behaviour with the damping time and the temperature, as the temperature increases the reaction rate increases until the reaction rate is comparable to the mode frequency. However as the temperature increases past this resonance, the reactions are too fast to impact the f-mode.

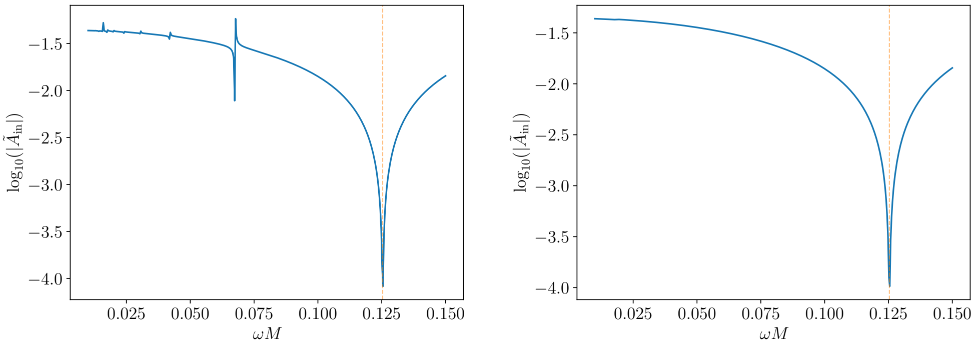

FIGURE 5.5: The oscillation spectrum for quadrupolar perturbations of the neutron star, visualised with the ingoing gravitational-wave amplitude against (real) oscillation frequency multiplied by the mass. The vertical orange dashed line corresponds to the first f-mode. On the left is the slow reaction limit $\mathcal{A} \to 0$ and on the right with the calculated reaction rates.

5.3 Summary

In this chapter we have gone beyond the Cowling approximation of the previous chapter and demonstrated how to solve the oscillation mode problem in a fully general relativistic framework. By using the linearised Einstein equations, one can set up the linear perturbation problem in an approach set out by Thorne and Campolattaro (1967) and Detweiler and Lindblom (1985). However, unlike in the Newtonian and Cowling approximation regimes, due to the equations coupling to the metric perturbations one must also solve the problem outside

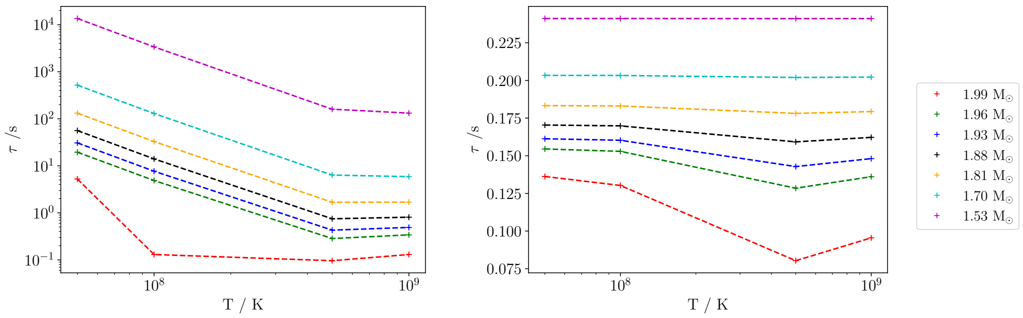

FIGURE 5.6: The damping time of the f-mode vs temperature for the background neutron stars using the Cowling approximation on the left and full general relativity on the right. A range of masses from $1.53M_\odot$ up to the TOV mass are considered.

the star in the vacuum, this external problem is solved using the approach of Andersson et al. (1995). To avoid numerical noise in the very low frequency region of the oscillation spectrum the augmentation introduced by Krüger (2015) was implemented.

The work of Chapter 3 was then extended to incorporate non-leptonic weak reactions involving hyperons. The microscopic reaction rates were calculated following the method of Lindblom and Owen (2002) which rely on the contact interaction matrix element. The oscillation problem was then solved using both the Cowling approximation and fully general relativistic approaches. By employing the HTZCS equation of state (Hornick et al., 2018) adjusted to include hyperons, specifically the Λ hyperon, using the methodology of Ghosh et al. (2022, 2024), we have shown how the reactions suppress the g-modes and generate additional damping on the f-mode. The additional damping is dependent on the mass and temperature of the background neutron star.

Future work would extend this calculation to include additional hyperon species such as the Σ^- hyperon. The equation of state HTZCS was chosen as a proof of principle. Quantitatively, changing the equation of state and hyperon species considered will obviously affect the specific damping times, however, qualitatively we expect that this resonance like behaviour with temperature would remain. The calculation of the microscopic reaction rates can also be improved upon, as the method from Lindblom and Owen (2002) can not compute all the occurring reactions. The next step would be to follow the approach of Alford and Haber (2021) which uses the combined strong-weak interaction matrix element and drops the non-relativistic approximations of Lindblom and Owen (2002).

Chapter 6

Detectability of Oscillation Modes

Using the analysis from the previous chapters, the mode spectrum of neutrons stars can be calculated numerically but what physical information of the star itself can be obtained by studying the modes?

If one considers a binary neutron star system, the emission of gravitational waves will cause the two stars to inspiral. As they get ever closer together, they are increasingly deformed by the tidal interaction. The associated finite-size effects manifest as a dephasing of the gravitational-wave signal, offering valuable information about the internal structure of neutron stars and, in turn, constraining the equation of state of high density nuclear matter (Flanagan and Hinderer, 2008; Hinderer et al., 2010). This effect was shown with the first direct detection of gravitational waves from a neutron star binary GW170817 (Abbott et al., 2017)). By analysing the gravitational wave signal, they were able to place constraints on the tidal deformability, λ (Abbott et al., 2018, 2019). The tidal deformability of a neutron star is a single parameter that quantifies how easily the star is deformed when subject to an external tidal field. In general, a larger tidal deformability signals a larger, less compact star that is easily deformable, while a smaller tidal deformability parameter signals a smaller, more compact star that is more difficult to deform. In the language of equations of state, this is what we referred to as “stiff” and “soft”, respectively.

This tidal response can be dynamical, as the tidal driving induces the resonant excitation of individual oscillation modes of the star. If the conditions are favourable, such resonances may leave an observable imprint on the gravitational-wave signal from the system. Because of its relatively strong coupling to the tidal potential, the f-mode dominates the star’s dynamical tidal response (Hinderer et al., 2016; Steinhoff et al., 2016; Andersson and Pnigouras, 2020, 2021; Steinhoff et al., 2021; Pitre and Poisson, 2024; Hegade K. R. et al., 2024), but additional (lower frequency) modes may also come into play. It is these other modes that this chapter will examine.

6.1 Phase Shift

As mentioned previously, if one considers a binary neutron star system, a coupling and resonance can occur between a mode frequency ω_n and the orbital frequency when $\omega_n \approx 2\Omega$ for $m = 2$. This causes energy to be transferred into the mode, exciting an oscillation and drawing energy from the orbit. As the orbit has lost energy, the orbit will decrease faster, manifesting as a change in the gravitational waveform (Lai, 1994; Kokkotas and Schafer, 1995; Reisenegger and Goldreich, 1994; Andersson and Ho, 2018). The goal is then to quantify this shift in the waveform for a given mode. First, assume, a Newtonian orbit, with masses M_1 and M_2 and an orbital separation $D(t)$, orbiting each other at an orbital frequency Ω. Then, the shift in orbital phase $\Delta\Phi$ due to energy transfer ΔE during the inspiral can be estimated as

$$\frac{\Delta\Phi}{2\pi} \approx -\frac{t_D}{t_{\rm orb}}\frac{\Delta E}{|E_{\rm orb}|}, \tag{6.1}$$

where $E_{\rm orb}$ is the orbital energy given by

$$E_{\rm orb} = -\frac{GM_1M_2}{2D}, \tag{6.2}$$

$t_{\rm orb}$ is the orbital period, given by

$$t_{orb} = \frac{2\pi}{\Omega}, \tag{6.3}$$

and t_D is the orbital decay timescale given by

$$t_D = \frac{D}{|\dot{D}|}, \tag{6.4}$$

where the dot indicates a derivative with respect to time. To leading order, the orbital separation evolves due to the emission of gravitational waves as

$$\dot{D} = -\frac{64}{5c^5}\frac{M_1M_2(M_1+M_2)}{D^3}. \tag{6.5}$$

The mode resonance then occurs when, the mode frequency ω_n is twice the orbital frequency. This can then be related to gravitational wave frequency f by

$$\omega_n = 2\Omega = 2\pi f. \tag{6.6}$$

One can also relate Ω to D by

$$\Omega = \sqrt{\frac{G(M_1+M_2)}{D^3}}. \tag{6.7}$$

For simplicity, it will be assumed from now on that the two masses are equal, $M = M_1 = M_2$. The last piece of the puzzle is then to quantify ΔE. From Lai (1994), one can relate the energy transfer to the mode overlap integral Q_{nl}

$$\Delta E \approx \frac{\pi^2}{512}\frac{GM^2}{R}\omega_n^{1/3} Q_{nl}^2 \left(\frac{Rc^2}{GM}\right)^{5/2}. \tag{6.8}$$

Putting all this together

$$\frac{\Delta\Phi}{2\pi} \approx -\frac{5\pi}{4096}\left(\frac{c^2 R}{GM}\right)^5 \frac{Q_{nl}^2}{\tilde{\omega}_n^2}, \tag{6.9}$$

where $\tilde{\omega}$ is the dimensionless mode frequency. The dimensionless overlap integral is defined as

$$\tilde{Q}_n = \frac{Q_n}{MR^l}. \tag{6.10}$$

In order to quantify if gravitational wave detectors such as LIGO and Virgo could detect these phase shifts we need to calculate the minimum detectable phase shift for each individual detector. This minimum value will be a function of frequency, $\Delta\Phi(f)$, as the sensitivity of each detector is frequency dependent. This is calculated from

$$|\Delta\Phi(f)| = \frac{\sqrt{S_n(f)}}{2A(f)\sqrt{f}}, \tag{6.11}$$

where $S_n(f)$ is the power spectral density of the noise for each detector and $A(f)$ is the gravitational wave amplitude of a generated test waveform as discussed by Read (2023). One still then needs to choose a waveform model. For simplicity, noting that recent work by Read (2023) shows that the differences in current waveform models are much smaller than the estimated data uncertainties for the low frequencies we are interested in, only one waveform model was considered. If a mode is detectable for one waveform model it should be detectable for others. Specifically, we used the IMRPhenomPv2_NRTidal model as it includes the static tidal deformabilities (Dietrich et al., 2019). It is important to note that, as the inferred phase uncertainties are estimated from expected gravitational-wave data and existing waveform models, they only serve as approximate upper limits on any effects not considered in the waveform modelling, like the influence of dynamical tides considered here.

Using (6.9) and (6.11) the Fig. 6.1 from Ho and Andersson (2023) was created showing the values of the overlap for various g-modes against the frequency. As before, the stratification is parameterised as $\Gamma - \gamma$, where in the notation used in previous chapters, $\Gamma \equiv \Gamma_1$ and γ is the polytropic index as used in (2.20). Also included in the graph are sensitivity curves for different detectors: LIGO's A+ upgrade and the proposed next generation Cosmic Explorer. The black dashed line are estimates based on the GW170817 detection.

While this analysis is more qualitative due to use of a polytropic equation of state, it can still be seen that the g-modes are quite weak and we will rely on future detectors to dectect them. Numerical values for the dimensionless overlap are calculated using the methods used in the previous chapters and are shown in Table 6.1 where the modes have been normalised so that $\mathcal{A}^2 = MR^2$. It shows that the frequencies and overlap integrals increase with increasing

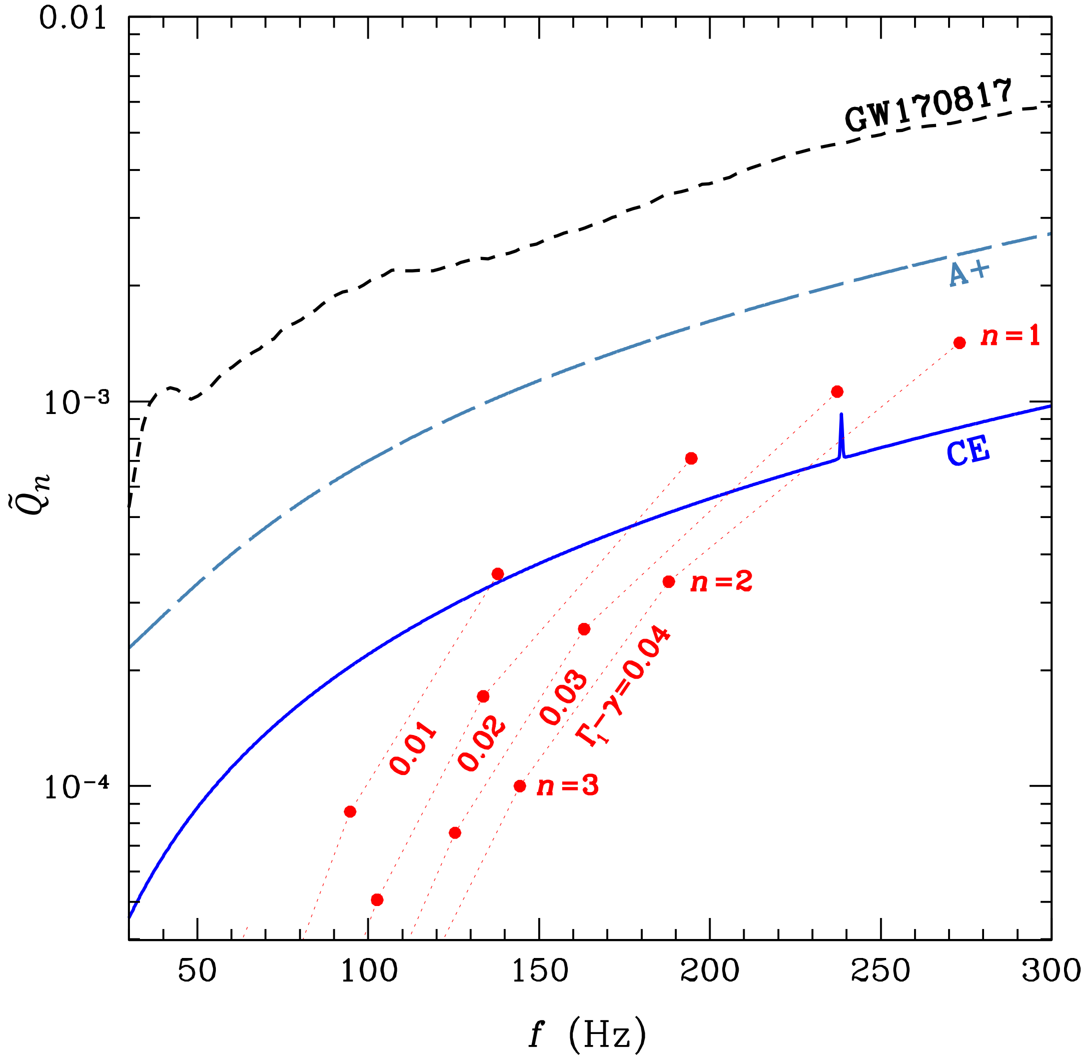

FIGURE 6.1: A plot of the overlap integral of g-modes against frequency from Ho and Andersson (2023). The stratification is parametrised as $\Gamma_1 - \gamma$, where γ is the polytropic index as used in (2.20). The red dashed lines correspond to different stratifications where n is the overtone of each mode. The other lines are sensitivity curves for different detectors: LIGO's new A+ upgrade and the proposed next generation Cosmic Explorer. The black dashed line are estimates based on the GW170817 detection.

stratification but decrease with increasing n. The prospect of detecting any g-modes is therefore most likely with the fundamental g-mode, g_1.

6.2 Scaling Relations

One can also examine the impact of stratification by examining scaling relations of the mode frequencies and overlap integrals. One can see in Table 6.1 that $\tilde{\omega}$ and $\tilde{Q}$ increase with increasing stratification. In work by Xu and Lai (2017), their numerical results show the following relations for the $l = 2$ g-modes of a non-rotating Newtonian neutron star with

TABLE 6.1: The dimensionless overlap is shown for different $l = 2$ g-modes for different stratifications Γ_1. The modes are calculated using a non-rotating Newtonian star with polytropic equation of state with $n = 1$. The notation e-p at the end of each number stands for $\times 10^{-p}$.

Mode	$\Gamma_1 = 2.01$		$\Gamma_1 = 2.05$		$\Gamma_1 = 2.1$		$\Gamma_1 = 2.2$		$\Gamma_1 = 2.3$	
	$\tilde{\omega}$	$\tilde{Q}_n$	$\tilde{\omega}$	$\tilde{Q}_n$	$\tilde{\omega}$	$\tilde{Q}_n$	$\tilde{\omega}$	$\tilde{Q}_n$	$\tilde{\omega}$	$\tilde{Q}_n$
g_1	0.0836	3.56e-4	0.1845	1.77e-3	0.2566	3.50e-3	0.3515	6.85e-3	0.4178	1.01e-2
g_2	0.0574	8.58e-5	0.1270	4.24e-4	0.1770	8.36e-4	0.2434	1.62e-3	0.2904	2.37e-3
g_3	0.0441	2.54e-5	0.0975	1.25e-4	0.1361	2.46e-4	0.1875	4.77e-4	0.2240	6.94e-4
g_4	0.0359	8.39e-6	0.0794	4.14e-5	0.1109	8.13e-5	0.1529	1.57e-4	0.1828	2.28e-4
g_5	0.0303	2.98e-6	0.0671	1.47e-5	0.0937	2.88e-5	0.1293	5.56e-5	0.1546	8.06e-5
g_6	0.0263	1.13e-6	0.0581	5.45e-6	0.0812	1.07e-5	0.1120	2.06e-5	0.1341	2.98e-5

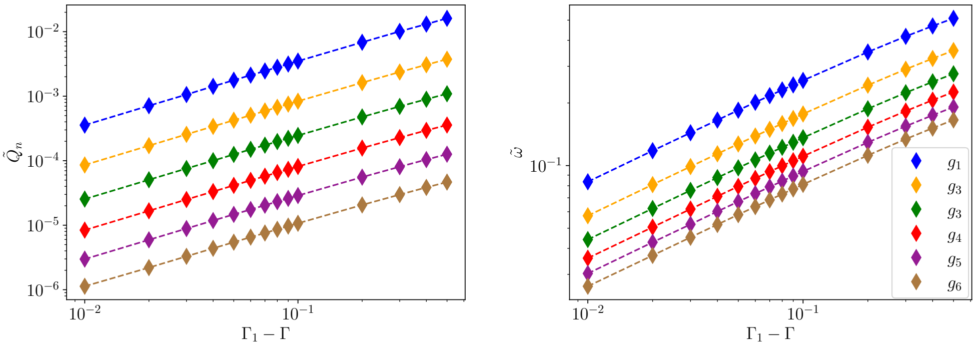

FIGURE 6.2: Plots of the dimensionless overlap integral $\tilde{Q}$ on the left and dimensionless frequencies $\tilde{\omega}$ on the right vs $\Gamma_1 - \gamma$ in log-log scales for the first six g-modes. The background star is polytropic with $\gamma = 2$, $R = 10\,\text{km}$ and $M = 1.4 M_\odot$. For the overlap integrals the slopes range from 0.95 - 0.98 and for the frequencies the slopes range from 0.46-0.47.

polytropic equation of state,

$$\tilde{\omega}_n \propto (\Gamma_1 - \gamma)^{1/2}, \tag{6.12}$$

$$\tilde{Q}_n \propto \Gamma_1 - \gamma. \tag{6.13}$$

Using the results from Table 6.1, these relations were tested and shown in Fig. 6.2 for the first six g-modes, where $\gamma = 2$ and Γ_1 is varied from 2.01-2.5. Using a linear regression function, for the overlap integrals the slopes range from 0.95 - 0.98 and for the frequencies the slopes range from 0.46-0.47. This is in agreement with (6.12) and (6.13) allowing for small numerical errors. These results along with that of Fig. 6.1 show the importance of stratification for the detectability of g-modes.

6.3 Relativistic Analogues

Now this analysis will be extended beyond Newtonian gravity using the relativistic Cowling approximation. In order to derive a overlap integral, consider a binary neutron star system, where the orbit is in the equatorial plane and it is assumed each star sees the other as a point mass. Focusing on one star, let its mass be M_1 and its companion be M_2. The gravitational energy that this star absorbs from the other is given by the tidal part of the Hamiltonian,

$$H_{\text{tid}} = \int \Phi^T \delta\varepsilon \sqrt{-g} \mathrm{d}^3 x, \tag{6.14}$$

where Φ^T is the tidal potential experienced by the star and the integral is over the star's volume (Kuan et al., 2021a). The tidal response of the neutron star and the influence on the orbit evolution are minimal except only the last few second before merger. As the focus of this work is on g-modes which have low frequency and would therefore appear early on in the inspiral, a Newtonian approximation is used here but with the gravitational mass. The use of this assumption is something that will need to be examined in future work. From Pnigouras et al. (2022),

$$\Phi^T = M_2 \sum_{l=2}^{\infty} \sum_{m=-l}^{l} \frac{W_{lm} r^l}{D(t)^{l+1}} Y_{lm} e^{-im\psi}, \tag{6.15}$$

where D is the distance between the companion and the centre of this star, $r = 0$, ψ is the orbital phase and where $W_{lm} = 0$ for odd $l + m$, else

$$W_{lm} = (-1)^{(l+m)/2} \sqrt{\frac{4\pi}{2l+1} (l-m)!(l+m)!} \left[2^l \left(\frac{l+m}{2}! \right) \left(\frac{l-m}{2}! \right) \right]. \tag{6.16}$$

Now $\delta\varepsilon$ can be expressed as the sum of contributions of all the modes, n

$$\delta\varepsilon = \sum_n \delta\varepsilon_n e^{i\omega_n t}. \tag{6.17}$$

From (4.60),

$$\partial_t \delta\varepsilon + \partial_t \xi^i \partial_i \varepsilon + \frac{(p+\varepsilon) e^{\nu/2}}{\sqrt{-g}} \partial_i \left[e^{-\nu/2} \sqrt{-g} \partial_t \xi^i \right] = 0. \tag{6.18}$$

Now consider ξ^i as the sum over modes,

$$\xi^i = \sum_n q_n \xi_n^i e^{i\omega_n t}, \tag{6.19}$$

where q_n is the contribution of each mode and is given by

$$q_n(t) = \frac{\langle \xi_n^i | \xi^i \rangle}{\mathcal{A}_n^2}, \tag{6.20}$$

where $\mathcal{A}_n^2$ is given by (4.109). Here ξ_n^i satisfy the relevant eigenfunction mode equations, which in this work will later be chosen to be (4.77) and (4.78). Now substituting this and (6.17) into (6.18) and simplifying gives

$$\delta\varepsilon_n = -q_n \left[\xi^i_n \partial_i \epsilon + \frac{(p+\varepsilon)e^{\nu/2}}{\sqrt{-g}} \partial_i \left(e^{-\nu/2} \sqrt{-g} \xi^i_n . \right) \right] \tag{6.21}$$

This can then put into (6.14) and after simplifying and integrating by parts gives

$$H_{\text{tid}} = -\sum_n q_n \int (p+\epsilon) \xi^i_n \nabla_i (\Phi^T) \sqrt{-g} \mathrm{d}^3 x. \tag{6.22}$$

Now using (6.15),

$$H_{\text{tid}} = -\sum_n q_n M_2 \sum_{l=2}^{\infty} \sum_{m=-l}^{l} \frac{W_{lm} r^l}{D(t)^{l+1}} Q_{nml} e^{-im\psi} \tag{6.23}$$

where Q_{nml} is identified as relativistic analogue of the overlap integral Q_{nlm} and is given by,

$$Q_{nlm} = \int (\varepsilon + p) \xi^i_n \nabla_i (r^l Y_{lm}) \sqrt{-g} \mathrm{d}^3 x, \tag{6.24}$$

Using the Cowling approximation setup from the previous chapter, for a specific mode, the dimensionless overlap simplifies to

$$\tilde{Q}_{nl} = \frac{1}{M_1 R^l} \int_0^R e^{(\nu+\lambda)/2} (\varepsilon + p) r^l \left[W_l + l(l+1) V_l \right] \mathrm{d}r. \tag{6.25}$$

Using the results from Chapter 4, $\tilde{Q}_{n2}$ was calculated for the f-mode and first two g-modes for a variety of total mass energies for the four different BSk equations of state. The results are shown in Table 6.2 and plotted in Fig. 6.3 where the modes have been normalised so that $\mathcal{A}^2 = MR^2$ where we have again assumed $M = M_1 = M_2$. A sanity check, that is immediately clear is that the value of $\tilde{Q}$ for the f-mode is several orders of magnitude greater than for the g-modes. This is as expected due to the f-mode most resembling the tidal potential. Looking closer at Fig. 6.3, one can see that for f-modes, the different equations of state behave very similarly to one another and excluding BSk26 are almost indistinguishable. However when moving onto the g-modes the behaviour is less smooth. This is to be somewhat expected, as the g-modes depend more on local variations with radius. In general as M increases, Q decreases although there exist certain values of M for which Q will dramatically spike before decreasing again.

Now on to the question of detectability. Using (6.9) for the results of Table 6.2, $\tilde{Q}_{n2}$ was plotted vs frequency with the same sensitivity curves used in the Newtonian case. The results are shown in Fig. 6.4, for the four different equations of state with each plot labelled for the different total mass energies M of each neutron star in the binary. It is assumed that it is an equal mass system. The results do not appear overly optimistic for the chances of detection. BSk22 appears the most promising candidate, suggesting g_1 could be detectable for $M < 1.5M\odot$ and g_2 detectable for $M < 1.4M\odot$. The other three BSk models are continually below the curve, with BSk26 having the lowest values. These results do indicate that the lower mass systems are preferred

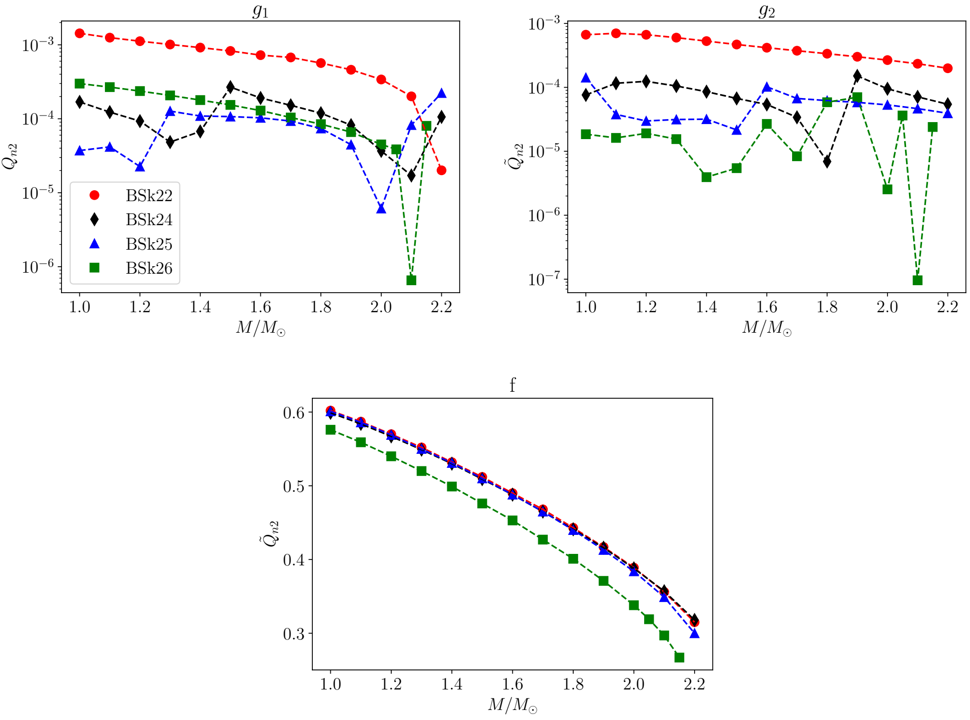

FIGURE 6.3: Plot of dimensionless overlap $\tilde{Q}$ vs total mass energy M for the fundamental f-mode and first 2 g-modes for background neutrons star using the BSk family of equations of state, specifically: BSk22; BSk24; BSk25 and BSk26.

There are caveats to this results, namely the assumptions of equal mass systems and use of Newtonian tidal potential, but BSk22 does provide hope of detection for future detectors.

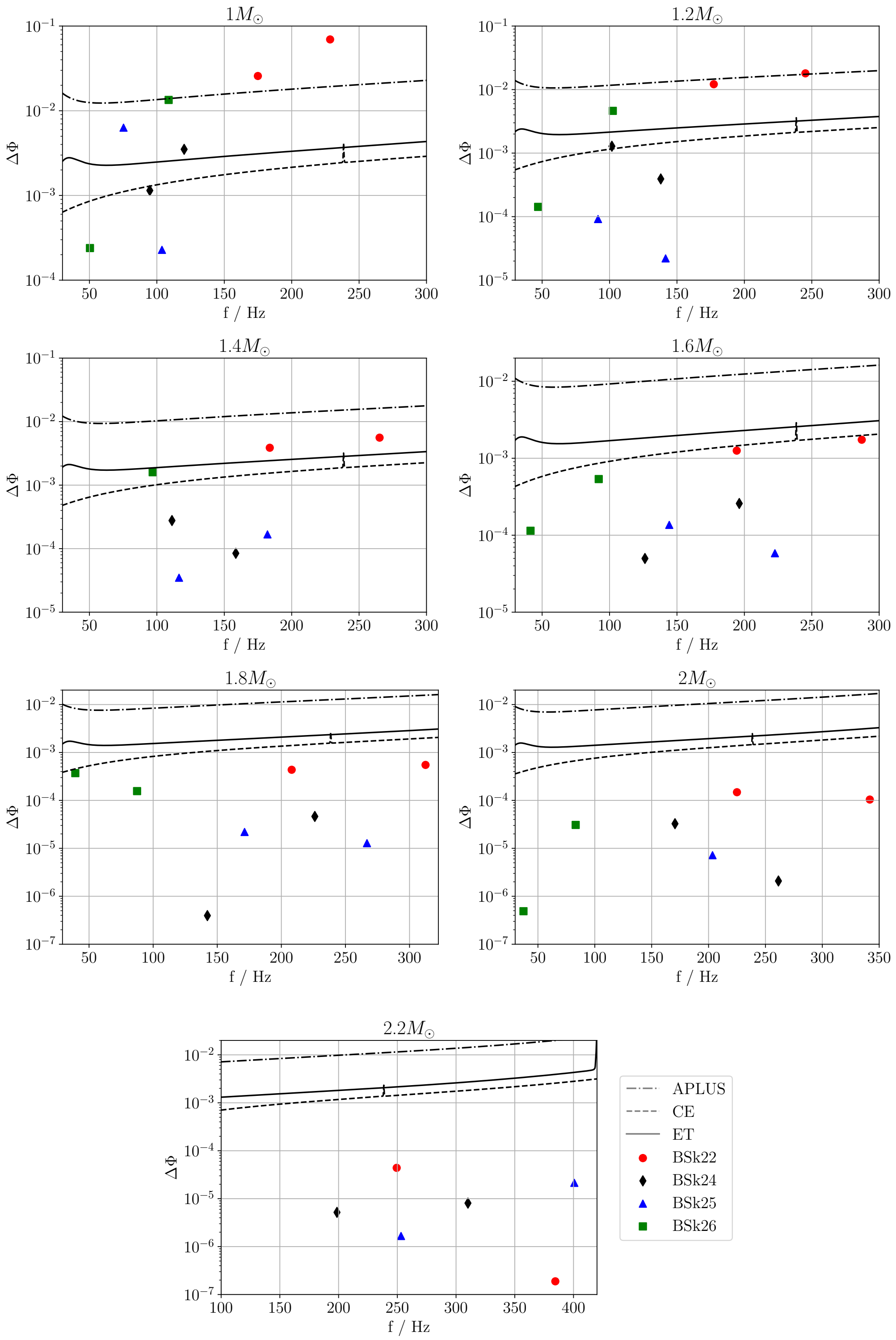

FIGURE 6.4: Plot of detectable shift in orbital phase $\Delta\Phi(f)$ (6.9) vs frequency for the first two core g-modes for the BSk22-26 equations of state. The curves are upper limits calculated using $\Delta\Phi$ from (6.11) for LIGO A+ (long-dashed), the Einstein Telescope (ET; solid) and Cosmic Explorer (CE; short-dashed). Each plot is labelled by the mass energy M of each individual neutron star. All the binaries are assumed to be equal mass systems and located 40Mpc from the detectors.

TABLE 6.2: The dimensionless mode frequencies are shown for different $l = 2$ modes for the four BSk equations of state for various total mass energies M. Also calculated is the dimensionless overlap integral Q_{n2} for each mode using (6.25)

M	Mode	BSk22		BSk24		BSk25		BSk26	
		$\tilde{\omega}_n$	$\tilde{Q}_{n2}$	$\tilde{\omega}_n$	$\tilde{Q}_{n2}$	$\tilde{\omega}_n$	$\tilde{Q}_{n2}$	$\tilde{\omega}_n$	$\tilde{Q}_{n2}$
1	f	1.576	0.441	1.568	0.4371	1.559	0.438	1.555	0.426
	g_1	0.1853	9.97e-4	0.09134	9.28e-5	0.07641	3.24e-5	0.07595	8.88e-5
	g_2	0.1418	2.95e-4	0.07199	4.62e-5	0.05542	4.77e-5	0.03519	3.82e-6
1.1	f	1.536	0.433	1.526	0.430	1.517	0.431	1.512	0.418
	g_1	0.1832	9.10e-4	0.09275	9.50e-5	0.08687	3.63e-5	0.07028	7.51e-5
	g_2	0.1362	3.22e-4	0.07196	6.24e-5	0.05623	2.62e-5	0.03239	2.60e-6
1.2	f	1.500	0.425	1.489	0.422	1.480	0.423	1.473	0.409
	g_1	0.1822	8.38e-4	0.09658	7.49e-5	0.09641	1.92e-5	0.06536	6.30e-5
	g_2	0.1317	3.26e-4	0.07120	6.66e-5	0.06228	2.14e-5	0.03002	3.13e-6
1.3	f	1.466	0.416	1.454	0.414	1.446	0.414	1.437	0.399
	g_1	0.1820	7.74e-4	0.1006	3.81e-5	0.1071	1.09e-4	0.06100	5.26e-5
	g_2	0.1284	3.16e-4	0.07111	6.17e-5	0.06828	2.24e-5	0.02797	2.26e-6
1.4	f	1.435	0.406	1.422	0.404	1.414	0.404	1.403	0.387
	g_1	0.1822	7.14e-4	0.10325	4.44e-5	0.11569	9.52e-5	0.05708	4.33e-5
	g_2	0.1263	2.98e-4	0.07242	5.30e-5	0.07400	2.27e-5	0.02617	3.27e-6
1.5	f	1.405	3.95e-1	1.392	0.393	1.384	0.393	1.370	0.375
	g_1	0.1827	6.52e-4	0.1157	2.12e-4	0.1242	9.41e-5	0.05349	3.54e-5
	g_2	0.1249	2.77e-4	0.07433	4.39e-5	0.07932	1.50e-5	0.02409	7.32e-7
1.6	f	1.377	3.83e-1	1.363	0.381	1.354	0.381	1.337	0.362
	g_1	0.1832	5.69e-4	0.1194	1.63e-4	0.1325	9.15e-5	0.05018	2.83e-5
	g_2	0.1240	2.55e-4	0.07682	3.60e-5	0.08587	6.72e-5	0.02258	2.57e-6
1.7	f	1.348	3.71e-1	1.334	0.369	1.326	0.368	1.305	0.347
	g_1	0.1845	5.41e-4	0.1238	1.32e-4	0.1406	8.29e-5	0.04705	2.25e-5
	g_2	0.1236	2.35e-4	0.07915	2.24e-5	0.09043	4.72e-5	0.02115	2.03e-6
1.8	f	1.319	3.57e-1	1.305	0.355	1.296	0.354	1.271	0.331
	g_1	0.1850	4.68e-4	0.1286	1.05e-4	0.1484	6.63e-5	0.04406	1.76e-5
	g_2	0.1232	2.15e-4	0.08084	4.00e-6	0.09528	4.44e-5	0.01978	3.52e-6
1.9	f	1.289	3.42e-1	1.275	0.340	1.266	0.339	1.235	0.313
	g_1	0.1856	3.86e-4	0.1330	7.32e-5	0.1561	4.03e-5	0.04112	1.26e-5
	g_2	0.1229	1.96e-4	0.08856	8.95e-5	0.10002	4.17e-5	0.01845	2.48e-7
2	f	1.257	3.25e-1	1.244	0.324	1.234	0.321	1.196	0.292
	g_1	0.1860	2.91e-4	0.1376	3.34e-5	0.1637	5.51e-6	0.03811	8.65e-6
	g_2	0.1224	1.77e-4	0.08972	6.53e-5	0.1046	3.84e-5	0.01709	2.47e-6
2.1	f	1.222	3.04e-1	1.209	0.304	1.197	0.299	1.146	0.265
	g_1	0.1860	1.76e-4	0.1422	1.53e-5	0.1715	7.68e-5	0.04202	7.11e-7
	g_2	0.1217	1.57e-4	0.09176	5.04e-5	0.10917	3.39e-5	0.02738	2.60e-7
2.2	f	1.176	2.78e-1	1.166	0.279	1.144	0.267		
	g_1	0.1853	1.82e-5	0.1467	1.01e-4	0.18066	2.15e-4		
	g_2	0.1202	1.37e-4	0.09393	3.95e-5	0.11414	2.93e-5		

Chapter 7

The Effective Love Number

A key difference between neutron stars and black holes is that neutron stars are extended material objects, therefore gravitational interactions with other bodies can depend on said material and how it tidally deforms. In the example of binary neutron star inspirals, this deformability causes finite size corrections to the gravitational wave signal produced by the system compared to one from binary black hole inspirals. Since the advent of gravitational wave astronomy several mergers from binary systems have been detected and while the majority have been black holes systems there has been some neutron star - neutron star systems such as the previously mention GW170817 and even some neutron star - black holes systems (Abbott et al., 2021). Measurements of these systems provide opportunities to constrain the internal structure and physics of the materials involved and thus provide more information on the equation of state.

The finite size effects are parametrised by tidal Love number, k_{lm} (Hinderer, 2008). It is defined as

$$\delta\Phi_{lm} = 2k_{lm}\chi_{lm}, \tag{7.1}$$

where quantities are defined at the surface and χ_{lm} is the tidal potential associated with the binary companion.

7.1 Newtonian

Works such as (Lai, 1994; Pnigouras et al., 2022), have shown that an effective Love number can be calculated from a sum over the stellar oscillations, where each oscillation mode provides a contribution to the tidal perturbation. They have generated expressions for k_{lm} for stationary, rotating and slowly rotating neutron stars in Newtonian gravity which will be defined below.

7.1.1 Mode-Sum

The tide raised by a binary companion (here treated as a point particle) induces a linear response in the primary. Provided the tidal influence is weak enough that the response can be treated perturbatively the problem can be linearised and hence different solutions to the perturbation equations can be added. We will assume this is the case in the work below where we follow the approach from Pnigouras et al. (2022).

7.1.1.1 Non-Rotating Stars

The perturbation in the fluid of the primary star—taken to have mass $M_\star$ and radius R—can be represented by the Lagrangian displacement ξ_i. If the background star is in hydrostatic equilibrium, the displacement satisfies

$$\partial_t^2 \xi_i + \frac{1}{\rho}\nabla_i \delta p - \frac{1}{\rho^2}\delta\rho \nabla_i p + \nabla_i \delta\Phi = -\nabla_i \chi \ . \tag{7.2}$$

We also have the Poisson equation for the star's gravitational potential $\delta\Phi$:

$$\nabla^2 \delta\Phi = 4\pi G \delta\rho \ , \tag{7.3}$$

where $\delta\rho$ is the perturbed mass density, the continuity equation for mass conservation, which leads to

$$\delta\rho = -\nabla_i \left(\xi^i\right) , \tag{7.4}$$

and an equations of state of form (assuming that the star is cold enough that thermal effects can be ignored) $p = p(\rho, Y_\mathrm{e})$. If the matter is in equilibrium then the lepton fraction Y_e can be determined as a function of ρ and the equation of state reduced to a single parameter functional.

The tidal potential due to the presence of the binary partner (which generates the fluid perturbation) is given by a solution to $\nabla^2 \chi = 0$. In a coordinate system centred on the primary, we have

$$\chi = -\frac{GM'}{|\boldsymbol{r} - \boldsymbol{D}(t)|} = -GM' \sum_{l \geq 2} \sum_{m=-l}^{l} \frac{W_{lm} r^l}{D^{l+1}(t)} Y_{lm} e^{-im\psi(t)} \ , \tag{7.5}$$

where M' is the mass of the secondary. The orbit of the companion has been taken to be in the plane $[D(t), \pi/2, \psi(t)]$ where D is the binary separation and ψ is the orbital phase. It should also be noted that the W_{lm} coefficients vanish for all odd $l + m$. In the following, the binary orbit is taken to be quasi-circular, in the sense that the inspiral evolves much more slowly than the orbital motion, that is

$$\frac{1}{D}\left|\frac{dD}{dt}\right| \ll \Omega_\mathrm{orb}, \tag{7.6}$$

with $\Omega_{\rm orb}$ denoting the orbital frequency. To leading order, the orbital separation evolves due to the emission of gravitational waves as

$$\frac{dD}{dt} = -\frac{64G^3}{5c^2}\frac{M_* M'(M_* + M')}{D^3} \tag{7.7}$$

and the phase evolves as

$$\frac{d\psi}{dt} = \Omega_{\rm orb} = \sqrt{\frac{G(M_* + M')}{D^3}}. \tag{7.8}$$

We want to work out the deformation of the primary induced by the companion's tidal field. In essence, we are looking for a solution to (7.2), (7.3) and (7.4) given some equation of state $p(\rho)$ and the specific form for χ.

As we have discussed previously, we will assume harmonic solutions for our eigenfunctions (2.13). In the absence of dissipation, ξ_i can be expressed as a sum over all the possible modes of the star

$$\xi^i(t, x^i) = \sum_n a_n(t)\xi^i_n(x^i). \tag{7.9}$$

where the mode amplitude a_n is given by

$$a_n = \frac{1}{\mathcal{A}_n^2}\langle\xi_n, \xi\rangle \tag{7.10}$$

where, as in previous chapters, the inner product is defined by (4.94) and $\mathcal{A}$ is the normalisation given by (4.100). As the eigenvalue is ω_n^2, the mode solutions of a non-rotating star are independent of the sign of the mode frequency. Also, as we have shown in previous chapter when discussing the Cowling approximation these mode solutions are orthogonal, which we require for the mode sum to be able to represent a real-valued function. Therefore, in order to obtain a complete basis we can restrict ourselves to solutions with $\omega_n \geq 0$ from now on. To be specific, one can show that, despite working with complex eigenfunctions as the basis vectors in the mode expansion (7.9), the physical perturbation ξ^i_n is real. This is most easily seen by considering mode pairs $(m, -m)$ which have the same eigenfrequency ω_n. These pairs combine in the mode summation to exactly cancel the imaginary parts. That this is the case should not be surprising since the field (7.5) that sources the perturbation is real. Additionally, when we discuss the rotating case later on, we need to be careful as each of the non-rotating modes split in two and we need to pay attention to the resulting change in the symmetry of the mode frequencies. As ξ^i is sourced by the tidal field of companion, inserting (7.9) into (7.2)

$$\ddot{a}_n + \omega_n^2 \dot{a}_n = -\frac{1}{\mathcal{A}_n^2}\langle\xi_n, \nabla\chi\rangle, \tag{7.11}$$

We then define the overlap integral

$$Q_n = -\langle\xi_n, \nabla\chi\rangle = -\int \delta\rho_n^* \chi dV, \tag{7.12}$$

where the last step was arrived at through integration by parts and $\delta\rho_n$ is the density perturbation associated with the mode as shown in previous chapters. As before all the perturbed variables are expanded in terms of spherical harmonics, thus

$$Q_n = K_{lm} I_n e^{-im\Omega_{\rm orb}t}, \tag{7.13}$$

where

$$K_{lm} = \frac{GM'W_{lm}}{D^{l+1}}, \tag{7.14}$$

and the mass-multipole moment for an individual mode is defined as

$$I_n = \int_0^R \delta\rho_n(r) r^{l+2} dr. \tag{7.15}$$

Now, each mode is driven by the tidal field at a frequency $m\Omega_{\rm orb}$ and provided the orbital motion does not resonantly excite the mode,

$$a_n(t) = \frac{K_{lm} I_n}{\mathcal{A}_n^2 \left[\omega_n^2 - (m\Omega_{\rm orb})^2\right]} e^{-im\Omega_{\rm orb}t} \tag{7.16}$$

This means that each mode n carries an (l, m) dependence and will be excited by the corresponding (l, m) component of the tidal field. However, note that the tidal forcing is only non-zero for even $l + m$, so modes with odd $l + m$ will not be excited as per the definition of W_{lm}. Now we can move on to calculating the love number itself k_{lm} (7.1) which is evaluated at the stellar surface. The (l, m) component of the tidal field is

$$\chi_{lm} = -K_{lm} r^l e^{-im\Omega_{\rm orb}t}. \tag{7.17}$$

Moving from the star to the vacuum exterior, the perturbed gravitational potential of the star is related to the multipole moments that characterise the departure from the equilibrium shape. Thus, for a given mode

$$\delta\Phi_n(R) = -\frac{4\pi G}{(2l+1)R^{l+1}} I_n. \tag{7.18}$$

Given that $\delta\Phi$ can be decomposed similarly to (7.9) and using (7.16)

$$\delta\Phi(t, R, \theta, \varphi) = -4\pi G \sum_n \frac{1}{(2l+1)R^{l+1}} \frac{I_n^2}{\mathcal{A}_n^2 \left[\omega_n^2 - (m\Omega_{\rm orb})^2\right]} K_{lm} e^{-im\Omega_{\rm orb}t} Y_l^m(\theta, \varphi). \tag{7.19}$$

To identify the contribution of a certain harmonic (l, m) of the gravitational potential, we introduce some further notation at this point. We use the label α' to denote the set of modes α' belonging to a given (l, m). Each subset of modes with fixed (l, m) would then include modes from different classes and overtones, thus

$$\delta\Phi_{lm} = -\frac{4\pi G}{(2l+1)R^{l+1}} K_{lm} e^{-im\Omega_{\rm orb}t} \sum_{\alpha'} \frac{I_{\alpha'}^2}{\mathcal{A}_{\alpha'}^2 \left[\omega_{\alpha'}^2 - (m\Omega_{\rm orb})^2\right]}. \tag{7.20}$$

Therefore the effective love number is

$$k_{lm} = \frac{2\pi G}{(2l+1)R^{l+1}} \sum_{\alpha'} \frac{I^2_{\alpha'}}{\mathcal{A}^2_{\alpha'}\left[\omega^2_{\alpha'} - (m\Omega_{\text{orb}})^2\right]}, \tag{7.21}$$

and the static Love number is then (in the limit $\Omega \longrightarrow 0$) is

$$k_{lm} = \frac{2\pi G}{(2l+1)R^{l+1}} \sum_{\alpha'} \frac{I^2_{\alpha'}}{\mathcal{A}^2_{\alpha'}\omega^2_{\alpha'}}. \tag{7.22}$$

Note, in most of the literature, the name Love number is used for the tidal deformation due to a static external field. In this work, we will use static Love number to mean (7.22), and just Love number or effective Love number for the general case of a time-varying tidal field, representing the dynamical tide (7.21).

7.1.1.2 Rotating Stars

Let us move on to the more general case of a rotating star. The issue is complicated by the cross coupling of the l-multipoles that arises from the rotation and there has previously been confusion surrounding the orthogonality of the modes (Lai, 1997; Ho and Lai, 1999). Looking at the equations, now using (2.10), the perturbed Euler equations take the form

$$\begin{aligned}\mathcal{A}^2_\alpha \ddot{a}_\alpha + i\left(\mathcal{B}_\alpha - 2\omega_\alpha\mathcal{A}^2_\alpha\right)\dot{a}_\alpha + \omega_\alpha\left(\mathcal{B}_\alpha - \omega_\alpha\mathcal{A}^2_\alpha\right)a_\alpha &= \\ Q_\alpha - \sum_{\beta\neq\alpha}\left[\ddot{a}_\beta - i\omega_\beta\dot{a}_\beta - i\omega_\alpha\left(\dot{a}_\beta - i\omega_\beta a_\beta\right)\right]&\langle\xi_\alpha,\xi_\beta\rangle.\end{aligned} \tag{7.23}$$

As the inner product $\langle\xi_\alpha,\xi_\beta\rangle$ does not vanish for the modes of a rotating star, this equation leads to a coupling of all the equations of motion of different modes. One can get around this issue by using a phase space expansion of the form Schenk et al. (2001)

$$\begin{bmatrix}\xi^i(t,x^i)\\ \partial_t\xi^i(t,x^i)\end{bmatrix} = \sum_\alpha\left\{c_\alpha(t)\begin{bmatrix}\xi^i_\alpha(t,x^i)\\ i\omega_\alpha\xi^i_\alpha(t,x^i)\end{bmatrix} + c^*_\alpha(t)\begin{bmatrix}\xi^{i*}_\alpha(t,x^i)\\ -i\omega_\alpha\xi^{i*}_\alpha(t,x^i)\end{bmatrix}\right\}, \tag{7.24}$$

where

$$c_\alpha = \frac{1}{\mathcal{B}_\alpha}\langle\xi_\alpha, \omega_\alpha\xi - i\partial_t\xi - iB\xi\rangle. \tag{7.25}$$

One can follow a similar method as in the non-rotating case, for brevity we will skip to the final result but one can find the details in Pnigouras et al. (2022). The effective Love number is

$$k_{lm} = \frac{2\pi G}{(2l+1)R^{l+1}}\frac{1}{K_{lm}}\sum_{l'}K_{l'm}\left[\sum_{\alpha'}\frac{I_{\alpha'l'}I_{\alpha'l}}{\mathcal{B}^2_{\alpha'}\left(\omega_{\alpha'} + m\bar{\Omega}\right)} + \sum_{\beta'}\frac{I_{\beta'l'}I_{\beta'l}}{\mathcal{B}^2_{\beta'}\left(\omega_{\beta'} - m\bar{\Omega}\right)}\right], \tag{7.26}$$

where first term corresponds to the mode (ω'_α, m), the second is its partner $(\omega'_\beta, -m)$ moving in the opposite direction and $\bar{\Omega} = \Omega_{\text{orb}} - \Omega$, where Ω is the rotational frequency of the neutron star. As a sanity check, in the non-rotating limit, $\Omega = 0$, each mode is characterised by a single degree l', so the only term retained in the sum over l' is the one for which $l' = l$. Furthermore, the mode pairs $(m, -m)$ have the same eigenfrequency ($\omega_{\alpha'} = \omega_{\beta'}$) and multipole moment ($I_{\alpha'} = I_{\beta'}$), whereas $\mathcal{B}_{\alpha'} \to 2\omega_{\alpha'}\mathcal{A}^2_{\alpha'}$. Thus, (7.26) reduces to (7.21).

7.1.1.3 Slow-Rotation Approximation

While (7.26) is valid for arbitrary rotation rates, in practice solving the mode equation for the eigenfunctions is difficult. As well as the modes no longer coupling to single spherical harmonics the rotation also deforms the background star away from spherical symmetry. Additionally a new subset of oscillation modes arise due to the Coriolis force, known as the inertial modes (Lockitch and Friedman, 1999). Therefore, in order to proceed analytically the slow-rotation approximation that was mentioned in previous chapters is used again. As before we can expand the variables to first order in rotation as in (2.53) where even though the degeneracy in m is lifted there is no cross coupling of the l-multipoles. As before, the method to find the love number is similar but for brevity we will simply show the final result with the full details found in Pnigouras et al. (2022). To first order in rotation, the effective Love number is

$$k_{lm} = \frac{2\pi G}{(2l+1)R^{2l+1}} \sum_{\alpha'} \frac{I^{(0)2}_{\alpha'}}{\mathcal{A}^{(0)2}_{\alpha'}[\omega^{(0)2}_{\alpha'} - (m\Omega_{\text{orb}})^2]} \Bigg[1 + 2m\Omega_{\text{orb}} \left(\frac{(C_{\alpha'} - 1)m\Omega}{\omega^{(0)2}_{\alpha'} - (m\Omega)^2} - \frac{\tilde{I}^{(1)}_{\alpha' l}}{\omega^{(0)}_{\alpha'} I^{(0)}_{\alpha'}} \right) \Bigg] + O(\Omega^2), \quad (7.27)$$

where

$$\mathcal{A}^{(1)}_{\alpha} = 2\int_0^R \left[W^{(0)}_{\alpha l} W^{(1)}_{\alpha l} + l(l+1) V^{(0)}_{\alpha l} V^{(1)}_{\alpha l} \right] \rho\, dr, \quad (7.28)$$

$$\tilde{I}^{(1)}_{\alpha l} = I^{(1)}_{\alpha} - \frac{\mathcal{A}^{(1)}_{\alpha}}{2\mathcal{A}^{(0)2}_{\alpha}} I^{(0)}_{\alpha}, \quad (7.29)$$

and C_α is the first order correction to the mode frequency from (2.57). One can see from this that in the static limit where $\Omega_{\text{orb}} = 0$, this equation collapses down to (7.22) at first order in Ω

$$k_{lm} = \frac{2\pi G}{(2l+1)R^{2l+1}} \sum_{\alpha'} \frac{I^{(0)2}_{\alpha'}}{\mathcal{A}^{(0)2}_{\alpha'} \omega^{(0)2}_{\alpha'}} + O(\Omega^2). \quad (7.30)$$

As we can see from (7.27) and (7.30) the effective Love number is affected by the star's rotation at first order but the static Love number will only be affected at second order.

Using the mode calculations from the previous chapters, the values for k_{lm} can be obtained numerically. Shown in Fig. 7.1 are values for the effect Love number for $l = m = 2$ for both a stationary and slowly rotating neutron star with $\Omega = 100\,\text{Hz}$. The values are plotted against different orbital frequencies. As can be seen in the graphs the values agree when $\Omega_{\text{orb}} = 0$ and agree with the theoretical value of $k_2 \approx 0.2599$ from Poisson and Will (2014). The calculation

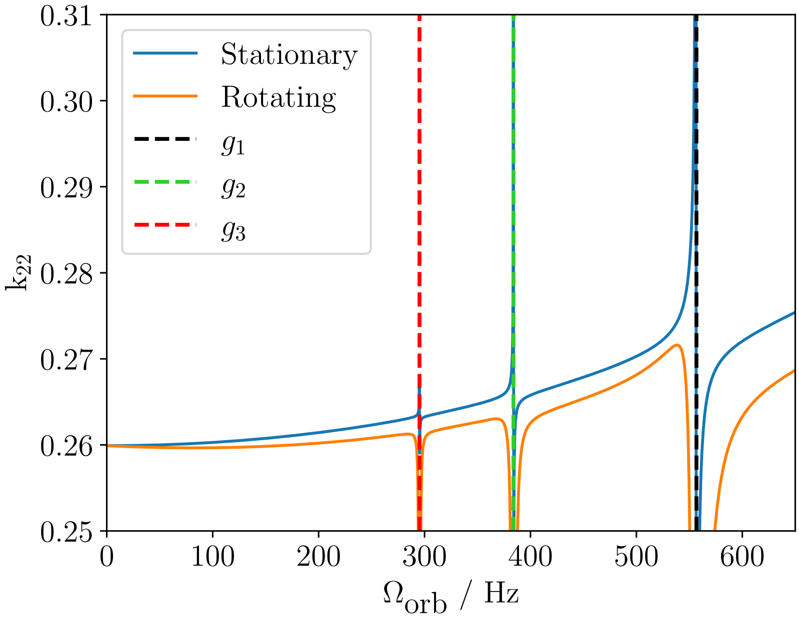

FIGURE 7.1: Plot of the effective Love $k_{2,2}$ against orbital frequency for both a stationary neutron star (blue) and a slowly rotating star with $\Omega = 100\,\mathrm{Hz}$ (orange). The calculation is truncated as only 6 modes are calculated : f; p_1; p_2; g_1; g_2 and g_3. The singularities associated with the three g-modes included in the calculation are prominent.

is however truncated as only 6 modes are calculated : f; p_1; p_2; g_1; g_2 and g_3. While this reduces the accuracy of the results, as the f-mode is dominant compared to the others it produces the largest contribution to k_{22} and therefore only a handful of additional modes are needed to approach the limiting value. Stratification however does not affect this calculation which is not entirely unsurprising as the f-mode provides the dominant contribution and is largely unaffected by stratification. As long as the summations over the modes are complete the results should agree with one another and default to the barotropic value. A common feature of both (7.21) and (7.27) is that the equations blow up when $\omega_\alpha \approx |m|\Omega_{\mathrm{orb}}$. This corresponds to a mode being resonantly excited by the tidal potential. A more careful analysis would be needed at those frequencies, see recent work by Hegade K. R. et al. (2024); Yu et al. (2024b); Pnigouras et al. (2025b).

7.2 Alternative Approach

This section spells out an equivalent way to formulate the Newtonian tidal problem in the vacuum exterior of the star. For this discussion, no assumption about the matter needs to be made. The tidal problem is illustrated in Fig. 7.2. Firstly, the binary problem can be separated into a near-zone and a wave-zone. In the latter, gravitational perturbations are represented by waves. Meanwhile, in the near-zone, where the two bodies reside, the gravitational perturbation can be viewed as slowly varying. Secondly, as long as the binary separation is large enough, the

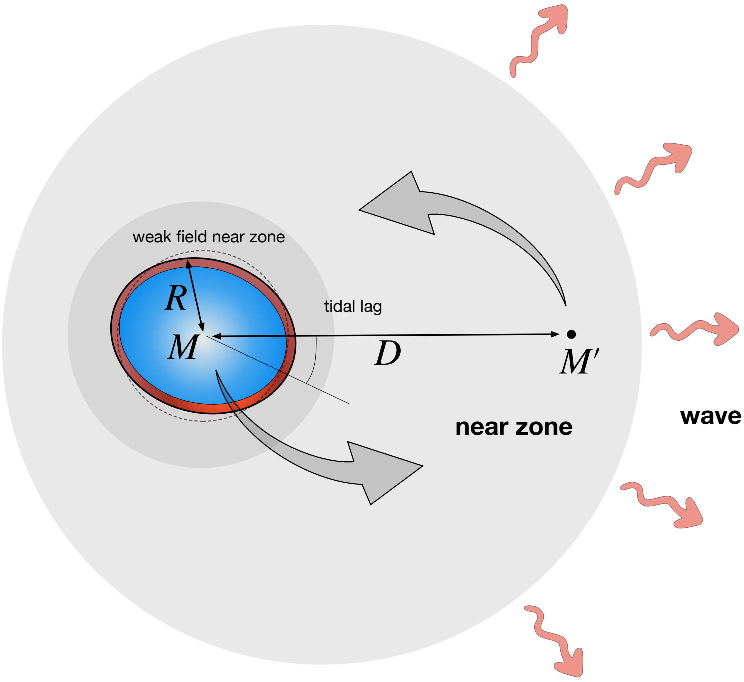

FIGURE 7.2: A schematic illustration of the tidal problem. A star of mass M and radius R a distance D from its companion of mass M'. The near zone is indicated as the region encompassing the two bodies, with the weak field near zone indicating the region around the star where the tidal interaction is weak enough to be treated perturbatively. The wave zone corresponds to the region far from the binary where the gravitational perturbation is represented by waves.

tidal interaction can be adequately described perturbatively. In essence, each star is tidally deformed by the presence of the binary partner but it is assumed that the interaction is weak enough that it induces a suitably small perturbation (e.g., linear) of star's equilibrium state. This then defines the weak-field near zone (indicated in Fig. 7.2). This region is key to the argument we will develop. In full generality, we have the Newtonian field equation for this interaction

$$\nabla^2(\Phi + \chi) = 4\pi G\rho. \tag{7.31}$$

In this expression, we are limiting our examination to the region of space enveloping the tidally distorted star. The external potential χ will be sourced by a remote distribution of matter. We now make the assumption that χ is weak, such that at leading order the star is spherically symmetric and satisfies

$$\nabla^2\Phi = 4\pi G\rho \qquad \Longrightarrow \qquad \Phi = -\frac{GM}{r}. \tag{7.32}$$

The tidal deformation of the star is therefore described by a perturbation on top of this equilibrium given by

$$\nabla^2 U = 4\pi G\delta\rho, \tag{7.33}$$

where $U = \delta\Phi + \chi$. Now, we focus our attention on the vacuum exterior outside the tidally deformed star, but still far away enough from the companion for the tidal field to be a perturbation. In essence, we operate in the weak-field near zone. In this region, given by $r \geq R$, the linearised field equation reduces to Laplace's equation

$$\nabla^2 U = 0, \tag{7.34}$$

which has the general solution

$$U(t,r,\theta,\phi) = \sum_{l,m} U_l(t,r) Y_l^m(\theta,\phi), \qquad U_l = \frac{U_l^1}{r^{l+1}} + U_l^2 r^l. \tag{7.35}$$

At this point, we comment on how the combined potential U separates neatly into a decaying component, which we identify with

$$\delta\Phi_l = \frac{U_l^1}{r^{l+1}}, \tag{7.36}$$

and a growing component, defined as

$$\chi_l = U_l^2 r^l. \tag{7.37}$$

There are no surprises here: $\delta\Phi_l$ is the gravitational potential of the tidally distorted star and χ_l is the tidal potential arising from the companion. That these terms can be decoupled is due to the fact that the Newtonian field equation is linear.

This example may seem somewhat contrived since we, from the outset, assumed that these two potentials entered the problem in a linear fashion. However, it is useful to observe that the vacuum field equation (7.34) automatically provides the two separate solutions.

In the exterior we can now write

$$U = \sum_{l,m} \left[2k_l \left(\frac{R}{r} \right)^{2l+1} + 1 \right] \chi_l Y_l^m, \tag{7.38}$$

7.2.1 Dynamical tides

Notice that the expressions we have provided so far apply to dynamical contexts. We have placed no explicit restriction on the time dependence of the tidal field. For slowly evolving, circular motion it then follows immediately that $\omega = m\Omega$, with Ω the Keplerian orbital frequency. Here, we will work in the frequency domain and denote variables that depend on the driving frequency ω by hats.

It is convenient to note the following relations:

$$l\hat{U}_l - r\partial_r \hat{U}_l = (2l+1)\delta\hat{\Phi}_l, \tag{7.39}$$

$$(l+1)\hat{U}_l + r\partial_r \hat{U}_l = (2l+1)\hat{\chi}_l. \tag{7.40}$$

Evaluating these relations at the surface of the star and using (7.1), we arrive at

$$2k_l(\omega) = \frac{l}{l+1}\left[1 - \frac{1}{l}\frac{R\partial_r \hat{U}_l(\omega, R)}{\hat{U}_l(\omega, R)}\right]\left[1 + \frac{1}{l+1}\frac{R\partial_r \hat{U}_l(\omega, R)}{\hat{U}_l(\omega, R)}\right]^{-1} . \tag{7.41}$$

This expression provides the effective, frequency dependent, Love number. This equation implies the following strategy. One numerically integrates the standard perturbation equations (2.22) - (2.24) for the interior with a given ω, where $\delta\hat{\Phi}_l$ may be replaced with $\hat{U}_l$ since they enter the problem in the same way. The boundary conditions at the centre of star come from the usual regularity considerations and the Lagrangian pressure perturbation must still vanish at the surface as in (2.27) (2.28) and (2.30). (The perturbation equations are usually reduced to a fourth-order system.) For a given ω, this leaves the problem specified up to an amplitude and the Love number is computed via (7.41). It is instructive to note that, in the absence of a tidal field $\hat{\chi}_l = 0$, (7.40) provides the final boundary condition needed to fix ω which is (2.29). In this way, ω becomes an eigenfrequency of the star. Also, as a sanity check, it is worth keeping in mind that the expression in (7.41) must limit to the usual Love number of the static ($\omega \to 0$) limit, as we will verify below.

The main advantage of this method is that we are notably not relying on the perturbation equation being Hermitian or involving an explicit mode sum. This will become more important when we extend the analysis to general relativity later.

7.2.2 Proof of Principle

Let us put the proposed new strategy to the test.

7.2.2.1 Incompressible star

As a first proof-of-principle calculation, we consider the case of an incompressible star. We then have $\Delta\hat{p} = 0$ and $\nabla_i \rho = 0$, which means that the continuity equation reduces to

$$\nabla_i \hat{\xi}^i = 0 . \tag{7.42}$$

Moreover

$$\delta\hat{p} = \Delta\hat{p} - \hat{\xi}^j \nabla_j \rho \Longrightarrow \delta\hat{p} = 0 . \tag{7.43}$$

The Euler equation then simplifies to

$$-\omega^2 \hat{\xi}_i + \nabla_i \left(\frac{\delta\hat{p}}{\rho}\right) + \nabla_i \hat{U} = 0 , \tag{7.44}$$

while the Poisson equation becomes

$$\nabla^2 \hat{U} = 0 . \tag{7.45}$$

It is easy to see that (7.42) implies that

$$\nabla^2 \delta\hat{p} = 0 \,. \tag{7.46}$$

Expanding the perturbations in spherical harmonics and introducing notation such that (omitting the m label on the different quantities for clarity)

$$\hat{U} = \sum_l \hat{U}_l Y_{lm} \,, \tag{7.47}$$

and similar for other perturbed quantities, the solution to the radial part of Laplace's equation for a given value of l can be written (suppressing the indices on the coefficients, which should not cause confusion)

$$\hat{U}_l = \hat{c} r^l + \frac{\hat{d}}{r^{l+1}} \,. \tag{7.48}$$

In the stellar interior, the regular solution is

$$\hat{U}_l = \hat{c} r^l \,. \tag{7.49}$$

Similarly, we have

$$\delta\hat{p}_l = \hat{b} r^l \,. \tag{7.50}$$

The radial component of (7.44) leads to (after using the orthogonality of the spherical harmonics and using primes for radial derivatives)

$$-\omega^2 \hat{\xi}_l + \frac{1}{\rho}\delta\hat{p}_l' + \hat{U}_l' = 0, \tag{7.51}$$

(here and in the following, we take $\hat{\xi}_l$ to represent the radial component of the displacement). This means that we have

$$\omega^2 \hat{\xi}_l = \left(\frac{1}{\rho}\hat{b} + \hat{c}\right) l r^{l-1}. \tag{7.52}$$

The Lagrangian variation of the pressure must vanish at the surface, so

$$\Delta\hat{p} = \delta\hat{p} + \hat{\xi}^j \nabla_j p = 0 \quad \Longrightarrow \quad \hat{b} r^l + \hat{\xi}_l p' = 0 \quad \text{at } r = R. \tag{7.53}$$

Using hydrostatic equilibrium for the unperturbed star

$$p' = -\rho\Phi' = -\frac{GM_\star \rho}{R^3} r, \tag{7.54}$$

we have

$$\hat{b} R^l - \hat{\xi}_l \frac{GM_\star \rho}{R^2} = 0 \Longrightarrow \frac{\hat{b} R^{l-1}}{\rho} = \hat{\xi}_l \frac{GM_\star}{R^3}. \tag{7.55}$$

At the surface of the star, it follows that

$$\left(\omega^2 - \frac{GM_\star l}{R^3}\right)\hat{\xi}_l(R) = \hat{c}lR^{l-1}, \tag{7.56}$$

or

$$\hat{c} = \frac{1}{lR^{l-1}}\left(\omega^2 - \frac{GM_\star l}{R^3}\right)\hat{\xi}_l(R). \tag{7.57}$$

Next, we need to ensure that the perturbed (total) gravitational potential $\hat{U}$ and its derivative are continuous at the surface. (However, the tidal potential is already continuous, so we could focus on Φ_l.) For a general frequency, the exterior solution will be given by (7.48) so we have

$$U_l^{\text{in}}(R) = U_l^{\text{out}}(R) = \hat{c}_R R^l + \frac{\hat{d}}{R^{l+1}}. \tag{7.58}$$

Meanwhile, the derivative of the potential must satisfy (remembering that the density is not continuous at the surface in this model problem)

$$(U_l^{\text{in}})'(R) = lR^{l-1}\hat{c}_R - (l+1)\frac{d}{R^{l+2}} - 4\pi G\rho\xi_l(R). \tag{7.59}$$

These two conditions lead to

$$\hat{c} = \hat{c}_R + \frac{\hat{d}}{R^{2l+1}}, \tag{7.60}$$

and

$$\hat{c} = \hat{c}_R - \frac{l+1}{l}\frac{\hat{d}}{R^{2l+1}} - \frac{4\pi G\rho}{lR^{l-1}}\hat{\xi}_l(R). \tag{7.61}$$

We see that we must have

$$\frac{\hat{d}}{R^{2l+1}} = -\frac{l+1}{l}\frac{\hat{d}}{R^{2l+1}} - \frac{4\pi G\rho}{lR^{l-1}}\hat{\xi}_l(R), \tag{7.62}$$

or

$$\hat{d} = -\frac{4\pi G\rho R^{l+2}}{2l+1}\hat{\xi}_l(R), \tag{7.63}$$

It then follows that

$$\hat{c}_R = \hat{c} - \frac{\hat{d}}{R^{2l+1}} = \hat{c} + \frac{4\pi G\rho}{(2l+1)R^{l-1}}\hat{\xi}_l(R), \tag{7.64}$$

or, making use of the result for c:

$$\begin{aligned}
\hat{c}_R &= \frac{1}{lR^{l-1}}\left(\omega^2 - \frac{GM_\star l}{R^3}\right)\hat{\xi}_l(R) + \frac{4\pi G\rho}{(2l+1)R^{l-1}}\hat{\xi}_l(R) \\
&= \frac{1}{lR^{l-1}}\left(\omega^2 - \frac{GM_\star l}{R^3}\right)\hat{\xi}_l(R) + \frac{3GM_\star}{(2l+1)R^{l+2}}\hat{\xi}_l(R) \\
&= \frac{1}{lR^{l-1}}\left[\omega^2 - \frac{GM_\star}{R^3}\left(l - \frac{3l}{2l+1}\right)\right]\hat{\xi}_l(R) \\
&= \frac{1}{lR^{l-1}}\left[\omega^2 - \frac{GM_\star}{R^3}\frac{2l\,(l-1)}{2l+1}\right]\hat{\xi}_l(R)\,.
\end{aligned} \tag{7.65}$$

Putting the pieces together, (and dropping the in out notation), the external solution takes the form

$$\hat{U}_l(\omega, r) = \frac{1}{lR^{l-1}}\left[\omega^2 - \frac{GM_\star}{R^3}\frac{2l\,(l-1)}{2l+1}\right]\hat{\xi}_l(R) r^l - \frac{4\pi G\rho R}{2l+1}\hat{\xi}_l(R)\left(\frac{R}{r}\right)^{l+1} . \tag{7.66}$$

In the absence of a tidal interaction (with $\chi = 0$), the exterior potential must decay as $r \longrightarrow \infty$. We see that this requires (given that we must have $\hat{\xi}_l(R) \neq 0$)

$$\omega^2 = \omega_l^2 = \frac{2l\,(l-1)}{2l+1}\frac{GM_\star}{R^3} . \tag{7.67}$$

These frequencies represent the free (f-mode) oscillations of the incompressible star. Away from the mode frequency the external solution will be such that $\hat{c}_R = 0$. However, the growing component must be sourced by the potential due to the binary companion. This means that we can identify

$$\hat{v}_l = \frac{1}{lR^{l-1}}\left[\omega^2 - \frac{GM_\star}{R^3}\frac{2l\,(l-1)}{2l+1}\right]\hat{\xi}_l(R) . \tag{7.68}$$

It follows that

$$\hat{\xi}_l(R) = \frac{lR^{l-1}}{\omega^2 - \omega_l^2}\hat{v}, \tag{7.69}$$

and then

$$\hat{\Phi}_l(r) = -\frac{4\pi G\rho R^l l}{(2l+1)(\omega^2 - \omega_l^2)}\hat{v}\left(\frac{R}{r}\right)^{l+1} . \tag{7.70}$$

Finally, let us make contact with the Love number and the tidal deformability. In general, the matching of the gravitational potential at the star's surface provides the multipole moment, I_l, of the body according to

$$\hat{\Phi}_l = -\frac{4\pi G}{2l+1}\frac{\hat{I}_l}{r^{l+1}}. \tag{7.71}$$

We thus identify

$$\hat{I}_l = \frac{\rho l R^{2l+1}}{\omega^2 - \omega_l^2}\hat{v}. \tag{7.72}$$

The Love number follows from

$$k_l(\omega) = \frac{1}{2}\frac{\hat{\Phi}_l(R)}{\hat{\chi}_l(R)} = \frac{\hat{d}}{2\hat{v}R^{2l+1}}, \tag{7.73}$$

so we get

$$k_l(\omega) = -\frac{2\pi G\rho l}{(2l+1)(\omega^2 - \omega_l^2)} = -\frac{3GM_\star}{R^3}\frac{l}{2(2l+1)(\omega^2 - \omega_l^2)}. \tag{7.74}$$

With dimensionless frequencies we arrive at

$$k_l(\omega) = \frac{\tilde{\omega}_l^2 - l}{2(\tilde{\omega}^2 - \tilde{\omega}_l^2)}, \tag{7.75}$$

which agrees with the result obtained in Andersson and Pnigouras (2020). The uniform density model is admittedly simplistic, but the calculation has still led to a couple of useful results/insights. In particular, the final relation (7.75) clearly links the tidal deformability—notably without any explicit mode expansion in the calculation—to the fundamental mode of the star. We also see that, in the limit $\tilde{\omega} \ll \tilde{\omega}_l$ we have

$$k_l^{\text{eq}} = \frac{1}{2}\frac{3l}{2l+1}\frac{1}{\tilde{\omega}_l^2} = \frac{1}{2}\frac{3l}{2l+1}\frac{2l+1}{2l(l-1)} = \frac{3}{4(l-1)}\,, \tag{7.76}$$

the expected result for the static tide of an incompressible body (Poisson and Will, 2014).

7.2.2.2 Compressible Star

The incompressible model does not shed particular light on the behaviour for more realistic matter models; in the first instance, when the fluid is compressible and composition stratification leads to the presence of g-modes. However, the generalisation to this case is straightforward. Formally, the only things that change are: (i) the interior solution must now account for internal density perturbations ($\delta\hat{\rho} \neq 0$), and (ii) one would typically have $\rho(R) = 0$, so the surface boundary condition on the pressure perturbation simplifies to $\delta\hat{p} = 0$ at $r = R$. Neither of these changes impact on (7.41). The only adjustment we need to make is that the perturbation equations have to be solved numerically.

As an illustration we compare our new method to the traditional mode-sum approach for a polytropic model with $\Gamma = 2$ and $\Gamma_1 = 2.05$ in Fig. 7.3 drawing on the results for the corresponding dimensionless mode frequencies and overlaps, $\tilde{\omega}_n$ $\tilde{Q}_n$, see Table 6.1. Evidently we see perfect agreement between our new method in blue (7.41) and the mode-sum in the dashed orange (7.21). The new method also recovers the underlying mode structures with the peaks corresponding to the first three quadrupolar g-modes lining up with the mode-sum. It is also notable that the effective Love number approaches the expected results $k_2 \approx 0.2599$ from (Poisson and Will, 2014) in the static limit. This demonstration provides further confidence in the strategy we are promoting.

With the two methods being identical in this case, an interesting question that arises is whether one can extract the overlap $\tilde{Q}_n$ from our new approach. This will be more beneficial later in full general relativity where we are not currently able to calculate the overlap integral. The mode sum (7.21) can be rewritten as

$$k_l = \frac{2\pi}{2l+1}\sum_n \frac{\tilde{Q}_n^2}{\tilde{\omega}_n^2 - \tilde{\omega}^2}. \tag{7.77}$$

Noting that each mode frequency represents a first order pole in the effective Love number, we recognise that the overlap integral can be calculated from the residue

$$\tilde{Q}_n^2 = -\frac{2l+1}{\pi}\tilde{\omega}_n \lim_{\tilde{\omega}\to\tilde{\omega}_n} (\tilde{\omega} - \tilde{\omega}_n) k_{lm}(\tilde{\omega}) = -\frac{2l+1}{\pi}\tilde{\omega}_n \text{Res}\, k_{lm}(\tilde{\omega}_n). \tag{7.78}$$

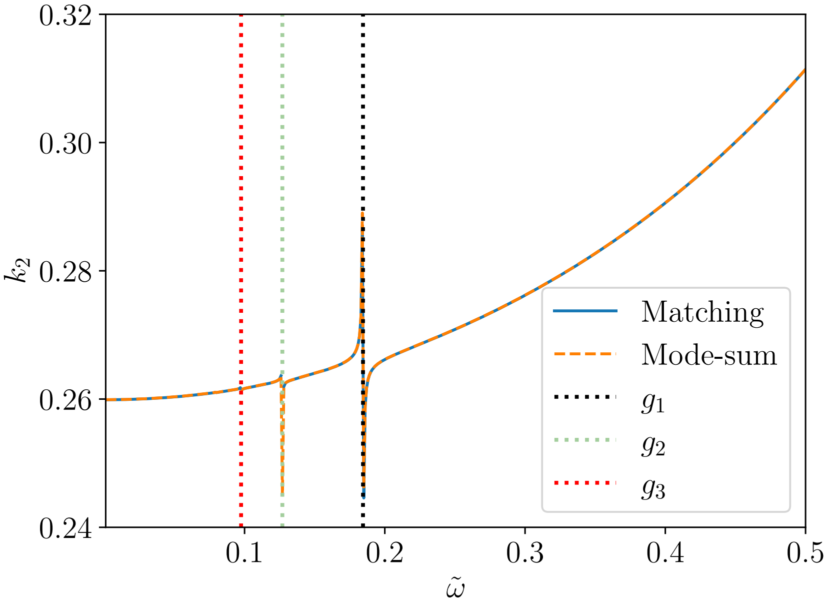

FIGURE 7.3: A comparison of the effective Love number obtained from i) the standard mode sum (7.21) (orange+dashed) and ii) the proposed matching approach (7.41) (blue+solid). The results, which correspond to a compressible polytropic model with $\Gamma = 2$ and $\Gamma_1 = 2.05$, are in perfect agreement. The tidal response singularities associated with the first two gravity modes of the modes are prominent.

In order to evaluate the residue we start from

$$k_l(\omega) = \frac{1}{2}\left[l\hat{U}_l(\omega, R) - R\partial_r\hat{U}_l(\omega, R)\right]\left[(l+1)\hat{U}_l(\omega, R) + R\partial_r\hat{U}_l(\omega, R)\right]^{-1}. \tag{7.79}$$

We can Taylor expand the denominator near a mode frequency. This leads to

$$\begin{aligned}(l+1)\hat{U}_l(\omega, R) + R\partial_r\hat{U}_l(\omega, R) &\approx \underbrace{(l+1)\hat{U}_l(\omega_n, R) + R\partial_r\hat{U}_l(\omega_n, R)}_{=0} \\ &+ (\omega - \omega_n)\left[(l+1)\left.\frac{d\hat{U}_l(\omega, R)}{d\omega}\right|_{\omega_n} + R\,\frac{d}{dr}\left.\frac{d\hat{U}_l(\omega, R)}{d\omega}\right|_{\omega_n}\right]_{\omega=\omega_n}\end{aligned} \tag{7.80}$$

Putting this all together we arrive at

$$\tilde{Q}_n^2 = -\frac{2l+1}{2\pi}\tilde{\omega}_n\left[l\hat{U}_l(\tilde{\omega}_n, R) - R\partial_r\hat{U}_l(\tilde{\omega}_n, R)\right]\left[(l+1)\frac{d\hat{U}_l(\tilde{\omega}, R)}{d\tilde{\omega}} + R\frac{d}{dr}\frac{d\hat{U}_l(\tilde{\omega}, R)}{d\tilde{\omega}}\right]^{-1}_{\tilde{\omega}=\tilde{\omega}_n} \tag{7.81}$$

Applying this relation to the Love number obtained from the matching argument we can infer the overlap integral associated with each mode. This approach is tested in Table 7.1 for two polytropic models, one with $\Gamma_1 = 2.05$ and one with $\Gamma_1 = 2.1$ and both with $\Gamma = 2$. The approach shows good agreement between the two methods, improving for the lower order g-modes. The errors are likely due to the numerical calculation of the residue. As the f-mode has the largest residue, the numerical inaccuracy will be largest. The results of Fig. 7.3 and

Table 7.1 provide us with the confidence to trust our new approach and we will now extend this formalism to full general relativity.

TABLE 7.1: Comparison of the overlap integral calculated using the normal approach (7.12) in column 2 and our new matching approach (7.81) in column 3 for the quadrupolar f- and g modes. Two polytropic equations of state were used $\Gamma_1 = 2.05$ and $\Gamma_1 = 2.1$ both with $\Gamma = 2$.

Mode	$\Gamma_1 = 2.05$			$\Gamma_1 = 2.1$		
	$\tilde{\omega}_n$	$\tilde{Q}_n$	Matching	$\tilde{\omega}_n$	$\tilde{Q}_n$	Matching
f	1.227	5.58E-01	5.38E-01	1.227	5.58E-01	5.56E-01
g_1	0.1845	1.77E-03	1.77E-03	0.2566	3.50E-03	3.50E-03
g_2	0.127	4.24E-04	4.23E-04	0.177	8.36E-04	8.34E-04
g_3	0.0975	1.25E-04	1.25E-04	0.1361	2.46E-04	2.48E-04
g_4	0.07942	4.14E-05	4.09E-05	0.1109	8.13E-05	8.14E-05

7.3 General Relativity

Having established the near-zone matching strategy for the tidal response we want to explore to what extent we can implement the idea in general relativity. The key point is that Eq. (7.41) demonstrates that we are able to calculate k_l without the need of a mode-sum. This is crucial because it suggests a way of circumventing the fact that the relativistic mode problem is not Hermitian, an issue which has hampered progress in describing dynamical tides of relativistic stars (Pitre and Poisson, 2024).

Two issues immediately manifest in general relativity. First, the Einstein field equations are non-linear. This means that we need to be careful in disentangling the ”tidal potential” from the “response” induced in the stellar fluid. However, this problem does not seem critical as long as we focus on the regime where the tide is weak. Assuming that the tidal problem is linear, the tidal driving may be considered a perturbation of the star (just as in the Newtonian case) and there is, in fact, no need to separate tidal driving from the star’s response. To be specific, the perturbation problem involves solving the linearised Einstein field equations

$$\delta G_{ab} = 8\pi\delta T_{ab}, \tag{7.82}$$

where the spacetime curvature associated with the metric g_{ab} is encoded in the Einstein tensor G_{ab} and the matter is represented by the stress-energy tensor T_{ab}. Here is the key point: As long as the tidal problem is in the linear regime—essentially, when the induced metric perturbations h_{ab} are small (in a suitable sense) compared to the gravitational field of the background—the problem we need to solve remain the same as for a perturbed isolated star. The only difference is that the interior solution must match to an exterior that represents the tidal environment. The fact that the difference between the two problems is encoded in the boundary should immediately remind us of the discussion of the matching argument from the Newtonian tidal problem. In essence, the perturbed metric, h_{ab}, is analogous to the combined potentials, $U = \delta\Phi + \chi$, in the Newtonian case and we already know that we can solve the tidal problem without separating these two contributions in the stellar interior. There is no obvious reason why the same strategy should not work in relativity.

The second issue presents more of a challenge. In the vacuum outside the star, the problem obviously reduces to

$$\delta G_{ab} = 0. \tag{7.83}$$

It is well-known that this problem has two degrees of freedom, representing gravitational waves. The corresponding equations are familiar from black-hole perturbation theory and commonly represented by either the Regge-Wheeler equation or the Zerilli equation as discussed in Chapter 5. These equations are known to be gauge invariant. Far away from a perturbed star, the two solutions to the linearised Einstein equations represent out- and ingoing gravitational waves. An isolated star can obviously only source outgoing waves, a boundary condition that corresponds to the star's oscillation modes being damped by gravitational-wave emission and hence quasi-normal, in the established parlance. The mode frequencies need to be complex in order to reflect the damping and the perturbation problem cannot be Hermitian. Strictly speaking, one would not expect a mode-sum representation for the relativistic star to exist (or at least not be complete), hence our previous need to make assumptions such as the Cowling approximation.

In general relativity (and Schwarzschild coordinates), the metric potential

$$g_{tt} = -e^{\nu} = -1 + \frac{2M}{r} \tag{7.84}$$

where M represents the mass insider radius r, effectively encodes the gravitational potential. This follows immediately from the Newtonian limit, where

$$g_{tt} = -\left(1 + \frac{1}{c^2} 2\Phi\right). \tag{7.85}$$

Given this correspondence with the Newtonian case, it is natural to focus a discussion of the tidal response on the corresponding metric perturbation

$$h_{tt} = -e^{\nu} H_0 Y_l^m e^{i\omega t}, \tag{7.86}$$

where we assume that we work in the frequency domain. In Regge-Wheeler gauge the equation that governs H_0 was written down some time ago by Lindblom et al. (1997). In this gauge we have (for a non-rotating star) reproduced Eqs. (12), (A7), (A8), (A11), (A18) and (A19) from Lindblom et al. (1997) specialised to the vacuum:

$$r^2 \frac{d^2 H_0}{dr^2} + (2 + r\eta_1) r \frac{dH_0}{dr} + [(r\omega)^2 e^{-\nu} - l(l+1) + r^2 \eta_2] e^{\lambda} H_0 = 0, \tag{7.87}$$

where

$$\eta_1 = \frac{1}{2}\left(\frac{d\nu}{dr} - \frac{d\lambda}{dr}\right) + \frac{2}{r}\left(2 - r\frac{d\nu}{dr}\right)(\beta_1 - 1), \tag{7.88}$$

$$\eta_2 = e^{-\lambda}\left[\frac{d^2\nu}{dr^2} + \left(\frac{d\nu}{dr}\right)^2 + \frac{1}{2r}\left(2 - r\frac{d\nu}{dr}\right)\left(4\beta_2 - \frac{d\nu}{dr} + \frac{d\lambda}{dr}\right)\right], \tag{7.89}$$

$$\beta_1 = \Delta\left\{-[2(r\omega)^2e^{-\nu} - (l-1)(l+2)]l(l+1)e^{\lambda} + 2(r\omega)^2e^{-\nu}\left(2 - r\frac{d\nu}{dr}\right)\right\}, \tag{7.90}$$

$$\begin{aligned}\beta_2 = \Delta\Bigg\{ & r\omega^2e^{-\nu}\left(2 - r\frac{d\nu}{dr}\right)\left[l(l+1)e^{\lambda} - 2\left(1 - r\frac{d\nu}{dr}\right)\right] \\ & - [(l-1)(l+2) - 2(r\omega)^2e^{-\nu}]\left[-l(l+1)\frac{d\nu}{dr} + 2r\omega^2e^{-\nu}\right]e^{\lambda}\Bigg\},\end{aligned} \tag{7.91}$$

$$\frac{1}{\Delta} = [(l-1)(l+2) - 2(r\omega)^2e^{-\nu}][l(l+1) - 2(r\omega)^2e^{-\nu}]e^{\lambda} + (r\omega)^2e^{-\nu}\left(2 - r\frac{d\nu}{dr}\right)^2. \tag{7.92}$$

These expressions assume that the star is non-rotating and oscillating with (possibly complex) frequency ω. Note that

$$e^{\nu} = 1 - \frac{2M}{r}, \tag{7.93}$$

$$\lambda = -\nu. \tag{7.94}$$

7.3.1 Static tide

In relativity, the static tidal problem has been solved (Hinderer, 2008; Binnington and Poisson, 2009). It will be useful to examine this case first. The static tide corresponds to $\omega \to 0$—that is, the tidal driving is slow compared to the dynamics. (This is similar to the near-zone limit of $r\omega \ll 1$ discussed later.) In this regime, (7.87) reduces to

$$r^2\frac{d^2H_0}{dr^2} + \left(2 - r\frac{d\lambda}{dr}\right)r\frac{dH_0}{dr} - \left[l(l+1)e^{\lambda} + r^2\left(\frac{d\lambda}{dr}\right)^2\right]H_0 = 0. \tag{7.95}$$

This admits the general solution

$$H_0(r) = AQ_l^2(r/M - 1) + BP_l^2(r/M - 1), \tag{7.96}$$

where P_l^2 and Q_l^2 are the associated Legendre polynomials of the first and second kind (of degree l), respectively and we have assumed $m = 2$. From now on we will restrict our discussion to the quadruploar $l = 2$ case for simplicity. From the Digital Library of Mathematical Functions we first of all have

$$P_m^m(x) = \frac{(2m)!}{2^m m!}\left(x^2 - 1\right)^{m/2}. \tag{7.97}$$

This leads to

$$P_2^2(x) = \frac{4!}{4 \cdot 2!}\left(x^2 - 1\right) = 3\left(x^2 - 1\right). \tag{7.98}$$

Therefore

$$P_2^2(r/M - 1) = 3\left[\left(\frac{r}{M} - 1\right)^2 - 1\right] = 3\left[\left(\frac{r}{M}\right)^2 - \frac{2r}{M}\right] = 3\left(\frac{r}{M}\right)^2\left(1 - \frac{2M}{r}\right). \tag{7.99}$$

Next we need

$$Q_n = \frac{1}{2}P_n(x)\ln\left(\frac{x+1}{x-1}\right) - W_{n-1}(x), \tag{7.100}$$

and

$$Q_n^m(x) = (x^2-1)^{m/2}\frac{d^m}{dx^m}Q_n(x). \tag{7.101}$$

Starting from

$$P_2(x) = \frac{3x^2-1}{2}, \tag{7.102}$$

and

$$W_1(x) = \frac{3x}{2}, \tag{7.103}$$

we get

$$Q_2(x) = \frac{3x^2-1}{4}\ln\left(\frac{x+1}{x-1}\right) - \frac{3x}{2}. \tag{7.104}$$

For Q_2^2 we need two derivatives so

$$\begin{aligned}\frac{dQ_2}{dx} &= \frac{3x}{2}\ln\left(\frac{x+1}{x-1}\right) + \frac{3x^2-1}{4}\left(\frac{1}{x+1} - \frac{1}{x-1}\right) - \frac{3}{2}\\ &= \frac{3x}{2}\ln\left(\frac{x+1}{x-1}\right) - \frac{3x^2-1}{2(x^2-1)} - \frac{3}{2},\end{aligned} \tag{7.105}$$

$$\begin{aligned}\frac{d^2Q_2}{dx^2} &= \frac{3}{2}\ln\left(\frac{x+1}{x-1}\right) + \frac{3x}{2}\left(\frac{1}{x+1} - \frac{1}{x-1}\right) - \frac{3x}{x^2-1} + \frac{x(3x^2-1)}{(x^2-1)^2}\\ &= \frac{3}{2}\ln\left(\frac{x+1}{x-1}\right) - \frac{6x}{x^2-1} + \frac{3x^3-x}{(x^2-1)^2}\\ &= \frac{3}{2}\ln\left(\frac{x+1}{x-1}\right) + \frac{x(5-3x^2)}{(x^2-1)^2}.\end{aligned} \tag{7.106}$$

It follows that

$$Q_2^2(x) = (x^2-1)\frac{3}{2}\ln\left(\frac{x+1}{x-1}\right) + \frac{x(5-3x^2)}{x^2-1}. \tag{7.107}$$

With $x = r/M - 1$ we get

$$\begin{aligned} Q_2^2(x) &= \frac{3}{2}\left(\left(\frac{r}{M} - 1\right)^2 - 1\right)\ln\left(\frac{\left(\frac{r}{M} - 1\right) + 1}{\left(\frac{r}{M} - 1\right) - 1}\right) + \frac{\left(\frac{r}{M} - 1\right)\left[5 - 3\left(\frac{r}{M} - 1\right)^2\right]}{\left(\frac{r}{M} - 1\right)^2 - 1} \\ &= \frac{3}{2}\left[\left(\frac{r}{M}\right)^2 - \frac{2r}{M}\right]\ln\left(\frac{\frac{r}{M}}{\frac{r}{M} - 2}\right) + \frac{\frac{r}{M} - 1}{\left(\frac{r}{M}\right)^2 - \frac{2r}{M}}\left[2 - 3\left(\frac{r}{M}\right)^2 + \frac{6r}{M}\right] \\ &= \left(\frac{r}{M}\right)^2\left(1 - \frac{2M}{r}\right)\left[\frac{M(r - M)\left(2M^2 + 6Mr - r^2\right)}{r^2\left(r - 2M\right)^2} + \frac{3}{2}\ln\left(\frac{r}{r - 2M}\right)\right]. \end{aligned} \tag{7.108}$$

In the weak-field regime $M/r \ll 1$, using (7.99) and (7.108), (7.96) reduces to

$$H_0(r) = \frac{8}{5}A\left(\frac{M}{r}\right)^3 + O[(M/r)^4] + 3B\left(\frac{M}{r}\right)^{-2} + O[(M/r)^{-1}]. \tag{7.109}$$

Here, we can identify the decaying term (A) with the stellar response and the growing term (B) with the external tidal field, precisely as we did in the Newtonian case. In fact, in the Newtonian limit we have

$$e^{\nu}H_0 = \frac{2}{c^2}(\delta\Phi_l + \chi_l), \tag{7.110}$$

and a comparison with Eq. (7.109) leads to

$$\delta\Phi_2 = \frac{4}{5}A\left(\frac{M}{r}\right)^3, \qquad \chi_2 = \frac{3}{2}B\left(\frac{M}{r}\right)^{-2}. \tag{7.111}$$

Recalling Eq. (7.1), we have

$$k_2 = \frac{4}{15}\left(\frac{M}{R}\right)^5\frac{A}{B}, \tag{7.112}$$

which is Eq. (22) from Hinderer (2008).

Finally, it is fairly straightforward to obtain the relativistic version of the matching relation (7.41). First we introduce k_2 in place of one of the two amplitudes A and B and then we combine the expressions for H_0 and its derivative dH_0/dr and solve for k_2 .

Another way to calculate k_2 from Hinderer (2008),

$$\begin{aligned} k_2 = \frac{8C^5}{5}\left(1 - C^2\right)[2 + 2C(y - 1) - y]\Big\{2C\,[6 - 3y + 3C(5y - 8)] \\ + 4C^3\left[13 - 11y + C(3y - 2) + 2C^2(1 + y)\right] \\ + 3\left(1 - 2C^2\right)[2 - y + 2C(y - 1)]\log(1 - 2C)\Big\}^{-1}, \end{aligned} \tag{7.113}$$

where C is the compactness of the star and

$$y = \frac{RH_0'(R)}{H_0(R)}. \tag{7.114}$$

When considering the dynamical tide we can use (7.113) to check how accurately our approach limits to the static value. However, due to the numerical methods used to solve the mode equations in full general relativity as discussed in Chapter 5, the zero frequency limit is numerically difficult to approach unlike in Newtonian gravity. However work by Krüger (2015) allows us to accurately calculate the first few g-modes.

7.3.2 Dynamical Tide

Let us now consider the problem of dynamical tides, which naturally involves solving the perturbation problem for finite frequencies. This is not, in itself, very challenging. It is regularly done in order to identify the star's oscillation modes. However, we need to adjust the strategy a little bit. In the mode problem the outgoing wave boundary condition is imposed asymptotically; in the wave zone, where the gravitational radiation can be identified. This is not what we need for the tidal response. Instead, we have to bring the analysis into the weak-field near zone (as indicated in Fig. 7.2). It is only in this region that the matching argument applies. It is obviously not the case that the solution to the binary problem can be obtained by solving for the perturbations of a single star, but we can quantify the star's tidal response in the part of spacetime where the tidal driving represents a small perturbation of the star's geometry. The argument may be familiar from recent work within world-line field theory (see Goldberger et al. (2021); Saketh et al. (2024)), where the tidal response problem is recast in terms of scattering amplitudes. In that context, a key step involves bringing the asymptotic solution into the near-zone to identify the multipole moments of the tidally perturbed body. Our aim here is the same, we want to work out the tidal response function which could (equivalently) be thought of as a set of frequency-dependent multipole moments. We differ from the (current) world-line field theory argument by not carrying out a low-frequency expansion. Why this makes a difference will be explained below.

Based on the fact that Eq. (7.96) provides the general solution for the static tide, which should represent the $\omega \longrightarrow 0$ limit of the dynamical response, we take as starting point the Ansatz

$$H_0(r,\omega) = A[1+\epsilon(r\omega)^2]Q_l^2(r/M-1) + B[1+\zeta(r\omega)^2]P_l^2(r/M-1), \tag{7.115}$$

which now has the leading order near-zone corrections. Substituting into (7.87), we find that, for $l = 2$, the solution to order $(r\omega)^2$ requires

$$\epsilon = -\frac{1}{2} + O\left(\frac{M}{r}\right) \tag{7.116}$$

and

$$\zeta = -\frac{11}{42} - \frac{107}{63}\frac{M}{r} + O\left[(M/r)^2\right] \tag{7.117}$$

The first of these agrees with Eq. (28) from Lindblom et al. (1997) and is based on their near zone boundary approach. While it is sufficient to use a constant value for ϵ, numerical

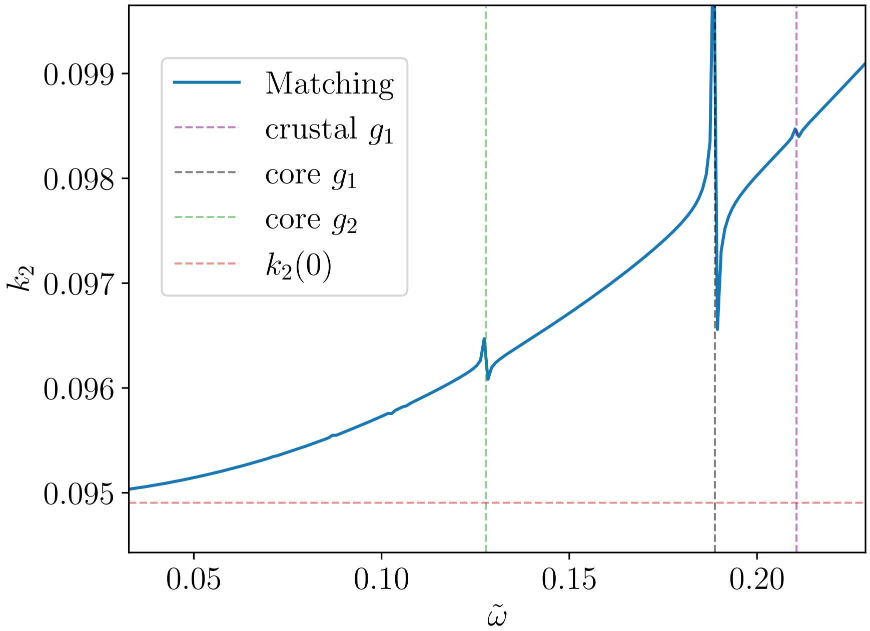

FIGURE 7.4: The effective Love number $k_2(\omega)$ calculated using (7.115) for a $1.4M_\odot$ neutron star using the BSk22 equation of state. The static result $k_2 \approx 0.0949$ from (7.113) is shown (horizontal dashed red line) along with the first two quadrupolar g-modes (vertical green dashed line) and the crustal g-mode (vertical dashed black line).

experimentation shows that we need to go beyond the leading order in ζ. If we only keep the constant contribution to ζ then the results we will see later in Fig. 7.6, would have errors at the level of a few percent. This is due to the M/r terms in the expansion of (7.99).

The method for quantifying the frequency dependent tidal response (the effective Love number) proceeds as follows. First solve the standard perturbation equations for a neutron star with the chosen matter model for a given frequency. This interior solution provides H_0 and its derivative at the stellar surface and satisfies all other required boundary conditions (e.g., regularity at the centre and a vanishing Lagrangian perturbation of the pressure at the surface). From this solution we can obtain the two amplitudes A and B from the near-zone boundary condition. With this information in hand, k_l follows from (7.112).

In order to test our new approach $k_2(\omega)$ was calculated for a realistic equation of state, BSk22, as used previously. The results are shown in Fig. (7.4) for a $M = 1.4M_\odot$ and $R \approx 13.03\,\text{km}$ neutron star. The horizontal red dashed line is the static Love number calculated from (7.113). We can see that in the limit $\omega \longrightarrow 0$, our effective Love number tends to the static $k_2 = 0.0949$ as expected from the Newtonian case. Also indicated are the location of the first few quadrupolar g-modes taken from Table 4.3. As mentioned in Chapter 4, we see the presence of the crustal g-mode, indicated by the vertical black dashed line. The first two core g-modes are indicated by the vertical green dashed lines.

7.3.2.1 Near Zone Boundary Conditions

In the Newtonian analysis the mode structure was perfectly recovered as shown by the agreement in Fig. 7.3. However in general relativity the modes are complex and we need to make sure we are accurately capturing the imaginary part of the modes. Therefore we need to formulate the near zone boundary conditions with a minor extension of the results from Lindblom et al. (1997). The argument involves two approximations. First, we examine Eq. (7.87) in the weak-field limit $M/r \ll 1$. We then have

$$r^2\frac{d^2H_0}{dr^2} + (2 + r\eta_1)r\frac{dH_0}{dr} + [(r\omega)^2 - l(l+1) + r^2\eta_2]H_0 + O(M/r) = 0, \tag{7.118}$$

where

$$r\eta_1 = 4\{(l-1)(l+2)\Delta[l(l+1) - 2(r\omega)^2] - 1\} + O(M/r), \tag{7.119}$$

$$r^2\eta_2 = 16(r\omega)^4\Delta + O(M/r) \tag{7.120}$$

and

$$\frac{1}{\Delta} = [(l-1)(l+2) - 2(r\omega)^2][l(l+1) - 2(r\omega)^2] + 4(r\omega)^2 + O(M/r). \tag{7.121}$$

It turns out that the weak-field equation (7.118) can be solved analytically. This has been known since the pioneering work of Thorne (1969). The solution can be expressed in spherical Bessel functions of the first and second kind (j_l and y_l, respectively) and we have

$$H_0 = r\omega\left[C\frac{d}{d(r\omega)}j_l(r\omega) + D\frac{d}{d(r\omega)}y_l(r\omega)\right] + \left[1 + \frac{1}{2}l(l+1) - (r\omega)^2\right][Cj_l(r\omega) + Dy_l(r\omega)] + O(M/r), \tag{7.122}$$

where C and D are arbitrary constants. Well away from the star (in the wave zone $r\omega \gg 1$) it is easy to show that

$$Cj_l(r\omega) + Dy_l(r\omega) = -\frac{1}{2r\omega}\left[(D + iC)e^{i(r\omega - l\pi/2)} + (D - iC)e^{-i(r\omega - l\pi/2)}\right] + O[1/(r\omega)^2]. \tag{7.123}$$

We see that a solution with no ingoing radiation (representing an oscillation mode for the star) corresponds to $D = -iC$. This identification is similar in spirit to setting $\hat{\chi}_l = 0$ in Eq. (7.40) in the Newtonian problem.

Next, we consider the solution in the near zone, where $r\omega \ll 1$. We then have

$$Cj_l(r\omega) + Dy_l(r\omega) = C\frac{(r\omega)^l}{(2l+1)!!}\{1 + O[(r\omega)^2]\} - D\frac{(2l-1)!!}{(r\omega)^{l+1}}\{1 + O[(r\omega)^2]\}. \tag{7.124}$$

The two approximations allow us to bring the outgoing-wave boundary condition into the weak-field near zone, albeit in an approximate fashion. This near-zone boundary condition was worked out by Lindblom et al. (1997) and they demonstrated its effectiveness by computing the f-mode.

There is naturally an element of tension between the two approximations we have introduced. The weak-field condition $M/r \ll 1$ improves as the matching boundary is taken further away from the star, but this reduces the validity of the near-zone condition $(r\omega)^2 \ll 1$, which improves for smaller radii. As argued in Lindblom et al. (1997) this tension favours implementing the matching at the star's surface, $r = R$.

The outgoing solution will then behave as

$$\begin{aligned} H_0 &= C\left[r\omega\frac{d}{d(r\omega)} + 1 + \frac{1}{2}l(l+1) - (r\omega)^2\right](j_l - iy_l) \\ &\approx C\left\{\frac{1}{(2l+1)!!}\left[l+1+\frac{1}{2}l(l+1)\right](r\omega)^l + i(2l-1)!!\left[-(l+1)+1+\frac{1}{2}l(l+1)\right]\frac{1}{(\omega r)^{l+1}}\right\} \\ &= C\left\{\frac{l+1}{(2l+1)!!}\frac{l+2}{2}(r\omega)^l + i(2l-1)!!\frac{l(l-1)}{2}\frac{1}{(\omega r)^{l+1}}\right\}, \end{aligned} \tag{7.125}$$

which for $l = 2$ becomes

$$H_0 = C\left[\frac{6}{15}(r\omega)^2 + 3i\frac{1}{(\omega r)^3}\right]. \tag{7.126}$$

In the limit $(r\omega)^2 \ll 1$, the outgoing solution to (7.122) can be simplified to

$$H_0 = \frac{C}{r^{l+1}}\left[1 - iN_l(r\omega)^{2l+1}\right], \tag{7.127}$$

with

$$N_l = \frac{(l+1)(l+2)}{l(l-1)(2l+1)[(2l-1)!!]^2}, \tag{7.128}$$

which for $l = 2$ becomes

$$H_0 = \frac{C}{r^3}\left[1 - \frac{2i}{15}(r\omega)^5\right]. \tag{7.129}$$

Now if we look at (7.125), the second term would behave like Q_2^2 to leading order provided we multiply by

$$-iK_l = \frac{-2i(l+2)!(M\omega)^{l+1}}{l(l-1)(2l-1)!!(2l+1)!!}, \tag{7.130}$$

or

$$-iK_2 = -\frac{8i(\omega M)^3}{15}, \tag{7.131}$$

where K_l agrees with the results from Lindblom et al. (1997). Comparing (7.125) and (7.127) with the factor K_l,

$$-\frac{8i(\omega M)^3}{15}\bar{C}\left[\frac{6}{15}(r\omega)^2 + 3i\frac{1}{(\omega r)^3}\right] = \frac{C}{r^3}\left[1 - \frac{2i}{15}(\omega r)^5\right], \tag{7.132}$$

we see that the results agree to leading order. Therefore, in the limit $M/r \ll 1$, we adjust (7.115) to

$$H_0(r,\omega) = A\left\{[1+\epsilon(r\omega)^2]Q_l^2(r/M-1) - iK_l\left[r\omega\frac{d}{d(r\omega)} + 1 + \frac{1}{2}l(l+1) - (r\omega)^2\right]j_l(r\omega)\right\} + B\left\{[1+\zeta(r\omega)^2]P_l^2(r/M-1)\right\}. \quad (7.133)$$

In the limit $(r\omega)^2 \ll 1$ and $\omega \to 0$ (7.133) reduces to (7.96). Moreover, the constants K_l ensures that the imaginary part of $H_0(r)$ reduces to Eq. (27) in Lindblom et al. (1997) in the appropriate $(r\omega)^2 \ll 1$ and $M/r \ll 1$ limit. The part of the solution associated with A corresponds to the solution with no ingoing radiation ($D = -iC$ in (7.123)), while the part associated with B corresponds to the solution with no outgoing radiation ($D = iC$ in (7.123)).

It is worth noting that we only adjust for the wave behaviour in the first term in (7.115). This makes sense because this is the solution that is associated with the outgoing gravitational waves in the distant wave zone, as indicated in Fig. 7.2. The other solution is identified with the tidal driving and does not induce wave-like behaviour far away from the system. At least not until we consider the “outer problem” and the connection between the tidal response and the orbital evolution but that will be left for future work.

It is also worth mentioning that in taking the $M/r \ll 1$ limit and evaluating at the star’s surface, we are assuming the compactness $C = M/R \ll 1$. This will not always be a good assumption for Neutron stars.

7.3.3 Results

To test the accuracy of our new approach we have calculated the *f* and first few quadrupolar *g*-modes using (7.115) and (7.133). An eigenfrequency ω_n corresponds to $B = 0$ in both equations. The results are shown in Table 7.2 for the BSk22 model with $M = 1.4M_\odot$. We have also compared to solutions obtained from the Cowling approximation in Chapter 4 and from using the external mode solution in Chapter 5. We see that both (7.115) and (7.133) recover the real parts of the mode frequencies to well within a percent. Moving on the imaginary part of the mode frequency, we have only compared the *f*-mode as the imaginary part of the *g*-modes are very small compared to their real part, leading to numerical inaccuracies. We see that (7.133) performs better than (7.115), which is to be expected as we included the imaginary corrections to the near zone boundary conditions.

Now that we have confidence in the boundary conditions we extend our effective love number calculations up to the *f*-mode frequency in Fig. 7.5 for the same background model as in Fig. 7.4. We have plotted the *f*-mode calculated from the general relativistic mode calculation (orange dashed line) and our near zone boundary condition (7.133) (black dotted line) to show how accurately the near zone boundary condition recovers the mode structure.

TABLE 7.2: The real and imaginary parts of the mode frequencies for our background BSk22 neutron star using the following methods: in column 2 the Cowling approximation, in column 3 the full relativistic mode equations, in column 4 the boundary condition (7.115) and in column 5 the boundary condition (7.133). The imaginary part of the g-modes was not included due to their small relative value.

Mode	$\mathrm{Re}(\tilde{\omega})$			
	Cowling	GR	Eq. (7.115)	Eq. (7.133)
f	1.4224	1.1272	1.1274	1.1274
crustal g_1	0.2111	0.2105	0.2105	0.2105
core g_1	0.1822	0.1888	0.1888	0.1888
core g_2	0.1263	0.1278	0.1278	0.1278
	$\mathrm{Im}(\omega)$			
f	-	1.26E-05	4.50E-6	1.13E-05

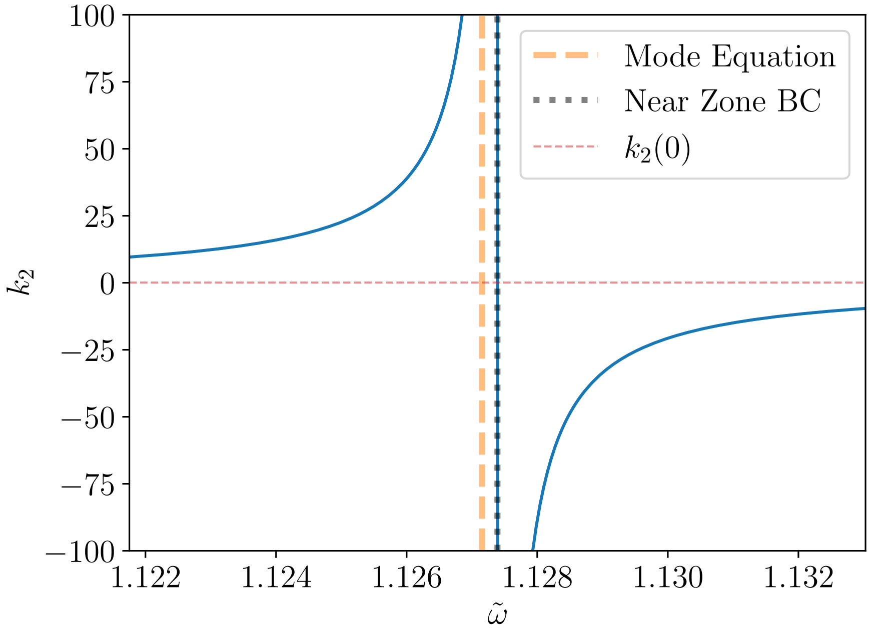

FIGURE 7.5: The effective Love number from (7.115) along with the static result $k_2 \approx 0.0949$ from (7.113) (horizontal dashed red line). Also plotted are the f-mode calculated from (7.115) (black dotted line) and the f-mode calculated from the fully relativistic mode equations in Chapter 5 (orange dashed line).

As mentioned previously we do not have a mode sum to compare our results to in general relativity but we can build an approximate mode sum by using a relativistic analogue of (7.78). In order to do this we want to explicitly write out our equation for $k_2(\omega)$, for simplicity using (7.115) instead of (7.133) as for the real mode frequencies there was negligible difference between them.

Starting from (7.115) and matching to the interior, we have for $l = 2$

$$H_0(R,\omega) = A\left[1+\epsilon(R\omega)^2\right]Q_2^2(R/M-1) + B\left[1+\zeta(R\omega)^2\right]P_2^2(R/M-1), \qquad (7.134)$$

and

$$H_0'(R,\omega) = A\left\{2\epsilon\omega^2 RQ_2^2(R/M-1) + \left[1+\epsilon(R\omega)^2\right]\left.\frac{dQ_2^2}{dr}\right|_{R/M-1}\right\} \tag{7.135}$$

$$+B\left\{2\zeta\omega^2 RP_2^2(R/M-1) + \left[1+\zeta(R\omega)^2\right]\left.\frac{dP_2^2}{dr}\right|_{R/M-1}\right\}. \tag{7.136}$$

As we want to compare these equations to the form of k_2 in (7.113), we need to solve these equations for A and B. Rewriting (7.135) and (7.136) as

$$H_0 = \alpha A + \beta B, \tag{7.137}$$

$$H_0' = \gamma A + \eta B, \tag{7.138}$$

we can rearrange to get

$$\gamma H_0 - \alpha H_0' = (\beta\gamma - \alpha\eta)B \implies B = -\frac{1}{\alpha\eta - \gamma\beta}\left[\gamma H_0 - \alpha H_0'\right]. \tag{7.139}$$

From this we see that the "outgoing-wave boundary condition" requires

$$\gamma H_0 - \alpha H_0' = 0, \tag{7.140}$$

or

$$\left\{2\epsilon\omega^2 RQ_2^2(R/M-1) + \left[1+\epsilon(R\omega)^2\right]\left.\frac{dQ_2^2}{dr}\right|_{R/M-1}\right\} H_0(R,\omega) - \left[1+\epsilon(R\omega)^2\right] Q_2^2(R/M-1)H_0'(R,\omega) = 0. \tag{7.141}$$

We also need

$$\delta H_0 - \beta H_0' = (\alpha\eta - \beta\gamma)A \implies A = \frac{1}{\alpha\eta - \gamma\beta}\left[\delta H_0 - \beta H_0'\right]. \tag{7.142}$$

The general expression for the tidal response, obtained from matching at the stellar surface, then becomes

$$k_2 = -\frac{4}{15}\left(\frac{M}{R}\right)^5 \frac{\eta H_0 - \beta H_0'}{\gamma H_0 - \alpha H_0'} \tag{7.143}$$

Close to a given mode frequency, we can Taylor expand (as in Newtonian)

$$\gamma H_0 - \alpha H_0' \approx (\omega - \omega_n)\frac{d}{d\omega}\left[\gamma H_0 - \alpha H_0'\right]_{\omega=\omega_n}. \tag{7.144}$$

However we need to keep in mind that the modes are now complex but we want to evaluate k_2 for real frequencies. Writing $\omega_n = \sigma_n + i/\tau_n$ and evaluating on the real axis, we would have

$$(\gamma H_0 - \alpha H_0')_{\omega=\sigma_n} \approx -\frac{i}{\tau_n}\frac{d}{d\omega}\left[\gamma H_0 - \alpha H_0'\right]_{\omega=\omega_n}, \tag{7.145}$$

leading to

$$\frac{d}{d\omega}\left[\gamma H_0 - \alpha H_0'\right]_{\omega=\omega_n} \approx i\tau_n(\gamma H_0 - \alpha H_0')_{\omega=\sigma_n}. \tag{7.146}$$

We will use this method to evaluate the residue for the *f*-mode. However as the imaginary parts of the *g*-mode frequencies are much smaller than the real parts, we will treat their frequencies as real. In this case we can evaluate the derivative as

$$\begin{aligned}\frac{d}{d\omega}\left[\gamma H_0 - \alpha H_0'\right]_{\omega=\omega_n} &= \left[\gamma\frac{dH_0}{d\omega} - \alpha\frac{dH_0'}{d\omega}\right]_{\omega=\omega_n} + \frac{d\gamma}{d\omega}H_0 - \frac{d\alpha}{d\omega}H_0' \\ &= \left[\gamma\frac{dH_0}{d\omega} - \alpha\frac{dH_0'}{d\omega}\right]_{\omega=\omega_n} + 2\epsilon\omega_n R\left[2Q_2^2(R/M-1) + R\left.\frac{dQ_2^2}{dr}\right|_{R/M-1}\right]H_0 \\ &\quad - 2\epsilon\omega_n R^2 Q_2^2(R/M-1)H_0'. \end{aligned} \tag{7.147}$$

Noting the symmetry of the relativistic modes; with $\tilde{\omega}_n = \pm\sigma_n + i\gamma_n$ we expect the mode sum to have the form

$$k_l = -\frac{2\pi}{2l+1}\sum_n \frac{Q_n^2}{(\tilde{\omega} + \sigma_n - i\gamma_n)(\tilde{\omega} - \sigma_n - i\gamma_n)}. \tag{7.148}$$

As the denominator expands as

$$(\tilde{\omega} + \sigma_n - i\gamma_n)(\tilde{\omega} - \sigma_n - i\gamma_n) = \tilde{\omega}^2 - \sigma_n^2 - 2i\gamma_n\tilde{\omega}, \tag{7.149}$$

this will lead to the resonance behaviour we are after at the real frequencies of the mode σ_n. We have also defined Q_n as the relativistic analogue of the dimensionless overlap integral. Due to the complex nature of the modes we now expect Q_n to be complex as well. This leads to

$$Q_n^2 = -\frac{2l+1}{\pi}\sigma_n \lim_{\tilde{\omega}\to\tilde{\omega}_n}(\tilde{\omega} - \tilde{\omega}_n)k_l(\tilde{\omega}) = -\frac{2l+1}{\pi}\tilde{\sigma}_n \mathrm{Res}\, k_l(\tilde{\omega}_n), \tag{7.150}$$

for which we need

$$\mathrm{Res}\, k_l(\tilde{\omega}_n) = -\frac{4}{15}\left(\frac{M}{R}\right)^5\left[\delta H_0 - \beta H_0'\right]\left[\left.\frac{d\left(\gamma H_0 - \alpha H_0'\right)}{d\omega}\right|_{\omega=\omega_n}\right]^{-1}. \tag{7.151}$$

The results for Q_n^2 are shown in Table 7.3 using the modes calculated from (7.115) in Table 7.2. We have also included the dimensionless overlap calculated in the Cowling approximation from Table 6.2. Our numerical results suggest that they are within a factor of a few. Unlike the Newtonian analysis, the results are not identical. This should be expected, as the Cowling approximation was a hybrid approach between Newtonian gravity and general relativity. However we see that there is a significant difference between the results for the crustal *g*-mode.

Due to the shape of the crustal mode being a confined to the small crustal region, this indicates there may be an error in the integration over the star when calculating Q_n^2 and this is worth future investigation. Though it is worth remembering that we do not consider a crust in our numerical calculations and this mode is a result of the equation of state functionals we are employing from Potekhin et al. (2013).

In order to test our mode sum approach, the percentage difference between the real parts $k_l(\omega)$ calculated from (7.148) and (7.115) is shown in Fig. 7.6 for our chosen BSk22 model. From this plot we see the difference around the *f*-mode is minimal however in the limit $\omega \to 0$, the error increases to a percent. The accuracy of these results, with a typical error below the 1% level, suggests that our analysis leading to the Q_n amplitude is robust. Therefore for all practical purposes one can safely replace the matching calculation with a sum over the modes. This obviously agrees with the intuition gleaned from the Newtonian case and neatly circumvents the non-Hermitian nature of the relativistic problem.

Moving on, the imaginary parts are shown in Fig. 7.7. We see that the notable contribution is around the *f*-mode which makes sense as the imaginary parts of the g-modes are negligible in comparison to the *f*-mode. The agreement between the imaginary parts of $k_l(\omega)$ and the mode sum is not as accurate as the real parts due to our treatment of the g-modes as real when calculating Q_n.

Further work would look to calculate (7.150) using the full near zone boundary condition (7.133) and try to link our new approach to the ”outer problem” of the tidaly dynamics of a companion neutron star.

TABLE 7.3: Comparison of the dimensionless overlap Q_n^2 calculated from (6.25) in the Cowling approximation in Table (6.2) and the inferred and real and imaginary parts of Q_n^2 calculated from (7.150) evaluated at the mode frequencies in Table 7.2. The result for the f-mode suggests that the f-mode resonance might be notably weaker in full relativity.

Mode	$\tilde{Q}_n^2$	Re (Q_n^2)	Im (Q_n^2)
f	2.83E-01	9.69E-02	-1.70E-04
core g_1	8.40E-07	2.48E-07	
core g_2	2.80E-07	1.91E-08	
crustal g_1	3.30E-06	8.29E-09	

Going back to the effective Love number itself, the next step would be to compare our approach to numerical simulations and waveform models that include the dynamical effects of the *f*-mode.

7.4 Summary

We have considered the dynamical tidal response of both a non-rotating and slowly rotating neutron star within the context of Newtonian gravity. We have shown how this response can be

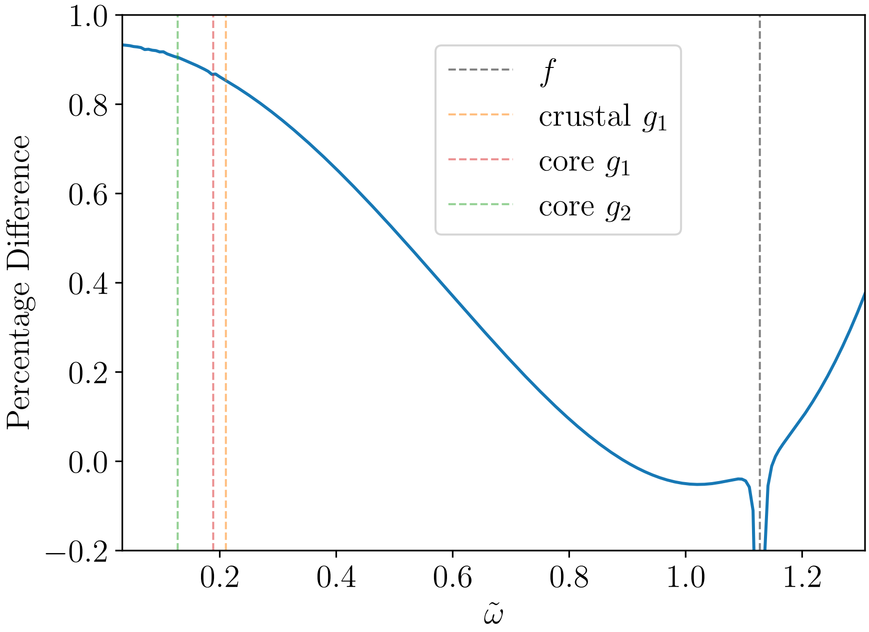

FIGURE 7.6: The percentage difference between the real part of the mode sum (7.148) and the effective Love number $k_2(\omega)$ (7.115). The mode sum includes the following modes: the f-mode (vertical dashed black line); the first two quadrupolar g-modes (vertical dashed lines, red and green) and the crustal g-mode (vertical dashed orange line)

described by an effective Love number which can be calculated by summing over contributions from all the oscillation modes of the star.

However this approach fails when extended to general relativity due to the fact the relativistic mode problem is not Hermitian (Pitre and Poisson, 2024). Therefore we have developed a fully relativistic approach for determining the frequency-dependent tidal response of a compact star that does not involve a sum over the oscillation modes. The strategy involves matching the solution for the linearised fluid dynamics in the star's interior to the spacetime perturbations in the near zone surrounding the body, along with an identification of the tidal driving and the star's response. We have provided an explicit demonstration of the fact that this identification is exact in Newtonian gravity and argue that the approach remains robust also in the relativistic case. Our numerical results, while admittedly a proof of principle, illustrate the method for a realistic matter model from the BSk family, including composition stratification leading to the presence of g-modes. We believe this represents the first set of fully relativistic dynamical tide results for a realistic neutron star equation of state.

The results for the tidal response rely on an implementation of near-zone boundary conditions for the perturbed spacetime metric. This approach was first advocated some time ago in Lindblom et al. (1997). We have revisited the argument and, for the first time, confirmed the accuracy of the strategy for a realistic neutron star model.

We have however, only made direct reference to our results in Chapter 6 obtained within the relativistic Cowling approximation. This comparison is more indicative than satisfactory,

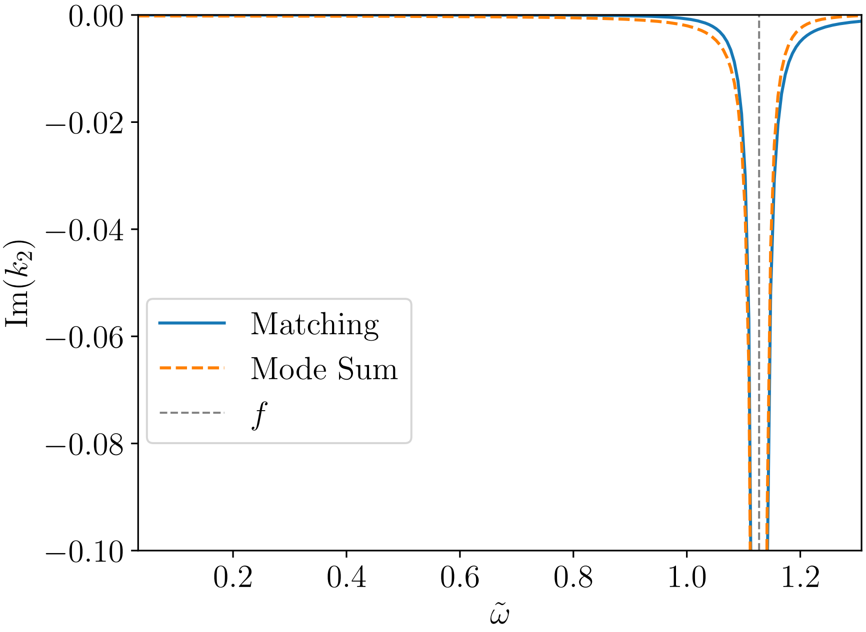

FIGURE 7.7: The imaginary part of the effective love number $k_2(\omega)$ obtained from the matching relation (7.115) and the mode sum (7.148). Also indicated is the f-mode (vertical black dashed line).

because as mentioned previously, the fully relativistic fundamental modes differs from the modes obtained in the Cowling approach by $\sim 15\%$ (Yoshida and Kojima, 1997). However, at the present time no other direct comparison—for realistic neutron star matter—is available to us. This should hopefully change in the near future once the mode-sum strategy outlined in Hegade K. R. et al. (2025) is completed. Both approaches involve approximations and if one could demonstrate that they agree with one another then this would provide mutual confidence.

Future work would also look to incorporate more realistic neutron star internal structure. As long as we can solve the perturbation equations, we may include features such as: an elastic neutron star crust; superfluid components; phase transitions; dissipation and so on. Second, it is clear that the effective mode-sum we obtain through the residue argument lends support for the commonly used Effective One Body models Steinhoff et al. (2016), which build on the assumption that the fluid response can be represented by adding a "harmonic oscillator" contribution to the system's Hamiltonian. This argument relies heavily on the Newtonian mode-sum intuition. The arguments we have provided here lends support for the strategy, which is (at least conceptually) satisfying. Having said that, the obvious weakness of the matching argument is that we do not have access to an underlying equation for the mode amplitudes that would allow us to extend the near resonance solution from, for example, Yu et al. (2024a); Pnigouras et al. (2025a) to relativity. We also do not have an explicit expression for the "energy" associated with the tidal response, as we do with Newtonian and Cowling approximation approaches, so there is still more work to be done in order to link these results to the methods used in Chapter 6.

Chapter 8

Interface Modes

As we have previously mentioned, the equation of state is still largely unknown in neutron star physics, in particular the behaviour and phase of matter in the core as seen in Fig. 1.2. Looking at the nuclear physics side of the picture, what do we know for certain? At low densities, nuclear interactions can be systematically described using chiral effective field theory (EFT) (Epelbaum et al., 2009; Machleidt and Entem, 2011), which provides an order-by-order expansion based on symmetries of quantum chromodynamics (QCD). Chiral EFT is reliable up to approximately $1 - 2$ times the nuclear-saturation density $n_{\mathrm{sat}} \approx 0.16\ \mathrm{fm}^{-3}$ (Tews et al., 2018a; Drischler et al., 2020). Neutron-star cores, however, reach central densities of a few up to $\sim 8 n_{\mathrm{sat}}$, where theoretical uncertainties remain significant. A particularly intriguing possibility is that, at sufficiently high densities, hadronic matter undergoes a phase transition to deconfined quark matter. This transition is a robust prediction of QCD, but its exact nature—whether it is a smooth crossover or a first-order transition with a sharp interface—remains unresolved. While collider experiments at RHIC may have provided tentative evidence for critical behaviour (see Du et al. (2024) and their Fig. 1), the results are far from conclusive. Astrophysical neutron-star observations present an opportunity to probe this phase transition, should they harbour it.

To date, the properties of dense nuclear matter have primarily been explored by measuring the mass M, radius R and tidal deformability Λ of neutron stars. Recent advances in observations have placed increasingly stringent constraints on these parameters. In particular, the X-ray timing mission NICER has provided mass-radius measurements for a few pulsars (Riley et al., 2019; Raaijmakers et al., 2019; Miller et al., 2019; Riley et al., 2021; Miller et al., 2021a; Raaijmakers et al., 2021). Meanwhile, gravitational-wave data, particularly from the landmark GW170817 event, have placed upper limits on the neutron-star tidal deformability (Abbott et al., 2017; De et al., 2018; Abbott et al., 2018, 2019). Combined, these observations suggest error bars of $O(1\mathrm{km})$ for the neutron-star radius. The next generation of gravitational-wave observatories—Cosmic Explorer (Reitze et al., 2019) and the Einstein Telescope (Punturo et al., 2010)—is expected to enhance our ability to measure these aspects, providing much tighter constraints on the high-density physics (Chatziioannou, 2022).

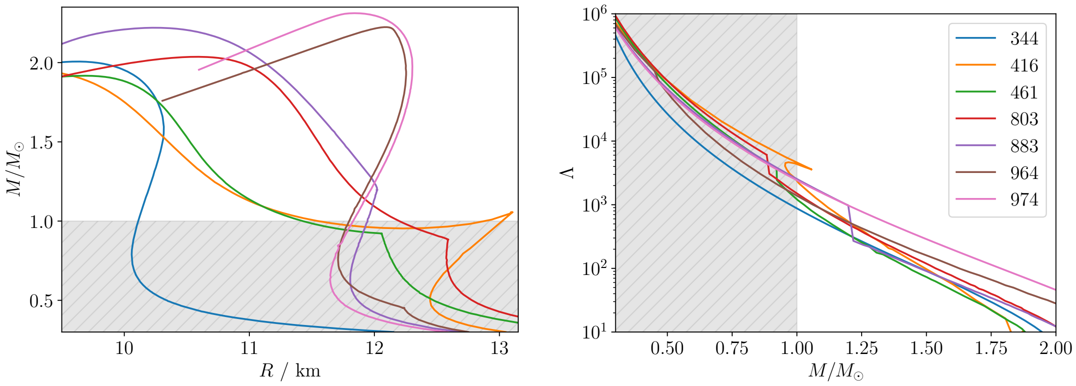

FIGURE 8.1: The mass-radius (left panel) and tidal deformability curves (right panel) for a selection of equation of state models from Capano et al. (2020), indexed by their ordering in radius at $M = 1.4M_\odot$. Five of these matter models possess first-order phase transitions—manifesting as kinks in the $M - R$ plot—while two do not. For the ensemble of 2000 models we consider here, the majority of phase transitions occur at sufficiently low densities such that their impact is only visible below $M = M_\odot$, as indicated by the shaded regions.

When it comes to the issue of unveiling the presence of a phase transition, it is important to note that M, R and Λ reflect global, averaged characteristics of the star. In particular, the tidal deformability Λ represents the star's susceptibility to an external gravitational field in the portion of the inspiral where the compact binary is well separated and the tidal field may be approximated as static (Flanagan and Hinderer, 2008; Hinderer, 2008). While these parameters do contain information about possible phase transitions, the relevant features may be masked or degenerate with other aspects of the equation of state (see, e.g. Alford et al. (2005); Han and Steiner (2019); Raithel and Most (2023b,a)). We illustrate the issue in Fig. 8.1 for a subset of the equation of state models we consider later. These models are consistent with chiral EFT up to nuclear saturation and then extrapolated to higher densities in such a way that each model supports the existence of $1.9M_\odot$ neutron stars, in agreement with heavy-pulsar observations. No other constraints were imposed (see Tews et al. (2018b); Capano et al. (2020) for more details). Some of these models include a phase transition. Fig. 8.1 displays M, R and Λ, highlighting the difficulty of unambiguously identifying a phase transition from these bulk observables alone. If the transition is of first order, the $M - R$ curve will exhibit a kink or jump, associated with an effective softening of the matter. In the $\Lambda - M$ curve, the transition manifests as a discontinuity over a small range in mass, leading to a sharp decrease in Λ; the higher the pressure at the transition, the less Λ decreases (Han and Steiner, 2019). Above the transition pressure, there are no distinguishable features and the curves behave as one would expect for a purely hadronic equation of state (compare, e.g., the two models labelled 964 and 974 in the region $1 - 2\,M_\odot$ in Fig. 8.1). This is a particular manifestation of the so-called *masquerade problem* (Alford et al., 2005).

For several of the models we consider, the phase transitions occur at masses $\lesssim M_\odot$. Assuming the standard supernova mechanism of generating neutron stars, recent work suggests a minimum formation mass of $\sim 1.17M_\odot$ (Suwa et al., 2018). Therefore, the phase-transition region is unlikely to be probed by neutron-star measurements. In order to identify the phase transition, one would need it to occur at sufficiently high mass and resolve the region around that transition mass to high enough precision. Assuming an exceptional GW170817-like event observed by third-generation detectors, one might be able to constrain the error in the neutron-star radius ΔR to $\sim 50 - 200\,\mathrm{m}$ and tidal deformability to a level of $\Delta\Lambda \sim 20$ for a range of masses (Chatziioannou, 2022). This ideal scenario, ignoring possible systematic errors (Boudon et al., 2025), would be enough to constrain the matter models in Fig. 8.1, provided the range of observations included the transition mass. Reaching the required level of precision for weaker events will be challenging.

There have, nevertheless, been valuable attempts to use measurements of M, R and Λ to search for the presence of phase transitions. Recent studies (Annala et al., 2020, 2023) argue that the most massive neutron stars contain quark-matter cores. Additionally, it has been shown that gravitational waves may provide evidence for strong phase transitions (Han and Steiner, 2019; Chatziioannou and Han, 2020; Pang et al., 2020). However, in this chapter we concern ourselves with a dynamical effect in binary inspirals that may provide additional information about the transition. As previously mentioned in this thesis, oscillation modes of a neutron star can be excited during a binary inspiral, causing the mode amplitude to rapidly grow as energy is extracted from the orbit, leaving an imprint on the gravitational-wave phase. Suppose the neutron star has a sharp density discontinuity in its interior, caused by a first order phase transition, and a fluid element traverses this interface. The fluid parcel, which maintains pressure equilibrium with its surroundings, has the properties of its original position. As it is displaced across the interface, the element will suddenly be in an environment of differing composition and density. Assuming that the reaction timescales that equilibrate the fluid element to its new environment are slower than the timescale of the perturbation, it will be subject to a buoyancy force that restores the parcel to its origin on the other side of the interface (analogous to compositional g-modes discussed in previous chapters.). This is expected to be the case if the relevant phase conversion (the speed of the phase boundary) is limited by the weak interaction, as in the models in Fig. 8.1. This type of oscillation is know as an interfacial or i-modes (also known as discontinuity g-modes) (Gabriel and Scuflaire, 1979; McDermott, 1990; Miniutti et al., 2003). If, on the other hand, the strong-interaction timescale applies then the fluid parcel will equilibrate too quickly to produce an oscillation mode. In this Chapter we present an observational strategy that could provide direct evidence for a sharp, first-order phase boundary using i-modes.

8.1 Toy Model

Before moving to the numerical results for realistic neutron-star models—especially the scaling with the parameters associated with a phase transition—we examine the spectrum of a Newtonian, two-layer, incompressible star with a sharp density discontinuity between the layers.

Consider a star with the following mass-density

$$\rho(r) = (\rho_{\rm i} - \rho_{\rm o})\Theta(r_{\rm i} - r) + \rho_{\rm o}\Theta(R - r)\,, \tag{8.1}$$

where $\Theta(r)$ represents the Heaviside step function,$\rho_{\rm i}$ is the density of the inner sphere that extends to radius $r_{\rm i}$, $\rho_{\rm o}$ is the density of the outer shell and R is the total radius of the star. The discontinuity occurs at $r = r_{\rm i}$ and corresponds to a jump of $\rho_{\rm i} - \rho_{\rm o}$. We will see later how we require this density jump to be positive in order for an interface mode to exist.

We consider perturbations about this equilibrium and treat them as incompressible, such that the Lagrangian variation of the density vanishes, $\Delta\rho = 0$. This then leads to

$$\nabla_j \xi^j = 0 \tag{8.2}$$

and

$$\delta\rho = \xi^r\left[(\rho_{\rm i} - \rho_{\rm o})\delta(r_{\rm i} - r) + \rho_{\rm o}\delta(R - r)\right], \tag{8.3}$$

where $\delta(r)$ is the Dirac delta function, ξ^j is the Lagrangian displacement vector and $\delta\rho$ is the Eulerian change of the density. As the displacement is divergence free, Eq. (8.2), the fluid flow is irrotational and we can freely define a scalar potential ψ such that

$$\xi^j = \nabla^j \psi \tag{8.4}$$

and therefore must satisfy Laplace's equation,

$$\nabla^2 \psi = 0\,. \tag{8.5}$$

As in the previous section, the main equation for the pulsations is the Euler equation. For simplicity, we will adopt the Cowling approximation and search for harmonic solutions of frequency ω. Thus,

$$-\omega^2 \xi_j = -\frac{1}{\rho}\nabla_j \delta p + \frac{\nabla_j p}{\rho^2}\delta\rho\,, \tag{8.6}$$

where p is the pressure and δp is its corresponding Eulerian perturbation. According to Eq. (8.3), $\delta\rho$ vanishes everywhere except at the two interfaces—inside the star at $r = r_{\rm i}$ and at the surface $r = R$. Hence, the linearised Euler equation (8.6) infers that δp also satisfies Laplace's equation,

$$\nabla^2 \delta p = 0 \quad \text{for } 0 \le r < r_{\rm i} \text{ and } r_{\rm i} < r < R\,, \tag{8.7}$$

away from the interfaces.

At this point, we know that ψ and δp obey Laplace's equation, Eqs. (8.5) and (8.7), in the regions of the star away from the interfaces. The solutions are then given by

$$\psi(r,\theta,\varphi) = \psi_l(r) Y_l^m(\theta,\varphi)\,, \tag{8.8}$$

$$\delta p(r,\theta,\varphi) = \delta p_l(r) Y_l^m(\theta,\varphi)\,, \tag{8.9}$$

where Y_l^m is a spherical harmonic of degree l and order m, and

$$\psi_l(r) = \begin{cases} a_l r^l + b_l/r^{l+1} & \text{for } 0 \le r < r_\mathrm{i}\,, \\ \bar{a}_l r^l + \bar{b}_l/r^{l+1} & \text{for } r_\mathrm{i} < r < R\,, \end{cases} \tag{8.10}$$

$$\delta p_l(r) = \begin{cases} c_l r^l + d_l/r^{l+1} & \text{for } 0 \le r < r_\mathrm{i}\,, \\ \bar{c}_l r^l + \bar{d}_l/r^{l+1} & \text{for } r_\mathrm{i} < r < R\,. \end{cases} \tag{8.11}$$

Since the background is spherically symmetric, there will be no explicit dependence on m in the radial eigenfunctions and eigenfrequency. We can straight away remove two constants by demanding regularity at the stellar centre,

$$b_l = d_l = 0\,. \tag{8.12}$$

To determine the variables, we require six conditions. Three are provided by examining the Euler equation (8.6) in the two regions. The remaining three constraints come from the boundary conditions: continuity of ξ^r and the Lagrangian perturbation of the pressure Δp at the interface $r = r_\mathrm{i}$, and vanishing pressure $\Delta p = 0$ at the surface $r = R$.

To make the calculation more tractable, we will assert that the density jump is small, such that

$$\rho_\mathrm{o} = \rho_\mathrm{i}(1-\epsilon)\,, \tag{8.13}$$

where $|\epsilon| \ll 1$ is a small, dimensionless parameter. We will see in a moment how we require that ϵ is positive in order for there to be an oscillation due to the interface. We work to leading order in ϵ to find the solutions to the perturbation problem. The boundary condition at the surface provides

$$\begin{aligned} &\left\{\bar{c}_l - l\bar{a}_l \frac{4\pi G\rho_\mathrm{i}^2}{3}\left[1+\epsilon\left(-2+\left(\frac{r_\mathrm{i}}{R}\right)^3\right)\right]\right\} R^l + \\ &\qquad \left\{\bar{d}_l + (l+1)\bar{b}_l \frac{4\pi G\rho_\mathrm{i}^2}{3}\left[1+\epsilon\left(-2+\left(\frac{r_\mathrm{i}}{R}\right)^3\right)\right]\right\} \frac{1}{R^{l+1}} = 0\,. \end{aligned} \tag{8.14}$$

We can eliminate the coefficients c_l, $\bar{c}_l$ and $\bar{d}_l$ using Eq. (8.6) on both sides of the interface. These terms appear in Eq. (8.14) and the continuity of Δp at $r = r_{\rm i}$, which become

$$\left[\omega^2(1-\epsilon)\bar{a}_l + \left(-\omega^2 + \epsilon l \frac{4\pi G\rho_{\rm i}}{3}\right) a_l\right] r_{\rm i}^l + \omega^2(1-\epsilon)\frac{\bar{b}_l}{r_{\rm i}^{l+1}} = 0\,, \tag{8.15}$$

$$\begin{aligned} &\left\{\omega^2 - l\frac{4\pi G\rho_{\rm i}}{3} - \epsilon\left[\,]\omega^2 + l\frac{4\pi G\rho_{\rm i}}{3}\left(-2 + \left(\frac{r_{\rm i}}{R}\right)^3\right)\right]\right\}\bar{a}_l R^l \\ &+ \left\{\omega^2 + (l+1)\frac{4\pi G\rho_{\rm i}}{3} - \epsilon\left[\omega^2 - (l+1)\frac{4\pi G\rho_{\rm i}}{3}\left(-2 + \left(\frac{r_{\rm i}}{R}\right)^3\right)\right]\right\}\frac{\bar{b}_l}{R^{l+1}} = 0\,. \end{aligned} \tag{8.16}$$

We are currently left with Eqs. (8.15) and (8.16), as well as the continuity of ξ^r, which depend on a_l, $\bar{a}_l$ and $\bar{b}_l$. We remove a_l by combining the continuity condition on ξ^r and (8.15) to obtain

$$\epsilon\left(\omega^2 - l\frac{4\pi G\rho_{\rm i}}{3}\right) l\bar{a}_l r_{\rm i}^l = \left\{(2l+1)\omega^2 - \epsilon l\left[\omega^2 + (l+1)\frac{4\pi G\rho_{\rm i}}{3}\right]\right\}\frac{\bar{b}_l}{r_{\rm i}^{l+1}}\,. \tag{8.17}$$

Since the coefficient of $\bar{a}_l$ in Eq. (8.17) is $O(\epsilon)$, we can immediately infer that $\bar{b}_l = 0$ if the discontinuity vanishes. This describes the standard f-mode behaviour, which rises as $\propto r^l$ up to the surface. In the absence of an interface, this is the only mode that a uniform-density star supports. We will encounter its solution for the star with a phase transition in a moment. Finally, we combine Eqs. (8.16) and (8.17) to remove $\bar{a}_l$ or $\bar{b}_l$ from the system. Either way, we arrive at a quadratic equation in ω^2,

$$\begin{aligned} &\Biggl\{-(2l+1) + \epsilon\Biggl[2l + 1 + l\Biggl(1 - \left(\frac{r_{\rm i}}{R}\right)^{2l+1}\Biggr)\Biggr]\Biggr\}\omega^4 + l\Biggl\{2l + 1 + \epsilon\Biggl[(2l+1)\Biggl(-2 + \left(\frac{r_{\rm i}}{R}\right)^3\Biggr) \\ &\qquad + 1 - \left(\frac{r_{\rm i}}{R}\right)^{2l+1}\Biggr]\Biggr\}\frac{4\pi G\rho_{\rm i}}{3}\omega^2 - \epsilon l^2(l+1)\left[1 - \left(\frac{r_{\rm i}}{R}\right)^{2l+1}\right]\left(\frac{4\pi G\rho_{\rm i}}{3}\right)^2 = 0\,. \end{aligned} \tag{8.18}$$

From the quadratic expression (8.18), we will determine the oscillation frequencies for the two modes that the star supports.

The first has frequency

$$\omega^2 = \frac{GM}{R^3}l\,, \tag{8.19}$$

where M represents the total mass of the star. This is the familiar result for the fundamental f-mode of an incompressible star (in the Cowling approximation). It is interesting to note that we obtain precisely the same formula in terms of M/R^3 as if the interface disappeared. This provides a simple illustration of why universal relations fare so well (Chan et al., 2014). We also observe that its amplitude is (to linear order) totally insensitive to the interface, since the coefficients are

$$\bar{a}_l = a_l\,, \qquad \bar{b}_l = 0\,. \tag{8.20}$$

As we noted above, the f-mode eigenfunctions rise gradually up the surface, which (effectively) behaves as an interface between the fluid and vacuum exterior. In this sense, the f-mode is like an interface mode. Since the f-mode couples so efficiently to the tide, this provides a hint for why i-modes may also have strong tidal couplings.

The second solution to Eq. (8.18) is $O(\epsilon)$ and thus arises due to the presence of the interface in the fluid interior. This mode oscillates at

$$\omega^2 = \epsilon \frac{GM}{R^3} \frac{l(l+1)}{2l+1} \left[1 - \left(\frac{r_\mathrm{i}}{R} \right)^{2l+1} \right] . \tag{8.21}$$

This is the interfacial *i*-mode of the star that is sourced by the presence of the density discontinuity ϵ. Here, we see that ϵ must be positive to give rise to a real, oscillating solution. Otherwise, the perturbation is immediately damped. The eigenfunctions of the *i*-mode are given by

$$\bar{a}_l = -a_l \frac{1}{(R/r_\mathrm{i})^{2l+1} - 1} (1+\epsilon) , \qquad \bar{b}_l = -a_l \frac{l}{l+1} \frac{R^{2l+1}}{(R/r_\mathrm{i})^{2l+1} - 1} \left[1 + \epsilon \left(\frac{r_\mathrm{i}}{R} \right)^{2l+1} \right] . \tag{8.22}$$

Here, we see that this mode rises in an identical fashion to the *f*-mode up to the interface and then obtains a non-vanishing $\bar{b}_l$ that decays as $\propto 1/r^{l+1}$. It is interesting to note that in the $\epsilon \longrightarrow 0$ limit, the *i*-mode becomes a trivial current in the star: both $\bar{a}_l$ and $\bar{b}_l$ are non-zero in this limit. Only when $\epsilon > 0$, the mode starts oscillating and sourcing finite density and pressure perturbations. One can estimate the frequency of this mode as

$$\omega^2 \approx (2\pi \times 686\ \mathrm{Hz})^2 \left(\frac{\epsilon}{0.1} \right) \left(\frac{M}{1.4 M_\odot} \right) \left(\frac{10\ \mathrm{km}}{R} \right)^3 \frac{l(l+1)}{2l+1} \left[1 - \left(\frac{r_\mathrm{i}}{R} \right)^{2l+1} \right] . \tag{8.23}$$

We will now examine the tidal overlap integrals of these two modes. The overlap is determined by (Lai, 1994)

$$\begin{aligned} Q_l &= \int \delta\rho_l r^{l+2}\, dr \\ &= \rho_\mathrm{i} \left\{ l \bar{a}_l \left[R^{2l+1} - \epsilon \left(R^{2l+1} - r_\mathrm{i}^{2l+1} \right) \right] - (l+1) \bar{b}_l \right\} , \end{aligned} \tag{8.24}$$

where $\delta\rho(r,\theta,\varphi) = \delta\rho_l(r) Y_l^m(\theta,\varphi)$. We observe that Q_l is the contribution of the mode to the mass multipole moment of degree l. Next, we note that the oscillating solutions we have found have free amplitudes. However, when the tide sources the perturbation, this amplitude is set by the tidal coupling. Therefore, it is necessary to introduce the mode normalisation constant

$$\begin{aligned} \mathcal{A}^2 &= \int \rho \left[\left(\frac{d\psi_l}{dr} \right)^2 r^2 + l(l+1)\psi_l^2 \right] dr \\ &= \rho_\mathrm{i} \left\{ l a_l^2 r_\mathrm{i}^{2l+1} + (1-\epsilon) \left[1 - \left(\frac{r_\mathrm{i}}{R} \right)^{2l+1} \right] \left[l \bar{a}_l^2 R^{2l+1} + (l+1) \frac{\bar{b}_l^2}{r_\mathrm{i}^{2l+1}} \right] \right\} . \end{aligned} \tag{8.25}$$

The choice of normalisation does not impact the result. It is the quantity $Q_l/\mathcal{A}$, which is independent of the amplitude, that describes the dynamics (Andersson and Pnigouras, 2020).

Now, we calculate the couplings for the two mode solutions. The overlap between the tide and the f-mode is particularly simple and we find that

$$\frac{Q_l}{\mathcal{A}/\sqrt{MR^2}} = MR^l\sqrt{\frac{3l}{4\pi}}\left\{1 - \epsilon\frac{1}{2}\left[\left(\frac{r_\mathrm{i}}{R}\right)^3 - \left(\frac{r_\mathrm{i}}{R}\right)^{2l+1}\right]\right\}. \tag{8.26}$$

In contrast to its eigenfrequency, the overlap integral for the f-mode does have a dependence on ϵ and r_i. The calculation for the i-mode is substantially more involved, requiring that the mode eigenfunctions are determined to second order in ϵ. Therefore, not an insignificant amount of algebra reveals

$$\frac{Q_l}{\mathcal{A}/\sqrt{MR^2}} = -\epsilon^2 MR^l\sqrt{\frac{3}{4\pi}\frac{l(l+1)}{2l+1}}\sqrt{1-\left(\frac{r_\mathrm{i}}{R}\right)^{2l+1}}\left(\frac{r_\mathrm{i}}{R}\right)^{(2l+1)/2}\left[1-\left(\frac{r_\mathrm{i}}{R}\right)^3\right]. \tag{8.27}$$

Here, we see that the overlap for the i-mode is also dependent on the depth of the phase transition and its position in the star. The overlap integral is a function of ϵ^2 and has a non-linear dependence on the position of the interface. We can estimate this as

$$Q_l = -10^{-2}\left(\frac{\epsilon}{0.1}\right)^2 MR^l\sqrt{\frac{3}{4\pi}\frac{l(l+1)}{2l+1}}\sqrt{1-\left(\frac{r_\mathrm{i}}{R}\right)^{2l+1}}\left(\frac{r_\mathrm{i}}{R}\right)^{(2l+1)/2}\left[1-\left(\frac{r_\mathrm{i}}{R}\right)^3\right]. \tag{8.28}$$

For $l = 2$, we find that the overlap has a maximum at $r_\mathrm{i} \approx 0.726R$.

8.2 Results

Now on to the numerical results. We will assume a barotropic equation of state $p = p(\varepsilon)$ This has two advantages. First, the star will not support composition g-modes, which simplifies the mode spectrum we have to consider. Second, treating the matter as a perfect fluid, we can immediately calculate the speed of sound c_s as measured by a co-moving observer using

$$\left(\frac{c_\mathrm{s}}{c}\right)^2 = \frac{dp}{d\varepsilon}, \tag{8.29}$$

where c is the speed of light. We adopt c_s^2 as the fundamental thermodynamical variable and integrate Eq. (8.29) to obtain $p = p(\varepsilon)$. Invoking causality and thermodynamical stability arguments lead to the trivial constraint $0 \leq (c_\mathrm{s}/c)^2 < 1$. Using results from low densities, where the theoretical understanding is robust, one can extend the equation of state to higher densities by sampling c_s^2 and ensuring that it obeys the constraints (Tews et al., 2018a,b). This sampling generates an equation of state family.

One may generate additional models by allowing for first-order phase transitions of arbitrary location and width. This approach does not allow us to extract information on the composition of dense matter or the type of a phase transition but it does provide a useful way to test the effect such a transition has on neutron-star properties and observables. Moreover, the collection of models we use (Capano et al., 2020) is agnostic in the sense that some of the models have phase transitions, while others do not.

To make progress beyond the incompressible model, we need to use general relativity. For simplicity, we ignore temperature, rotation and continue to assume a perfect-fluid star and thus use the Cowling approximation methodology discussed in Chapter 4. Unlike previous calculations of interface modes, such as Miao et al. (2024), we do not include any jump conditions or perform matching at the phase transition when solving the oscillation mode equations. Instead, we take an agnostic approach and solve the equations in an identical manner regardless of whether or not a phase transition is present, allowing the numerics to identify any discontinuities.

It is, however, important to add caveats to these assumptions. In particular, it is clear that some of the interface modes shown in Fig. 8.3 have frequencies such that they would only become resonant very late in the binary inspiral. Some of the models may, in fact, not be relevant as the stars would merge before the mode resonance (see Read et al. (2013) for realistic estimates of the merger frequency). Later on we will check this by estimating the merger frequency. Moreover, in the relevant regime the Newtonian inspiral estimate we are relying on is—at best—indicative as it ignores the impact of the curved spacetime and non-linear aspects of the tide (see Yu et al. (2023) for a relevant discussion). However, given the lack of fully relativistic models for the dynamical tide (including actual resonances) and the challenges associated with developing such models (Pitre and Poisson, 2024), we have to resort to this approximate analysis. Our expectation is that our proof-of-principle demonstration will stimulate the development of truly quantitative tidal models along with parallel work on the problems of detection and parameter inference.

Using our collection of equation of state models, the quadrupolar $l = 2$ interface modes were calculated for a set of neutron-star masses. An example of the eigenfunctions $W_l(r)$ and $V_l(r)$ for an i-mode are shown in Fig. 8.2 for one of our equation of state models. As explored in the incompressible stellar model, the eigenfunctions rise up to the location of the interface and then inherit a sharp kink. The radial eigenfunction W_l is continuous across the interface, while the tangential eigenfunction V_l is not.

We then used the obtained values for $\Delta\Phi$ from Eq. (6.9) for an equal-mass system at a luminosity distance of 40 Mpc (the inferred distance to GW170817) to estimate the detectability of each resonance. Results for $M = 1.4M_\odot$ are summarised by Fig. 8.3. The results show that the frequency of the mode typically lies between that of the f-mode, $O(2\text{ kHz})$, and the frequency range where one would expect to find the composition g-modes of non-barotropic models, $O(100\text{ Hz})$ as demonstrated by the results of the previous chapters. This makes the interface-mode resonance distinct from the rest of the oscillation spectrum. The results for $\Delta\Phi$ are compared to the sensitivity curve of LIGO Livingston during the observation of GW170817 and the anticipated sensitivities of LIGO A+, Cosmic Explorer and the Einstein Telescope. For completeness the results were repeated for additional neutron star masses as

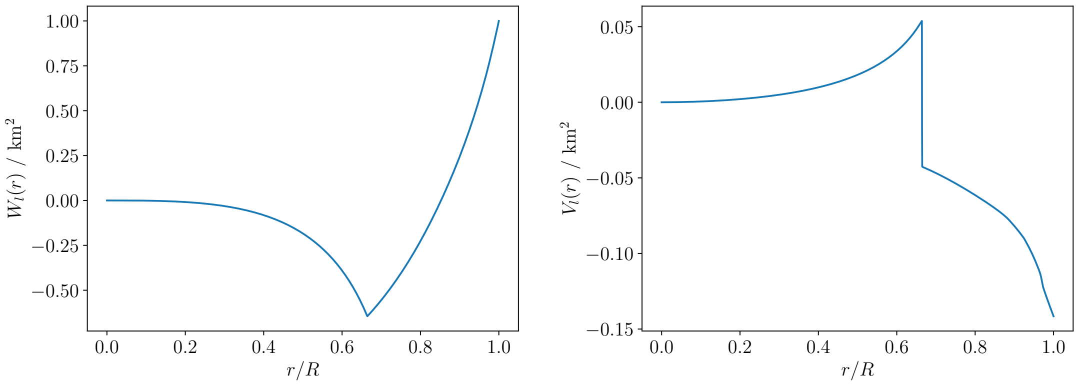

FIGURE 8.2: Eigenfunctions $W_l(r)$ and $V_l(r)$ for a typical interface mode of an $M = 1.4M_\odot$ neutron star. As explored in the incompressible stellar model, the eigenfunctions rise up to the location of the interface and then inherit a sharp kink. The radial eigenfunction W_l is continuous across the interface, while the tangential eigenfunction V_l is not.

shown in Fig. 8.4. The trend with the location of the interface r_i is also shown in Fig. 8.5 though the trend here is less discernable.

While the overall trends are not easily extractable, the main result is clear: the majority of the identified interface-mode resonances would be detectable already by an instrument at the LIGO A+ level and (nearly) all of them would be within reach of next-generation detectors. In accordance with the analytical calculation that led to Eqs. (8.23) and (8.28), we see that generally the larger the relative energy-density jump, the greater the mode frequency and the phase shift. This agrees with the (obvious) expectation that detection prospects are more favourable for stronger phase transitions. For higher masses, despite the phase-shift decrease with M in Eq. (6.9), our results show that approximately half of the models would still be detectable by next-generation instruments for equal-mass $M = 1.8M_\odot$ systems as shown in Fig. 8.4.

At this point, we make it clear that in Figs. 8.3 - 8.4, r_i/R is not fixed while $\Delta\epsilon/\epsilon_\mathrm{i}$ is varied and vice-versa in Fig. 8.5, this is due to the generation of the models allowing for first-order phase transitions of arbitrary location and width. Future work would generate additional models where $\Delta\epsilon/\epsilon_\mathrm{i}$ and r_i/R are allowed to be fixed and varied in respect to one another in order to further investigate the trends seen in this thesis.

It is worth emphasising that the interface modes may provide access to a lower density portion of the equation of state. For example, in Fig. 8.3 we highlight the i-mode resonance of model 964. As is evident from Fig. 8.1, the phase transition in this equation of state would be *inaccessible* with measurements of M, R and Λ.

An important sanity check, as mentioned earlier, is to make sure these modes are resonant in the inspiral in order to be detected by gravitational waves. To do this we first estimate the

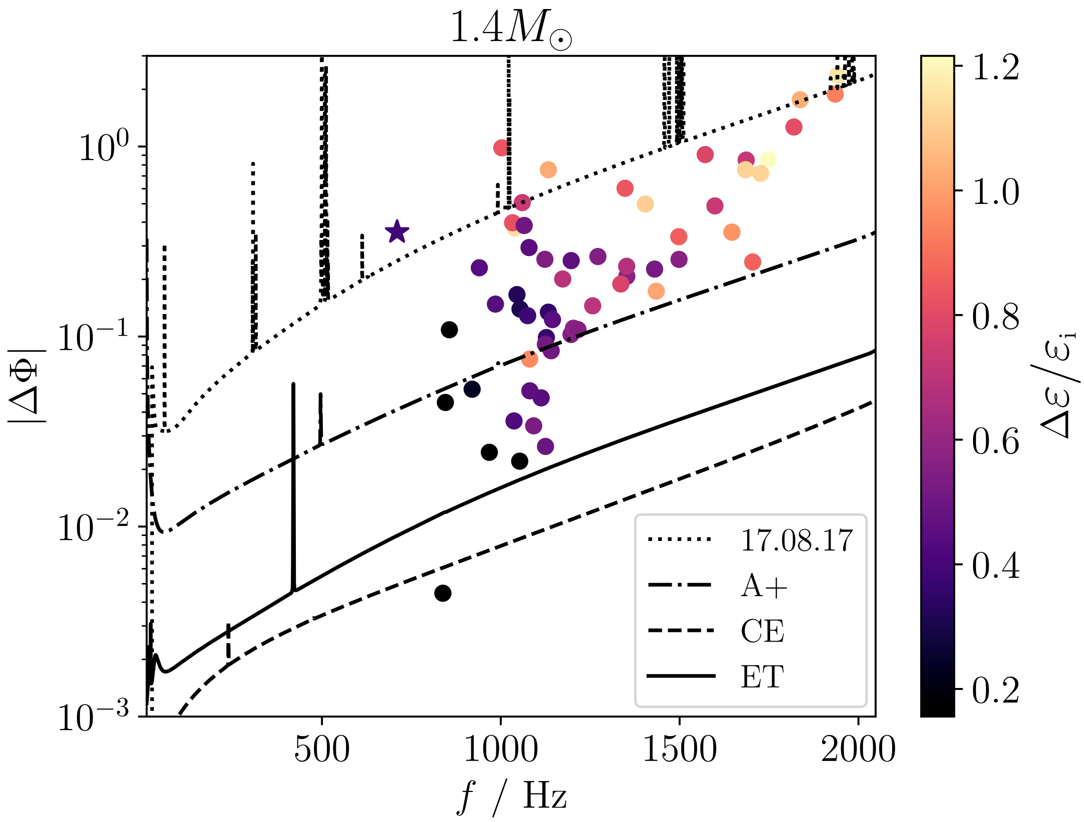

FIGURE 8.3: Estimated shift in orbital phase $|\Delta\Phi|$ against gravitational-wave frequency f for an equal-mass $M = 1.4M_\odot$ binary. Each marker corresponds to an $l = 2$ i-mode resonance computed from a different equation of state in the ensemble, coloured by the relative jump in energy density $\Delta\varepsilon/\varepsilon_{\rm i}$. We indicate with a star the interface mode associated with model 964 in Fig. 8.1. Also inlaid are the sensitivity curves for LIGO Livingston during the GW170817 event, LIGO A+ (dot-dashed), Cosmic Explorer (CE, dashed) and the Einstein Telescope (ET, solid), assuming the binary is at a luminosity distance of 40 Mpc from the instrument.

merger frequency f for the binary using the following relation from Damour et al. (2012)

$$(\pi M f)^{\frac{1}{2}} \approx C \tag{8.30}$$

where C is the compactness. Next we want to know the number of cycles that would be observed between the i-mode and the merger. This is estimated using the leading-order point-particle radiation reaction

$$\mathcal{N} = \frac{1}{2\pi}\frac{c^5}{32(G\mathcal{M})^{5/3}}\left(\frac{1}{\Omega_i^{5/3}} - \frac{1}{\Omega_f^{5/3}}\right) \approx 1285\left(\frac{1.22M_\odot}{\mathcal{M}}\right)^{5/3}\left(\frac{30\,\mathrm{Hz}}{\Omega_i/\pi}\right)^{5/3}\left[1 - \left(\frac{\Omega_i}{\Omega_f}\right)^{5/3}\right] \tag{8.31}$$

where $\mathcal{M}$ is the chirp mass and $\Omega_{i,f}$ are the initial and final orbital angular velocities. The results for all the models in Fig. 8.3 are shown in Table 8.1. As we can seen all the modes are resonant before merger and the majority at least one full cycle before but it is worth mentioning that the i-mode and merger frequencies are both estimates.

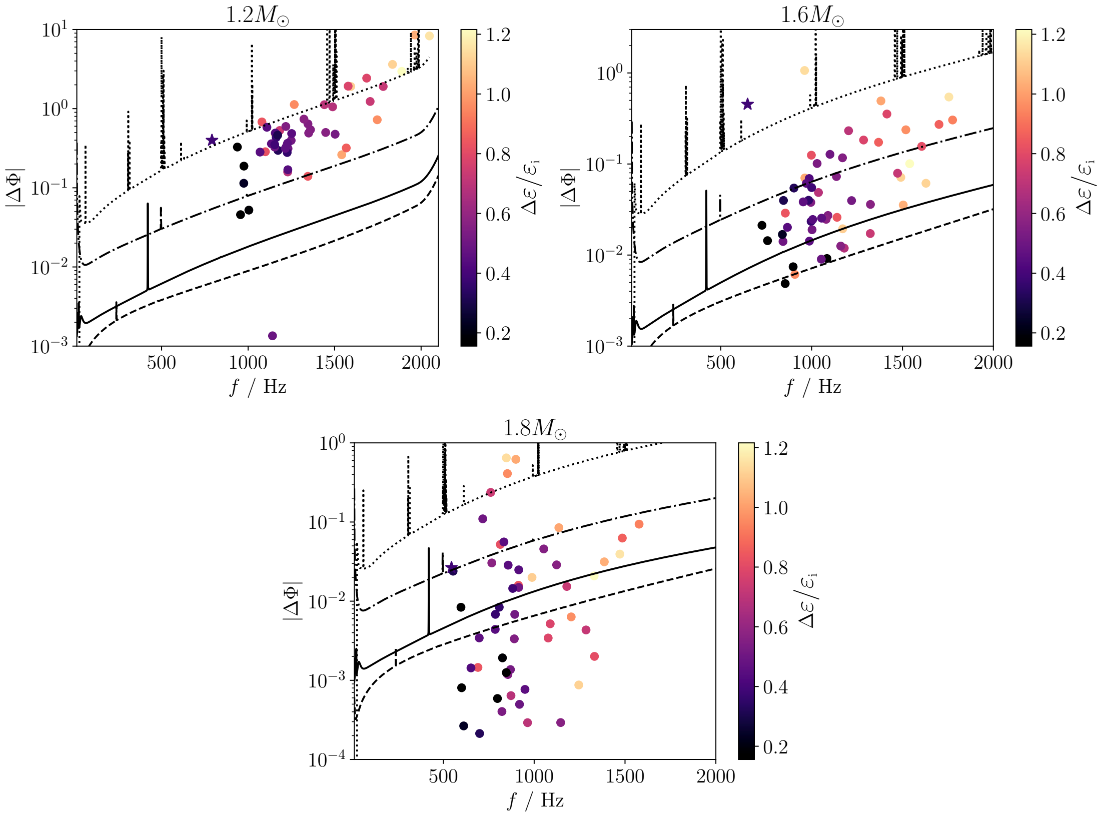

FIGURE 8.4: Estimated shift in orbital phase $|\Delta\Phi|$ against gravitational-wave frequency f for equal-mass $M = 1.2M_\odot$, $1.6M_\odot$ and $1.8M_\odot$ binaries. The markers, curves and colour bar are described in Fig. 8.3, which this figure complements by illustrating the scaling with mass.

It should also be mentioned that not all first order phase transitions would produce an *i*-mode. As seen in our toy model, the key criterion for the existence of an *i*-mode is the positive discontinuity in the density. If we consider the conditions present in an isolated neutron star: cold; neutrino-less and in beta-equilibrium, the first order transition can be modelled as either a Maxwell or Gibbs type (Glendenning, 1992; Constantinou et al., 2023). While a Maxwell type transition would produce the positive discontinuity needed for an *i*-mode, a Gibbs type transition would instead produce a mixed phase between the particle species either side of the transition. This would then smooth out the discontinuity and prevent an *i*-mode from occurring. Therefore while a single *i*-mode resonance signature would identify the presence of a phase transition, the absence of a detection would not rule out the existence of first order phase transitions due to the possibility of mixed phases.

The next challenge would be to constrain the onset density and size of the energy-density jump. As the frequency and phase shift depend on both parameters, multiple detections of the *i*-modes for different masses may be able to constrain both.

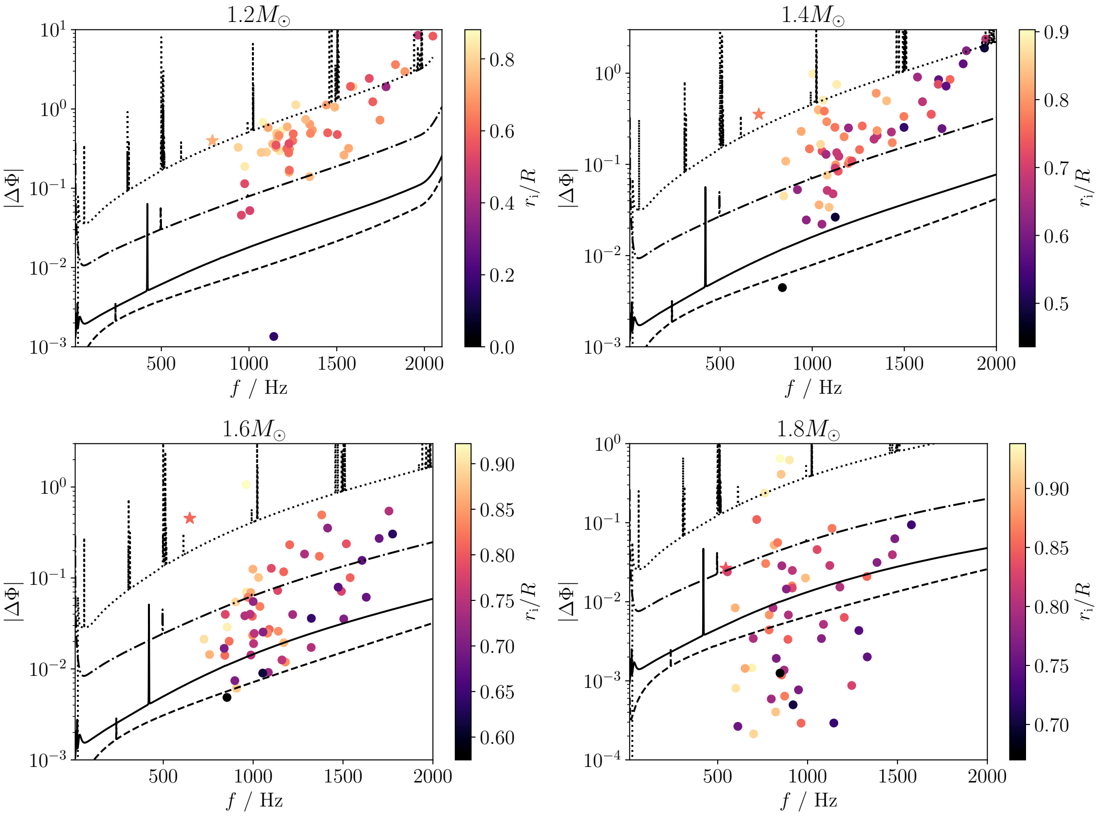

FIGURE 8.5: Estimated shift in orbital phase $|\Delta\Phi|$ against gravitational-wave frequency f for equal-mass $M = 1.2M_\odot$, $1.4M_\odot$, $1.6M_\odot$ and $1.8M_\odot$ binaries. The markers and curves are described in Fig. 8.3, which this figure complements by illustrating the scaling with mass. The colour bar shows the location of the phase transition r_i/R for each star. As one might expect from the incompressible-model problem, it is not straightforward to identify an overall trend from these results.

TABLE 8.1: Table listing the number of cycles, $\mathcal{N}$ between the i-mode, ω_i and the merger frequency f for each of the equation of state models used in Fig. 8.3 estimated using (8.30) and (8.31). Also listed in the table is the compactness C.

Model	ω_i/Hz	C	f/Hz	$\mathcal{N}$
14	1040	0.231	2562	2.72
19	1133	0.229	2529	2.23
31	1060	0.226	2480	2.56
33	1404	0.225	2463	1.29
37	1003	0.225	2463	2.88
55	1092	0.221	2398	2.35
62	845	0.220	2382	4.06
92	1045	0.217	2333	2.56
103	1352	0.216	2317	1.34
113	1081	0.215	2301	2.34
171	1748	0.211	2237	0.50
187	1435	0.210	2221	1.06
192	1037	0.210	2221	2.52
195	1646	0.210	2221	0.64
204	1498	0.209	2205	0.90
209	1033	0.209	2205	2.53
231	1347	0.208	2189	1.26
247	940	0.207	2174	3.11
275	1272	0.205	2142	1.45
288	1127	0.205	2142	2.01
293	1196	0.204	2127	1.71
322	1203	0.203	2111	1.67
325	1257	0.202	2095	1.46
332	1173	0.202	2095	1.77
346	856	0.201	2080	3.73
367	1684	0.200	2064	0.45
395	1079	0.198	2033	2.14
396	1942	0.198	2033	0.09
401	1216	0.198	2033	1.55
402	985	0.198	2033	2.68
405	1599	0.198	2033	0.56
416	1813	0.197	2018	0.23
429	1053	0.196	2003	2.25
438	1352	0.196	2003	1.08
441	1123	0.196	2003	1.90
452	1054	0.195	1987	2.23
461	1430	0.195	1987	0.87
466	1065	0.195	1987	2.17
495	1141	0.193	1957	1.77
500	968	0.193	1957	2.72
513	1113	0.192	1942	1.89
532	1133	0.191	1927	1.78
556	1704	0.190	1911	0.27
593	1336	0.188	1881	1.00
616	1837	0.187	1866	0.04
641	1081	0.185	1837	1.92
654	1125	0.185	1837	1.71
665	1572	0.185	1837	0.40
667	1144	0.184	1822	1.61
673	1820	0.184	1822	0.01
717	1686	0.182	1792	0.15
721	920	0.182	1792	2.87
750	1727	0.181	1777	0.07
773	1498	0.179	1748	0.43
803	1075	0.178	1733	1.81
811	1125	0.178	1733	1.57
816	1197	0.177	1719	1.25
883	838	0.175	1690	3.45
964	710	0.171	1632	4.95

Chapter 9

Conclusions

In this thesis, we have shown how asteroseismology can be used to shine a light on the multiple facets of a neutron star. Multiple regimes have been examined: Newtonian gravity; the relativistic Cowling approximation and full General Relativity. The pros, cons and limitations of the various regimes have been discussed. The Newtonian regime is relatively simple to solve numerically and thus new physics (e.g. rotation, phase transitions etc.) can be added to the problem without making the equations computationally expensive. However, as we know a neutron star is a relativistic object and thus the Newtonian equations can only serve as estimates or illustrate the problem. That is why the next regime, the Cowling approximation was explored. While the metric perturbations are ignored, the rest of the equations are relativistic and as discussed in Chapter 4 for modes such as the *g*-mode, this approximation is reliable. However the frequency of the *f*-mode can be overestimated by roughly 15 %. Therefore the fully relativistic regime was explored, the most accurate but numerically complicated of all three regimes. One downside of this regime is that, unlike the other two, the modes do not form a complete basis due to the eigenfrequencies now being complex. A consequence of this is that we can no longer calculate an overlap integral to represent the tidal response in general relativity. In Chapter 6 we therefore use our Newtonian and Cowling results when estimating the detectability of oscillation modes due to resonance in binary inspirals.

The main focus of our mode calculations have been the quadrupolar *g*-modes. In comparison to other oscillation modes such as the *f*- and *p*-modes, the *g*-modes are more sensitive to the underlying nuclear physic beyond macroscopic variables such as mass and radius. This is demonstrated in Chapter 4, where four different BSk equation of state models were employed. The differences between the BSk models used are in their fitting to nuclear parameters that have not been constrained by experimental or theoretical observations. While our results for mode frequencies will quantitively change for different equation of state models, the *g*-mode spectrum is still expected to be highly sensitive to the underlying nuclear physics, thus highlighting the importance of composition and stratification. With this in mind, the precise dependence on uncertain aspects of the underlying nuclear physics need to be further explored in future work.

In Chapter 6 we demonstrated how one could estimate the detectability of oscillation mode resonances in a gravitational wave signal emitted during a binary inspiral. A detection of a g-mode resonance during such an event would thus help better constrain the equation of state. However, our results indicate that such a detection would rely on next generation gravitational wave detectors such as the Einstein Telescope or Cosmic Explorer.

We have also expanded on the work of Andersson and Pnigouras (2019), in Chapter 3 and shown how the presence of weak nuclear reactions in a neutron star leads to a damping of the composition g-modes for arbitrary reaction rates. However realistic nuclear reactions tend to be very slow compared to the oscillation timescale of the low-order g-modes, leading to negligible damping. Work has begun extending this formalism to the incorporate non-leptonic weak reactions involving hyperons in Chapter 5. Due to the faster reaction rates involved, we have shown how the reactions suppress the g-modes and generate additional damping on the f-mode. Future work would extend this calculation to include additional hyperon species such as the Σ^- hyperon and fully explore the dependence of the mode damping times on the temperature of the neutron star.

In Chapter 8, the prospect of detecting the presence of first-order phase transitions via the resonance of a different class of oscillation mode, the interface or i-mode. The presence of the first-order phase transition in the equation of state gives rise to this oscillation mode. By examining an ensemble of equation of state we showed how the i-modes are tidally excited almost as strongly as the f-mode and should be excited before the merger. Such a detection would be a smoking-gun signal of a phase transition. One such phase transition that could be probed by this method is that from hadronic matter to deconfied quarks in the neutron star core, a robust prediction of quantum chromodynamics. The exact nature of this transition remains unsolved and therefore an i-mode detection would be a breakthrough discovery for nuclear physics. Future work would examine the possibility of constraining the onset density and size of the energy-density jump caused by the interface. As the frequency and phase shift depend on both parameters, multiple detections of the i-modes for different masses may be able to constrain both.

As well as studying the oscillation spectrum itself, in Chapter 7 we have examined the effective Love number, a key parameter that is sensitive to the internal structure of the neutron star and is linked to the star's dynamical tidal response. The standard approach of using a mode-sum has been analysed in Newtonian gravity for both non-rotating and slowly rotating background configurations. This method is, however, not extendable to general relativity, hence we presented our new approach that bypasses the problem. This strategy involves matching the solution for the linearised fluid dynamics in the star's interior to the spacetime perturbations in the near zone surrounding the body, along with an identification of the tidal driving and the star's response. We have exactly recreated the static and effective Love numbers in Newtonian gravity and have presented numerical results applying this approach in general relativity. Future work would seek to incorporate more realistic neutron star internal structure, beyond just composition and stratification. Also a disadvantage of our new approach is that we do not have access to an underlying equation for the mode amplitudes that would allow us to extend the near resonance solution from, for example, Yu et al. (2024a); Pnigouras et al. (2025a) to relativity. Therefore future work would also seek to link this methodology to the results in Chapter 6, extending those results from Newtonian gravity and the Cowling approximation to full general relativity.

The rapidly growing field of gravitational wave research is opening new windows into the very cores of neutron stars. As technology and theory both advance, we have shown how multiple aspects of the signal that can discern the underlying equation of state. While we are hoping for another GW170817-like event, there are still many future directions for this work.

References

A. Abac et al. The science of the einstein telescope, 2025. URL `https://arxiv.org/abs/2503.12263`.

B. P. Abbott et al. Observation of gravitational waves from a binary black hole merger. *Phys. Rev. Lett.*, 116:061102, Feb 2016. . URL `https://link.aps.org/doi/10.1103/PhysRevLett.116.061102`.

B. P. Abbott et al. GW170817: Observation of Gravitational Waves from a Binary Neutron Star Inspiral. *Phys. Rev. Lett.*, 119(16):161101, October 2017. .

B. P. Abbott et al. GW170817: Measurements of Neutron Star Radii and Equation of State. *Phys. Rev. Lett.*, 121(16):161101, October 2018. .

B. P. Abbott et al. Properties of the Binary Neutron Star Merger GW170817. *Phys. Rev. X*, 9 (1):011001, January 2019. .

R. Abbott et al. Observation of gravitational waves from two neutron star–black hole coalescences. *The Astrophysical Journal Letters*, 915(1):L5, jun 2021. . URL `https://dx.doi.org/10.3847/2041-8213/ac082e`.

M. Alford, M. Braby, M. Paris, and S. Reddy. Hybrid Stars that Masquerade as Neutron Stars. *ApJ*, 629(2):969, August 2005. .

Mark G. Alford and Alexander Haber. Strangeness-changing rates and hyperonic bulk viscosity in neutron star mergers. *Phys. Rev. C*, 103(4):045810, April 2021. .

N Andersson and P Pnigouras. The g-mode spectrum of reactive neutron star cores. *Monthly Notices of the Royal Astronomical Society*, 489(3):4043–4048, 09 2019. ISSN 0035-8711. . URL `https://doi.org/10.1093/mnras/stz2449`.

N. Andersson and P. Pnigouras. Exploring the effective tidal deformability of neutron stars. *Phys. Rev. D*, 101(8):083001, April 2020. .

N. Andersson and P. Pnigouras. The phenomenology of dynamical neutron star tides. *MNRAS*, 503(1):533–539, May 2021. .

Nils Andersson. A Numerically Accurate Investigation of Black-Hole Normal Modes. *Proceedings of the Royal Society of London Series A*, 439(1905):47–58, October 1992. .

Nils Andersson. *Gravitational-Wave Astronomy: Exploring the Dark Side of the Universe*. 2019. .

Nils Andersson. A Gravitational-Wave Perspective on Neutron-Star Seismology. *Universe*, 7 (4):97, April 2021. .

Nils Andersson and G. Comer. Relativistic fluid dynamics: physics for many different scales. *Living Reviews in Relativity*, 24, 12 2021. .

Nils Andersson and Fabian Gittins. Formulating the r-mode problem for slowly rotating neutron stars. *The Astrophysical Journal*, 945(2):139, mar 2023. . URL `https://dx.doi.org/10.3847/1538-4357/acbc1e`.

Nils Andersson and Wynn C. G. Ho. Using gravitational-wave data to constrain dynamical tides in neutron star binaries. *Phys. Rev. D*, 97:023016, Jan 2018. . URL `https://link.aps.org/doi/10.1103/PhysRevD.97.023016`.

Nils Andersson and Kostas D. Kokkotas. Towards gravitational wave asteroseismology. *Monthly Notices of the Royal Astronomical Society*, 299(4):1059–1068, 10 1998. ISSN 0035-8711. . URL `https://doi.org/10.1046/j.1365-8711.1998.01840.x`.

Nils Andersson, Kostas D. Kokkotas, and Bernard F. Schutz. A new numerical approach to the oscillation modes of relativistic stars. *MNRAS*, 274(4):1039–1048, June 1995. .

Nils Andersson, Kostas D. Kokkotas, and Nikolaos Stergioulas. On the relevance of the r-mode instability for accreting neutron stars and white dwarfs. *The Astrophysical Journal*, 516(1): 307, may 1999. . URL `https://dx.doi.org/10.1086/307082`.

Nils Andersson, Rhys Counsell, Fabian Gittins, and Suprovo Ghosh. The tidal response of a relativistic star. *arXiv e-prints*, art. arXiv:2511.05139, November 2025. .

E. Annala, T. Gorda, A. Kurkela, J. Nättilä, and A. Vuorinen. Evidence for quark-matter cores in massive neutron stars. *Nat. Phys.*, 16(9):907, June 2020. .

E. Annala, T. Gorda, J. Hirvonen, O. Komoltsev, A. Kurkela, J. Nättilä, and A. Vuorinen. Strongly interacting matter exhibits deconfined behavior in massive neutron stars. *Nat. Commun.*, 14:8451, December 2023. .

Richard Arnowitt, Stanley Deser, and Charles W. Misner. Republication of: The dynamics of general relativity. *General Relativity and Gravitation*, 40(9):1997–2027, September 2008. .

W. Baade and F. Zwicky. Cosmic rays from super-novae. *Proceedings of the National Academy of Sciences of the United States of America*, 20(5):259–263, 1934a. ISSN 00278424. URL `http://www.jstor.org/stable/86841`.

W. Baade and F. Zwicky. Cosmic Rays from Super-novae. *Contributions from the Mount Wilson Observatory*, 3:79–83, January 1934b.

Peter G. Bergmann. Summary of the Chapel Hill Conference. *Reviews of Modern Physics*, 29 (3):352–354, July 1957. .

T. Binnington and E. Poisson. Relativistic theory of tidal Love numbers. *Phys. Rev. D*, 80(8): 084018, October 2009. .

George David Birkhoff and Rudolph Ernest Langer. *Relativity and modern physics*. 1923.

David Blaschke and Nicolas Chamel. Phases of Dense Matter in Compact Stars. In Luciano Rezzolla, Pierre Pizzochero, David Ian Jones, Nanda Rea, and Isaac Vidaña, editors, *Astrophysics and Space Science Library*, volume 457 of *Astrophysics and Space Science Library*, page 337, January 2018. .

J. Boguta and A. R. Bodmer. Relativistic calculation of nuclear matter and the nuclear surface. , 292(3):413–428, December 1977. .

Ignazio Bombaci. The Hyperon Puzzle in Neutron Stars. In *Proceedings of the 12th International Conference on Hypernuclear and Strange Particle Physics (HYP2015*, page 101002, January 2017. .

H. Bondi. Plane Gravitational Waves in General Relativity. , 179(4569):1072–1073, May 1957. .

A. Boudon, H. Qi, J.-F. Coupechoux, P. Landry, and V. Sordini. A realistic projection for constraining neutron star equation of state with the ligo-virgo-kagra detector network in the a+ era. preprint, 2025. URL `https://arxiv.org/abs/2501.11585`.

C. D. Capano, I. Tews, S. M. Brown, B. Margalit, S. De, S. Kumar, D. A. Brown, B. Krishnan, and S. Reddy. Stringent constraints on neutron-star radii from multimessenger observations and nuclear theory. *Nat. Astron.*, 4:625, March 2020. .

James Sir Chadwick. The existence of a neutron. *Proceedings of The Royal Society A: Mathematical, Physical and Engineering Sciences*, 136:692–708, 1932. URL `https://api.semanticscholar.org/CorpusID:91182340`.

N. Chamel and P. Haensel. Physics of Neutron Star Crusts. *Living Rev. Rel.*, 11:10, 2008. .

N. Chamel, S. Goriely, and J. M. Pearson. Further explorations of Skyrme-Hartree-Fock-Bogoliubov mass formulas. XI. Stabilizing neutron stars against a ferromagnetic collapse. *Phys. Rev. C*, 80(6):065804, December 2009. .

N. Chamel, A. F. Fantina, J. L. Zdunik, and P. Haensel. Neutron drip transition in accreting and nonaccreting neutron star crusts. *Phys. Rev. C*, 91:055803, May 2015. . URL `https://link.aps.org/doi/10.1103/PhysRevC.91.055803`.

T. K. Chan, Y. H. Sham, P. T. Leung, and L. M. Lin. Multipolar universal relations between f-mode frequency and tidal deformability of compact stars. *Phys. Rev. D*, 90(12):124023, December 2014. .

K. Chatziioannou. Uncertainty limits on neutron star radius measurements with gravitational waves. *Phys. Rev. D*, 105(8):084021, April 2022. .

K. Chatziioannou and S. Han. Studying strong phase transitions in neutron stars with gravitational waves. *Phys. Rev. D*, 101(4):044019, February 2020. .

Constantinos Constantinou, Tianqi Zhao, Sophia Han, and Madappa Prakash. Framework for phase transitions between the Maxwell and Gibbs constructions. *Phys. Rev. D*, 107(7): 074013, April 2023. .

A R Counsell, F Gittins, and N Andersson. The impact of nuclear reactions on the neutron-star g-mode spectrum. *MNRAS*, 531(1):1721–1729, 05 2024. ISSN 0035-8711. . URL `https://doi.org/10.1093/mnras/stae1242`.

A. R. Counsell, F. Gittins, N. Andersson, and P. Pnigouras. Neutron star g modes in the relativistic Cowling approximation. *Mon. Not. R. Astron. Soc.*, 536(2):1967, January 2025a. .

A. R. Counsell, F. Gittins, N. Andersson, and I. Tews. Interface Modes in Inspiralling Neutron Stars: A Gravitational-Wave Probe of First-Order Phase Transitions. *Phys. Rev. Lett.*, 135(8): 081402, August 2025b. .

T. G. Cowling. The Non-radial Oscillations of Polytropic Stars. *Monthly Notices of the Royal Astronomical Society*, 101(8):367–375, 12 1941. ISSN 0035-8711. . URL `https://doi.org/10.1093/mnras/101.8.367`.

Thibault Damour, Alessandro Nagar, and Loïc Villain. Measurability of the tidal polarizability of neutron stars in late-inspiral gravitational-wave signals. *Phys. Rev. D*, 85(12):123007, June 2012. .

S. De, D. Finstad, J. M. Lattimer, D. A. Brown, E. Berger, and C. M. Biwer. Tidal Deformabilities and Radii of Neutron Stars from the Observation of GW170817. *Phys. Rev. Lett.*, 121(9):091102, August 2018. .

S. Detweiler and L. Lindblom. On the nonradial pulsations of general relativistic stellar models. *ApJ*, 292:12–15, May 1985. .

Steven L. Detweiler and James R. Ipser. A Variational Principle and a Stability Criterion for the Non-Radial Modes of Pulsation of Stellar Models in General Relativity. *ApJ*, 185:685–708, October 1973. .

Tim Dietrich, Sebastian Khan, Reetika Dudi, Shasvath J. Kapadia, Prayush Kumar, Alessandro Nagar, Frank Ohme, Francesco Pannarale, Anuradha Samajdar, Sebastiano Bernuzzi, Gregorio Carullo, Walter Del Pozzo, Maria Haney, Charalampos Markakis, Michael Pürrer, Gunnar Riemenschneider, Yoshinta Eka Setyawati, Ka Wa Tsang, and Chris Van Den Broeck. Matter imprints in waveform models for neutron star binaries: Tidal and self-spin effects. *Phys. Rev. D*, 99:024029, Jan 2019. . URL `https://link.aps.org/doi/10.1103/PhysRevD.99.024029`.

C. Drischler, J. A. Melendez, R. J. Furnstahl, and D. R. Phillips. Quantifying uncertainties and correlations in the nuclear-matter equation of state. *Phys. Rev. C*, 102(5):054315, November 2020. .

L. Du, A. Sorensen, and M. Stephanov. The QCD phase diagram and Beam Energy Scan physics: A theory overview. *Int. J. Mod. Phys. E*, 33(7):2430008-374, January 2024. .

Robert C. Duncan and Christopher Thompson. Formation of Very Strongly Magnetized Neutron Stars: Implications for Gamma-Ray Bursts. *Astrophysical Journal Letters*, 392:L9, June 1992. .

A. Einstein. Die Grundlage der allgemeinen Relativitätstheorie. *Annalen der Physik*, 354(7): 769–822, January 1916a. .

A. Einstein and N. Rosen. On Gravitational Waves. *Journal of the Franklin Institute*, 223: 43–54, January 1937. .

Albert Einstein. Näherungsweise Integration der Feldgleichungen der Gravitation. *Sitzungsberichte der Königlich Preussischen Akademie der Wissenschaften*, pages 688–696, January 1916b.

Albert Einstein. Über Gravitationswellen. *Sitzungsberichte der Königlich Preussischen Akademie der Wissenschaften*, pages 154–167, January 1918.

E. Epelbaum, H. W. Hammer, and Ulf-G. Meißner. Modern theory of nuclear forces. *Rev. Mod. Phys.*, 81(4):1773, October 2009. .

M. Evans et al. Cosmic explorer: A submission to the nsf mpsac nggw subcommittee, 2023. URL `https://arxiv.org/abs/2306.13745`.

Edward D. Fackerell. Solutions of Zerilli's Equation for Even-Parity Gravitational Perturbations. *ApJ*, 166:197, May 1971. .

A. F. Fantina, N. Chamel, J. M. Pearson, and S. Goriely. Neutron star properties with unified equations of state of dense matter. *Astronomy and Astrophysics*, 559:A128, November 2013. .

Lee Samuel Finn. G-modes in zero-temperature neutron stars. *MNRAS*, 227:265–293, July 1987. .

Lee Samuel Finn. Relativistic stellar pulsations in the Cowling approximation. *MNRAS*, 232: 259–275, May 1988. .

É. É. Flanagan and T. Hinderer. Constraining neutron-star tidal Love numbers with gravitational-wave detectors. *Phys. Rev. D*, 77(2):021502, January 2008. .

J. L. Friedman and B. F. Schutz. Lagrangian perturbation theory of nonrelativistic fluids. *ApJ*, 221:937–957, May 1978a. .

J. L. Friedman and B. F. Schutz. Lagrangian perturbation theory of nonrelativistic fluids. *The Astrophysical Journal*, 221:937–957, May 1978b. .

M. Gabriel and R. Scuflaire. Properties of non-radial stellar oscillations. *Acta Astronaut.*, 29 (1):135, January 1979.

Suprovo Ghosh, Bikram Keshari Pradhan, Debarati Chatterjee, and Jürgen Schaffner-Bielich. Multi-Physics Constraints at Different Densities to Probe Nuclear Symmetry Energy in Hyperonic Neutron Stars. *Frontiers in Astronomy and Space Sciences*, 9:864294, March 2022. .

Suprovo Ghosh, Bikram Keshari Pradhan, and Debarati Chatterjee. Tidal heating as a direct probe of strangeness inside neutron stars. *Phys. Rev. D*, 109(10):103036, May 2024. .

F. Gittins and N. Andersson. Neutron-star seismology with realistic, finite-temperature nuclear matter. *Phys. Rev. D*, 111:083024, April 2025. .

F. Gittins, R. Matur, N. Andersson, and I. Hawke. Problematic systematics in neutron-star merger simulations. *Phys. Rev. D*, 111:023049, January 2025. .

Fabian Gittins and Nils Andersson. The r-modes of slowly rotating, stratified neutron stars. *Monthly Notices of the Royal Astronomical Society*, 521(2):3043–3057, 03 2023. ISSN 0035-8711. . URL `https://doi.org/10.1093/mnras/stad672`.

Fabian Gittins and Nils Andersson. Neutron-star seismology with realistic, finite-temperature nuclear matter, 2024. URL `https://arxiv.org/abs/2406.05177`.

Norman K. Glendenning. The hyperon composition of neutron stars. *Physics Letters B*, 114(6): 392–396, August 1982. .

Norman K. Glendenning. First-order phase transitions with more than one conserved charge: Consequences for neutron stars. *Phys. Rev. D*, 46(4):1274–1287, August 1992. .

Walter D. Goldberger, Jingping Li, and Ira Z. Rothstein. Non-conservative effects on spinning black holes from world-line effective field theory. *Journal of High Energy Physics*, 2021(6): 53, June 2021. .

S. Goriely, N. Chamel, and J. M. Pearson. Further explorations of skyrme-hartree-fock-bogoliubov mass formulas. xiii. the 2012 atomic mass evaluation and the symmetry coefficient. *Phys. Rev. C*, 88:024308, Aug 2013. . URL `https://link.aps.org/doi/10.1103/PhysRevC.88.024308`.

P. Haensel, K. P. Levenfish, and D. G. Yakovlev. Adiabatic index of dense matter and damping of neutron star pulsations. *Astron. Astrophys.*, 394:213–217, October 2002. .

P. Haensel, A. Y. Potekhin, and D. G. Yakovlev. *Neutron Stars 1 : Equation of State and Structure*, volume 326. 2007.

S. Han and A. W. Steiner. Tidal deformability with sharp phase transitions in binary neutron stars. *Phys. Rev. D*, 99(8):083014, April 2019. .

A. Hegade K. R., K. J. Kwon, Tejaswi Venumadhav, Hang Yu, and Nicolás Yunes. Relativistic and Dynamical Love. *arXiv e-prints*, art. arXiv:2507.10693, July 2025. .

Abhishek Hegade K. R., Justin L. Ripley, and Nicolás Yunes. Dynamical tidal response of nonrotating relativistic stars. *Phys. Rev. D*, 109(10):104064, May 2024. .

Jason W. T. Hessels, Scott M. Ransom, Ingrid H. Stairs, Paulo C. C. Freire, Victoria M. Kaspi, and Fernando Camilo. A Radio Pulsar Spinning at 716 Hz. *Science*, 311(5769):1901–1904, March 2006. .

A. Hewish, S. J. Bell, J. D. H. Pilkington, P. F. Scott, and R. A. Collins. Observation of a Rapidly Pulsating Radio Source. *Nature*, 217(5130):709–713, February 1968. .

T. Hinderer. Tidal Love Numbers of Neutron Stars. *ApJ*, 677(2):1216, April 2008. .

Tanja Hinderer. Tidal love numbers of neutron stars. *The Astrophysical Journal*, 677(2):1216, apr 2008. . URL `https://dx.doi.org/10.1086/533487`.

Tanja Hinderer, Benjamin D. Lackey, Ryan N. Lang, and Jocelyn S. Read. Tidal deformability of neutron stars with realistic equations of state and their gravitational wave signatures in binary inspiral. *Phys. Rev. D*, 81(12):123016, June 2010. .

Tanja Hinderer, Andrea Taracchini, Francois Foucart, Alessandra Buonanno, Jan Steinhoff, Matthew Duez, Lawrence E. Kidder, Harald P. Pfeiffer, Mark A. Scheel, Bela Szilagyi, Kenta Hotokezaka, Koutarou Kyutoku, Masaru Shibata, and Cory W. Carpenter. Effects of Neutron-Star Dynamic Tides on Gravitational Waveforms within the Effective-One-Body Approach. *Phys. Rev. Lett.*, 116(18):181101, May 2016. .

Wynn C. G. Ho. Gravitational waves from neutron stars and asteroseismology. *Philosophical Transactions of the Royal Society of London Series A*, 376(2120):20170285, May 2018. .

Wynn C. G. Ho and Nils Andersson. New dynamical tide constraints from current and future gravitational wave detections of inspiralling neutron stars. *Phys. Rev. D*, 108:043003, Aug 2023. . URL `https://link.aps.org/doi/10.1103/PhysRevD.108.043003`.

Wynn C. G. Ho and Dong Lai. Resonant tidal excitations of rotating neutron stars in coalescing binaries. *Mon. Not. R. Astron. Soc.*, 308(1):153–166, September 1999. .

Nadine Hornick, Laura Tolos, Andreas Zacchi, Jan-Erik Christian, and Jürgen Schaffner-Bielich. Relativistic parameterizations of neutron matter and implications for neutron stars. *Phys. Rev. C*, 98(6):065804, December 2018. .

R. A. Hulse and J. H. Taylor. Discovery of a pulsar in a binary system. *The Astrophysical Journal Letters*, 195:L51–L53, January 1975. .

Richard A. Isaacson. Gravitational Radiation in the Limit of High Frequency. II. Nonlinear Terms and the Effective Stress Tensor. *Physical Review*, 166(5):1272–1279, February 1968. .

J. T. Jebsen. On the General Spherically Symmetric Solutions of Einstein's Gravitational Equations in Vacuo. *Arkiv for Matematik, Astronomi och Fysik*, 15(18):18, January 1921.

P. B. Jones. Bulk viscosity of neutron-star matter. *Phys. Rev. D*, 64(8):084003, October 2001. .

Sanika Khadkikar, Ish Gupta, Rahul Kashyap, Koustav Chandra, Rossella Gamba, and Bangalore S. Sathyaprakash. Precise and accurate neutron star radius measurements with next-generation gravitational wave detectors. *Phys. Rev. D*, 112(6):063020, September 2025. .

H. S. Köhler. Skyrme force and the mass formula. , 258(2):301–316, February 1976. .

Y. Kojima. Two Families of Normal Modes in Relativistic Stars. *Progress of Theoretical Physics*, 79(3):665–675, March 1988. .

K. D. Kokkotas and B. F. Schutz. W-modes - A new family of normal modes of pulsating relativistic stars. *MNRAS*, 255:119–128, March 1992. .

Kostas D. Kokkotas and Gerhard Schafer. Tidal and tidal-resonant effects in coalescing binaries. *MNRAS*, 275(2):301–308, July 1995. .

Scott Koranda, Nikolaos Stergioulas, and John L. Friedman. Upper Limits Set by Causality on the Rotation and Mass of Uniformly Rotating Relativistic Stars. *ApJ*, 488(2):799–806, October 1997. .

A. Kosovichev, J. Schou, Philip Scherrer, Philip Goode, W. Dziembowski, Edward Rhodes, and SOI Team. Spherical and aspherical structure of the sun: First year of soho/mdi observations. *Proceedings of the International Astronomical Union*, 185:157, 01 1998.

Nicolas Kovensky and Andreas Schmitt. Holographic quarkyonic matter. *Journal of High Energy Physics*, 2020(9):112, September 2020. .

C. J. Krüger, W. C. G. Ho, and N. Andersson. Seismology of adolescent neutron stars: Accounting for thermal effects and crust elasticity. *Phys. Rev. D*, 92:063009, Sep 2015. . URL `https://link.aps.org/doi/10.1103/PhysRevD.92.063009`.

Christian Krüger. *Seismology of adolescent general relativistic neutron stars*. PhD thesis, University of Southampton, November 2015. URL `https://eprints.soton.ac.uk/384187/`.

Hao-Jui Kuan and Kostas D. Kokkotas. Last three seconds: Packed message delivered by tides in binary neutron star mergers. *Phys. Rev. D*, 108(6):063026, September 2023. .

Hao-Jui Kuan, Arthur G Suvorov, and Kostas D Kokkotas. General-relativistic treatment of tidal g-mode resonances in coalescing binaries of neutron stars – I. Theoretical framework and crust breaking. *Monthly Notices of the Royal Astronomical Society*, 506(2):2985–2998, 07 2021a. ISSN 0035-8711. . URL `https://doi.org/10.1093/mnras/stab1898`.

Hao-Jui Kuan, Arthur G Suvorov, and Kostas D Kokkotas. General-relativistic treatment of tidal g-mode resonances in coalescing binaries of neutron stars – II. As triggers for precursor flares of short gamma-ray bursts. *MNRAS*, 508(2):1732–1744, 09 2021b. ISSN 0035-8711. . URL `https://doi.org/10.1093/mnras/stab2658`.

Ankit Kumar and Hajime Sotani. Asteroseismology and universal relations in neutron stars with gravitationally bound dark matter. *Phys. Rev. D*, 111(12):123028, June 2025. .

Deepak Kumar, Tuhin Malik, Hiranmaya Mishra, and Constança Providência. Robust universal relations in neutron star asteroseismology. *Phys. Rev. D*, 108(8):083008, October 2023. .

D. Lai. Resonant Oscillations and Tidal Heating in Coalescing Binary Neutron Stars. *Mon. Not. R. Astron. Soc.*, 270:611, October 1994. .

Dong Lai. Resonant oscillations and tidal heating in coalescing binary neutron stars. *Monthly Notices of the Royal Astronomical Society*, 270(3):611–629, 10 1994. ISSN 0035-8711. . URL `https://doi.org/10.1093/mnras/270.3.611`.

Dong Lai. Dynamical Tides in Rotating Binary Stars. *ApJ*, 490(2):847–862, December 1997. .

J. M. Lattimer and M. Prakash. The Physics of Neutron Stars. *Science*, 304(5670):536–542, April 2004. .

James M. Lattimer and Madappa Prakash. Neutron star observations: Prognosis for equation of state constraints. *Phys. Rept.*, 442(1-6):109–165, April 2007. .

Hong-Bo Li, Yong Gao, Lijing Shao, and Ren-Xin Xu. Asteroseismology of Compact Stars. *Universe*, 10(4):157, March 2024. .

L. Lindblom, G. Mendell, and J. R. Ipser. Relativistic stellar pulsations with near-zone boundary conditions. *Phys. Rev. D*, 56(4):2118, August 1997. .

Lee Lindblom and Benjamin J. Owen. Effect of hyperon bulk viscosity on neutron-star r-modes. *Phys. Rev. D*, 65(6):063006, March 2002. .

Keith H. Lockitch and John L. Friedman. Where are the modes of isentropic stars? *The Astrophysical Journal*, 521(2):764–788, aug 1999. . URL `https://doi.org/10.10862F307580`.

Domenico Logoteta. Hyperons in Neutron Stars. *Universe*, 7(11):408, October 2021. .

Mia Sloth Lundkvist, Daniel Huber, Víctor Silva Aguirre, and William J. Chaplin. *Characterizing Host Stars Using Asteroseismology*, pages 1655–1678. Springer International Publishing, Cham, 2018. ISBN 978-3-319-55333-7. . URL `https://doi.org/10.1007/978-3-319-55333-7_177`.

R. Machleidt and D. R. Entem. Chiral effective field theory and nuclear forces. *Phys. Rept.*, 503 (1):1, June 2011. .

Michele Maggiore. *Gravitational Waves: Volume 1: Theory and Experiments*. 2007. .

P. N. McDermott. Density Discontinuity G-Modes. *Mon. Not. R. Astron. Soc.*, 245:508, July 1990.

P. N. McDermott, H. M. van Horn, and J. F. Scholl. Nonradial g-mode oscillations of warm neutron stars. *The Astrophysical Journal*, 268:837–848, May 1983. .

Z. Miao, E. Zhou, and A. Li. Resolving Phase Transition Properties of Dense Matter through Tidal-excited g-mode from Inspiralling Neutron Stars. *ApJ*, 964(1):31, March 2024. .

M. C. Miller, F. K. Lamb, A. J. Dittmann, S. Bogdanov, Z. Arzoumanian, K. C. Gendreau, S. Guillot, A. K. Harding, W. C. G. Ho, J. M. Lattimer, R. M. Ludlam, S. Mahmoodifar, S. M. Morsink, P. S. Ray, T. E. Strohmayer, K. S. Wood, T. Enoto, R. Foster, T. Okajima, G. Prigozhin, and Y. Soong. PSR J0030+0451 Mass and Radius from NICER Data and Implications for the Properties of Neutron Star Matter. *ApJ*, 887(1):L24, December 2019. .

M. C. Miller, F. K. Lamb, A. J. Dittmann, S. Bogdanov, Z. Arzoumanian, K. C. Gendreau, S. Guillot, W. C. G. Ho, J. M. Lattimer, M. Loewenstein, S. M. Morsink, P. S. Ray, M. T. Wolff, C. L. Baker, T. Cazeau, S. Manthripragada, C. B. Markwardt, T. Okajima, S. Pollard, I. Cognard, H. T. Cromartie, E. Fonseca, L. Guillemot, M. Kerr, A. Parthasarathy, T. T. Pennucci, S. Ransom, and I. Stairs. The Radius of PSR J0740+6620 from NICER and XMM-Newton Data. *ApJ*, 918(2):L28, September 2021a. .

M. C. Miller et al. The Radius of PSR J0740+6620 from NICER and XMM-Newton Data. *The Astrophysical Journal Letters*, 918(2):L28, September 2021b. .

G. Miniutti, J. A. Pons, E. Berti, L. Gualtieri, and V. Ferrari. Non-radial oscillation modes as a probe of density discontinuities in neutron stars. *MNRAS*, 338(2):389–400, 01 2003. ISSN 0035-8711. . URL `https://doi.org/10.1046/j.1365-8711.2003.06057.x`.

J. R. Oppenheimer and G. M. Volkoff. On massive neutron cores. *Phys. Rev.*, 55:374–381, Feb 1939. . URL `https://link.aps.org/doi/10.1103/PhysRev.55.374`.

P. T. H. Pang, T. Dietrich, I. Tews, and C. Van Den Broeck. Parameter estimation for strong phase transitions in supranuclear matter using gravitational-wave astronomy. *Phys. Rev. Res.*, 2(3):033514, September 2020. .

J. M. Pearson, N. Chamel, S. Goriely, and C. Ducoin. Inner crust of neutron stars with mass-fitted skyrme functionals. *Phys. Rev. C*, 85:065803, Jun 2012. . URL `https://link.aps.org/doi/10.1103/PhysRevC.85.065803`.

C. L. Pekeris. Nonradial Oscillations of Stars. *The Astrophysical Journal*, 88:189, September 1938. .

A. J. Penner, N. Andersson, D. I. Jones, L. Samuelsson, and I. Hawke. Crustal failure during binary inspiral. *The Astrophysical Journal Letters*, 749(2):L36, apr 2012. . URL `https://dx.doi.org/10.1088/2041-8205/749/2/L36`.

F. A. E. Pirani. On the physical significance of the Riemann tensor. *Acta Physica Polonica*, 15: 389–405, January 1956.

F. A. E. Pirani. Invariant Formulation of Gravitational Radiation Theory. *Physical Review*, 105 (3):1089–1099, February 1957. .

T. Pitre and E. Poisson. General relativistic dynamical tides in binary inspirals without modes. *Phys. Rev. D*, 109(6):064004, March 2024. .

Tristan Pitre and Eric Poisson. General relativistic dynamical tides in binary inspirals without modes. *Phys. Rev. D*, 109:064004, Mar 2024. . URL `https://link.aps.org/doi/10.1103/PhysRevD.109.064004`.

P. Pnigouras, F. Gittins, A. Nanda, N. Andersson, and D. I. Jones. The dynamical tides of spinning Newtonian stars. *MNRAS*, 527(3):8409–8428, January 2024. .

P. Pnigouras, N. Andersson, F. Gittins, and A. R. Counsell. Dynamical neutron star tides: the signature of a mode resonance. *Mon. Not. R. Astron. Soc.*, 542(2):1375–1387, September 2025a. .

P. Pnigouras, N. Andersson, F. Gittins, and A. R. Counsell. Dynamical neutron-star tides: The signature of a mode resonance. in preparation, 2025b.

Pantelis Pnigouras. *Saturation of the f-mode instability in neutron stars*. PhD thesis, U. Tubingen, 2017.

Pantelis Pnigouras and Kostas D. Kokkotas. Saturation of the f -mode instability in neutron stars: Theoretical framework. *Phys. Rev. D*, 92(8):084018, October 2015. .

Pantelis Pnigouras, Fabian Gittins, Amlan Nanda, Nils Andersson, and David Ian Jones. Rotating love: The dynamical tides of spinning newtonian stars, 2022. URL `https://arxiv.org/abs/2205.07577`.

Eric Poisson and Clifford M. Will. *Structure of self-gravitating bodies*, page 63–137. Cambridge University Press, 2014. .

A. Y. Potekhin, A. F. Fantina, N. Chamel, J. M. Pearson, and S. Goriely. Analytical representations of unified equations of state for neutron-star matter. *Astronomy and Astrophysics*, 560:A48, December 2013. .

M. Punturo et al. The Einstein Telescope: a third-generation gravitational wave observatory. *Classical Quant. Grav.*, 27(19):194002, October 2010. .

G. Raaijmakers, T. E. Riley, A. L. Watts, S. K. Greif, S. M. Morsink, K. Hebeler, A. Schwenk, T. Hinderer, S. Nissanke, S. Guillot, Z. Arzoumanian, S. Bogdanov, D. Chakrabarty, K. C. Gendreau, W. C. G. Ho, J. M. Lattimer, R. M. Ludlam, and M. T. Wolff. A Nicer View of PSR J0030+0451: Implications for the Dense Matter Equation of State. *ApJ*, 887(1):L22, December 2019. .

G. Raaijmakers, S. K. Greif, K. Hebeler, T. Hinderer, S. Nissanke, A. Schwenk, T. E. Riley, A. L. Watts, J. M. Lattimer, and W. C. G. Ho. Constraints on the Dense Matter Equation of State and Neutron Star Properties from NICER's Mass-Radius Estimate of PSR J0740+6620 and Multimessenger Observations. *ApJ*, 918(2):L29, September 2021. .

C. A. Raithel and E. R. Most. Tidal deformability doppelgänger: Implications of a low-density phase transition in the neutron star equation of state. *Phys. Rev. D*, 108(2):023010, July 2023a. .

C. A. Raithel and E. R. Most. Degeneracy in the Inference of Phase Transitions in the Neutron Star Equation of State from Gravitational Wave Data. *Phys. Rev. Lett.*, 130(20):201403, May 2023b. .

J. S. Read, L. Baiotti, J. D. E. Creighton, J. L. Friedman, B. Giacomazzo, K. Kyutoku, C. Markakis, L. Rezzolla, M. Shibata, and K. Taniguchi. Matter effects on binary neutron star waveforms. *Phys. Rev. D*, 88(4):044042, August 2013. .

Jocelyn Read. Waveform uncertainty quantification and interpretation for gravitational-wave astronomy. *Class. Quantum Grav.*, 40(13):135002, may 2023. . URL `https://dx.doi.org/10.1088/1361-6382/acd29b`.

D. Reese, F. Lignieres, and M. Rieutord. Oscillations of rapidly rotating stars. *Communications in Asteroseismology*, 147:65–68, January 2006. .

Tullio Regge and John A. Wheeler. Stability of a Schwarzschild Singularity. *Physical Review*, 108(4):1063–1069, November 1957. .

A. Reisenegger and P. Goldreich. Excitation of Neutron Star Normal Modes during Binary Inspiral. *ApJ*, 426:688, May 1994. .

Andreas Reisenegger and Peter Goldreich. A New Class of g-Modes in Neutron Stars. *ApJ*, 395:240, August 1992a. .

Andreas Reisenegger and Peter Goldreich. A New Class of g-Modes in Neutron Stars. *The Astrophysical Journal*, 395:240, August 1992b. .

D. Reitze et al. Cosmic Explorer: The U.S. Contribution to Gravitational-Wave Astronomy beyond LIGO. Provided by the SAO/NASA Astrophysics Data System, 2019.

T. E. Riley, A. L. Watts, S. Bogdanov, P. S. Ray, R. M. Ludlam, S. Guillot, Z. Arzoumanian, C. L. Baker, A. V. Bilous, D. Chakrabarty, K. C. Gendreau, A. K. Harding, W. C. G. Ho, J. M. Lattimer, S. M. Morsink, and T. E. Strohmayer. A NICER View of PSR J0030+0451: Millisecond Pulsar Parameter Estimation. *ApJ*, 887(1):L21, December 2019. .

T. E. Riley, A. L. Watts, P. S. Ray, S. Bogdanov, S. Guillot, S. M. Morsink, A. V. Bilous, Z. Arzoumanian, D. Choudhury, J. S. Deneva, K. C. Gendreau, A. K. Harding, W. C. G. Ho, J. M. Lattimer, M. Loewenstein, R. M. Ludlam, C. B. Markwardt, T. Okajima, C. Prescod-Weinstein, R. A. Remillard, M. T. Wolff, E. Fonseca, H. T. Cromartie, M. Kerr, T. T. Pennucci, A. Parthasarathy, S. Ransom, I. Stairs, L. Guillemot, and I. Cognard. A NICER View of the Massive Pulsar PSR J0740+6620 Informed by Radio Timing and XMM-Newton Spectroscopy. *ApJ*, 918(2):L27, September 2021. .

Thomas E. Riley et al. A nicer view of the massive pulsar psr j0740+6620 informed by radio timing and xmm-newton spectroscopy. *The Astrophysical Journal Letters*, 918(2):L27, sep 2021. . URL `https://dx.doi.org/10.3847/2041-8213/ac0a81`.

Stefan B. Rüster, Matthias Hempel, and Jürgen Schaffner-Bielich. Outer crust of nonaccreting cold neutron stars. *Phys. Rev. C*, 73:035804, Mar 2006. . URL `https://link.aps.org/doi/10.1103/PhysRevC.73.035804`.

H. Saio. Rotational and tidal perturbations of nonradial oscillations in polytropic star. *The Astrophysical Journal*, 244:299–315, February 1981. .

M. V. S. Saketh, Zihan Zhou, and Mikhail M. Ivanov. Dynamical tidal response of Kerr black holes from scattering amplitudes. *Phys. Rev. D*, 109(6):064058, March 2024. .

A. K. Schenk, P. Arras, É. É. Flanagan, S. A. Teukolsky, and I. Wasserman. Nonlinear mode coupling in rotating stars and the r-mode instability in neutron stars. *Phys. Rev. D*, 65(2): 024001, December 2001. .

Brian D. Serot. A relativistic nuclear field theory with π and ρ mesons. *Physics Letters B*, 86 (2):146–150, September 1979. .

N. N. Shchechilin, N. Chamel, and J. M. Pearson. Unified equations of state for cold nonaccreting neutron stars with brussels-montreal functionals. iv. role of the symmetry energy in pasta phases. *Phys. Rev. C*, 108:025805, Aug 2023. . URL `https://link.aps.org/doi/10.1103/PhysRevC.108.025805`.

Hajime Sotani and Bharat Kumar. Universal relations between the quasinormal modes of neutron star and tidal deformability. *arXiv e-prints*, art. arXiv:2109.08145, September 2021. .

William M. Spinella. *A Systematic Investigation of Exotic Matter in Neutron Stars*. PhD thesis, Claremont Colleges Consortium, California, January 2017.

Jan Steinhoff, Tanja Hinderer, Alessandra Buonanno, and Andrea Taracchini. Dynamical tides in general relativity: Effective action and effective-one-body Hamiltonian. *Phys. Rev. D*, 94 (10):104028, November 2016. .

Jan Steinhoff, Tanja Hinderer, Tim Dietrich, and Francois Foucart. Spin effects on neutron star fundamental-mode dynamical tides: Phenomenology and comparison to numerical simulations. *Phys. Rev. Res.*, 3(3):033129, August 2021. .

L. Suleiman, M. Fortin, J. L. Zdunik, and P. Haensel. Influence of the crust on the neutron star macrophysical quantities and universal relations. *Phys. Rev. C*, 104:015801, Jul 2021. . URL `https://link.aps.org/doi/10.1103/PhysRevC.104.015801`.

Y. Suwa, T. Yoshida, M. Shibata, H. Umeda, and K. Takahashi. On the minimum mass of neutron stars. *Mon. Not. R. Astron. Soc.*, 481(3):3305, December 2018. .

I. Tews, J. Carlson, S. Gandolfi, and S. Reddy. Constraining the Speed of Sound inside Neutron Stars with Chiral Effective Field Theory Interactions and Observations. *ApJ*, 860(2):149, June 2018a. .

I. Tews, J. Margueron, and S. Reddy. Critical examination of constraints on the equation of state of dense matter obtained from GW170817. *Phys. Rev. C*, 98(4):045804, October 2018b. .

the Digital Library of Mathematical Functions. Nist digital library of mathematical functions. URL `https://dlmf.nist.gov`.

K. S. Thorne. Nonradial Pulsation of General-Relativistic Stellar Models. IV. The Weakfield Limit. *ApJ*, 158:997, December 1969. .

Kip S. Thorne and Alfonso Campolattaro. Non-Radial Pulsation of General-Relativistic Stellar Models. I. Analytic Analysis for L ¿= 2. Astrophysical Journal, vol. 149, p.591, September 1967.

Richard C. Tolman. Static solutions of einstein's field equations for spheres of fluid. *Phys. Rev.*, 55:364–373, Feb 1939. . URL `https://link.aps.org/doi/10.1103/PhysRev.55.364`.

Alejandro Torres-Forné, Pablo Cerdá-Durán, Andrea Passamonti, Martin Obergaulinger, and José A. Font. Towards asteroseismology of core-collapse supernovae with gravitational wave observations - II. Inclusion of space-time perturbations. *MNRAS*, 482(3):3967–3988, January 2019. .

Vinh Tran, Suprovo Ghosh, Nicholas Lozano, Debarati Chatterjee, and Prashanth Jaikumar. g -mode oscillations in neutron stars with hyperons. *Phys. Rev. C*, 108(1):015803, July 2023. .

David Tsang, Jocelyn S. Read, Tanja Hinderer, Anthony L. Piro, and Ruxandra Bondarescu. Resonant shattering of neutron star crusts. *Phys. Rev. Lett.*, 108:011102, Jan 2012. . URL `https://link.aps.org/doi/10.1103/PhysRevLett.108.011102`.

Wasaburo Unno, Yoji Osaki, Hiroyasu Ando, H. Saio, and H. Shibahashi. *Nonradial oscillations of stars*. University of Tokyo Press, 1989.

R. V. Wagoner. Test for the existence of gravitational radiation. *The Astrophysical Journal Letters*, 196:L63–L65, March 1975. .

J. D. Walecka. A theory of highly condensed matter. *Annals of Physics*, 83:491–529, January 1974. .

Anna L. Watts. Constraining the neutron star equation of state using pulse profile modeling. *AIP Conference Proceedings*, 2127(1):020008, 07 2019. . URL `https://doi.org/10.1063/1.5117798`.

Nevin N. Weinberg, Phil Arras, and Joshua Burkart. An instability due to the nonlinear coupling of p-modes to g-modes: Implications for coalescing neutron star binaries. *The Astrophysical Journal*, 769(2):121, may 2013. . URL `https://dx.doi.org/10.1088/0004-637X/769/2/121`.

Clifford Will. The confrontation between general relativity and experiment. *Living Reviews in Relativity*, 17, 06 2014. .

Wenrui Xu and Dong Lai. Resonant tidal excitation of oscillation modes in merging binary neutron stars: Inertial-gravity modes. *Physical Review D*, 96(8), oct 2017. . URL `https://doi.org/10.11032Fphysrevd.96.083005`.

Shijun Yoshida and Yasufumi Kojima. Accuracy of the relativistic Cowling approximation in slowly rotating stars. *MNRAS*, 289(1):117–122, 07 1997. ISSN 0035-8711. . URL `https://doi.org/10.1093/mnras/289.1.117`.

H. Yu, N. N. Weinberg, P. Arras, J. Kwon, and T. Venumadhav. Beyond the linear tide: impact of the non-linear tidal response of neutron stars on gravitational waveforms from binary inspirals. *Mon. Not. R. Astron. Soc.*, 519(3):4325–4343, March 2023. .

Hang Yu, Phil Arras, and Nevin N. Weinberg. Dynamical tides during the inspiral of rapidly spinning neutron stars: Solutions beyond mode resonance. *Phys. Rev. D*, 110(2):024039, July 2024a. .

Hang Yu, Phil Arras, and Nevin N. Weinberg. Dynamical tides during the inspiral of rapidly spinning neutron stars: Solutions beyond mode resonance. *Phys. Rev. D*, 110(2):024039, July 2024b. .

Tianqi Zhao, Peter B. Rau, Alexander Haber, Steven P. Harris, Constantinos Constantinou, and Sophia Han. Suppression of composition g-modes in chemically-equilibrating warm neutron stars. *arXiv e-prints*, art. arXiv:2504.12230, April 2025. .